

**Evolutionary Stages of Massive Star
Formation**

by

Samuel John Billington

Thesis

Submitted to the University of Kent

for the degree of

Doctor of Philosophy

School of Physical Sciences

September 2019

**University of
Kent**

ABSTRACT

Massive stars play a vital role in the evolutionary of the Galaxy; they produce powerful outflows, strong stellar winds and large amounts of ultraviolet radiation, while being responsible for the chemical enrichment of heavy materials within the interstellar medium. Due to the importance and effects of these celestial objects, not only on their local environments but also on their host galaxy, it is necessary to understand the earliest stages of their formation. However, our knowledge of how massive stars form is still fairly limited due to their rarity and rapid evolution, along with observational limitations. This Thesis presents three studies of massive star forming regions and utilises various molecular line transitions to investigate the initial environments and evolutionary stages of massive star formation.

The first study presents the results from the ammonia mapping of 34 regions in the southern Galactic plane. The first two inversion transitions of the ammonia molecule have been used to map the dense gas within these star formation regions. Physical properties of these regions have been derived from the observed ammonia spectra and supplemented with the results from the ATLASGAL compact source catalogue. These data have been used to construct a rudimentary evolutionary sequence for massive star formation based on the morphology of the associated high-density gas; it is shown that there are no observed changes in the morphology of the dust emission within the regions of interest, however, changes are observed in the morphology of the molecular line emission, which is sensitive to high densities. Maser catalogues from the MMB and HOPS surveys are also employed, and are shown to be an effective and useful tool in the study of star formation; these provide an insight into regions of possible triggered star formation and as a tool to identify the locations of young massive stars.

In the second study, the association rate between the class II 6.7 GHz methanol maser and interstellar dust clumps is investigated, and found to be 99%. The physical parameters of maser associated clumps are determined and these clumps are found to be generally more compact, dense and luminous. Only clumps with volume densities of $n \geq 10^{4.1} \text{ cm}^{-3}$ are shown to be hosting masers, and using the bolometric luminosities of embedded objects, a minimum required mass for maser emission is derived to be $6 M_{\odot}$. The free-fall times and volume densities of maser associated clumps are used to calculate a statistical lifetime for the 6.7 GHz methanol maser, and this is found to be $\sim 3.3 \times 10^4$ yrs, which is in excellent agreement with theoretical predictions.

The third study considers further maser species that are associated with star formation, which include the 12.2 GHz methanol maser, the 22.2 GHz water maser, and

the four base transitions of the hydroxyl maser (1612, 1665, 1667 and 1720 MHz). The clumps associated with these species are found to be similar in nature to clumps coincident with the 6.7 GHz methanol maser. The timescales of these maser species are derived, in the same fashion as the 6.7 GHz methanol maser, and it is found that they all occupy the same phase of evolution, as shown by the $L_{\text{bol}}/M_{\text{fwhm}}$ ratios ($\sim 10^{0.6}$ and $10^{2.5} L_{\odot} M_{\odot}^{-1}$). Statistical lifetimes are also calculated for each species and these are found to be $\sim 2.0, 1.6, 0.5 \times 10^4$ yrs for the 12.2 GHz methanol, water and hydroxyl masers, respectively. The methanol maser lifetimes are found to be consistent with previous works, although the derived water and hydroxyl lifetimes are considerably shorter.

Overall, the work presented herein supports previous studies in constructing evolutionary sequences based on interstellar molecular emission. The spectral line emissions considered throughout are useful in showing that the physical properties of dense dust clumps across the Galactic plane are ingrained at their formation, and that maser emission of any type is present at the same period during star formation, casting doubt on the previously accepted “straw man” model that proposes that masers can be used as a framework for the evolutionary sequence of massive star formation.

DECLARATIONS

The content herein was composed by the author, and has not been submitted for the purposes of a qualification at any other institution or for any other degree.

The content comprising Chapter 3 was adapted and extended from work which has been published as Billington et al. (2019a).

The content comprising Chapter 4 was adapted and extended from work which has been published as Billington et al. (2019b).

All instances where use has been made of other work has been cited.

ACKNOWLEDGMENTS

First and foremost, I would like to thank my supervisor, *Dr James Urquhart*, not only for being an outstanding supervisor but also for being a good friend and a true legend. There is no way I would have been able to accomplish what I have in the past 3 years without your support and guidance. Thank you for teaching me everything I know about radio astronomy and star formation, and for many drinks down the pub and away. Secondly, thank you to *Dr Dirk Froebrich* for allowing me to observe with the Beacon Observatory and be a part of the SPARK project. These skills have taught me how to be a practical astronomer and I am sure I will continue to put this knowledge to good use in my future endeavours.

Special thanks goes to *Dr Justyn Campbell-White*, thank you for many interesting conversions, drinks down the pub and great times away, I hope that Dundee is treating you well and while I highly doubt that I will be able to match your achievements (especially no corrections!), just remember, at least I know how to comment code correctly! I would also like to thank *Dr Tim Kinnear* for literally being the kindest and most helpful person ever to exist on this planet and *Dr Sally Makin* for continuously making me question my work and for the laughs during PH512. Thank you to *Cordi* for being a great friend and keeping me straight during the difficult times and to *Luke* and *Callum* for the many games of diep and surviv, and for the 104 banter.

There is no way I would have been able to write this thesis without the encouragement and reassurance of *Faith* for which I am extremely grateful. Thank you for being there for me over the past 6 months. I only hope that I can return the support you

have given me when it is time to write your thesis.

Last but not least, I would like to thank my family for their support over the past 3 years. Firstly to my Mum, *Clare*, you have never given up on me, have been there for me no matter what and always made sure that I'm okay. Secondly to my Dad, *Dean*, you are the reason I decided to become a scientist in the first place and I hope that I have made you proud. And finally to my sister, *Stacey*, and her (soon-to-be) husband, *Ricky*. Both of you have helped and encouraged me on this journey and Stacey, you are the best sister anyone could ask for and you have never let me down, so thank you.

P.S. Thank you to James, Mark, Justyn and Sally for reading the draft of this thesis and providing your useful advice and insight. Also thank you to *Lillie* for being the best and cutest little niece in the world, let's hope you do turn out ginger like your uncle!

CONTENTS

Abstract	i
Declarations	iii
Acknowledgments	iv
List of Figures	x
List of Tables	1
Chapter 1 Introduction	1
1.1 Evolutionary Stages of Massive Star Formation	1
1.2 History of Radio Astronomy	2
1.3 The Radio Window	3
1.4 Continuum Emission	4
1.4.1 Thermal Dust Emission	4
1.4.2 Bremsstrahlung	5
1.5 Spectral Line Emission	6
1.5.1 Interstellar Molecules	6
1.5.2 Spectral Line Tracers	7
1.5.3 Masers	8
1.6 Interstellar Medium	10
1.6.1 Molecular Clouds	11
1.6.2 Support Mechanisms within MCs	14
1.6.3 Interstellar Dust	15
1.7 Massive Star Formation	18
1.7.1 Differences between low- and high-mass star formation	20

1.7.2	Formation Sequence	20
1.7.3	Competing Theories	23
1.8	Thesis Aims and Structure	24
1.9	Summary	25
Chapter 2 Theory and Observations		26
2.1	Radiation, Radiative Transfer	26
2.2	Spectral Line Emission	31
2.2.1	Molecular Basics	31
2.2.2	Types of Molecules	31
2.2.3	Types of Emission	32
2.2.4	Emission and Absorption	37
2.2.5	Line Broadening	39
2.2.6	Radiative Transfer with Einstein Coefficients	42
2.2.7	Molecular Temperatures and LTE	44
2.3	Radio Telescopes and Detection	46
2.3.1	Single Dish	46
2.3.2	Interferometers	48
2.3.3	Detectors	49
2.4	The Ammonia Molecule	50
2.5	Deriving Physical Properties - Dust	56
2.6	Summary	61
Chapter 3 Ammonia mapping of the environment of young massive stellar objects		62
3.1	Introduction	62
3.2	Sample selection and archival data	63
3.2.1	the Galactic Legacy Infrared Mid-Plane Survey Extraordinaire (GLIMPSE)	64
3.2.2	the APEX Telescope Large Area Survey of the GALaxy (ATLASGAL)	64
3.2.3	the Methanol MultiBeam (MMB) survey	67
3.2.4	the H ₂ O southern Galactic Plane Survey (HOPS)	67
3.2.5	Extracted properties	68
3.3	Observational data	70
3.3.1	ATCA observations and data reduction	70
3.4	Methods and Source Identification	73
3.4.1	Source extraction	73

3.4.2	RMS and Maser associations	79
3.5	Determination of Physical Properties	86
3.5.1	Ammonia line fitting	86
3.6	Discussion of Physical Parameters	93
3.6.1	Overview of Derived Properties	93
3.6.2	Evolutionary Sequence	94
3.6.3	Comparison of Physical Parameters	96
3.6.4	Interesting Sources	99
3.6.5	Triggered Star Formation	105
3.7	Conclusions	107

Chapter 4 The physical parameters of dust clumps associated with

6.7 GHz methanol masers	109	
4.1	Introduction	109
4.2	Survey Descriptions	110
4.2.1	the Methanol Multibeam (MMB) survey	111
4.2.2	the JCMT Plane Survey (JPS)	111
4.3	MMB Associations	113
4.3.1	Angular correlation of the $60^\circ \geq \ell \geq 20^\circ$ masers	115
4.3.2	Velocity correlation of the $60^\circ \geq \ell \geq 20^\circ$ masers	117
4.3.3	Matching statistics for the whole MMB catalogue	119
4.4	Physical Parameters of Maser Clumps	120
4.4.1	Spectral Energy Distributions	123
4.4.2	Clump Sizes	125
4.4.3	Clump masses and volume densities	128
4.4.4	Stability and free-fall collapse	130
4.4.5	Bolometric and maser luminosities	132
4.4.6	Uncertainties in the physical parameters	134
4.5	Discussion	135
4.5.1	Luminosity, mass and radius correlations	135
4.5.2	$L_{\text{bol}}/M_{\text{fwhm}}$ Ratio Correlations	137
4.5.3	Lower limits on physical conditions	140
4.5.4	Maser Lifetimes	143
4.5.5	Embedded Evolutionary Stages	145
4.6	Conclusions	148

Chapter 5	Investigating the evolutionary stages of star formation through various maser species	151
5.1	Survey Descriptions	153
5.1.1	the HI/OH/Recombination (THOR) line survey	153
5.1.2	the Methanol Multibeam (MMB) survey	153
5.2	Maser Associations	154
5.2.1	Spatial Matching	155
5.2.2	Velocity Offsets	157
5.2.3	Total matched sample	157
5.2.4	Combined window	160
5.3	Physical parameter calculations	163
5.3.1	FWHM radius and clump mass	164
5.3.2	Stability and free-fall times	164
5.3.3	Maser and Bolometric Luminosities	165
5.3.4	$L_{\text{bol}}/M_{\text{fwhm}}$ ratios	166
5.3.5	Uncertainties in Physical Parameters	167
5.4	Discussion	169
5.4.1	Combined Window	169
5.4.2	Physical Parameters	170
5.4.3	“Straw man” model comparison	174
5.5	Conclusions	175
Chapter 6	Summary and Conclusions	178
6.1	Summary	178
6.2	Overall Conclusions	182
6.3	Future Work	183
Bibliography		185

LIST OF FIGURES

1.1 Atmospheric transmission windows	3
1.2 Bremsstrahlung emission	5
1.3 Example images of molecular clouds	13
1.4 Interstellar extinction curve	17
1.5 Galactic distribution of massive stars	19
2.1 Planck spectra	27
2.2 Illustration of brightness	28
2.3 Examples of molecular types	32
2.4 Electronic hydrogen transitions	33
2.5 Morse potential	36
2.6 Emission decay law and associated emission broadening	40
2.7 Antenna beam pattern	47
2.8 Energy levels of the vibrational ground state of ammonia	51
2.9 Ammonia hyperfine splitting and associated spectra	54
2.10 Rotational and kinetic temperatures of ammonia	55
2.11 Example of a fitted spectral energy distribution	57
3.1 Example 8 μ m and associated velocity maps for two regions	65
3.2 Clump aspect ratios	77
3.3 Clump angular offsets	78
3.4 RGB GLIMPSE image of region G344.4257+00.0451	80
3.5 Example maps of early star forming regions	82
3.6 Example maps of late star forming regions	83
3.7 GLIMPSE 8 μ m image examples	85
3.8 Example parameter maps for region G330.9288-00.4070	89

3.9	Example NH ₃ spectra of field G345.5043+00.3480	90
3.10	GLIMPSE RGB images of the differing morphological structure	95
3.11	Example parameter maps of field G318.9480-00.1969	98
3.12	Example parameter maps of field G328.8074+00.6324	100
3.13	Absorption and emission spectra from field G328.8074+00.6324	102
3.14	Example parameter maps of field G345.5043+00.3480	104
3.15	Example GLIMPSE images of potential triggered star formation	106
4.1	Distribution of methanol maser peak flux densities versus the maser integrated flux densities	112
4.2	Example maps of JPS 850 μ m emission from two regions	113
4.3	Maser-dust offset distributions	116
4.4	Venn diagram of maser-dust matches	117
4.5	Maser velocity distributions	118
4.6	Histogram of maser-dust angular offsets	120
4.7	Histogram presenting the distribution of clump heliocentric distances	126
4.8	Example spectral energy distribution and corresponding best fit	126
4.9	Differences between previous and current clump radius values	127
4.10	Distributions of clump FWHM, radius, mass and volume density	129
4.11	Distribution of clump FWHM mass versus $L_{\text{bol}}/M_{\text{fwhm}}$ ratio	130
4.12	Distribution of virial parameter versus clump FWHM mass	131
4.13	Histogram and CDF of clump luminosity	132
4.14	Histogram and CDF of maser luminosity	133
4.15	Distribution of maser velocity range versus maser integrated luminosity	134
4.16	Parameter plots comparing physical properties	135
4.17	Histogram and CDF of $L_{\text{bol}}/M_{\text{fwhm}}$ ratios	137
4.18	Distributions of maser and clump luminosities versus $L_{\text{bol}}/M_{\text{fwhm}}$ ratios	139
4.19	Distance limited sample of volume density versus $L_{\text{bol}}/M_{\text{fwhm}}$ ratio	141
4.20	Distance limited sample of methanol maser luminosity versus volume density	142
4.21	Statistical lifetime for the 6.7 GHz methanol maser	144
4.22	Histogram of clump evolutionary stage denoted by $L_{\text{bol}}/M_{\text{fwhm}}$ ratios	146
4.23	Venn diagram presenting the overlap between methanol masers and HII regions	148
5.1	Maser-ATLASGAL angular offsets	154
5.2	Maser-ATLASGAL velocity offsets	155
5.3	Maser velocity offsets	156

5.4	Venn diagram of hydroxyl transitions associations	158
5.5	Example image of region G301.136-00.226	159
5.6	Venn diagram of Maser-ATLASGAL associations	160
5.7	Physical parameter distributions	161
5.8	Virial parameters versus clump FWHM mass	163
5.9	Luminosity parameter distributions	166
5.10	$L_{\text{bol}}/M_{\text{fwhm}}$ ratio parameter distribution	167
5.11	Distance limited sample of volume density versus $L_{\text{bol}}/M_{\text{fwhm}}$ ratio . . .	168
5.12	Statistical lifetimes for all maser species	173

LIST OF TABLES

1.1	Phases of the interstellar medium	11
1.2	Physical parameters of HII regions	22
3.1	Extracted field parameters from the ATLASGAL survey	69
3.2	Observed field parameters	71
3.3	Table 3.2 continued	72
3.4	Fe11Walker source catalogue for detected clumps	74
3.5	RMS associations	76
3.6	Distribution of masers across the sample	85
3.7	Detected NH ₃ clump parameters	91
3.8	Statistical properties for the whole sample	92
4.1	MMB survey catalogue distribution	111
4.2	Matched MMB sources with the ATLASGAL and JPS catalogues . . .	114
4.3	Unassociated MMB sources	115
4.4	MMB-ATLASGAL matches ($60^\circ > \ell > 20^\circ$)	121
4.5	Maser-dust matches for entire MMB catalogue	122
4.6	Total statistical parameters for all maser associated clumps	124
5.1	Matches between maser species and ATLASGAL	157
5.2	Total statistical parameters for all maser associated clumps	162
5.3	Maser luminosity conversion factors	165
5.4	$L_{\text{bol}}/M_{\text{fwhm}}$ ratio, volume density and luminosities parameter ranges . .	171

CHAPTER 1

INTRODUCTION

1.1 EVOLUTIONARY STAGES OF MASSIVE STAR FORMATION

While the field of astronomy dates back over 5000 years, the study of massive star formation is relatively new. Until recently, stars were thought to be unchanging point-like sources of light. However, around 200 years ago, astronomers realised that stars evolve, that they are born, live for some amount of time and then fade.

The largest and brightest stars in the Galaxy are known as massive stars. These stars are between one and two orders of magnitude larger than our own star and yet can produce over 1000 times the luminosity of the Sun. Massive stars also evolve quickly and live for short amounts of time ($\sim 3\,000\,000 - 10\,000\,000$ years) and are born while still deeply embedded within their natal environments. Furthermore, they end their lives by violently erupting, distributing excessive amounts of energy back into the Galaxy; explosions known as supernovae.

To fully understand the nature of massive stars, a fundamental understanding of their formation is required. The aim of this Thesis is to investigate the evolutionary stages of massive star formation and the molecular emission that exists within the surrounding environments. However, before we can begin to understand the theory of

star formation, we must study the tools that are used to investigate it, starting with radio astronomy.

1.2 HISTORY OF RADIO ASTRONOMY

Radio astronomy was born in the early 1930s; while working at Bell Laboratories, Karl Jansky built a steerable antenna in order to determine the origin of a source of noise that was being detected by receivers operating at 20.5 MHz ($\lambda = 14.6$ m) within the electromagnetic (EM) spectrum (Jansky, 1933a). Jansky discovered that this noise originated from extraterrestrial sources, the maximum intensity of which came from a well determined location in the constellation of Sagittarius (Jansky, 1933b). As Jansky continued his observations he showed that these sources of radiation were distributed throughout the Milky Way; this work was followed up, and improved on, by Grote Reber (Reber, 1940) some years later. During World War II, radio physics had improved due to developments in radar applications and, after the war, scientists turned their attention back to the mysterious radio noise coming from extraterrestrial sources.

Jansky's discovery of radio emission came to be seen as the birth of the new science of radio astronomy and after the major discoveries in the 1950s and 1960s, including the 21-cm hydrogen line (Ewen and Purcell, 1951), quasars (Matthews and Sandage, 1963), pulsars (Hewish et al., 1968) and the cosmic microwave background (Penzias and Wilson, 1965), radio astronomy became fully assimilated into main-stream science. It is now regarded as one of the most important tools available to astronomers in their pursuit of understanding our Galaxy and beyond.

Radio astronomy has opened a new realm of science and enhanced the study of celestial objects. Interstellar sources radiating in the optical spectrum are generally governed by thermal processes due to their relatively high temperatures and are therefore dominated by thermal physics. Many non-thermal processes radiate in the radio spectrum and so different physical mechanisms apply that can be detected and subsequently studied, such as rotational emission from cold molecules and free-free emission from ionised gas. As interstellar extinction decreases with increasing wavelength, molecular material and dust grains are transparent at radio wavelengths and so by using radio waves it also became possible to peer into the depths of giant molecular clouds to study various processes, including the formation of massive stars.

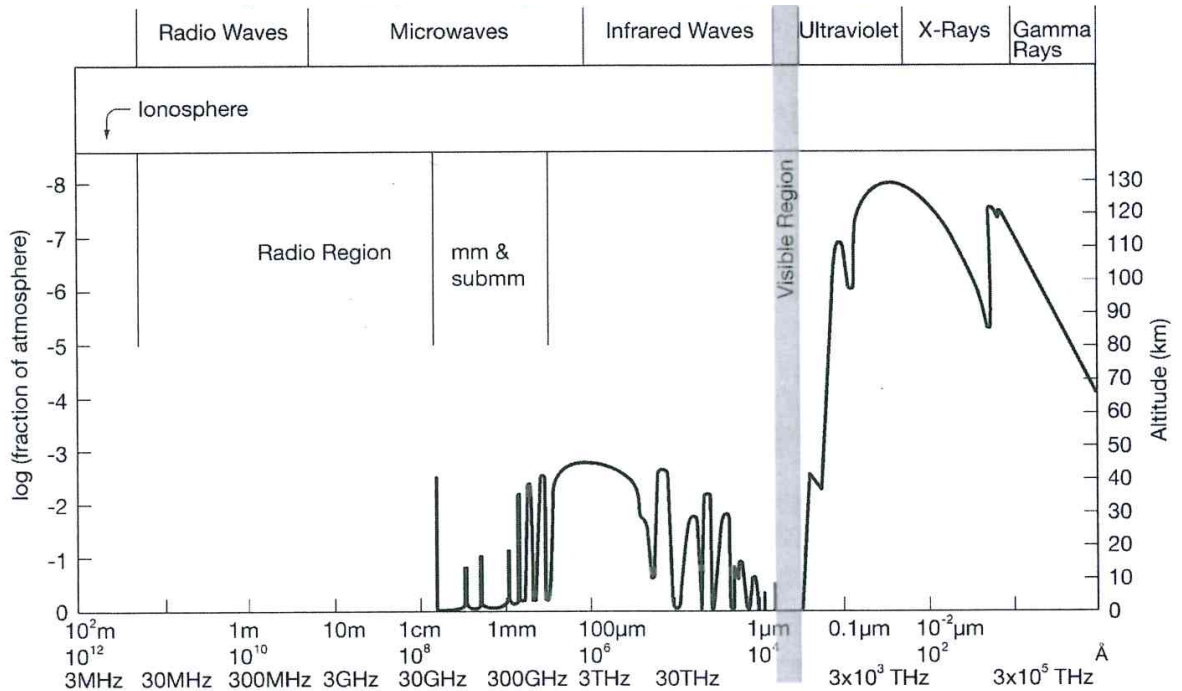


Figure 1.1: Diagram presenting the electromagnetic radiation transmission windows of the Earth's atmosphere. The vertical axes present the fraction of the Earth's atmosphere and the corresponding altitude for radiation to be attenuated by a factor of one half. Figure 1.1 of Wilson et al. (2013).

1.3 THE RADIO WINDOW

Observations at radio wavelengths also have the advantage of the radio transmission window of the Earth's atmosphere. Radiation at radio wavelengths is able to penetrate through the terrestrial atmosphere to the surface of the planet where ground-based instruments can detect these wavelengths. There exists only two regions in the EM spectrum where the atmosphere is sufficiently transparent so that EM radiation can reach the planet's surface, the optical and radio windows. Figure 1.1 shows the altitude within the Earth's atmosphere at which incoming radiation is attenuated by one half, as a function of wavelength and frequency; at visible and radio frequencies the atmosphere is transparent to cosmic radiation. The radio window roughly extends between 30 m (10 MHz) and 0.2 mm (1.5 THz), covering the radio and submillimetre/millimetre (submm/mm) wavelengths, although these limits are dependent on geographical location and time. At higher frequencies ($\nu > 1.5$ THz), the limitation on the detection of radio waves is due to the water vapour and O₂ present in the troposphere, along with other abundant radio absorbing molecules, such as CO₂. Due to this high frequency

cut off at approximately 1.5 THz, radio telescopes are positioned at specific locations which are located at high altitudes. At higher altitudes the amount of water vapour between incoming radio radiation and a receiving instrument is dramatically reduced, hence this is why radio instruments are found in such places. At lower frequencies ($\nu < 10$ MHz), the atmosphere begins to become opaque due to free electrons in the ionosphere. Transmission of radio waves through the atmosphere is impossible if the frequency of the waves is below the plasma frequency of the atmosphere, which is dependent on the atmospheric electron density. The density of free electrons will vary over the course of a 24 hour period and is dependent on solar activity. At frequencies less than 10 MHz, radio astronomy would need to be performed from satellites above the Earth's ionosphere.

Radio emission can be classified into two distinct groups, continuum emission and spectral line emission. A description of each is given below.

1.4 CONTINUUM EMISSION

Continuum emission arises from any source which emits electromagnetic radiation over a range of frequencies. The most common of these sources is that of blackbody emitters. However, while all blackbodies radiate a continuous spectrum, not all continuum emission originates from black bodies. The two most important radio continuum sources in the interstellar medium are those of thermal dust emission and Bremsstrahlung emission (thermal and non-thermal).

1.4.1 THERMAL DUST EMISSION

Dust grains in the interstellar medium (ISM; the material between the stars) will be discussed in the next section. Dust plays a significant role in the cooling of the ISM through thermal dust emission. Interstellar dust is heated through the absorption of energy due to three-body reactions and collisions within the ISM. Over time, this energy is spontaneously emitted at infrared wavelengths, known as thermal dust emission. Dust grains are also responsible for reprocessing ultraviolet photons ($\sim 1\%$) into shorter wavelengths within star formation regions. Mean dust temperatures across the Galaxy are ~ 10 K (Peretto et al., 2010; Zhu and Huang, 2014; Guzmán et al., 2015), and so this emission radiates as a blackbody at these temperatures. This is the main cooling method for the dense molecular ISM, since infrared wavelengths can more easily pass through interstellar material, internal energy within molecular clouds is radiated away

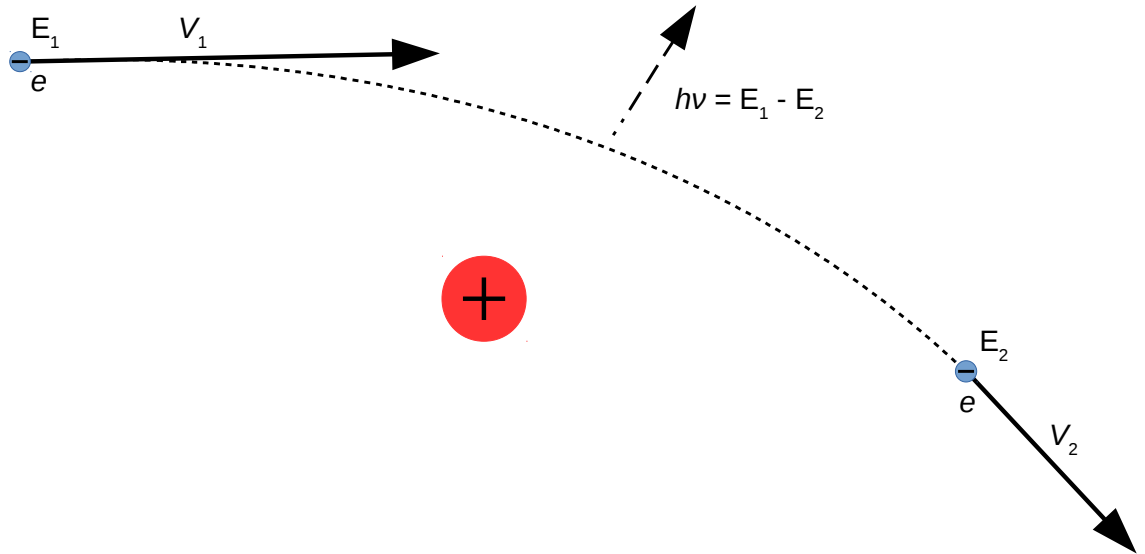


Figure 1.2: Diagram of the Bremsstrahlung emission process. The blue markers represent a decelerating electron at two positions in time with two different velocities (V_1 and V_2), and the red marker represents a positively charged particle. As the electron moves close to the positively charged particle it is accelerated, releasing a radio photon of some energy $h\nu$ (dash-dotted arrow).

keeping temperatures constant. This mechanism is important when investigating the distribution of dust across the Galactic plane. Within regions of star formation, cold dense cores within molecular clouds, dust emission is dominant at wavelengths between $\sim 20\text{--}1\,000\ \mu\text{m}$. The information obtained by thermal dust emission can be used to derive physical parameters of these regions, which will be discussed in Chapter 2.

1.4.2 BREMSSTRAHLUNG

Bremsstrahlung, or free-free emission, is radiation produced by the acceleration of charged particles by magnetic or electric fields of atomic nuclei and dominates at low frequencies ($\nu < 20\ \text{GHz}$) over thermal dust emission. Free-free emission always involves interactions between unbound particles (hence free-free emission) and can either be thermal or non-thermal in nature, which depends on whether or not the constituents involved follow a Maxwell-Boltzmann distribution, if they do then the emission is considered to be thermal in nature. This is the case for emission produced by HII regions, which are regions of intense ultraviolet (UV) radiation which originate from massive stars ($> 8 M_\odot$). These UV photons ionize the surrounding environment creating bubbles of ionised material in the Galaxy. A diagram of thermal Bremsstrahlung emission

is shown in Fig. 1.2. On the other hand, non-thermal Bremsstrahlung is caused by the oscillations of electrons entangled in the magnetic fields of extended coronas of certain kinds of stars, and collimated outflows known as bipolar jets. As these electrons undergo deceleration they will emit non-thermal radio emission.

1.5 SPECTRAL LINE EMISSION

Many types of molecules exist in the Galactic environment (Wilson et al., 2013) that can undergo certain types of emission processes causing radio waves to be emitted. Of particular interest are the vibrational and rotational transitions associated with certain molecular species, such as the 23.7 GHz inversion emission (discussed in Sect 2.4) of ammonia (NH_3), or the 6.7 GHz rotational spectra of methanol (CH_3OH). Energies of these transitions range between 0.1 (infrared regime) to 0.001 eV (cm/mm regime). These spectral line emissions are useful signposts of various environmental conditions and can also be used to derive physical conditions of these environments as described below.

1.5.1 INTERSTELLAR MOLECULES

Before we can consider the theory of molecular emission in interstellar space, we must first look at why interstellar molecules are important, and the types of emission that can be found.

The existence of molecules in interstellar space has only been known for around 75 years since the 1940s (McKellar, 1941), with more than 170 interstellar molecules having been discovered, some containing up to 13 atoms (Bell and Matthews, 1997). These range from simple molecules, such as H_2 , to complex organics, such as ethanol ($\text{CH}_3\text{CH}_2\text{OH}$; Millar et al. 1988) and propanal ($\text{CH}_3\text{CH}_2\text{CHO}$; Hollis et al. 2004).

The foundation for the existence of microwave and radio frequency spectral lines dates back to Townes (1957), who predicted the existence of certain line emissions across the Galaxy. The first molecule to be detected using radio wavelengths was hydroxyl (OH) when Weinreb et al. (1963) observed the absorption spectra of the Λ -type doublet transition of this molecule toward Cassiopeia A. The importance of such science was not realised until 1968 when Cheung et al. (1968) detected the inversion transition emission of ammonia emission towards the Galactic centre. Cheung et al. (1969) also detected emission at 22.2 GHz, known to be a rotational emission line of water, this was also found to be due to maser action, which will be discussed in

Sect. 1.5.3. The first organic molecule detected was formaldehyde (H_2CO) (Snyder et al., 1969), followed closely by the discoveries of hydrogen cyanide (HCN) and carbon monoxide (CO). The majority of molecules have been detected using their rotational spectral lines in the radio regime, while others have been identified using optical or infrared observations of vibrational or electronic emission lines.

The discovery of interstellar molecules led to the birth of astrochemistry, and understanding how these compounds react and form has become a focal point in astronomy. As molecular abundances and detection rates for different emission lines changes across a range of physical environments, the chemical composition of regions in the Galaxy allows for an understanding of what is actually happening within these areas. Chemical composition within dense cores can be used to determine their ages, while other molecules may only emit at particular frequencies when subjected to shocks or high temperatures.

1.5.2 SPECTRAL LINE TRACERS

One of the most important features of interstellar molecules is the different physical processes that they are capable of tracing. The most abundant molecule in the ISM is that of molecular hydrogen (H_2), however, H_2 does not possess a permanent electric dipole moment and so has no detectable rotational transitions. Instead other molecules must be used, the most significant of which is that of carbon monoxide (CO). CO is the most abundant gas phase molecule (Langer, 1976) which emits a rotational spectra at mean interstellar temperatures, and these rotational transitions have been used to extensively study the structure, physical conditions and distribution of molecular clouds (e.g. Rigby et al. 2016; Schuller et al. 2017). CO line data are the main source for estimating the H_2 column density within molecular clouds. The four properties of CO which make it an excellent tool are: low critical density, high line intensities, excitation close to local thermodynamic equilibrium and a large relative abundance to H_2 ($\sim 10^4$; Lacy et al. 1994). CO has also been observed in nearby galaxies and has opened the realm of extragalactic molecular line astronomy.

Another important molecule, and one essential to the work conducted in this thesis, is that of ammonia (NH_3). The ammonia molecule can be used to survey and investigate regions of dense star forming gas as it does not deplete from the gas phase in the cold ($T \sim 10\text{--}40\text{ K}$; Ho and Townes 1983; Mangum et al. 1992) and high-density ($n > 10^4\text{ cm}^{-3}$) conditions that are typical of these natal clumps (Urquhart et al., 2011), making it an excellent probe of the physical conditions in the early stages of star formation.

Ammonia observations have been used by the H_2O Southern Galactic Plane Survey

(HOPS; Walsh et al. 2011; Purcell et al. 2012; Longmore et al. 2017) to map the distribution of dense star forming gas; other studies have used it to investigate the physical properties and kinematics of different kinds of star formation environments in the Galaxy, such as infrared dark clouds (e.g. Pillai et al. 2006; Ragan et al. 2011; Chira et al. 2013) and high-mass star forming regions (e.g. Dunham et al. 2011, Urquhart et al. 2011). The main reason for the wide-spread use of ammonia transitions is that the hyperfine structure of the emission can be used to derive multiple free parameters allowing for an in-depth analyses of the kinematics, morphology and thermodynamics of such regions. This hyperfine structure will be discussed more thoroughly in Chapter 2.

1.5.3 MASERS

As mentioned previously, Weinreb et al. (1963) was the first to detect interstellar hydroxyl. Of the four OH ground state emission lines (1612, 1665, 1667 and 1720 MHz), the two most intense lines, 1665 and 1667 MHz were seen in absorption, whereas the 1720 MHz line appeared in emission. Under local thermodynamic equilibrium conditions this is impossible and so what was observed is the occurrence of a natural interstellar maser.

Masers (Microwave Amplification by Stimulated Emission of Radiation) are systems that produce coherent EM radiation through the amplification by stimulated emission. These are similar to modern laser devices, which are familiar to all of us these days, except produce light at microwave and radio frequencies rather than at optical ones. Masers sources are quite sensitive and require a number of physical conditions in order to produce coherent radiation. These are: a gain medium, a population inversion and a pumping mechanism.

A gain medium is simply the material that produces maser emission and allows amplification of the light produced. The amount of gain these media can generate are dependent on two factors: abundance and density of the emitting material. If an emitting molecule is more abundant, or exists with a higher density, then the amount of potential gain is increased, and therefore, so is the intensity of any potential maser emission.

Another factor required for masers is a population inversion, which occurs within a system when higher energy states are more populated than lower energy states. This is contrary to common physical systems in which lower energy states are more populated. A population inversion allows for stimulated emission to take place and in the absence of an inversion, photons are simply absorbed instead of stimulated as the processes which govern these effects are identical. The theory of stimulated emission will be discussed in greater depth in the next Chapter.

The last piece of the puzzle is that of a pumping mechanism. Once a population inversion is achieved, and for a maser to continuously emit, energy must be constantly injected into the system. This is known as pumping. For interstellar masers the pumping mechanism can either be radiative or collisional, naturally radiative processes rely on a central source emitting at the correct frequencies, usually a star, whereas collisions are connected with the density of the maser regions. Both mechanisms energise molecules into upper energy states allowing for stimulated emission to proceed. Collisionally pumped masers are known as class I masers whereas class II masers are radiatively pumped.

Once these three factors are satisfied maser emission can be produced. Since the gain medium for a maser is generally confined to small spatial regions, radiation produced from masers is considerably focussed, and therefore, this type of emission can be used for measuring distances to celestial objects through the use of parallax measurements. Furthermore, since masers will only exist in certain conditions, they can be used to investigate current physical processes that are happening at their source.

The most relevant maser to this Thesis is the class II 6.7 GHz methanol maser and was first reported by Menten (1991). Multiple studies have found that this maser is exclusively associated with high-mass YSO candidates (e.g. Minier et al. 2003; Xu et al. 2008; Breen et al. 2013) and subsequent submillimetre surveys (e.g. Hill et al. 2005; Breen et al. 2010; Urquhart et al. 2013, 2015b) have found that the majority of 6.7 GHz methanol masers are found to be almost ubiquitously associated with dense clumps across the Galactic plane ($\sim 99\%$; Urquhart et al. 2015b). This provides a simple and convenient method of identifying potential regions of embedded massive star formation in a range of different environments across the Galaxy. It is thought that these masers exist within circumstellar disks around high-mass protostars and that the conditions required for their presence are temperatures of above 150 K, methanol column densities of $> 2 \times 10^{15} \text{ cm}^{-2}$ and hydrogen number densities of $< 10^8 \text{ cm}^{-3}$ (Sobolev et al., 1997), conditions which are only likely to be realised due to the effects of massive star formation. Below the threshold temperature of 90 K methanol is not abundant within protostellar disks Wilson et al. (2013) and stays depleted onto dust grains and if the region densities are too low then the gain medium is ineffective.

Another maser transition of interest is the 22.2 GHz emission produced by water molecules. Interstellar water masers have also been found to be associated with star formation, although are not exclusive to high-mass star formation. In the majority of Galactic sources it is thought that water masers are pumped through collision with atomic and molecular hydrogen within post-shocked gas (Hollenbach and McKee, 1989). Furthermore, it has been theorised that water masers are present in post-shocked

regions associated with outflow and/or accretion processes (Elitzur et al. 1989; initial pre-shocked densities of $n \sim 10^7 \text{ cm}^{-3}$ and temperatures of $\sim 400 \text{ K}$) such as collimated jets from protostars, however, there have also been examples claiming that water emission is produced in circumstellar disks (Garay and Lizano, 1999), much like methanol masers.

The final maser of relevance in this thesis is that of hydroxyl, as mentioned at the beginning of this subsection. Hydroxyl masers produce radiation at four different frequencies: 1612, 1665, 1667 and 1720 MHz. The most abundant of these transitions at 1612 MHz, is typically found to trace the expanding shells of evolved stars (Wilson and Barrett, 1968; Elitzur et al., 1976), while the the emission lines of 1665 and 1667 MHz have generally be found towards regions of star formation (Argon et al., 2000; Qiao et al., 2014, 2016). The 1720 MHz transition is the least frequently found and is mostly associated with shock excited regions within star formation sites and supernovae remnants (Claussen et al., 1999; Caswell, 2004). However, none of these associations are exclusive and all four transitions can be found within different environments and even toward the same region (Caswell et al., 2013; Walsh et al., 2016).

1.6 INTERSTELLAR MEDIUM

The interstellar medium (ISM) is the material that exists between the stars. The material comprising ISM is incredibly inhomogeneous and is constantly evolving. Hydrogen is the main constituent of the ISM, comprising approximately 70% of its mass, with helium contributing a further $\sim 28\%$ and the final 2% is in the form of heavier elements and dust (Spitzer, 1978). The total mass of the Milky Way is unknown but has been estimated to be $\sim 10^{10} M_{\odot}$ (Kalberla and Kerp, 2009). Throughout the Galaxy, the bulk of the mass of the ISM has average particle densities of $n \sim 100 \text{ cm}^{-3}$ and temperatures of between 10 and 100 K (Smith, 2004). However, the ISM also accounts for around 10–15% of the Galactic mass (Mihalas and Binney, 1981).

The dynamics of the ISM are extremely complex and are affected by turbulence, shocks and Galactic magnetic fields that permeate across interstellar space (Indrani and Deshpande, 1999). The ISM is composed of multiple phases depending on the temperature, density and whether the material is in ionic, atomic or molecular form. Table 1.1 presents the phases of the ISM and shows the average physical properties for each phase and their combined total mass. These phases are dynamic and potentially short-lived at any given location within the Galaxy. While the ISM is often divided into these five phases, the question remains on how distinct these phases actually

Table 1.1: Phases of the interstellar medium. Adapted from Klessen and Glover (2016) and Smith (2004).

Phase	Temperature (K)	Particle Density (cm^{-3})	Mass (M_{\odot})
Hot ionised medium	$\sim 10^6$	$\sim 10^{-2}$	3×10^6
Warm ionised medium	~ 8000	0.2–0.5	5×10^7
Warm neutral medium	6 000–10 000	0.2–0.5	2×10^8
Cold neutral medium	50–100	20–50	3×10^9
Molecular clouds	10–20	$> 10^2$	3×10^9

are from one another. Therefore, this classification of material can be seen as an oversimplification as the ISM is highly turbulent and constantly evolving.

The ISM also exists in a constant state of heating and cooling by various physical processes. Heating of the ISM is executed through cosmic ray interactions, photoelectric heating, chemical heating and interstellar shocks. To balance these heating processes, cooling mechanisms also exist, whereby the most effective mechanism is the emission of infrared photons, which are less likely to be scattered and can more readily pass through the ISM and transport energy away. However, since the majority of the ISM possesses very low densities, these heating and cooling process are only typically effective when considering molecular clouds.

1.6.1 MOLECULAR CLOUDS

Molecular clouds (MCs) account for approximately 10–15% of the mass of the ISM, while only occupying ~ 1 –2% of the interstellar volume (Shu et al., 1987; Ferrière, 2001). These clouds are huge entities comprised mainly of molecular hydrogen and are seen across the Milky Way. They are the densest and most massive constituents of the ISM, ranging in size from one parsec to hundreds of parsecs and with mean particle densities of 10^2 – 10^6 cm^{-3} (Larson, 1981), masses up to $10^6 M_{\odot}$ and very low temperatures of approximately 15 K (e.g. Minamidani et al. 2008; Roman-Duval et al. 2010) due to the thermal balance between cosmic ray heating and infrared emission cooling.

Molecular clouds are complicated structures and are at the mercy of destructive physical processes which exist in interstellar space. However, due to the relatively high column densities within these clouds, internal material is shielded from external UV photons, which are capable of photodissociating H_2 molecules. Due to these high densities and protective properties, it is currently accepted that the majority of star formation happens within these entities (Zuckerman and Palmer, 1974). Molecular clouds can be separated into two broad classes, giant molecular clouds and isolated molecular clouds, both of which are discussed in the following subsections. However,

while these classes can be taken as a broad division between the types of molecular clouds, this is not a perfect classification and the properties of molecular clouds can be seen as continuous.

1.6.1(a) GIANT MOLECULAR CLOUDS (GMCs)

Giant molecular clouds (GMCs) are enormous complexes where the majority of massive star formation in the Galaxy takes place. GMCs range in size from 20 to 100 parsecs across (Solomon et al., 1979) and have fairly constant temperatures (~ 15 K) due to the balance of heating and cooling processes (Vázquez-Semadeni et al., 2000). Masses for these clouds can also be estimated from the measurements of carbon monoxide isotopomers and it has been found these masses range between 10^4 to $10^6 M_{\odot}$. Carbon monoxide is preferentially used instead of H_2 , the most abundant molecule, as CO has a rich and useful rotational spectra, which H_2 does not possess due to its lack of permanent dipole moment. Carbon monoxide observations have also shown that the GMCs have an internal structure formed from a number of smaller clumps and filamentary structures, with sizes between 0.1–5 pc and average particle densities of $n \sim 10^3 \text{ cm}^{-3}$ (Shu et al., 1987). Furthermore, these clumps also contain a number of smaller localised regions with high densities ($n \sim 10^6 \text{ cm}^{-3}$) known as molecular cores. These cores possess sizes of < 0.1 pc and masses of 10–1000 M_{\odot} (Bergin and Tafalla, 2007). It is currently thought that these cores can collapse in the absence of any supporting mechanisms and lead to the formation of stars (Shu, 1977). The left panel of Fig. 1.3 presents an image of the Taurus molecular cloud as an example of a GMC.

1.6.1(b) ISOLATED MOLECULAR CLOUDS (IMCs)

Isolated molecular clouds (IMCs), also known as Bok globules (Bok and Reilly, 1947), are located in isolation, outside of larger molecular complexes and are relatively spherical clouds of material. These clouds are characterised by large visual extinctions, low temperatures ($T \sim 10$ K), number densities greater than 10^{10} cm^{-3} and have mean masses of $\sim 10 M_{\odot}$ (Clemens et al., 1991). They are also relatively small regions, typically less than 1 pc in size. In fact, Bok globules may be dense cores which have been stripped of surrounding molecular gas by nearby massive stars. The right panel of Fig 1.3 presents an example of Bok globules located within the NGC281 nebula.



Figure 1.3: Example images of molecular clouds. The left panel presents an European Southern Observatory image of the Taurus molecular cloud, whereas the right panel presents a Hubble Space Telescope image of Bok globules located within the NGC281 nebula.

1.6.2 SUPPORT MECHANISMS WITHIN MCs

If only gravity is taken into consideration then molecular clouds will collapse on the order of their free-fall timescales. This period is the time for a pressure-free, spherical cloud to collapse down to a single point under the effect of its own gravity and is defined as:

$$t_{\text{ff}} = \sqrt{\frac{3\pi}{32G\rho}}, \quad (1.1)$$

where G is the gravitational constant ($6.67 \times 10^{-11} \text{ m}^3 \text{ kg}^{-1} \text{ s}^{-2}$) and ρ is the initial mean density of the cloud (kg m^{-3}). Therefore, clouds with initial densities of $n = 10^3 \text{ cm}^{-3}$ will collapse on a timescale of 10^7 yrs. However, molecular clouds have been predicted to have lifetimes of ~ 1.5 to 27 Myr (Vázquez-Semadeni et al., 2018) which are far longer than the free-fall timescale. This is because free-fall collapse does not take into consideration any internal support mechanisms that can counteract gravity. These support mechanisms are only relevant at the global scale of cloud collapse as on the local scale cores are still capable of collapsing giving birth to new generations of stars. Therefore, molecular clouds can be assumed to be virial objects where self-gravity balances internal disruptive motions. These internal supporting processes are discussed in the follow paragraphs.

1.6.2(a) TURBULENCE

Turbulence is defined as the non-linear state of fluid motions characterised by chaotic changes in pressure and flow velocity at many scales; it exists within the ISM and can be observed through spectral line emission. Line broadening present in observed spectra cannot be explained by thermal processes and are due to the effect of turbulence on the emission source. Typical line-widths observed for CO are $\sim 2\text{--}5 \text{ km s}^{-1}$ (e.g. Wolfire et al. 1993) while the expected thermal line-widths are only a few tenths of 1 km s^{-1} , highlighting the presence of non-thermal supersonic motions affecting the gas. A more detailed explanation of line broadening effects is given in Chapter 2.

Under the conditions within molecular clouds, turbulence likely dissipates on the free-fall timescale (Mac Low and Klessen, 2004) and so for continued turbulence a continuous injection of energy into the material is needed. However, the main driving source for turbulence in the Galaxy is still not clear, although it has been suggested that while feedback from celestial objects may play a role in the production of turbulence (such as HII regions and supernova explosions), it may actually be that gravity plays the most significant role (Krumholz and Burkhardt, 2016). Regardless of the main process,

all turbulent driving sources are non uniform and completely inhomogeneous.

1.6.2(b) THERMAL PRESSURE

Thermal pressure arises from the kinetic energy of material and as the temperature of material rises so does the pressure. On small scales, such as dense cores, thermal pressure can be taken into account as the temperature of such regions are generally higher than the mean of the ISM. However, on global scales, thermal pressure is likely to be ineffective as the average temperature of molecular clouds is ~ 15 K.

1.6.2(c) MAGNETIC FIELDS

Magnetic fields exist across the entire Galaxy and, at different scales, also provide a way to counteract global free-fall. Although magnetic fields can support against collapse they can also aid gravity. The direction of the magnetic field lines will determine this as a cloud is only supported in the direction perpendicular to field lines. Naturally, magnetic fields only affect charged particles such as ions or free electrons while the majority of material in a molecular clouds is electronically neutral. Charged particles can collide with neutrals travelling across field lines, which will inhibit collapse in the parallel direction and assist collapse in the perpendicular direction, a process known as ambipolar diffusion. However, this process is far less effective in low densities regions where neutral particles will rarely encounter a charged particle.

1.6.3 INTERSTELLAR DUST

While interstellar dust grains constitute only 1% of the ISM by mass, it is exceedingly important in determining how chemical and physical processes evolve. Dust grains mainly consist of non-volatile silicates (e.g. olivines, pyroxenes, $\text{Mg}_{2x}\text{Fe}_{2-2x}\text{SiO}_4$ and $\text{Mg}_x\text{Fe}_{1-x}\text{SiO}_3$) and carbonaceous compounds (Knacke, 1977). Typical grain cores are on the order of $0.1 \mu\text{m}$ (Mathis and Whiffen, 1989) and are much larger than molecular species. There also exist smaller grains which have an unknown composition but who also produce spectral features in the near IR between $3-17 \mu\text{m}$ (Leger and Puget, 1984); these are referred to as Polycyclic Aromatic Hydrocarbons (PAHs) (see Tielens 2005). PAHs are hydrocarbons composed of multiple aromatic rings which have a large surface area-to-volume ratio when compared to other dust grain types. On the opposite end of the size scale, very large carbon compounds, such as Fullerene aggregates, have also been observed as a dust constituent (Dartois, 2011; Cami et al., 2011). Dust grains which exist within molecular clouds will be surrounded by a grain mantle consisting of water ice containing various molecules which have depleted onto grain surfaces.

Currently, the nature of how these grains form is still unclear. The amount of dust in the Galaxy appears to remain constant, however, it has been shown that dust grains have lifetimes of $\sim 22\text{--}72$ Myrs (Temim et al., 2015) and are destroyed through UV and X-ray radiation and, therefore, there must be some production mechanism at work; it is likely that dust grains are formed via coagulation. Observations have shown that grains can be formed in the envelopes of cool stars where production is increased due to enhancement in density within these regions (e.g. Riebel et al. 2012; Dell’Agli et al. 2015). However, the cosmic dust destruction rate is faster than the production rate which has been observed in stellar regions and so other supplementary production processes must also be present. Fulvio et al. (2017) showed that carbonaceous grains can in fact be formed in low temperatures “in situ” through condensation processes. Supernovae remnants have also been shown to be significant production sites of dust particles (Dunne et al., 2003). These mechanisms aid in the explanation of the observed dust grain quantity.

Another impact of dust grains on observational astronomy is that of interstellar extinction. When looking up to the Milky Way at optical wavelengths, patches of darkness can be seen stretching across the night sky. These regions appear devoid of stars and light. However, these regions are not in fact absent of stars, rather what we see are dust clouds which obscure the light from stars behind them as we look into the Galaxy. The amount of attenuation of distance star-light depends on the number density and size of dust grains, thickness of the cloud and wavelength of EM radiation trying to transverse the material. Extinction can be modelled using the Mie theory of scattering and so longer wavelengths are capable of passing through dust clouds, whereas shorter wavelength radiation is more likely to be scattered and absorbed. The transmission of longer wavelength radiation through these regions causes Galactic sources to appear redder in colour as we view them, an effect known as interstellar reddening. Blue light which is scattered from its original path can cause objects known as reflection nebula to be seen, a process which is analogous to Rayleigh scattering within the Earth’s atmosphere (causing the sky to appear blue). Therefore, when looking towards and into regions with high dust grain number densities, radio wavelengths are employed as this type of radiation can travel through these regions unhindered. By measuring the different colours of a interstellar source, it is possible to calculate the amount of extinction at any particular wavelength by creating an interstellar extinction curve (Savage and Mathis, 1979), an example of which is shown in Fig. 1.4 and it can be seen that extinction decreases with increasing wavelength. There is also a well known feature at $4.6\ \mu\text{m}^{-1}$ known as the $2175\ \text{\AA}$ bump (Stecher, 1965), the origin of this is not well understood although there is a general agreement it is caused by graphite, or

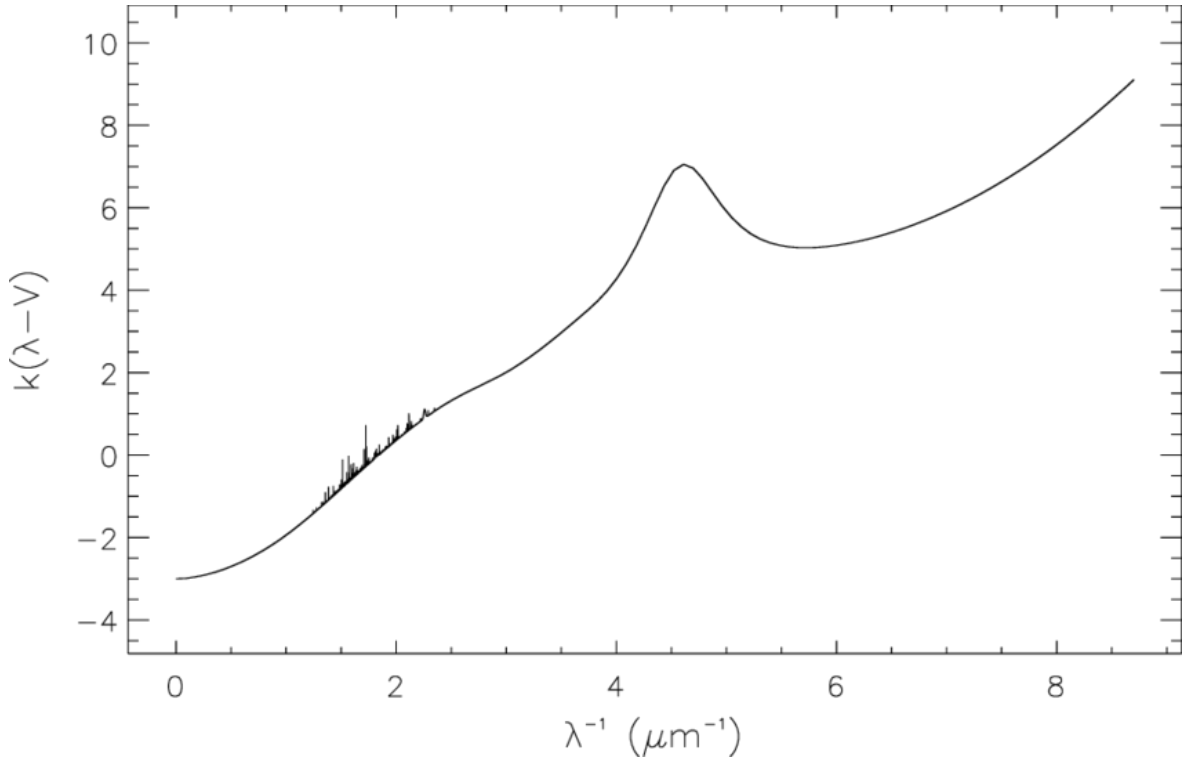


Figure 1.4: An example of an interstellar extinction curve. Figure 1 of Mulas et al. (2011).

some less well-ordered form of carbon that cannot attenuate light as efficiently.

The final and arguably most important aspect of interstellar dust is molecular formation. This type of chemistry which encompasses grain-surface reactions, is critically important in astrochemistry and explains how complex molecules are capable of being formed in the interstellar medium. In high density regions, such as cold molecular cores, atoms and molecules can adsorb onto the surface of dust grains through collisions. These molecules stay attached to the surface of grains through Van der Waals forces, or physisorption and, in some cases, chemisorption. Molecules move across grain surfaces by thermal hopping, allowing for reactions to take place according to the Langmuir-Hinshelwood mechanism. In short, dust grains are collection sites for molecules in interstellar space, which are then able to react with each other and sufficiently increase the formation rates of simple and complex molecules alike. An important factor in this discussion is the formation of molecular hydrogen, the most abundant constituent of the ISM. Atomic hydrogen adsorbs onto grain surfaces and, due to the high surface mobility of hydrogen, can quickly react with other H atoms and convert into molecular form. The grains also act as a third body to absorb excess energy during this reaction and therefore stabilise the molecular formation. This excess energy heats the dust and also contributes to the ejection of the newly formed H_2 . This production process is

efficient up to 300 K (Cazaux and Tielens, 2002) and is responsible for the quantity of molecular hydrogen seen in the Galaxy.

1.7 MASSIVE STAR FORMATION

Massive stars ($> 8 M_{\odot}$) play a vital role in the evolution of the Galaxy due to their powerful outflows, strong stellar winds, large amounts of UV radiation and chemical enrichment of material of the ISM. These feedback processes can have a dramatic impact on the local environment by changing the chemistry and injecting huge amounts of energy into the ISM. They are also responsible for driving strong shocks into the surrounding molecular clouds, which can have a direct affect on future generations of stars through the compression, and subsequent collapse, of molecular structures, often referred to as triggered star formation (e.g. Elmegreen and Lada 1977; Elmegreen 2002; Urquhart et al. 2007c; Thompson et al. 2012). Massive stars therefore play an important role in regulating future generations of stars and driving the evolution of their host galaxies (Kennicutt 2005).

Our knowledge of massive star formation is still fairly limited as relatively few of these objects are located closer than a few kpc and they almost exclusively form in tight clusters or loosely bound associations, making it difficult to distinguish between individual protostellar cores and stars observationally. More importantly, high-mass stars are relatively rare and evolve far more quickly than lower-mass stars, and so will reach the main sequence while still deeply embedded within their initial environment. Even though high-mass stars are difficult to observe, given the extensive effect that high-mass stars have, not only on their local environments but also on the whole of their host galaxy, it is important to understand the underlying processes of the earliest stages of their formation.

These stars generally form in two distinct ways, either in tightly bound gravitational OB clusters, or in loose unbound OB associations. OB clusters can contain upwards of 100 massive stars in a very compact region (< 1 pc), whereas for an association, OB stars can be spread over the entire face of a giant molecular cloud and are not confined to a dense region with distances between the stars of between 1 pc and 10 pc. This could imply that two different methods of star formation are ongoing, leading to different end products, although it has been observed that OB associations also contain compact clusters as well. The currently known Galactic distribution of massive stars, above $10^4 L_{\odot}$ is shown in Fig. 1.5.

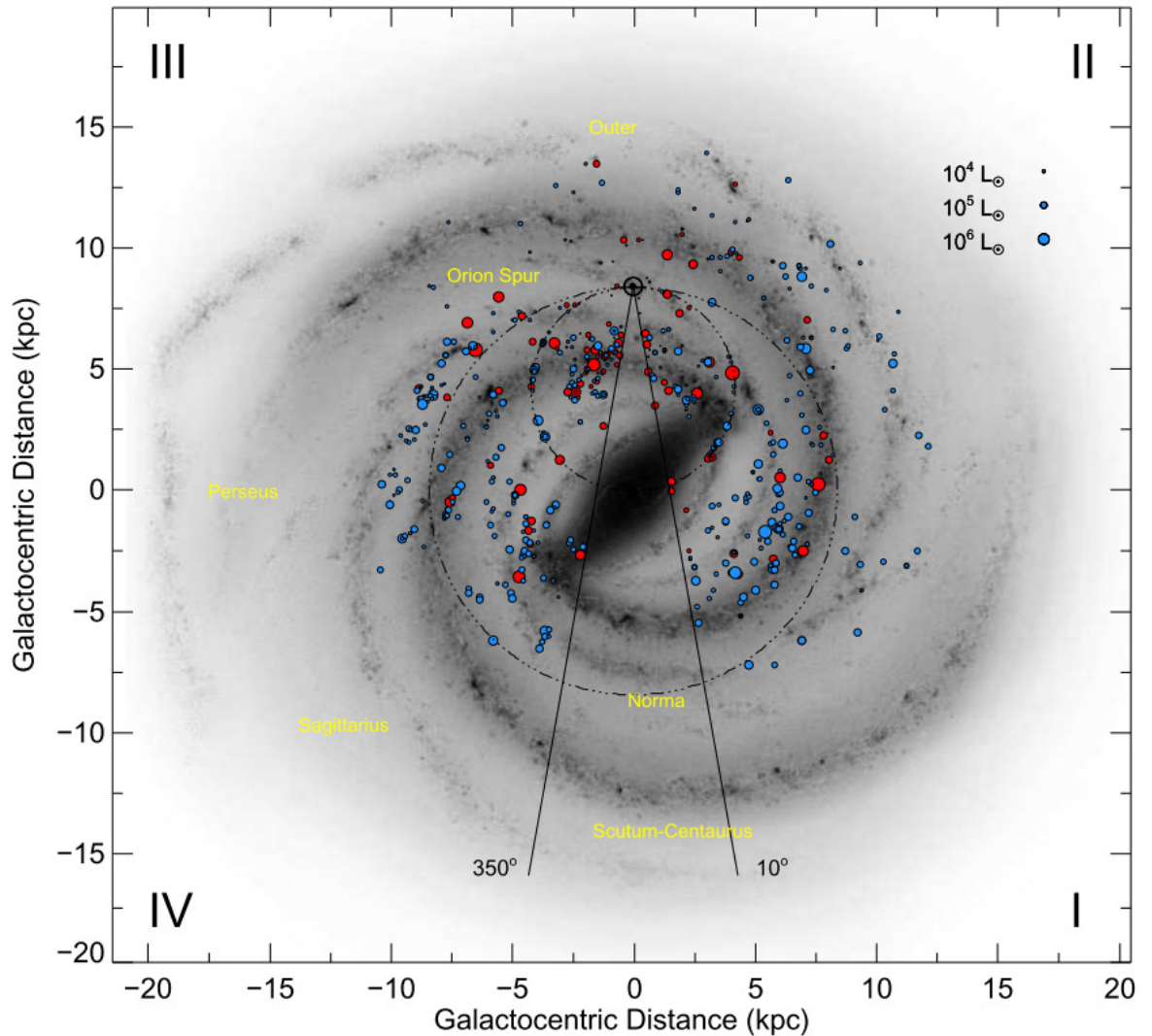


Figure 1.5: The Galactic distribution of all massive young stellar objects and HII regions above bolometric luminosities of $10^4 L_{\odot}$. Figure 6 from Urquhart et al. (2014b). Red and blue circles show the kinematic positions of complexes and individual sources respectively, with the size of the markers being proportional to luminosity. The two solid black lines enclose the Galactic centre that has been excluded due to source confusion and poor distance determination. The larger dot-dashed circle presents the solar circle and the smaller dot-dashed line represents the locus of the tangent points.

1.7.1 DIFFERENCES BETWEEN LOW- AND HIGH-MASS STAR FORMATION

Now that an understanding of the ISM has been discussed, and the importance of massive stars has been stated, we can begin to build a picture of how stars are born. While it may be logical to assume that massive star formation is simply a scaled up version of low- and intermediate-mass star formation, this is not the case. This is due to the different timescales at work in star formation regions. The first has already been discussed and that is the free-fall timescale. The second is the Kelvin-Helmholtz timescale, which is the time required to reach thermal equilibrium:

$$t_{\text{KH}} = \frac{GM^2}{RL}, \quad (1.2)$$

where G is the gravitational constant ($6.67 \times 10^{-11} \text{ m}^3 \text{ kg}^{-1} \text{ s}^{-2}$), M is the mass of a core (kg), R is the radius (m) and L is the luminosity (W). For high-mass star formation t_{KH} is less than the free-fall timescale, whereas the opposite is true for low-mass formation. This means that a massive star will continue to accrete material after it has reached the main sequence, unlike their lower mass counterparts which finish accreting millions of years before they contract onto the main sequence. In general, any star with a mass greater than $8 M_{\odot}$ is considered a massive star.

Another distinct difference between low- and high-mass star formation is the excess of UV radiation which is produced by the latter. Due to massive stars containing far more material than average sized stars, their temperature is greatly increase when compared to low-mass stars and so the blackbody radiation they produce is shifted into the UV regime, causing the production of HII regions as mentioned previously. The free-free radiation produced in these regions, along with radio recombination lines, are signposts of massive stars.

1.7.2 FORMATION SEQUENCE

Massive star formation can be divided into four distinct phases following the general initial lifetime for the birth of a star: compression, collapse, accretion and disruption; these are explained in the following subsections.

1.7.2(a) COMPRESSION

It is a currently accepted that stars are born from the compression and collapse of dense cores of gas and dust within molecular clouds. As mentioned previously, molecular clouds are extremely inhomogeneous and contain dense cores and clumps. The first

stage of the formation process is the fragmentation of molecular clouds into starless clumps ($\sim 1\,000\,M_\odot$), which are induced by cloud inhomogeneities and gravo-turbulent cloud fragmentation. These clumps will then proceed to fragment further into individual starless cores ($\sim 100\,M_\odot$). These cores generally have temperatures of around 10–15 K and densities of 10^5 cm^{-3} . If affected by only gravity, these cores would collapse very quickly (on free-fall timescales) towards their respective centre of mass. However, as discussed above, there are various support mechanisms that likely play a role on local core scales and well as global molecular cloud scales.

1.7.2(b) COLLAPSE

Over time, each core continues to attract mass from its natal molecular reservoir eventually forming a star. By using the virial theorem, which describes the condition of equilibrium for a stable, gravitationally bound system (i.e. $2K + U = 0$), we can define the Jeans criterion:

$$M_c > M_J,$$

where M_c is the mass of the core and M_J is the Jeans mass, defined as:

$$M_J \simeq \left(\frac{5k_B T}{G\mu m_H} \right)^{\frac{3}{2}} \left(\frac{3}{4\pi\rho_0} \right)^{\frac{1}{2}}, \quad (1.3)$$

where k_B is the Boltzmann constant ($1.38 \times 10^{-23}\text{ m}^2\text{ kg s}^{-2}\text{ K}^{-1}$), T and ρ_0 are the mean temperature (K) and density of the cloud (kg m^{-3}) respectively, G is the gravitational constant ($6.67 \times 10^{-11}\text{ m}^3\text{ kg}^{-1}\text{ s}^{-2}$), μ is the mean molecular weight and m_H is the atomic mass of hydrogen (kg). The Jeans criterion states that if the mass of a core is above the Jeans mass then a spontaneous collapse will be initiated and, therefore, the Jeans mass is the absolute minimum mass required for a cloud or core to begin collapsing. The core will continue to collapse and fragment until it becomes optically thick, at this point, the temperature of the core will increase, and therefore, the Jeans mass will also increase. Once the core is optically thick, fragmentation will cease and the core will collapse as a single entity to a single star. Once the core begins collapsing into a protostar, it will continue to accrete material.

1.7.2(c) ACCRETION

Once a protostellar object has formed, and has achieved hydrostatic equilibrium (gravity is balanced with radiation pressure), it continues to grow in mass through accretion. Large accretion disks form around these objects due to the increase in rotational forces

Table 1.2: Physical parameters of HII regions. Adapted from Kurtz (2005).

Class of Region	Size (pc)	Particle Density (cm^{-3})	Ionized Mass (M_{\odot})
Hypercompact	$\lesssim 0.03$	$\gtrsim 10^6$	$\sim 10^{-3}$
Ultracompact	$\lesssim 0.1$	$\gtrsim 10^4$	$\sim 10^{-2}$
Compact	$\lesssim 0.5$	$\gtrsim 10^3$	~ 1
Classical	~ 10	~ 100	$\sim 10^5$

during gravitational collapse (Yorke and Bodenheimer, 1999). Material is transported from the accretion disks onto the main core over time, although the exact details of this process are still unclear. During this accretion phase, the star will only gain mass if its accretion rate is higher than the mass it loses through stellar winds and outflows. Therefore, gravity must exceed the outward flowing radiative pressure of the accreting core. For this to happen there are three solutions; (a) the effective opacity of the accretion disk must be sufficiently low so radiation pressure has a small effect on the inflowing material; (b) total luminosity of the star must be reduced and therefore less radiation is affecting the disk; (c) the stellar mass must be increased in order for gravity to have a greater effect.

1.7.2(d) DISRUPTION

Once a massive star reaches the main sequence it will begin to produce copious amounts of ultraviolet radiation, unlike low-mass stars. This radiation ionises the local environment and creates a bubble of ionised material, known as a HII region. HII regions are initially small and are known as hypercompact HII regions with sizes of ~ 0.01 pc. This is thought to be when the UV radiation begins to ionise the outer layer of circumstellar disks (Zinnecker and Yorke, 2007). As HII regions expand, they start ionizing the surrounding environment, and become ultracompact with sizes of ~ 0.1 pc. The existence of an ultracompact HII region may mark the end of the existence of an accretion disk. Over time, these regions will continue to expand into the ISM for as long as their driving star is burning ($\sim 10^6$ yrs), becoming compact and then classical HII regions. The physical parameters for the different classes of HII regions are given in Table 1.2. Stars which can form HII regions are known as OB stars according to their spectral classification.

The effects of this phase contribute an interesting problem; inevitably a massive star will reach the main sequence and be exerting huge amounts of radiation pressure against its local environment and therefore any material it is capable of accreting, hence there must be an upper mass limit for the size of a star. Statistical techniques have

been used in order to try and determine this upper mass limit using the initial mass function; Oey and Clarke (2005) find a value of $120\text{--}200 M_{\odot}$ whereas Koen (2006) finds a value of between $140\text{--}160 M_{\odot}$; massive stars are generally observed to have such masses and so an accepted mass limit for the size of stars is $150 M_{\odot}$, however the mass of some stars has been calculated far above this value (Crowther et al., 2010).

One last effect to consider is that of triggered star formation. This is a concept first proposed by Elmegreen and Lada (1977), wherein an ionization shock front produced by the expansion of HII regions created by one group of massive stars provides the external pressure to compress adjacent material in a molecular cloud, thereby inducing subsequent generations of massive stars to form. This mechanism may play a significant role in the evolution of massive star forming regions (e.g. Thompson et al. 2012).

1.7.3 COMPETING THEORIES

Currently there are three competing theories of how massive stars accrete their mass and then subsequently form, they are monolithic collapse, competitive accretion and star mergers; a brief description of each is given below.

Monolithic collapse (McKee and Tan, 2003) assumes that a certain amount of material within a molecular cloud is gravitational bound during the initial start point of the formation of a star, and that the only competition for the infalling material is between close members of a cluster. This method essentially assumes that before a star is formed it has access to a limited amount of mass from within its natal cloud and that the initial mass necessary for the formation of massive stars is directly proportional to the end product.

Competitive accretion (Bonnell et al., 1997, 2001) differs in that the material reservoir that is available to any one star depends on where that star is located in relation to its natal cloud. For an accreting object at the centre of a cloud, its gravitational domain, and area from which it can accrete mass, is essentially the entire cloud, whereas the domain of an off-centre protostar is tidally limited by the total mass in the inner part of the cloud. Since the gas reservoir available to all protostars within a cloud is limited, these objects eventually compete for matter as the accretion domains inevitably overlap. This also means that due to the preferential location of central stars, they are able to accrete more mass than their counterparts due to material flowing down through the cloud to its gravitational centre. Therefore, it would be expected that the largest star in a cluster or association would be found towards the centre.

Finally, stellar mergers (or collisions) have also been proposed for forming massive stars (Bonnell and Bate, 2002). It is possible, due to the density of OB clusters, that two intermediate mass stars could collide, creating a much larger object. However, not

all OB stars form in clusters and so this method cannot necessarily explain how all high-mass stars form. Gravitational focusing can enhance the effective cross-section of collisions and therefore close stellar encounters become realistic and it is thought that stellar mergers do contribute to a proportion of massive stars but are unlikely to be the reason behind all formations.

It is likely that the majority of massive stars are formed by a combination of the first two methods. A star may naturally have a reservoir of material only available to itself during the initial phases of a core and while it moves throughout a molecular cloud, more material becomes available for accretion.

1.8 THESIS AIMS AND STRUCTURE

The main aims and structure of this Thesis are as follows:

THEORY AND OBSERVATIONS (Chapter 2)

This Chapter covers the theory and relevant knowledge required for an understanding of the work presented. The concepts of radiative transfer and spectral line emission are discussed, followed by a description of telescope systems. Finally the methods used throughout this Thesis to obtain physical parameters are derived.

AMMONIA MAPPING OF THE ENVIRONMENT OF YOUNG MASSIVE STELLAR OBJECTS (Chapter 3)

This Chapter presents ammonia observations towards 34 regions of interest in the southern hemisphere. The first two inversion transitions of the ammonia molecule, along with archival data from various Galactic surveys, has been used to investigate the morphological and physical differences within regions of star formation.

THE PHYSICAL PARAMETERS OF DUST CLUMPS ASSOCIATED WITH 6.7 GHz METHANOL MASERS (Chapter 4)

This Chapter investigates the relationship between dust continuum emission and the class II 6.7 GHz methanol maser. The Methanol MultiBeam (MMB) survey catalogue is matched to the APEX Telescope Large Area Survey of the GALaxy

(ATLASGAL) and JCMT Plane Survey (JPS) dust emission catalogues to provide insight into the association between maser emission and Galactic dust. The physical parameters of maser associated clumps are derived and where these masers fit into the current theory of massive star formation is analysed.

INVESTIGATING THE EVOLUTIONARY STAGES OF STAR FORMATION THROUGH VARIOUS MASER SPECIES (Chapter 5)

This Chapter investigates the evolutionary stages of massive star formation through various maser species. Methanol, water and hydroxyl masers are matched to dust continuum sources as identified by the ATLASGAL survey. The properties of maser associated clumps are analysed and the period where maser emission exists during star formation is quantified, along with the statistical lifetimes of the maser species.

SUMMARY & CONCLUSIONS (Chapter 6)

This Chapter provides a detailed summary of the Thesis and overall conclusions from the results and discussions. Future work is also outlined and discussed.

1.9 SUMMARY

This Chapter has provided background information on radio astronomy, the interstellar medium and high-mass star formation, along with the aims and structure of the Thesis. While this Chapter gives an introduction to the work presented herein, the theoretical foundation for the forthcoming studies is given in the next chapter.

CHAPTER 2

THEORY AND OBSERVATIONS

2.1 RADIATION, RADIATIVE TRANSFER

Almost everything that is known about the Universe is derived through the study of electromagnetic radiation. This is due to the large relative distances in astronomy and the extreme conditions which exist. Radio wavelengths in the mm and submm range have proven to be some of the most useful tools in studying the initial conditions of star formation, as they are capable of penetrating through regions of dense gas and large visual extinctions.

Interstellar sources that thermally radiate and are also in thermal equilibrium, can be described as a blackbody and are governed by the Planck law:

$$B_\nu(T) = \frac{2h\nu^3}{c^2} \frac{1}{e^{h\nu/kT} - 1}, \quad (2.1)$$

where h is the Planck constant ($6.63 \times 10^{-34} \text{ m}^2 \text{ kg s}^{-1}$), c is the speed of light ($3 \times 10^8 \text{ m s}^{-1}$), k is the Boltzmann constant ($1.38 \times 10^{-23} \text{ m}^2 \text{ kg s}^{-2} \text{ K}^{-1}$) and T is the temperature of the body (K). The Planck function describes the spectral density of a source. Figure 2.1 presents a number of blackbody curves with differing temperatures for a large frequency range.

Electromagnetic radiation at radio wavelengths is governed by the processes of waves rather than particles, however, if the size of a system is large compared to the

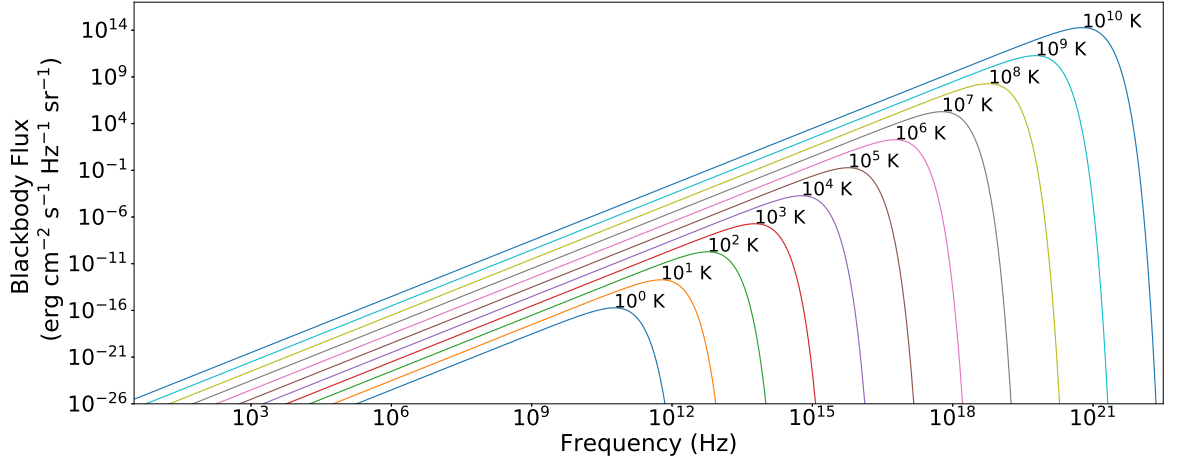


Figure 2.1: Examples of Planck blackbodies curves at different temperatures.

wavelength of interest then we may consider light to travel as rays. The intensity of a source, or brightness (I_ν), is defined by the equation:

$$dP = I_\nu \cos\theta \, d\Omega \, d\sigma \, d\nu, \quad (2.2)$$

where dP is the infinitesimal power (W), $d\sigma$ is the infinitesimal source area (m^2), $d\nu$ is the infinitesimal bandwidth (Hz), θ is the angle between the normal to $d\sigma$ and in the direction of $d\Omega$ (sr). I_ν is usually called the intensity ($\text{W m}^{-2} \text{Hz}^{-1} \text{sr}^{-1}$), or specific intensity, rather than brightness and is independent of the distance between the source and observer. If we integrate the full intensity of a source that subtends some solid angle on the sky ($d\Omega$) we can obtain the total intensity of a source:

$$S_\nu = \int_{\Omega_s} I_\nu(\theta, \varphi) \cos\theta \, d\Omega, \quad (2.3)$$

The solid angle of a source is measured in steradians (sr), which is a dimensionless unit and is equivalent to square radians; the total solid angle of a sphere viewed from an internal observer is equal to 4π steradians. This total intensity, known as the source's flux density, is measured in units of $\text{W m}^{-2} \text{Hz}^{-1}$, i.e. the flux per unit frequency. This can be simplified as:

$$S_\nu = I_\nu \Delta\Omega. \quad (2.4)$$

The majority of radio sources have very low intensities and so a special unit of flux density exists which is used when dealing with radio emission known as the Jansky:

$$1 \text{ Jy} = 10^{-26} \text{ Wm}^{-2} \text{ Hz}^{-1}. \quad (2.5)$$

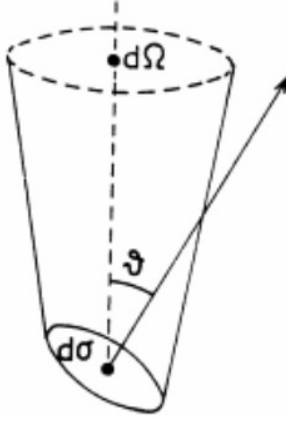


Figure 2.2: A sketch to illustrate the definition of brightness. Figure 1.2 from Wilson et al. (2013).

As previously mentioned, specific intensity is independent of the distance between a source and an observer and so any changes of specific intensity along a ray path is due to emission and absorption processes. These mechanisms are governed by the equation of radiative transfer:

$$\frac{dI_\nu}{ds} = -\alpha_\nu I_\nu + j_\nu, \quad (2.6)$$

where α_ν is the absorption coefficient and j_ν is the emissivity. The equation of transfer shows that the change in intensity along the path of the light is a combination of the amount of absorbed light, which is intrinsically linked with the intensity of a source, and the emissivity along the ray path. There exist three limiting cases for this differential equation each with their own solution:

1. Emission only ($\alpha_\nu = 0$):

$$\frac{dI_\nu}{ds} = j_\nu, \quad I_\nu(s) = I_\nu(s_0) + \int_{s_0}^s j_\nu(s) ds. \quad (2.7)$$

2. Absorption only ($j_\nu = 0$):

$$\frac{dI_\nu}{ds} = -\alpha_\nu I_\nu, \quad I_\nu(s) = I_\nu(s_0) \exp \left[- \int_{s_0}^s \alpha_\nu(s) ds \right]. \quad (2.8)$$

3. Thermodynamic Equilibrium (TE):

$$\frac{dI_\nu}{ds} = 0, \quad I_\nu = B_\nu(T) = \frac{j_\nu}{\alpha_\nu}. \quad (2.9)$$

Under thermodynamic equilibrium, the spectral distribution of a source is described by the Planck function which, according to Kirchhoff's law of thermal radiation, is equal to the ratio between the emissivity and absorption coefficient (j_ν/α_ν). Thermodynamic equilibrium is rarely achieved and instead local thermodynamic equilibrium (LTE) is used, where the changes in temperature vary sufficiently slowly that TE can be assumed locally.

We can define the optical depth of a material as:

$$d\tau_\nu = -\kappa_\nu ds, \quad (2.10)$$

or

$$\tau_\nu(s) = \int_{s_0}^s \kappa_\nu(s) ds. \quad (2.11)$$

The optical depth (τ) is a dimensionless constant that relates the thickness of a material and its absorption coefficient, and due to this definition, s and τ are inversely proportional. We can insert Eq. 2.10 into Eq. 2.6 and rewrite the equation of radiative transfer in terms of optical depth:

$$\frac{dI_\nu}{d\tau} = I_\nu - \frac{j_\nu}{\alpha_\nu}. \quad (2.12)$$

In LTE, $B_\nu(T) = j_\nu/\alpha_\nu$ and so:

$$\frac{dI_\nu}{d\tau} = I_\nu - B_\nu(T), \quad (2.13)$$

the solution to which is:

$$I_\nu(s) = I_\nu(0) e^{-\tau_\nu(s)} + \int_0^{\tau_\nu(s)} B_\nu(T(\tau)) e^{-\tau} d\tau, \quad (2.14)$$

and if the medium is isothermal, we can calculate this integral exactly:

$$I_\nu(s) = I_\nu(0) e^{-\tau_\nu(s)} + B_\nu(T) (1 - e^{-\tau(s)}). \quad (2.15)$$

As the optical depth of a source approaches 0, $e^{-\tau} \rightarrow 1$ (optically thin), Eq. 2.15 becomes $I_\nu(s) = I_\nu(0)$, i.e. the observed intensity is simply the background emission seen towards the source. Conversely, for large optical depths (optically thick), $e^{-\tau} \rightarrow 0$, and we find that $I_\nu(s) = B_\nu(T)$. Therefore, in the optically thick case, the observed intensity from a source is equal to the Planck function and is independent of the emitting material. This result can be modified by removing any contribution to intensity from an intervening medium:

$$I_{\text{source}} = \Delta I_{\nu}(s) = I_{\nu}(s) - I_{\nu}(0) = [B_{\nu}(T) - I_{\nu}(0)](1 - e^{-\tau}). \quad (2.16)$$

When considering the Planck function, if $h\nu \ll kT$ then we obtain the Rayleigh-Jeans law:

$$B_{\text{RJ}}(\nu, T) = \frac{2\nu^2}{c^2} kT. \quad (2.17)$$

This classical limit of the Planck law shows that the temperature and brightness of a source are strictly proportional and so we can define the brightness temperature by rearranging Eq. 2.17:

$$T_{\text{B}} = \frac{c^2}{2k\nu^2} I_{\nu}, \quad (2.18)$$

which presents the temperature, at which, a given brightness would be found if inserted into the Rayleigh-Jeans law. By equating the Planck function (Eq. 2.1) with the Rayleigh-Jeans law (Eq. 2.17), one can define the radiation temperature as:

$$J(T) = \frac{c^2}{2k\nu^2} I_{\nu} = \frac{h\nu}{k} \frac{1}{e^{h\nu/kT} - 1}, \quad (2.19)$$

which is the observed intensity of a source above the background emission. By inserting values for the Planck and Boltzmann constants into Eq. 2.19, we can show that the Rayleigh-Jeans approximation of the Planck law is valid for frequencies $\ll 21 T$ GHz. It can also be seen that at these frequencies the brightness and radiation temperatures are equal in TE.

If the equation for brightness temperature is inserted into the radiative transfer equation, and assuming that the source medium is isothermal, we can solve the radiative transfer equation in the same way as Eq. 2.15 but in terms of temperature, which gives:

$$T_{\text{B}}(s) = T_{\text{B}}(0) e^{-\tau_{\nu}(s)} + T_{\text{ex}}(1 - e^{-\tau_{\nu}(s)}), \quad (2.20)$$

where T_{ex} is excitation temperature of the source (K). If we assume that the temperature of the background is negligible (i.e. $T_{\text{B}}(0) \simeq 0$), then there are two limiting cases to this solution:

1. Optically thin ($\tau \ll 1$):

$$T_{\text{B}} = \tau T_{\text{ex}}. \quad (2.21)$$

2. Optically thick ($\tau \gg 1$):

$$T_{\text{B}} = T_{\text{ex}}. \quad (2.22)$$

As long as the geometry of the source, background and radiating medium is not important then these relations are correct. If the temperature of a background source is subtracted from Eq. 2.20 and we know that the brightness temperature is equivalent to the radiation temperature we find that:

$$T_B(s) = J_\nu(T) = [J_\nu(T_{\text{ex}}) - J_\nu(T_{\text{bg}})](1 - e^{-\tau_\nu(s)}), \quad (2.23)$$

where T_{bg} is the temperature of the background. In the Rayleigh-Jeans limit ($h\nu/kT \ll 1$) Eq. 2.23 can be simplified as:

$$T_B = (T_{\text{ex}} - T_{\text{bg}})(1 - e^{-\tau_\nu(s)}). \quad (2.24)$$

2.2 SPECTRAL LINE EMISSION

2.2.1 MOLECULAR BASICS

Fundamental to this Thesis are certain species of interstellar molecules and their associated spectral emission lines. Before we discuss the spectral line emission of interest, an understanding of how molecules form and the different types of molecules is necessary.

As mentioned in Section 1.5.1, interstellar molecules have been identified, ranging from simple homonuclear diatomic molecules such as H_2 , O_2 and N_2 , to more complex structures such as $\text{CH}_3\text{CH}_2\text{CHO}$ and NH_2CHO . After the discovery of various molecules in the Galaxy it became important to understand the chemical processes of their formation and how the chemical evolution in certain regions changes over time.

2.2.2 TYPES OF MOLECULES

Molecules can be divided into four distinct groups based on molecular rotation: linear, spherical, symmetric top and asymmetric top. The rotation of any molecule can be considered to be the superposition of rotations around three orthogonal axes.

The simplest type of molecules are linear molecules. When all atoms within a molecule lie along the same axes that molecule can be considered linear. In this case the moment of inertia along this axis will be effectively 0, and the moments across the remaining axis will be equal. If Θ is the moment of inertia along an axis then for a linear molecule $\Theta_a = 0$, $\Theta_b = \Theta_c$, where a, b, c are the corresponding axes. In general, when defining our nomenclature, the axis 'a' is considered to have the smallest moment, followed by 'b' and 'c'. Examples of linear molecules include H_2 and CO_2 .

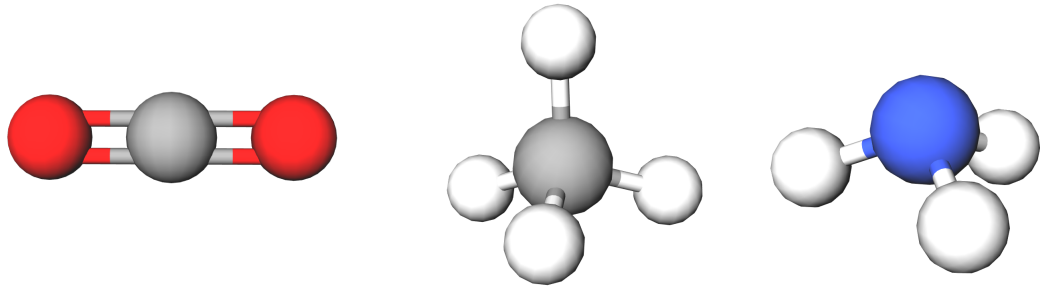


Figure 2.3: Presented from left to right are examples of a linear (carbon dioxide), spherical (methane) and symmetric top (ammonia) molecules.

Spherical molecules have the same moment of inertia across each axes ($\Theta_a = \Theta_b = \Theta_c$) and include CH₄ or Fullerenes. Symmetric top molecules have an 'a' axis with a non-zero moment and the two other moments are equal to each other, $\Theta_a \neq 0$ and $\Theta_b = \Theta_c$. In this case Θ_a can either be smaller than the other two moments, known as prolate symmetrical top molecules, or larger, known as oblate symmetric top molecules. Examples of symmetric top molecules include CH₃CN and NH₃. Finally we have asymmetric top molecules, which have three different moments of inertia across all three of their axes, one example of this type is H₃BO₃. Figure 2.3 presents examples of linear, spherical and symmetric top molecules.

2.2.3 TYPES OF EMISSION

The energy states of atoms and molecules are quantised and when a transition of these states occurs, radiation is emitted with a discrete energy, known as spectral line emission. There exists three processes that may cause the discharge of spectral line emission: electronic, rotational and vibrational transitions. In all three of these processes, systems in a higher energy state fall into a lower energy state and emit a photon whose frequency is determined by the difference in the energy levels, i.e. $\Delta E = h\nu$, and so molecular line emission results from a transition between two states that can be described by different quantum numbers. The total energy of a molecular system can be defined as:

$$W^{\text{tot}} = W^{\text{el}} + W^{\text{vir}} + W^{\text{rot}}, \quad (2.25)$$

where W^{el} is the energy of the electrons and where W^{vir} and W^{rot} are the vibrational and rotational energies respectively, and so W^{tot} is essentially the Hamiltonian of the system.

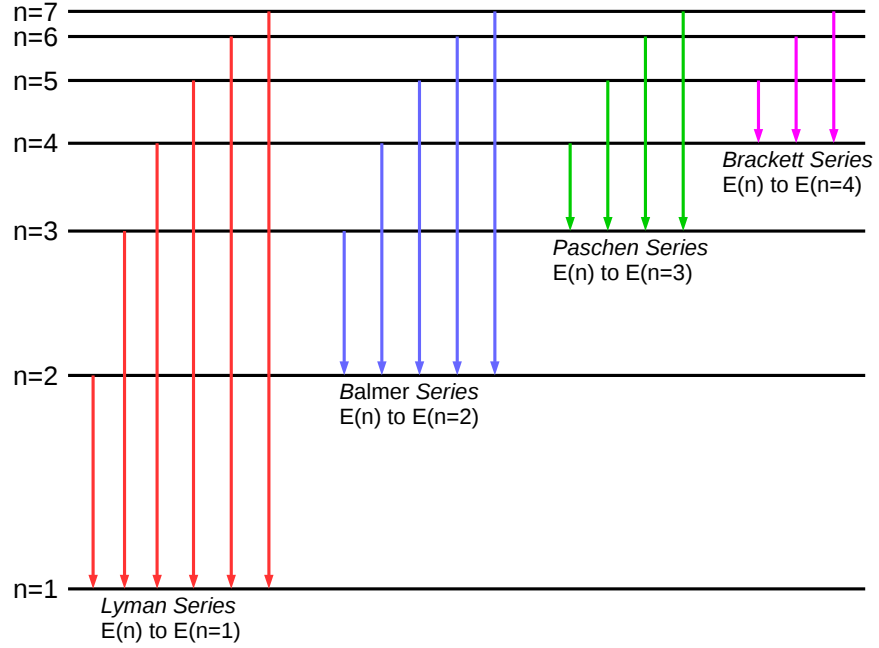


Figure 2.4: Diagram presenting the different series of the electron transitions for the hydrogen atom.

Electronic transitions occur when bound electrons drop into a lower energy orbits around atoms or molecules, these generally have energies of a few eV and the photons that are emitted lie within the visual or UV spectral range. When discussing electronic transitions of the hydrogen atom one commonly refers to the Lyman and Balmer series, which refers to the photons released when an electron moves from a higher electronic state to the ground or first excited energy states respectively (Fig. 2.4). There are situations where useful electronic transitions exist within the radio portion of the EM spectrum; these are known as radio recombination lines (RRLs). Once material has become ionised, such as in HII regions, electrons can recombine with ions and as the electrons cascade down through the energy levels of atomic orbits, recombination line photons are released. This is possible as the time for re-ionisation of the ion ($\sim 10^6$ yrs) is generally of much longer timescales than it takes for the recombination of electrons within a gas ($\sim 10^4$ yrs).

Rotational transitions are caused by the rotation of a molecule around its centre of mass. These transitions generally occur within the radio wavelength regime and have typical energies of $\sim 10^{-3}$ eV. The kinetic energy of rotation is given by:

$$H_{\text{rot}} = \frac{1}{2} \Theta \omega^2 = \frac{\mathbf{L}^2}{2\Theta}, \quad (2.26)$$

where \mathbf{L}^2 is the angular momentum of the rotation ($\mathbf{L}^2 = \Theta \omega$; $\text{kg m}^2 \text{s}^{-1}$). For a diatomic molecule, the moment of inertia Θ (kg m^2) is:

$$\Theta = \frac{m_a m_b}{m_a + m_b} (r_a - r_b), \quad (2.27)$$

where m_a and m_b are the masses of the two nuclei of the molecule (kg), with r_a and r_b being the distances between the nuclei and centre of mass of the molecule (m). If this Hamiltonian is used to solve the Schrödinger equation and derive the eigenvalues for the rotational energy we see that:

$$E_{\text{rot}} = W(J) = \frac{\hbar}{2\Theta} J(J+1), \quad (2.28)$$

where J is the angular momentum quantum number and can only take integer values ($J = 0, 1, 2, \dots$), and \hbar equal to the Planck constant divided by 2π ($\hbar = \frac{h}{2\pi}$). This solution is only correct if we are considering a rigid rotor, however, in reality molecules will be somewhat elastic in nature and will stretch with increasing rotational energy, this is known as centrifugal stretching. In this case, Eq. 2.28 needs to be modified by adding an extra term:

$$E_{\text{rot}} = W(J) = \frac{\hbar}{2\Theta} J(J+1) - hD [J(J+1)]^2, \quad (2.29)$$

where D is the constant for centrifugal stretching. We can then derive an expression that represents the pure rotation spectrum:

$$v(J) = \frac{1}{h} [W(J+1) - W(J)] = 2B_e (J+1) - 4D(J+1)^3, \quad (2.30)$$

with the rotational constant defined as:

$$B_e = \frac{\hbar}{4\pi\Theta}. \quad (2.31)$$

Since the centrifugal stretching constant, D , is positive, the observed line emission from molecular rotation will be lower than those predicted based on a rigid rotator. As J increases, the difference between the predicted frequencies for a rigid rotator and the observed frequencies becomes rapidly larger. One final point to note is that transition between rotational states will only occur if a molecule possess a permanent electric dipole moment and thus homonuclear diatomic molecules, such as H_2 and O_2 , cannot undergo these transitions as they do not possess one, explaining why it is difficult to detect these particular species in interstellar space.

As mentioned previously, there exist symmetric top molecules where $\Theta_b = \Theta_c \neq \Theta_a \neq 0$, which can either be prolate or oblate depending on the value of Θ_a with respect to Θ_b and Θ_c . By using the definition of a symmetric top molecule we obtain a Hamiltonian operator:

$$H = \frac{\mathbf{L}^2}{2\Theta_{b/c}} + L_a^2 \left(\frac{1}{\Theta_a} - \frac{1}{\Theta_{b/c}} \right), \quad (2.32)$$

which has eigenvalues:

$$W(J, K) = J(J+1) \frac{\hbar^2}{2\Theta_a} + K^2 \hbar^2 \left(\frac{1}{\Theta_a} - \frac{1}{\Theta_{b/c}} \right), \quad (2.33)$$

where K is the eigenvalue from the operator L_a^2 and is associated with the principal rotational axis a, and J is the eigenvalue for the operator \mathbf{L}^2 . Simply, J is the quantum number associated with the total angular momentum of the molecule whereas K is the quantum number associated with the angular momentum of the principal rotation axis. The values of these quantum numbers are restricted to:

$$J = 0, 1, 2, \dots \quad K = 0, \pm 1, \pm 2, \dots, \pm J. \quad (2.34)$$

The quantum number J can only be an integer as a photon that is emitted or absorbed can only contribute a change of one in terms of angular momentum, and since K is a portion of J , K must be equal to or less than J . The selection rules for symmetric tops are therefore:

$$\Delta J = 0, \pm 1 \quad \Delta K = 0. \quad (2.35)$$

During a rotational transition there will be no change in K as there is no dipole moment across the principal axis. For vibrational transitions both the J and K values will be constant and so $\Delta J = 0$ and $\Delta K = 0$.

The final type of line emission is that of vibrational transitions. If a nuclei within a molecule is displaced from its equilibrium distance, r_e , from the centre of mass, it will perform an oscillation about r_e , the Schrödinger equation for this scenario is:

$$\left(\frac{p^2}{2m} + P(r) \right) \text{vib}(x) = W^{\text{vib}} \text{vib}(x), \quad (2.36)$$

where $x = r - r_e$ and $P(r)$ is the potential energy of the nuclei. The potential curve of a diatomic molecule is well represented by the Morse potential:

$$P(r) = D_e [1 - e^{-a(r-r_e)}]^2. \quad (2.37)$$

The constant a in this expression represents the curvature of the potential of a simple harmonic oscillator. D_e is the dissociation energy of the molecule at which point the constituents of a molecule will become separated, defined as:

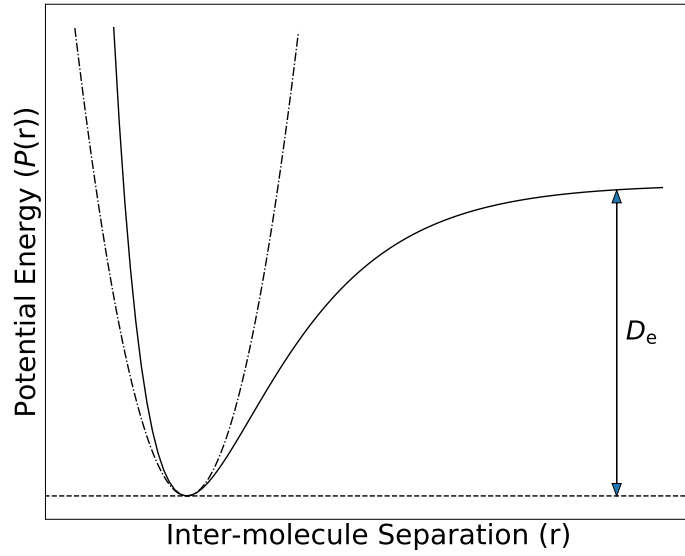


Figure 2.5: The Morse potential for the a simple binary molecule is shown as a solid black line with the corresponding dissociated energy D_e . A simple harmonic approximation is also shown as a dash-dotted line.

$$D_e = P(\infty) - P(r_e). \quad (2.38)$$

Figure 2.5 presents a diagram of the Morse potential for a simple binary molecule. While the Morse potential represents well the potential energy of the nuclei, a simple harmonic approximation is generally sufficient when considering small values of x :

$$P(r) = a^2 D_e (r - r_e)^2. \quad (2.39)$$

In this case, nuclei will oscillate with a classical oscillation frequency:

$$\omega = 2\pi\nu = a \sqrt{\frac{2 D_e}{m}}. \quad (2.40)$$

The eigenvalues for Eq. 2.36 are:

$$W^{\text{vib}} = W(v) = \hbar\omega \left(v + \frac{1}{2}\right), \quad (2.41)$$

where v is the associated quantum number and is an integer value. For a molecule in a particular rotational state, the vibrational transitions will be separated by a constant frequency interval.

2.2.4 EMISSION AND ABSORPTION

In Sect. 2.1 the concept of radiative transfer was introduced and it is seen that two variables control how radiation is affected as it travels through space: the absorption coefficient and the emissivity. The processes of emission and absorption are separated into three different mechanisms: spontaneous emission, absorption and stimulated emission. The transitions within atoms and molecules are caused by one of these processes. However, on a microscopic scale these are difficult to predict and so for large systems we are restricted to looking at the macroscopic scale. At these scales we can use the Einstein coefficients which are intrinsic values for any particular transition. Einstein coefficients govern the rates of absorption and emission of photons by atoms and molecules, and are macroscopic approximations of complex stochastic quantum processes.

We can begin to dissect the emission and absorption mechanisms, along with the associated Einstein coefficients, by investigating the process of spontaneous emission. Let us consider a two-level energy system, with the upper excited energy state defined by u and the lower ground state by l , and at any point in time there will exist a number of particles in the upper state n_u and a number in the lower state n_l . For spontaneous emission, transitions occur from the upper to the lower energy states spontaneously and according to a decay law:

$$n_u \propto e^{-t/\tau}, \quad (2.42)$$

where τ is the time constant of the decay (s) and is intrinsic to any specific transition. We can define the Einstein A coefficient as:

$$A_{ul} = \frac{1}{\tau}, \quad (2.43)$$

and so will have units of s^{-1} . This is the rate at which transitions will occur spontaneously and a larger A coefficient implies emission happens more rapidly than a lower coefficient. From this we can derive differential equations of the spontaneous emission rate:

$$\frac{dn_u}{dt} = -n_u A_{ul} \quad \frac{dn_l}{dt} = n_u A_{ul}, \quad (2.44)$$

Let us now consider absorption, which is when a system absorbs a photon of some frequency causing a transition from the lower energy state to the upper energy state. It is logical to assume that absorption is the inverse of spontaneous emission and so will be governed by the same Einstein coefficient, however, this is not the case. The rate of absorption depends on the intensity and frequency of light that is irradiating

our system and we can define this rate as:

$$\frac{1}{\tau} = I_\nu B_{lu}. \quad (2.45)$$

While the units of the A coefficient are s^{-1} , it can be seen that the B coefficient has units of $\text{Hz cm}^2 \text{sr ergs}^{-1}$. We can determine the rate of change of molecules in the upper energy states by:

$$\frac{dn_u}{dt} = n_l B_{lu} \bar{J}, \quad \frac{dn_l}{dt} = -n_l B_{lu} \bar{J}, \quad (2.46)$$

where \bar{J} is the average energy density of the radiation field:

$$\bar{J} = \frac{4\pi}{c} \int_0^\infty I_\nu \varphi(\nu) d\nu. \quad (2.47)$$

The quantity $\varphi(\nu)$ is the line profile function, which is the function that defines the possible frequencies that are capable of being absorbed by any particular transition. It is not required for a photon to have the exact energy of a transition between two states and the difference in energy between photons and transitions can be rectified through the quantum mechanical uncertainty in the photon's energy, or from the motion of the molecule with respect to the photon. The line profile function is sharply peaked and normalised so that:

$$\int_0^\infty \phi(\nu) d\nu = 1. \quad (2.48)$$

Finally we have stimulated emission, which can be considered to be the opposite of absorption. When a photon with a frequency equivalent to the energy difference between our upper and lower states, passes nearby a constituent of our system, that photon will not be absorbed if the constituent is already in the upper energy state. Instead the photon will agitate the constituent and cause the emission of another photon of the same phase and frequency, and in the same direction as the stimulating photon. Mathematically, stimulated emission is the same as absorption and we can define the rate of emission in the same way (see Eq.2.45). Stimulated emission is efficient when $n_u > n_l$ and this process is the basis for interstellar maser emission.

We have assumed that the Einstein coefficients are intrinsic properties of transitions and so must occur in any situation, including thermodynamic equilibrium. In TE, the rate of emission must balance the rate of absorption and so we can equate spontaneous and stimulated emission with absorption:

$$n_u A_{ul} + n_u B_{ul} \bar{J} = n_l B_{lu} \bar{J}. \quad (2.49)$$

If our two-level system contains many constituents, and is in thermodynamic equilibrium, then at any point in time, a number of constituents will be in both the upper and lower energy states which is described by the Boltzmann distribution:

$$\frac{n_u}{n_l} = \frac{g_u}{g_l} \exp\left(-\frac{\Delta E}{kT}\right), \quad (2.50)$$

where g_u and g_l are the statistical weights of the energy states, ΔE is the energy difference between the states (J), ν_0 is the base frequency of the transition between the states (Hz) and T is known as the excitation temperature of the system (K), which is the temperature required to have the specific ratio of n_u/n_l . If Eq. 2.49 is rearranged in terms of \bar{J} then we see that:

$$\bar{J} = \frac{A_{ul}}{\frac{n_l}{n_u} B_{lu} - B_{ul}}, \quad (2.51)$$

and by substituting n_l/n_u with the Boltzmann distribution:

$$\bar{J} = \frac{A_{ul}}{\frac{g_l}{g_u} \exp\left(\frac{\Delta E}{kT}\right) - 1}. \quad (2.52)$$

However, in TE, I_ν must be given by the Planck function (Eq. 2.1):

$$\bar{J} = \frac{4\pi}{c} B_\nu(T) = \frac{8\pi h\nu^3}{c^3} \frac{1}{\exp\left(\frac{\Delta E}{kT}\right) - 1}. \quad (2.53)$$

Equations 2.52 and 2.53 should be identical which is only true if:

$$g_l B_{lu} = g_u B_{ul}, \quad (2.54)$$

and

$$A_{ul} = \frac{8\pi h\nu^3}{c^3} B_{ul}. \quad (2.55)$$

These are known as the Einstein relations and since we have made no reference to the thermodynamic property of our system, they must be valid for all systems independent of the assumption of TE and so must be intrinsic properties of any specific transition.

2.2.5 LINE BROADENING

When an atom or molecule decays into a lower energy state, releasing a photon with energy $E = h\nu$, it might be expected that the photon's frequency is exactly proportional to the difference between the energy states. However, as stated in the previous section, each transition actually has an associated line profile function (Eq. 2.48) which is a

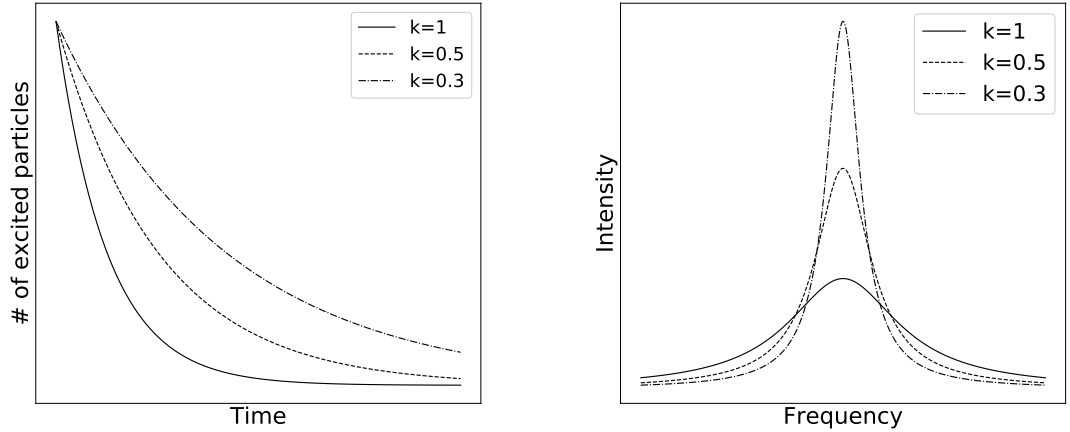


Figure 2.6: Example graphs for the process of natural line broadening. The left panel presents examples of exponential decay laws for various decay constants and the right panel presents the Fourier transform of each decay law. As the decay constant is increased (faster decay) the amount of natural line broadening also increases and vice versa.

function of photon frequency corresponding to any particular transition. In simple terms, when a photon is released from a system it may have a slight difference in frequency from what we would expect by only looking at the energy difference between two energy states. This can be caused by three different mechanisms as described in the following paragraphs.

If a system contains a number of particles in an upper energy state, over time these particles will decay and transition to a lower energy state, the timescale for which is given in Eq. 2.42. Any function that has a profile in time can also be thought of in frequency space by taking the Fourier transform of that function. The Fourier transform of this decay law will produce a line profile as a function of frequency with some line width, as shown in Fig. 2.6. This line profile will be represented by a Lorentzian function. This can then be related to the Einstein A coefficient, which as shown in Eq. 2.43, is proportional to the decay constant. We see how the line profile relates to the Einstein A coefficient using the Lorentzian function:

$$\phi(\nu) d\nu = \frac{A_{ul}}{4\pi^2} \frac{1}{(\nu - \nu_0)^2 + (A_{ul}/4\pi)^2} d\nu. \quad (2.56)$$

Transitions with larger A coefficients will have broader line profiles than those with lower A coefficients.

The next type of broadening is that of Doppler broadening. A system of many particles with some temperature above zero will have constituents moving relative to

one another and to an observer of the system. Therefore, at the time of emission, the photons will either be blue or red shifted depending on if a particle is moving toward or away from the observer. In this case we assume the macroscopic movement of the system is zero relative to the observation, otherwise every photon will be frequency shifted at the same rate which will have little impact on the actual line broadening. For simplicity, we will only consider the Doppler effect in a single dimension. The change in frequency due to Doppler shifting can be expressed as:

$$\Delta\nu = \frac{\nu_0 \Delta v}{c}, \quad (2.57)$$

where ν_0 is the rest frequency (Hz), Δv is the velocity of a particle (m s^{-1}) and c is the speed of light (m s^{-1}). Doppler broadening is governed by the particle velocity distribution of the system, which is defined by the Maxwell-Boltzmann distribution:

$$f(v) dv = \left(\frac{m}{2\pi kT} \right)^{\frac{1}{2}} \exp\left(-\frac{mv^2}{2kT} \right) dv. \quad (2.58)$$

We can substitute Eq. 2.57 into Eq. 2.58 in order to derive the line profile function in terms of frequency:

$$\phi(\nu) d\nu = \left(\frac{mc^2}{2\pi kT\nu_0^2} \right)^{\frac{1}{2}} \exp\left(-\frac{mc^2 \Delta\nu_0^2}{2kT\nu^2} \right) d\nu, \quad (2.59)$$

It can be seen that Doppler broadening is represented by a Gaussian distribution with standard deviation:

$$\sigma = \sqrt{\frac{kT}{mc^2}} \nu_0, \quad (2.60)$$

and since Doppler broadening is caused by the velocity distribution of a system, any physical effects which can alter velocities of the system's constituents will cause broadening. This is the case for interstellar turbulence, as this will affect the differential velocities that particles have relative to one another, and will cause non-thermal broadening of spectral lines, which is regularly seen in molecular observations.

Finally we have collisional broadening, which is only effective when the collisional timescales within a system are equivalent to the emission timescales. As mentioned previously, natural broadening is an effect due to the fact that upper energy states undergo spontaneous decay and can be modelled using a decay law. If there is a steeper decay function, i.e. photons are being emitted more quickly from a system, then this will cause an increase in the line width of the spectral emission. Collisions can cause the constituents of a system to decay more quickly and therefore, increase the rate of emission. This in turn will cause the observed line profile to be broader in

the same way as the intrinsic line-width. So essentially, collisions amplify the effect of natural line-width broadening. The rate of collisions is dependent upon the density of the system, collisional cross-sectional area of the constituents and their corresponding velocities. Therefore collisional broadening is important when we are considering a dense gas with constituents moving relative to one another at high velocities.

It is possible to estimate the non-thermal contributions to spectral line width, if we equate the thermal energy of a system with the kinetic energy then we find:

$$v = \sqrt{\frac{kT_{\text{kin}}}{m}}, \quad (2.61)$$

where m is the mass of a constituent (kg) and v is the velocity dispersion of the line profile (m s^{-1}). The velocity dispersion is essentially the standard deviation of the Gaussian profile and this is related to the FWHM line width (Δv) by a conversion factor of $\sqrt{8 \ln 2}$. By substituting $\Delta v = \sqrt{8 \ln 2} v$ into Eq. 2.61, we find:

$$\Delta v_{\text{th}} = \sqrt{\left(\frac{8 \ln 2 k T_{\text{kin}}}{m}\right)}, \quad (2.62)$$

where Δv_{th} is the thermal line width of the line profile. To estimate the non-thermal line width we can simply subtract this value from the observed line-width:

$$\Delta v_{\text{nt}} = \sqrt{\Delta v_{\text{obs}}^2 - \Delta v_{\text{th}}^2}, \quad (2.63)$$

where Δv_{obs} is the observed line width.

2.2.6 RADIATIVE TRANSFER WITH EINSTEIN COEFFICIENTS

In Sect. 2.1 we considered the theory of radiative transfer using the two radiative properties of a system, emissivity (j_ν) and absorptivity (α_ν). However, we have not seen how these parameters relate to the atomic properties of matter. This can be done by using the Einstein coefficients, which are directly linked to the properties of transitions responsible for spectral line emission.

Let us consider a slab of material with thickness ds and the change of intensity through this material. As a system undergoes a transition from E_u to E_l , the energy is distributed over the full solid angle 4π . The amount of energy emitted or absorbed from our material of volume dV can be divided into the three processes which govern these effects:

1. Spontaneous emission:

$$dE_e(\nu) = h\nu n_u A_{ul} \varphi_e(\nu) dV \frac{d\Omega}{4\pi} d\nu dt. \quad (2.64)$$

2. Absorption:

$$dE_a(\nu) = h\nu n_l B_{lu} \frac{4\pi}{c} I_\nu \varphi_a(\nu) dV \frac{d\Omega}{4\pi} d\nu dt. \quad (2.65)$$

3. Stimulated emission:

$$dE_s(\nu) = h\nu n_u B_{ul} \frac{4\pi}{c} I_\nu \varphi_a(\nu) dV \frac{d\Omega}{4\pi} d\nu dt. \quad (2.66)$$

The line profiles for each of these expressions can be thought to be the same ($\varphi_e(\nu) = \varphi_a(\nu) = \varphi_s(\nu)$), although in reality they could differ. The intensity of light passing through a slab of material must be equal to the changes caused by emission and absorption:

$$dE_e(\nu) + dE_s(\nu) - dE_a(\nu) = dI_\nu d\Omega d\sigma d\nu dt. \quad (2.67)$$

This is true if we set $dV = d\sigma ds$. This results in the equation of radiative transfer using Einstein coefficients:

$$\frac{dI_\nu}{ds} = -\frac{h\nu}{c} (n_l B_{lu} - n_u B_{ul}) I_\nu \varphi(\nu) + \frac{h\nu}{4\pi} n_u A_{ul} \varphi(\nu). \quad (2.68)$$

By comparing this with Eq. 2.6 it can be seen that the absorption coefficient and emissivity can be written in terms of the Einstein coefficients. If we also use the Einstein relations (Eq. 2.54 and 2.55) we find that:

$$\alpha_\nu = \frac{h\nu}{c} n_l B_{lu} \left(1 - \frac{g_l n_u}{g_u n_l} \right) \varphi(\nu), \quad (2.69)$$

and

$$j_\nu = \frac{h\nu}{4\pi} n_u A_{ul} \varphi(\nu). \quad (2.70)$$

The factor in brackets within Eq. 2.69 is the correction for stimulated emission. However, in TE the distribution of energy states is given by the Boltzmann equation, and therefore, the bracketed factor can be written as:

$$1 - \exp\left(-\frac{h\nu}{kT}\right). \quad (2.71)$$

It can be seen that for the lower frequencies in the radio regime, this term is not

insignificant. In fact, generally, the stimulated emission at radio wavelengths almost completely cancels the effect of absorption.

2.2.7 MOLECULAR TEMPERATURES AND LTE

The expressions for the absorption coefficient and emissivity can only be solved if the Einstein coefficients and the number densities for each energy state are known. In LTE, the ratio between two energy states is given by the Boltzmann distribution, however, there are many cases where LTE does not apply, and so, the actual processes leading to changes in energy state populations must be considered. So far we have only looked at a two level system, but the processes in LTE likely involve many more energy states. Let us define R_{jk}^y as the transition probability between the two states $j \rightarrow k$ which is caused by the process y , then the population of the energy state j over time is:

$$\frac{dn_j}{dt} = -n_j \sum_k \sum_y R_{jk}^y + \sum_k n_k \sum_y R_{kj}^y. \quad (2.72)$$

where n_j and n_k are the populations of the j and k state respectively. We will investigate two simplistic situations to derive solutions to this rate equation.

First, consider our previous two-energy state system, which will only change state due to the effects of radiation, i.e. only emission and absorption process apply and any injected energy to our system through collision is negligible. For a stationary situation:

$$n_l B_{lu} \bar{J} = n_u (A_{ul} + B_{ul} \bar{J}), \quad (2.73)$$

with

$$\bar{J} = \frac{4\pi}{c} \bar{I} = \frac{8\pi h\nu^3}{c^3} \frac{1}{\exp\left(\frac{h\nu}{kT_B}\right) - 1}, \quad (2.74)$$

where \bar{I} is the average intensity of the radiation field. The brightness temperature can be written as:

$$T_B = \frac{h\nu}{k} \frac{1}{\ln\left(\frac{8\pi h\nu^3}{c^3 \bar{J}} + 1\right)}. \quad (2.75)$$

If we insert the Einstein A coefficient from Eq. 2.55 into Eq. 2.73, then we can obtain:

$$\frac{n_u}{n_l} = \frac{B_{lu}}{B_{ul}} \frac{\bar{I}}{\frac{2h\nu^3}{c^2} + \bar{I}} = \frac{g_u}{g_l} \exp\left(-\frac{h\nu}{kT_B}\right). \quad (2.76)$$

This shows that in this limiting case, the populations n_l and n_u , are described by a Boltzmann distribution and that the thermodynamic properties do not affect this

result. The brightness temperature describes the radiation density at the frequency between the upper and lower energy states.

The second case we can examine is when collisions govern the state populations and transitions between them. Again, we only consider a two level system. We define the collisional probabilities for $u \rightarrow l$ and $l \rightarrow u$ as C_{ul} and C_{lu} respectively and can be written as:

$$C_{ik} = n_i C_{ik} = n_i \int_0^\infty \sigma_{ik}(V) V f(V) dV, \quad (2.77)$$

where C_{ik} is in units of $\text{cm}^3 \text{s}^{-1}$, σ_{ik} is the collisional cross section (cm^2) and $f(V)$ is the velocity distribution function of the colliding particles. Therefore, the rate equation for a stationary situation will be:

$$n_l(C_{lu} + B_{lu} \bar{J}) = n_u(A_{ul} + B_{ul} \bar{J} + C_{ul}), \quad (2.78)$$

and if collisions dominate, we see that:

$$\frac{C_{lu}}{C_{ul}} = \frac{n_u}{n_l} = \frac{g_u}{g_l} \exp\left(-\frac{h\nu}{kT_K}\right). \quad (2.79)$$

The T_K in this expression is the kinetic temperature of the system (K) which describes the velocity distribution of the particles, which is characterised by the Maxwell-Boltzmann distribution:

$$f(v) = \left(\frac{2}{\pi}\right)^{\frac{1}{2}} V^2 \left(\frac{m_r}{kT_K}\right)^{\frac{3}{2}} \exp\left(-\frac{m_r V^2}{2kT_K}\right), \quad (2.80)$$

where

$$m_r = \frac{m_a m_b}{m_a + m_b}, \quad (2.81)$$

is the reduced mass of the particles undergoing collisions.

The two cases we have examined provide two different temperatures that we can use to determine if radiation or collisions are dominating within a system. To do this we can compare these temperatures to the excitation temperature of the system, as defined by the Boltzmann distribution:

$$\frac{n_u}{n_l} = \frac{g_u}{g_l} \exp\left(-\frac{\Delta E}{kT_{\text{ex}}}\right), \quad (2.82)$$

which is the temperature that a system has depending on the population of two energy states and this is the mean of the brightness and kinetic temperatures. If radiation is dominant then the excitation temperatures tends toward the brightness tempera-

ture, or if collisions dominate, the excitation temperature tends towards the kinetic temperature. In general, it can be seen that collisions dominate at high densities and radiation dominates at low densities.

2.3 RADIO TELESCOPES AND DETECTION

Unlike other areas of astronomy at different frequencies, such as optical and x-ray astronomy, incoming radio radiation is treated as a superposition of classical electromagnetic radiation, as opposed to photons, which are discrete packets of energy known as quanta. The principal difference between these areas of astronomy is that radio astronomy employs the use of low-noise amplifiers prior to the signal detection and the possibility of using signal-processing techniques. A distinct feature of radio telescopes is that this radiation is not measured immediately, but instead is first amplified and manipulated while preserving its character before it is finally detected. In this Section we will describe the fundamentals of radio telescope systems, however, as this Thesis is mainly based on archival data we shall not examine the intricate theory behind radio signal processing.

Radio telescopes (or antennas) differ in many ways but all have three main basic components and the principles for each are the same. Incoming radiation is reflected off a large curved primary surface (known as a dish) and focused onto a smaller secondary surface (sub-reflector), which in turn focuses the light onto a detector that converts the EM waves into an electronic signal that can be measured (Jones, 1953). Since a telescope's resolution is proportional to the wavelength of interest and the diameter of the telescope's collecting area, radio telescopes require large primary surfaces to obtain reasonable resolutions. The resolution of a telescope is calculated by:

$$\theta \propto \lambda/D, \tag{2.83}$$

where λ is the observing wavelength (m) and D is the diameter of the primary collecting area (m). The resolution θ is also known as the beam size in radians. Radio telescopes can be divided into two classes: single dish telescopes and interferometers.

2.3.1 SINGLE DISH

Single dish telescopes are stand-alone antennas with dish sizes ranging from 5 m to \sim 500 m. The most important characteristic of an antenna is its ability to detect incident

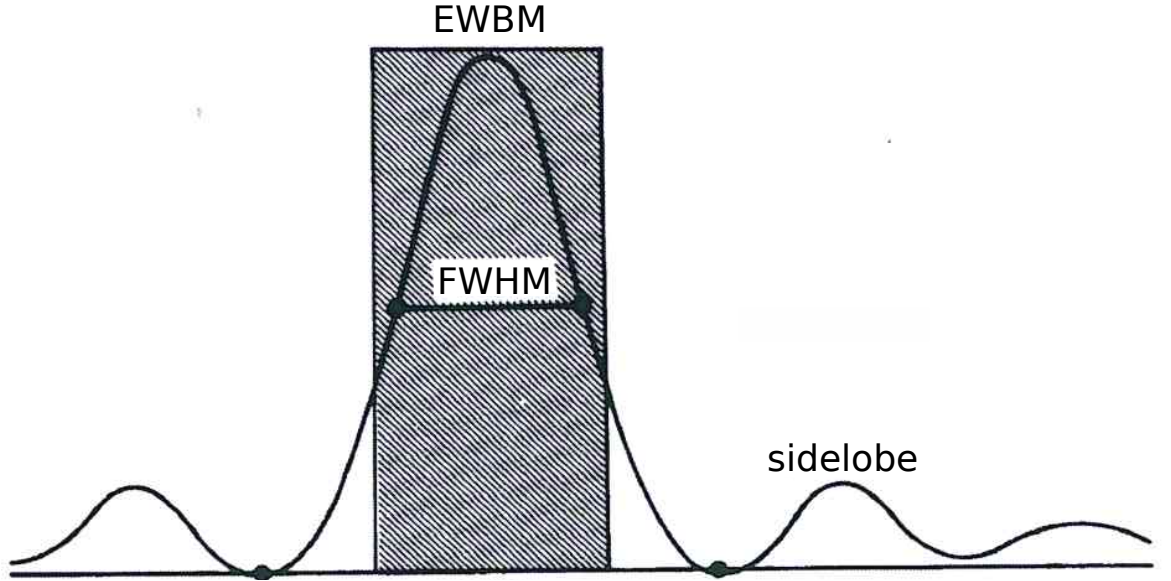


Figure 2.7: A diagram of an antenna beam pattern. Adapted from Fig. 7.2 of Wilson et al. (2013). The FWHM and equivalent width of the full half power beam with (EWBM) are shown.

radio waves. The directional power that can be collected by an antenna is described by a normalised power pattern:

$$P_n(\theta, \phi) = \frac{1}{P_{\max}} P(\theta, \phi). \quad (2.84)$$

This power pattern represents how spatially sensitive a telescope is and can be calculated by using small point-like sources with known flux densities. We define the beam solid angle of an antenna as:

$$\Omega_A = \iint_{4\pi} P_n(\theta, \phi) d\Omega. \quad (2.85)$$

The beam solid angle is integrated over the full sphere of 4π steradians such that Ω_A has $P_n = 1$ over the sphere and is 0 everywhere else. This is an idealised scenario and in reality no antenna has such a power pattern. For the majority of antennae the power pattern has larger values for certain positions, known as the main beam. The remainder of the power pattern is distributed among side and back lobes. Figure 2.7 presents a diagram of an antenna power pattern. The main beam solid angle is defined as:

$$\Omega_{\text{MB}} = \iint_{\text{main lobe}} P_n(\theta, \phi) d\Omega. \quad (2.86)$$

Since the main beam is essentially Gaussian, then the solid angle of the beam and the

full-width half-maximum of the beam are equated by:

$$\Omega_{\text{MB}} = \left(\frac{\pi}{4 \ln 2} \right) \theta_{\text{FWHM}}^2. \quad (2.87)$$

We can also define the main beam efficiency as:

$$\eta_{\text{MB}} = \frac{\Omega_{\text{MB}}}{\Omega_{\text{A}}}. \quad (2.88)$$

The main beam efficiency is important when observing extended sources, as low main beam efficiencies means high side lobe contributions and so this is unsuitable for extended source observations. The difference between the size of the beam and the angular coverage of a radio source is called the beam filling factor:

$$B_{\text{ff}} = \frac{\Omega_{\text{S}}}{\Omega_{\text{B}}}, \quad (2.89)$$

which is an important factor when considering sources much smaller, or larger, than the beam size. When observing towards a source of NH_3 spectral line inversions emission and if the source is smaller than the beam size, then the measured excitation temperature of the source (Eq. 2.24) would be lower than expected due to the dispersion of energy across the telescope beam. If multiple transitions of the NH_3 inversion emissions are measured then the Boltzmann distribution can be employed to calculate the expected rotational temperature (Eq. 2.50). The difference between these two temperatures would also be equal to the beam filling factor:

$$B_{\text{ff}} = \frac{T_{\text{ex}}}{T_{\text{rot}}}, \quad (2.90)$$

where T_{ex} is the observed excitation temperature of a source that is less than the size of the beam and T_{rot} is the calculated rotational temperature between two inversion transitions.

2.3.2 INTERFEROMETERS

Radio wavelengths are orders of magnitude larger than their optical counterparts (wavelengths of 1 mm to 200 m compared to that of 550 nm for optical light) and so single dish telescopes are severely diffraction limited with much lower angular resolutions than optical telescopes. The resolution of a telescope is proportional to the ratio between the wavelength of interest and the diameter of the telescope dish as stated above. Therefore, to obtain the highest angular resolution it is necessary to build large dishes. However, it is impractical and very expensive to build telescope surfaces bigger than 100 m in size and so this would imply that the resolution at radio wavelengths is limited

by engineering capabilities. However, to overcome this obstacle we can use a technique called aperture synthesis that relies on the physics of interferometry.

Aperture synthesis combines the measurements from a number of individual antennas to produce higher quality images with much greater resolutions. By increasing the distance between antennas (baselines) the amount of finer detail in source structure can be resolved and so by increasing this distance, the resolution of the telescope system increases. However, at larger baselines more diffuse and extended emission is removed through filtering and so the instrument becomes more sensitive to compact structures. At smaller baselines the telescope resolution is reduced and point sources are less resolved but extended emission can instead be measured.

2.3.3 DETECTORS

There exist two types of radio telescope detectors: incoherent and coherent radiometers. Incoherent radiometers do not preserve phase and as such are simply direct detection systems. At submillimetre and millimetre wavelengths the most common type of incoherent radiometer is that of a bolometer. These devices are essentially very sensitive thermometers with no specific response to the frequency or polarisation of incident radio waves. The electronic resistance of a material varies with temperature and a bolometer operates based on this effect. As incoming radiation is detected by a bolometer its temperature varies. The temperature which is measured is directly proportional to the intensity of the incident radiation. This temperature change is independent of frequency and phase meaning that bolometers are broadband devices and can detect radiation at a range of wavelengths. The sensitivity of a bolometer depends on the noise temperature known as Johnson-Nyquist noise. At any given temperature the electrons within a resistor will produce some current which corresponds to a physical temperature. While the mean average of this produced current is zero, the rms current will have some value above zero. The rms value of any particular detector can be designated as the sensitivity of that detector; as to measure any changes in the temperature of the bolometer due to the incoming radiation must be larger than from the thermal noise of the detector itself.

The second type of detectors are coherent radiometers. These systems are much more complex than their incoherent counterparts. Coherent radiometers are sensitive to polarisation and can be used for spectral line observations. Coherent devices are heterodyne systems which are common in radio frequency equipment. Essentially a heterodyne system observes incoming radiation at a particular frequency and then converts this into a different frequency (usually a lower frequency) before the information is processed. Coherent radiometers can therefore be split into two parts: front-ends and

back-ends. The dividing point for these system is arbitrary but generally the front-ends operate at the incident radiation frequencies while back-ends operate at lower frequencies. Two main detectors have been used for the research presented here, the first is the Large APEX Bolometer Camera (LABOCA; Siringo et al. 2009) instrument on the Atacama Pathfinder EXperiment (APEX) telescope, which is an array of 295 composite bolometers operating at 870 micron. The second are the 12 mm instruments on the Australia Telescope Compact Array (ATCA) antennas operating at frequencies between 16 and 26 GHz, useful for observing molecular line emission from ammonia and water vapour.

2.4 THE AMMONIA MOLECULE

Chapter 3 is largely concerned with interstellar ammonia and its use as a signpost of dense, cold gas and its usefulness in determining various gas temperatures (T_{ex} , T_{rot} , T_{kin}). Ammonia was the first polyatomic detected in the ISM (Cheung et al., 1968), and is second only in importance to carbon monoxide in the study of ISM chemistry. NH_3 is a symmetric top molecule with a pyramidal shape and is well understood; a diagram of the molecular structure is shown in the upper right of Fig. 2.8.

The abundance of ammonia (NH_3/H_2) has been measured in a selection of different regions and environments, and has been estimated to range from 10^{-7} in small dark clouds (Ungerechts et al., 1980) to 10^{-5} in dense cores (Genzel et al., 1982). Herbst and Klemperer (1973) proposed a synthetic scheme for the formation for ammonia through gas-phase ion-molecule synthesis:



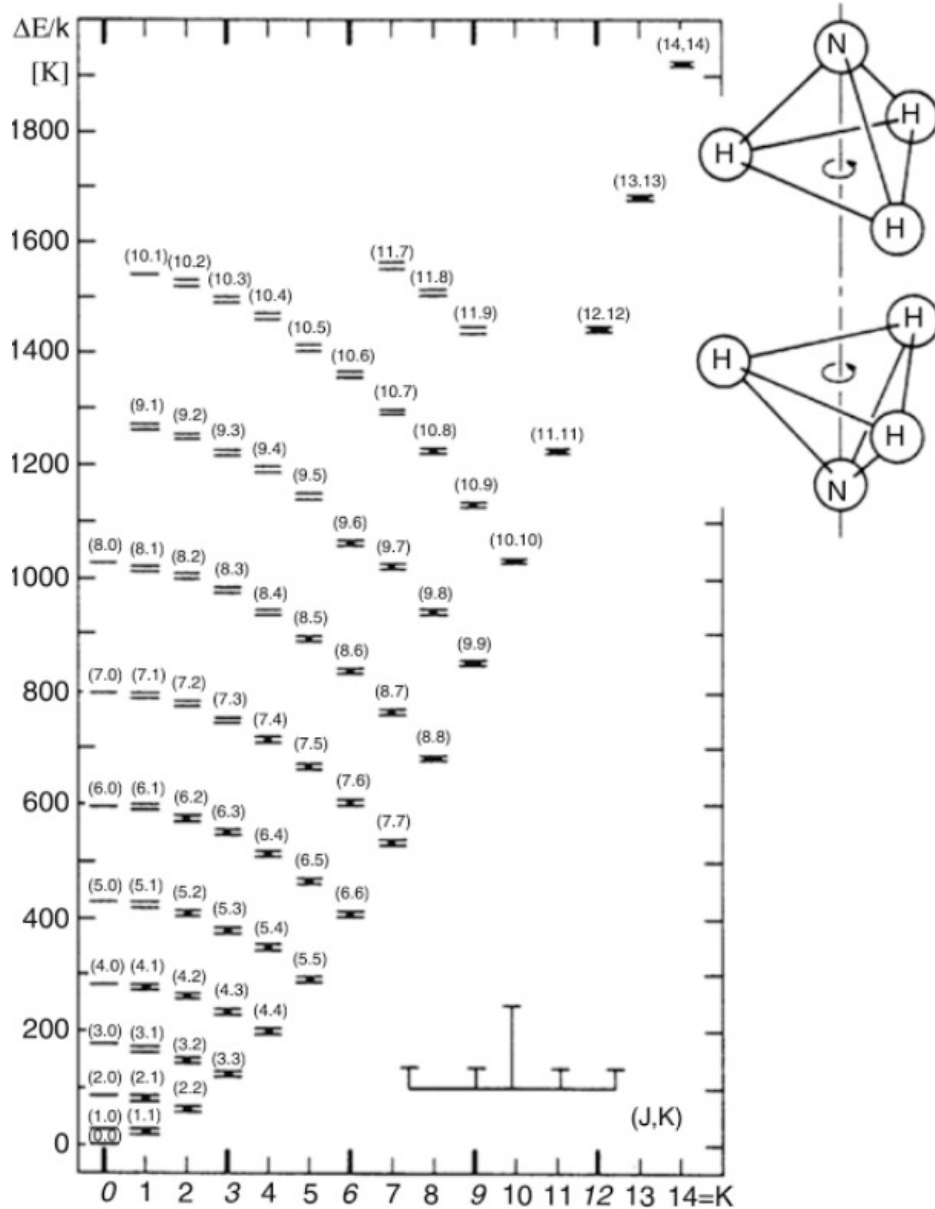


Figure 2.8: Diagram of the energy levels for the vibration ground state of the ammonia molecule. The molecular structure of the ammonia molecule is also shown in the upper right of the panel. Figure 15.5 of Wilson et al. (2013).

However, an alternative synthesis scheme has also been proposed which bypasses the first two reactions that are stated in Eqs. 2.91 and 2.92 (Dalgarno 1975; Scott et al. 1997):



There are two types of ammonia molecule, known as ortho-NH₃ ($K = 3n$, where n is an integer) and para-NH₃ ($K \neq 3n$, where n is an integer), which depend on whether the spin orientation of the hydrogen nuclei are all parallel or anti-parallel respectively. In TE, collisions will slowly change the spin orientations on large timescales ($> 10^6$ yrs), although this process may be more rapid on grain surfaces, or with charged particles. If the exchange between the molecule types is slow it could be used as an indication of temperatures that existed in the distant past, likely during the formation of the molecule itself.

Of interest to this Thesis is the inversion transition emissions of ammonia which occur when the nitrogen nucleus of the molecule quantum tunnels through the plane of the hydrogen atoms, causing emission to be released. The potential barrier of the hydrogen nuclei is low enough that this effect is rapid and the radiation released is at microwave frequencies (~ 23.7 GHz).

For inversion emissions $\Delta J = 0$ and $\Delta K = 0$ and, therefore, these inversion emissions are actually doublet transitions. The inversion transitions across the doublets are allowed from symmetry considerations (Townes and Schawlow, 1955). Moreover, these transitions are further split into hyperfine components, caused by the interaction between the inversion emission and the quadruple moment of the nitrogen nucleus, along with further magnetic hyperfine splitting. Due to the unity of the ¹⁴N spin, each doublet level is split by the nuclear orientation into three distinct hyperfine components which results in five frequency components: a main line which contributes at least 50% of the total intensity and two pairs of satellite lines either side of the main line; these main and satellite lines are separated by approximately 1 MHz. Further hyperfine splitting due to magnetic interactions with the atomic spins of the constituent nuclei, where the frequency difference between the components is on the order of ~ 40 kHz.

The upper panel of Fig. 2.9 presents the energy levels of the hyperfine splitting of the NH_3 molecule. In total the NH_3 (1,1) emission has 18 individual components whereas the (2,2) emission has 21. The hyperfine splitting of the energy levels gives rise to an interesting and unique spectra, and an example of the NH_3 (1,1) emission spectra is shown in the lower panel of Fig. 2.9.

The NH_3 inversion transitions can be used to measure the physical properties of any region where it is found, due to the nature of the produced spectra. Where the spectra for a single transition has been observed, one can use the main line and satellite lines produced from the quadrupole hyperfine structure to calculate the optical depth of the transition:

$$\frac{T_B(J, K, m)}{T_B(J, K, s)} = \frac{1 - e^{\tau(J, K, m)}}{1 - e^{\alpha\tau(J, K, m)}}, \quad (2.100)$$

where T_B is the observed brightness temperature (Eq. 2.24), $\tau(J, K, m)$ is the optical depth of the main emission line, m and s refer to the main and satellite components respectively and α is the ratio of intensity between the satellite and main components ($\alpha = 0.28$ and 0.22 depending on the exact satellite hyperfine components used for the calculation). The ratio between the main and satellite line components are known from laboratory experiments.

With a value for the optical depth, the excitation temperature of the gas can be computed using Eq. 2.23:

$$T_B = [J_\nu(T_{\text{ex}}) - J_\nu(T_{\text{bg}})](1 - e^{-\tau}), \quad (2.101)$$

where T_{bg} is the temperature of the cosmic microwave background ($\approx 2.73 \text{ K}$), T_B is the measured brightness temperature (K) and T_{ex} is the measured excitation temperature (K) of the source.

If the first two inversion transitions of ammonia are observed then from the definition of optical depth:

$$\frac{\tau(2, 2)}{\tau(1, 1)} = \frac{n(2, 2)}{n(1, 1)} \frac{v^2(2, 2)}{v^2(1, 1)} \frac{\Delta v(1, 1)}{\Delta v(2, 2)} \frac{T_{\text{ex}}(1, 1)}{T_{\text{ex}}(2, 2)} \frac{|\mu(2, 2)|^2}{|\mu(1, 1)|^2}, \quad (2.102)$$

where n is the population of energy level $n(J, K)$, v is the rest frequency of the transition, δv is the width of the line profile, T_{ex} is the excitation temperature of the transition and $|\mu(J, K)|$ is the dipole matrix of a transition, defined as:

$$|\mu|^2 = \frac{\mu^2 K^2}{J(J+1)}, \quad (2.103)$$

where μ is the permanent electric dipole moment of the molecule (for ammonia this

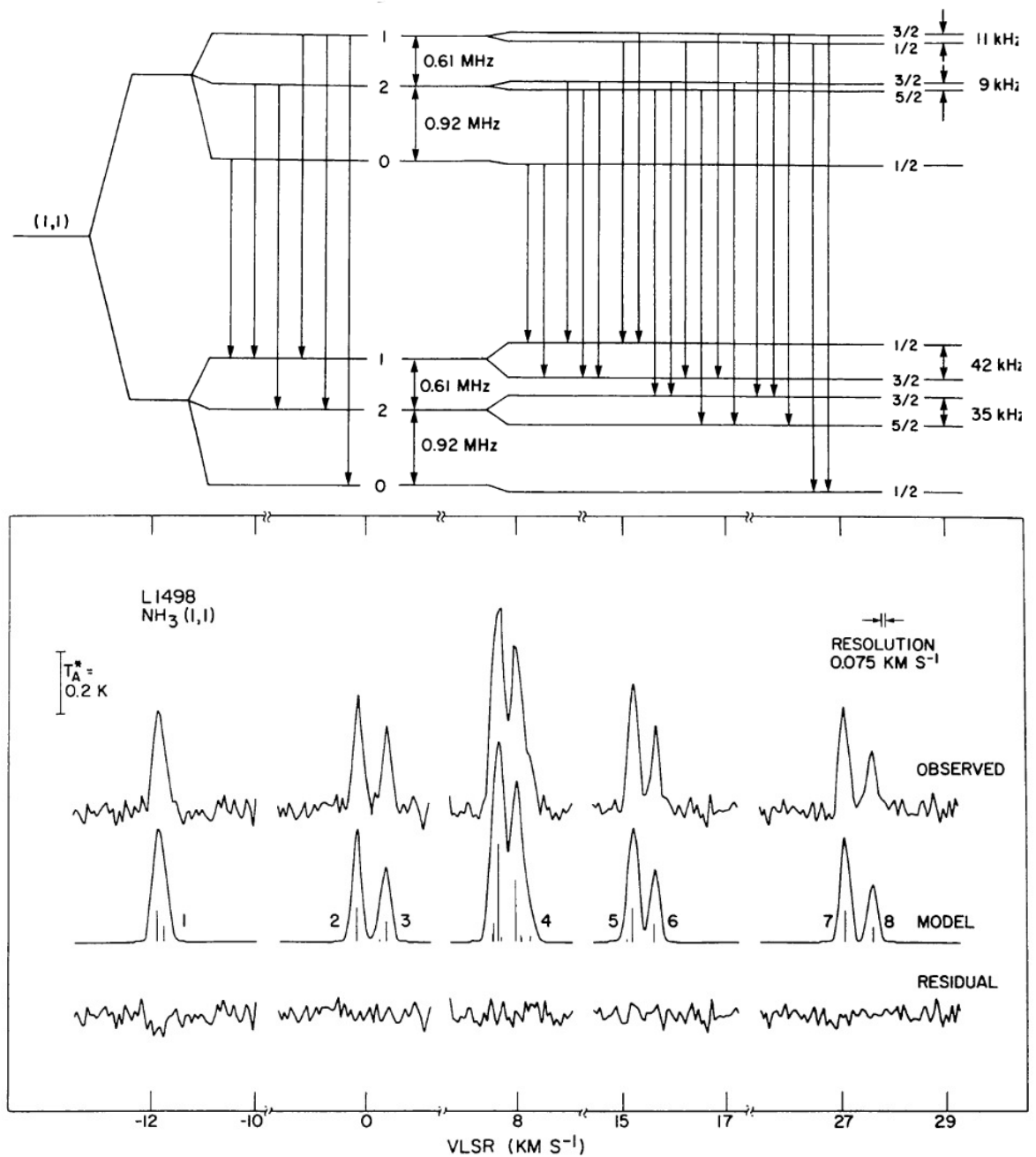


Figure 2.9: The upper panel presents a diagram of the hyperfine splitting energy levels for the $\text{NH}_3(1,1)$ inversion emission with the allowed transitions indicated. The lower panel presents an example spectrum of this transition towards L1498 with the relative strengths of the hyperfine components indicated by the vertical tick marks under the model spectrum. Figures 2 and 3 of Ho and Townes (1983).

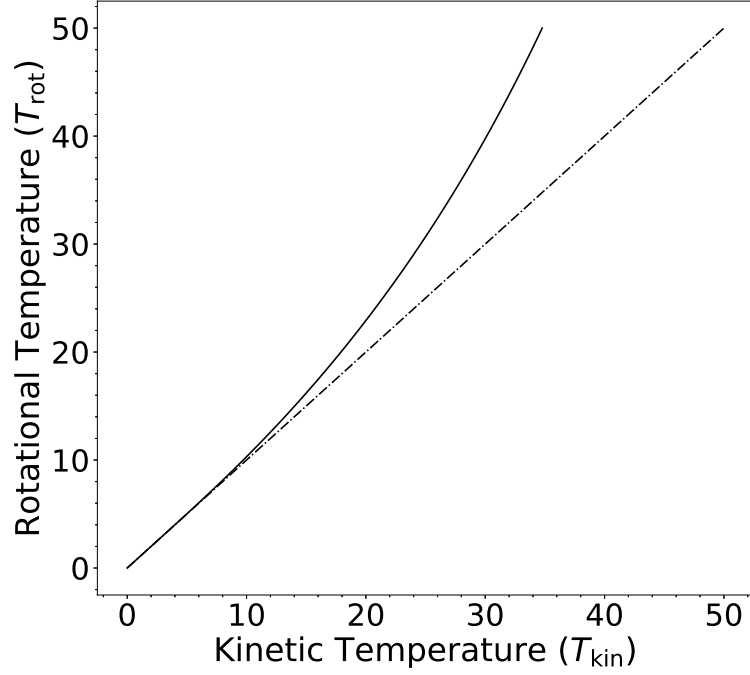


Figure 2.10: Plot presenting the variation of rotational temperature with increasing kinetic temperature. The 1:1 line (dash-dotted) is also shown.

value is 1.47 Debye). We can then combine Eqs. 2.100, 2.101 and 2.102 to produce an expression for the rotational temperature between the two inversion transitions:

$$T_R(2, 2; 1, 1) = -T_0 \div \ln \left[\frac{-0.282}{\tau_m(1,1)} \ln \left\{ 1 - \frac{\Delta T_a^*(2,2,m)}{\Delta T_a^*(1,1,m)} \right\} \times (1 - e^{-\tau_m(1,1)}) \right], \quad (2.104)$$

where T_0 is the energy difference in Kelvin between the $J = 1$ and $J = 2$ energy states, and is equal to 41.5 K. If the rotational temperature is much less than the energy difference between the two transitions ($T_{\text{rot}} \ll 41.5 \text{ K}$), then the kinetic temperature is approximately equal to the rotational temperature and can be calculated by:

$$T_R = T_{\text{kin}} \left\{ 1 + \frac{T_{\text{kin}}}{T_0} \ln [1 + 0.6 \exp(-15.7/T_{\text{kin}})] \right\}^{-1}. \quad (2.105)$$

Figure 2.10 shows how the rotational and kinetic temperatures diverge with increasing temperature.

2.5 DERIVING PHYSICAL PROPERTIES - DUST

The physical properties derived from interstellar dust are used consistently within this Thesis and while this work does not calculate any properties, it makes extensive use of values available from other studies and so it is necessary to provide a short discussion on their derivations.

Recall from Sect. 1.4.1 that the thermal dust emission seen across the Galaxy is an example of blackbody radiation and if observations are made of this emission at different wavelengths, then it is possible to reconstruct the spectral energy distribution (SED) of the Galactic dust. By reconstructing the SEDs, physical parameters of dusty environments can be derived.

As multi-wavelength data are required for this process, data has been taken from the MSX (Egan et al., 2003) or the WISE (Wright et al., 2010) surveys, which cover the mid-infrared regions of the dust blackbody spectra (8, 12, 14, 21 μm for MSX and 3, 4, 12, 22 μm for WISE), and from the SPIRE (Griffin et al., 2010) and PACS (Poglitsch et al., 2010) instruments aboard the Herschel Space Observatory (Pilbratt et al., 2010), which operates within the far-infrared regime (at wavelengths 70, 160, 250, 350, 500 μm). Aperture photometry can then be undertaken which measures the flux of a source at each wavelength and once the source flux at each wavelength has been computed, the SED can be fitted using a blackbody model. An example of a blackbody curve for the Galactic source G189.030+00.783 is shown in Fig. 2.11. It can be seen that the SED is comprised of two components, one is attributed to the thermal dust emission at longer wavelengths, while the other is associated with the hot, more compact emission surrounding the embedded protostellar or young stellar objects.

When a blackbody curve for a source has been fitted, the temperature will be known as it is a required parameter for the fitting method. The bolometric flux can also be calculated by integrating the fitted blackbody curve. If a distance is known to any particular source then that source's bolometric luminosity can be found by:

$$L_{\text{bol}} = F_{\text{bol}}^2 4\pi D^2, \quad (2.106)$$

where D is the distance to the source (m) and F_{bol} is the bolometric flux of the source (W m^{-2}).

Using the dust emission it is also possible to calculate the H_2 column density. If we equate Eq. 2.4 with Eq. 2.18 we obtain:

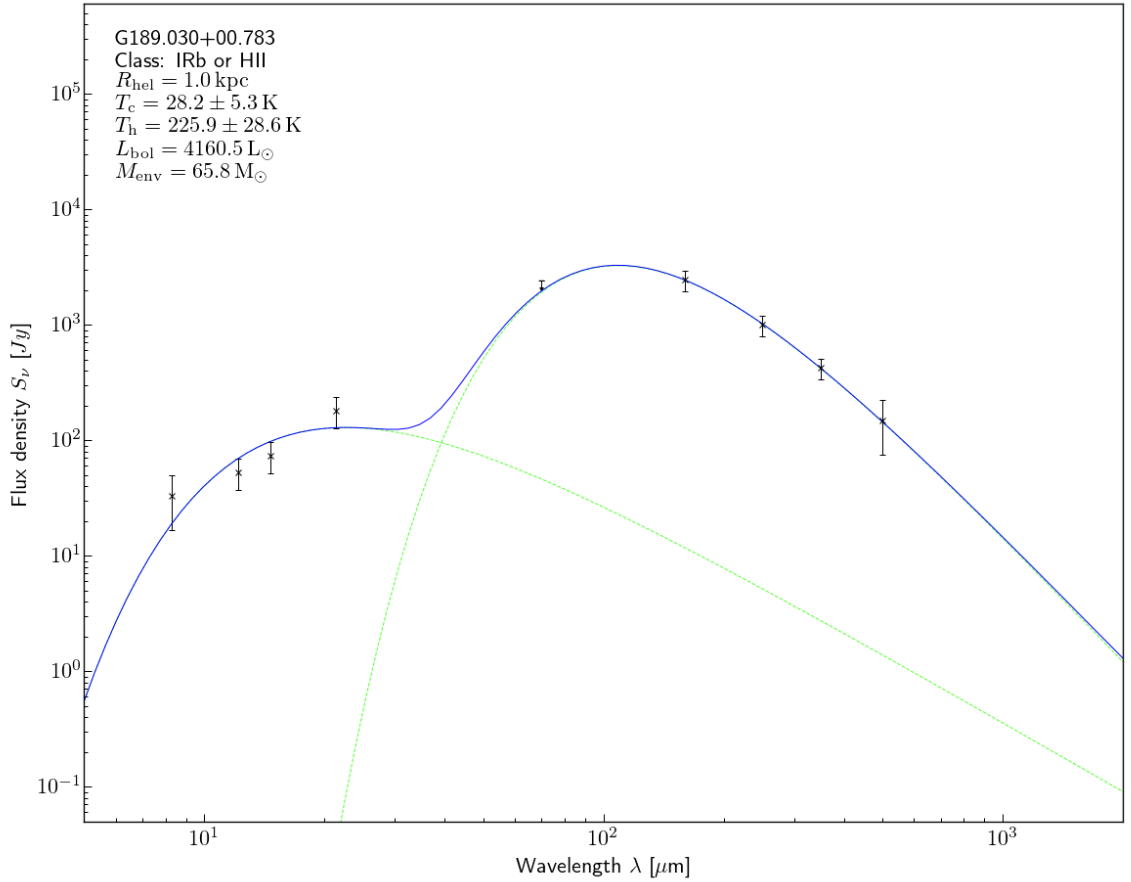


Figure 2.11: An example of a spectral energy distribution for G189.030+00.783. The flux density measurements at nine distinct wavelengths are shown along with the corresponding errors for each measurement. The solid blue line is the best model fit for the flux density observations, while the two green dotted lines represent individual components of the full energy distribution. The parameters then derived from the SED fitting method are shown in the upper left of the panel. A more complete description of this method is presented in König et al. (2017).

$$S_\nu = \frac{2k\nu^2}{c^2} T \Delta\Omega, \quad (2.107)$$

we can then equate Eq. 2.18 with Eq. 2.16:

$$T = \frac{c^2}{2k\nu^2} [B_\nu(T) - I_\nu(0)](1 - e^{-\tau}), \quad (2.108)$$

which can be simplified by setting $I_\nu(0) = 0$:

$$T = \frac{c^2}{2k\nu^2} B_\nu(T) (1 - e^{-\tau}). \quad (2.109)$$

We can now insert Eq. 2.109 into Eq. 2.107 and by using the definition of the optical depth ($\tau = j_\nu N$; where N is the column density) and assuming the optical depth is small, we find:

$$N = \frac{S_\nu}{\Omega j_\nu B_\nu(T)}, \quad (2.110)$$

however, this only provides the mass of dust per area (g cm^{-2}). In order to derive the H_2 column density we must divide N by two other parameters. The first is the mean molecular weight (μ) and secondly, the mass of a hydrogen atom (m_{H}). Finally we obtain an equation to calculate the H_2 column density:

$$N(\text{H}) = \frac{S_\nu}{\Omega \mu m_{\text{H}} j_\nu B_\nu(T)}. \quad (2.111)$$

Equation 2.110 allows for the calculation of the dust mass if a distance to a source is known. As Eq. 2.110 will have units of g cm^{-2} , we must integrate over the full spatial area of a source, which is a function of distance to the source and the angle subtended by it. Also, we must estimate the dust-to-gas ratio for any region of interest. By applying these factors to Eq. 2.110 we find:

$$M = \frac{D^2 S_\nu R}{B_\nu(T) j_\nu}, \quad (2.112)$$

where D is the distance to the source (m) and R is the dust-to-gas ratio which for the purpose of this Thesis we take to be 100, meaning that the dust contributes only 1% of the mass in any region.

Furthermore, it is also possible to employ the use of the virial theorem to calculate the mass of a clump. The virial theorem is a general relation between the total kinetic energy of a stable, self-gravitating, spherical distribution of equal mass objects and can be written as:

$$-2\langle K \rangle = \langle U \rangle, \quad (2.113)$$

where $\langle K \rangle$ is the average kinetic energy of a system and $\langle U \rangle$ is the average potential energy of that system. Before we can derive an equation for the mass according to the virial theorem, we must first derive an expression for the potential energy of a self-gravitating, spherical system. If we consider such a system of mass, M , then the potential energy of any point mass, m_i , around the centre of mass of this system can be written as:

$$dU = -G \frac{M_r dm_i}{r_i}, \quad (2.114)$$

where G is the gravitational constant ($6.67 \times 10^{-11} \text{ kg s}^2 \text{ m}^{-3}$) and r_i (m) is the distance between a point mass and the centre of gravity of the spherical system. If we now assume that the point masses are distributed uniformly within a shell of thickness, dr , and mass, dm ($dm = \Sigma dm_i$), then we see:

$$dm = 4\pi r^2 \rho dr, \quad (2.115)$$

where ρ is the mass density of the shell (kg m^{-3}) and $4\pi r^2 dr$ is the shell volume (m^{-3}). Inserting this expression into Eq. 2.114, we find:

$$U = -4\pi G \int_0^R M_r \rho r dr. \quad (2.116)$$

This integral requires knowledge of how the density of the system and how the m depends on r , however, approximations can be made by assuming the density of the system is constant:

$$\rho \sim \bar{\rho} = \frac{M}{\frac{4}{3}\pi R^3}, \quad (2.117)$$

and so:

$$M_r \sim \frac{4}{3}\pi r^3 \bar{\rho}. \quad (2.118)$$

By inserting Eq. 2.118 into Eq. 2.114 and integrating then we obtain:

$$U \sim -\frac{16\pi^2}{15} G \bar{\rho} R^5 \sim -\frac{3}{5} \frac{GM^2}{R}. \quad (2.119)$$

Returning to the Virial theorem, if we continue to consider a spherical system of N particles, then Eq. 2.113 can be rewritten as:

$$-2 \sum_{i=1}^N \frac{1}{2} m_i v_i^2 = U, \quad (2.120)$$

where v_i is the velocity of each particle (km s^{-1}). The total mass of a system can be written as $M = Nm$ and inserting this into the above equation yields:

$$-\frac{m}{N} \sum_{i=1}^N v_i^2 = \frac{U}{N}. \quad (2.121)$$

In general, when observing such a system we can only measure radial velocities, although on average, the velocity in any direction is likely to be the same as in the radial direction, and so:

$$\frac{1}{N} \sum_{i=1}^N v_i^2 = \langle v^2 \rangle = 3 \langle v_r^2 \rangle = 3\sigma_r^2, \quad (2.122)$$

where $\langle v \rangle$ is the average velocity (km s^{-1}) and σ_r is the dispersion in radial velocity (km s^{-1}). Using $M = Nm$ and inserting Eqs. 2.122 and 2.119 into Eq. 2.121 and then solving for mass, we obtain a relation for the virial mass:

$$M_{\text{virial}} \approx \frac{5\sigma_r^2 R}{G}. \quad (2.123)$$

Furthermore, we can define the virial parameter which is a measure of the stability of a self-gravitating system and for the purpose of this Thesis, that system will be a dense Galactic clump. The virial parameter can be written as:

$$\alpha_{\text{virial}} = \frac{M_{\text{virial}}}{M_{\text{clump}}} = \frac{5\sigma_r^2 R}{GM_{\text{clump}}}. \quad (2.124)$$

A virial parameter of less than 2 indicates that a clump is unstable and will undergo global collapse if only gravity is taken into account (Kauffmann et al., 2013).

The final parameter of interest is that of the free-fall time. A spherical system, affected by only gravity, will collapse on the order of the free-fall timescale, as mentioned in Sect 1.6.2. In order to derive Eq. 1.1, we can equate the kinetic energy of a particle to the change in gravitational potential energy:

$$\frac{1}{2} m_i v_i^2 = GMm_i \left[\frac{1}{r_i} - \frac{1}{r_0} \right], \quad (2.125)$$

where r is the distance between the particle and the centre of mass of the system, and r_0 is the initial radius of the system. Rearranging for v_i we find:

$$v_i = \frac{dr}{dt} = \sqrt{\frac{8\pi}{3} G \rho_0 r_0^2 \left[\frac{r_0}{r_i} - 1 \right]}, \quad (2.126)$$

integrating this expression provides an equation for the free-fall time:

$$t_{\text{ff}} = \sqrt{\frac{3\pi}{32G\rho}}, \quad (2.127)$$

where G is the gravitational constant as before and ρ is the density of the system (kg m^{-3}).

2.6 SUMMARY

This Chapter has provided a theoretical foundation to the forthcoming chapters, along with the derivations and information necessary for a complete understanding of the work presented in this Thesis. All of the equations used beyond this point are derived in this Chapter and will be referred to when required.

CHAPTER 3

AMMONIA MAPPING OF THE ENVIRONMENT OF YOUNG MASSIVE STELLAR OBJECTS

3.1 INTRODUCTION

This Chapter presents a morphological study of 34 star forming regions in the southern Galactic plane. These regions have been mapped using the first two inversion transition emissions of the ammonia (NH_3) molecule, and archival data from the APEX Telescope Large Area Survey of the GALaxy (ATLASGAL; Schuller et al. 2009) and the Galactic Legacy Infrared Mid Plane Survey Extraordinaire (GLIMPSE; Churchwell et al. 2009) surveys have also been used to investigate the regions further in the infrared and submillimetre regimes.

The Red MSX Source (RMS) survey (Lumsden et al., 2013), has identified $\sim 3\,000$ MYSOs and HII regions candidates located throughout the Galactic plane. These sources were initially identified from their mid-infrared colours using the MSX point source catalogue (Price et al., 2001) and 2MASS data (Cutri et al. 2003). The nature of these candidates were later confirmed through an extensive multi-wavelength follow-up campaign (e.g. Urquhart et al. 2007a,b; Mottram et al. 2007; Urquhart et al. 2008,

2009, 2011; Cooper et al. 2013). This survey has identified ~ 1700 MYSOs and HII regions and is the largest and most well-characterised catalogue of these stages of massive star formation that has been compiled with determined distances (Urquhart et al. 2012, 2014b) and luminosities (Mottram et al. 2011a,b; Urquhart et al. 2014b) and is an order of magnitude larger than any previous study. The RMS catalogue sample is therefore an ideal starting point for more detailed studies of these massive star forming regions, and as such, the observations of the 34 regions of interested in this study were taken towards known high-mass star formation regions identified by the RMS survey.

Ammonia observations have been used by the H₂O Southern Galactic Plane Survey (HOPS; Walsh et al. 2011; Purcell et al. 2012; Longmore et al. 2017) to map the distribution of dense star forming gas; other studies have used it to investigate the physical properties and kinematics of different kinds of star formation environments in the Galaxy, such as infrared dark clouds (e.g. Pérault et al. 1996; Pillai et al. 2006; Ragan et al. 2011; Chira et al. 2013) and high-mass star forming regions (e.g. Longmore et al. 2007, Dunham et al. 2011, Urquhart et al. 2011). The main reason for the widespread use of ammonia transitions is that the hyperfine structure of the emission can be used to derive multiple free parameters allowing for an in-depth analysis of the kinematics, morphology and thermodynamics of such regions.

The main aims of this study are to compare the physical properties of different stages of high-mass star formation and investigate how feedback from outflows and UV-radiation can affect the local environment as the embedded high-mass stars evolve.

3.2 SAMPLE SELECTION AND ARCHIVAL DATA

The sample selection for this study was based on Red MSX Source (RMS) survey objects towards which both strong NH₃ (1,1) and (2,2) inversion transition emission has previously been detected. The observational data set along with data reduction techniques is outlined in Sect. 3.3. The majority of objects that were selected lie within the inner Galactic plane and so are complemented by a wealth of additional data provided by other surveys such as ATLASGAL, HOPS, GLIMPSE and the Methanol MultiBeam (MMB) survey. Therefore, complementary data has been taken from these Galactic surveys in order to improve the understanding of the surrounding environments for the regions that are presented herein.

3.2.1 THE GALACTIC LEGACY INFRARED MID-PLANE SURVEY EXTRAORDINAIRE (GLIMPSE)

Images have been used from the GLIMPSE Legacy Survey (Benjamin et al., 2003; Churchwell et al., 2009) in order to investigate the surrounding environments at mid-infrared wavelengths. Three-colour images have been created using data at IRAC 3.4, 4.5 and $8\ \mu\text{m}$ wavelength bands from the Spitzer Space Telescope (Fazio et al., 1998).

These images are capable of revealing the position of embedded objects with respect to the ammonia emission, such as MYSOs and compact HII regions under investigation here. The $8\ \mu\text{m}$ band is also sensitive to the emission from polycyclic aromatic hydrocarbons (PAHs) that have been excited by UV radiation of embedded or nearby HII regions, making it an excellent tracer of the boundaries between molecular and ionized gas (Urquhart et al., 2007c) (right panel of Figure 3.1). Additionally, Cyganowski et al. (2008) have used the $4.5\ \mu\text{m}$ band images in order to create a catalog of extended green objects. These objects have an excess of $4.5\ \mu\text{m}$ emission, which is thought to be the result of shock-excited H_2 ($v = 0-0$) S(9, 10, 11) lines and/or CO ($v = 1-0$) bandhead (Churchwell et al., 2009) associated with molecular outflows from MYSOs, and therefore considered to be a good indicators for ongoing massive star formation.

These mid-infrared images can therefore provide a useful overview of the position of the embedded MYSOs and HII regions, the structure of their host clumps and their local environment. The GLIMPSE images show a range of environments as shown in Fig. 3.1. The upper left panel presents a region with an offset HII region, which appears to be affecting the nearby dense gas, while the rest of the field appears to be quiescent. This source highlights the distribution of $8\ \mu\text{m}$ emission produced by polycyclic aromatic hydrocarbons (PAHs) excited in the interaction layers between ionization fronts and molecular gas. The upper right panel shows a much more evolved region with a number of evolved background stars, with some diffuse extended emission.

GLIMPSE images are presented throughout this study, and for each region which lies within the GLIMPSE survey coverage, their corresponding RGB image is given in the appendix. The wavelengths used for the three-colour images are 8 , 4.5 and $3.4\ \mu\text{m}$ for the red, green and blue channels respectively.

3.2.2 THE APEX TELESCOPE LARGE AREA SURVEY OF THE GALAXY (ATLASGAL)

The APEX Telescope Large Area Survey of the GALaxy (ATLASGAL; Schuller et al. 2009) is the largest, most sensitive ground-based submillimetre wavelength survey to date. It traces dust emission at $870\ \mu\text{m}$ across the Galactic plane and covers 420

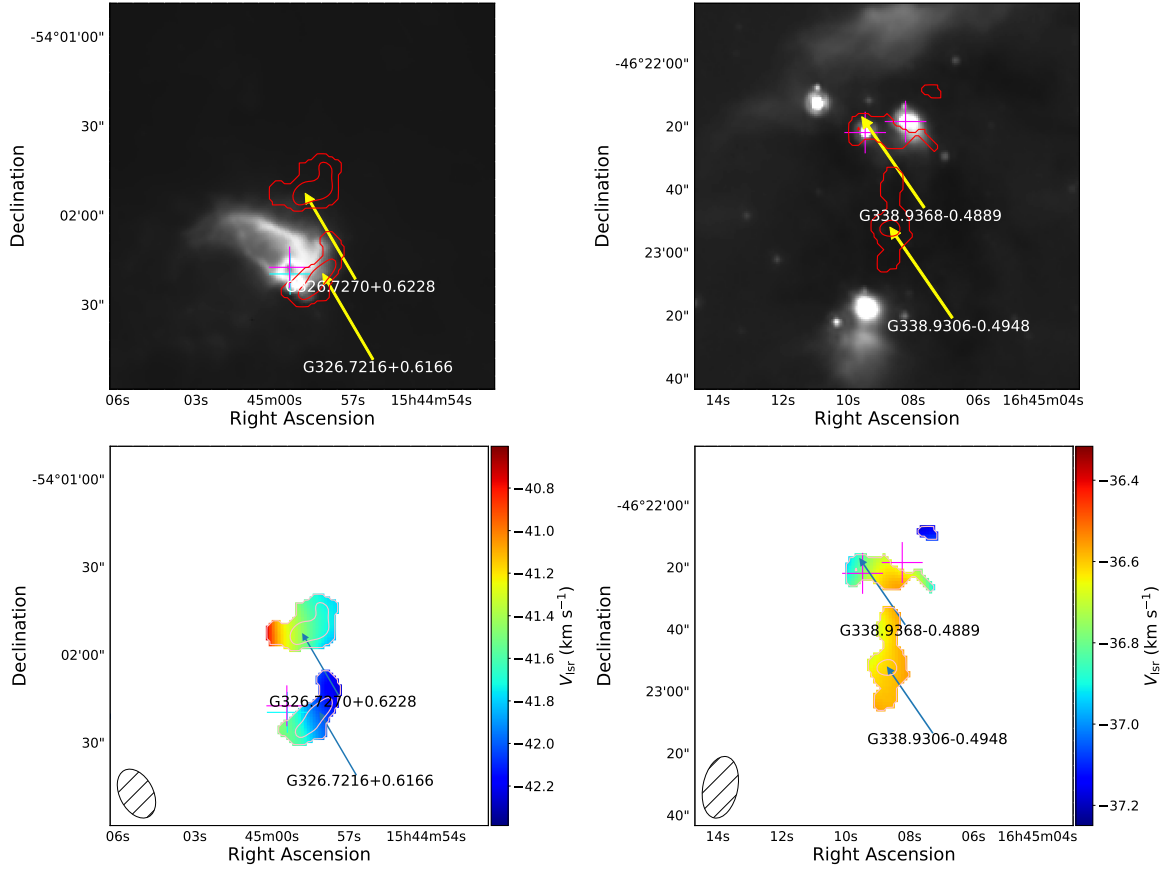


Figure 3.1: The upper panels present example $8\mu\text{m}$ images taken from the GLIMPSE Legacy survey, while the lower panels show the velocity maps for the same regions. Magenta and cyan crosses mark the positions of any MYSOs or HII regions respectively. NH_3 (1,1) integrated emission contours are overlotted on both sets of images, the contours begin at 3σ and increase in steps of 0.5σ (Values for σ/rms noise can be found in Table 3.2).

sq. degrees ($60 > \ell > -60^\circ$, $|b| < 1.5^\circ$ and $300^\circ \geq \ell \geq 280^\circ$ with $-2^\circ \leq b \leq 1^\circ$). The ATLASGAL survey was carried out using the Large APEX Bolometer Camera (LABOCA; Siringo et al. 2009), an array of 295 composite bolometers centred at a wavelength of $870 \mu\text{m}$ with a passband of $150 \mu\text{m}$; this instrument was specifically designed for fast mapping of large areas of the sky at moderate resolution and with high sensitivity. The 12 m diameter APEX telescope has a full width at half-maximum (FWHM) resolution of $19.2''$.

Approximately 10 000 dense clumps have been identified from the ATLASGAL maps (Contreras et al. 2013; Urquhart et al. 2014b). Many of these have since been followed-up with molecular line observations to obtain radial velocities (Wienen et al., 2012; Csengeri et al., 2016; Wienen et al., 2018; Urquhart et al., 2018, 2019), which when combined with a Galactic rotation curve can be used to calculate kinematic distances and derive physical properties (Wienen et al. 2015). Images from the HiGAL survey (Molinari et al. 2010, 2016) have been used to fit the spectral energy distributions (SED), to determine the dust temperatures and bolometric luminosities of the embedded protostellar objects (König et al. 2017). Many of these techniques have been applied to determine the physical properties of a large fraction (~ 8000 ; Urquhart et al. 2018) of the clumps located outside the Galactic centre region (i.e. $|\ell| > 5^\circ$); the Galactic centre region has been excluded due to issues with source confusion and the difficulty obtaining reliable kinematic distances. However, reliable distances and physical properties are now available for a large fraction of the ATLASGAL catalogue. Every ATLASGAL source has also been classified into one of four evolutionary groups based on infrared and radio counterparts, and are defined as quiescent, protostellar, young stellar object (YSO) and HII region (König et al., 2017).

The ATLASGAL survey covers 33 out of 34 of the observed fields (G261.6429–02.0922 lies outside of the ATLASGAL region). Emission contours have been overlaid onto the three-colour GLIMPSE images to compare the distribution of interstellar dust with the integrated ammonia emission and the mid-infrared environment for each observed field. These data are used to build a detailed picture of these star-forming environments and examine their physical properties, such as clump mass and luminosity (see Sect. 2.5 and Urquhart et al. (2018) for details of how these parameters are determined).

The clump masses and luminosities for 32 of the 33 fields covered by ATLASGAL range between $\sim 10^{2.5} - 10^4 M_\odot$ and $\sim 10^3 - 10^6 L_\odot$, respectively. Although G286.2086+00.1694 is located in the ATLASGAL region it was not included in the study by Urquhart et al. (2018) and so the luminosity and clump masses were not available. These extracted data complement the sample by providing masses and luminosities of the entire regions as opposed to the small, denser substructures mapped by the NH_3 emission.

3.2.3 THE METHANOL MULTIBEAM (MMB) SURVEY

The Methanol Multibeam (MMB) survey (Green et al. 2009) has surveyed $60^\circ \geq \ell \geq 186^\circ$ and $|b| < 2^\circ$ of the Galactic plane in search of the 6.7 GHz methanol masers using the Parkes 64 m radio telescope. Detected maser emission sites were followed-up using the Australia Telescope Compact Array (ATCA) or the Multi-Element Radio Linked Interferometer Network (MERLIN; Thomasson 1986) to determine accurate positions ($< 1''$) for those sources that did not have previously determined positions. This species of astronomical maser is one of the most frequently detected and is considered to be exclusively associated with the early stages of high-mass star formation (e.g. Minier et al. 2003; see Sect. 1.5.3). Comparison between the MMB catalogue and the ATLASGAL CSC (Urquhart et al. 2013) and a set of dedicated dust continuum observations (Urquhart et al. 2015b) found that 99% of methanol masers are associated with dense star-forming clumps. There is an MMB source present in 20 of the 34 fields observed ($\sim 59\%$).

3.2.4 THE H₂O SOUTHERN GALACTIC PLANE SURVEY (HOPS)

The H₂O southern Galactic Plane Survey (HOPS; Walsh et al. 2011) is an unbiased survey of 100 sq. degrees of the Galactic plane ($30^\circ \geq \ell \geq 290^\circ$, $|b| < 0.5^\circ$). HOPS was performed using the Australia Telescope National Facility (ATNF) Mopra 22 m radio telescope and detected 540 22.2 GHz H₂O maser emission sites. Walsh et al. (2014) performed follow-up observations of these maser sites using ATCA, to provide accurate positions for individual maser spots within $1''$. A number of fields that HOPS identified also appeared to consist of multiple maser sites and therefore, in total, 2790 individual spectral features (maser spots) were found towards 631 of the regions across the Galactic plane.

Out of the 631 maser sites detected in Walsh et al. (2011), 433 were identified as being associated with star formation, 121 sites with evolved stars and 77 as unknown. H₂O masers are excellent tracers of shocked gas often associated with molecular outflows from protostellar objects. They are known to occur in all regions of star formation (Claussen et al., 1996; Forster and Caswell, 1999), within both high-mass and low-mass environments. While the majority of the currently known H₂O masers are associated with star-forming regions, they can also be found in other environments, including evolved stars (Dickinson, 1976) and planetary nebulae (Miranda et al., 2001). H₂O masers are present in 11 of the fields: this constitutes 52% of the 21 fields that are covered by HOPS.

3.2.5 EXTRACTED PROPERTIES

Distances have been determined for all of the fields either by Urquhart et al. (2014b) or from the Reid et al. (2016) Bayesian model (see discussion presented in Sect. 3.4.2(a)).

Due to the large uncertainties in the derived NH_3 column densities, the dust clump masses derived from the ATLASGAL survey (Urquhart et al., 2018) have been used in this analysis. These values are naturally higher than expected for the NH_3 emission itself as the thermal dust emission encompasses a larger area. It is assumed, when using these values, that the densities of the regions are sufficiently high that the gas and dust are well-coupled and in local thermodynamic equilibrium.

Values for both the mass and luminosity for each region have been taken from the ATLASGAL compact-source catalogue (Urquhart et al., 2018), and are used to give a global overview of the regions. While the NH_3 emission can be used to derive parameters for individual clumps, the dust emission values are representative of the entire regions and surrounding environmental material. Bolometric luminosities for the sample range from ~ 1300 to $\sim 670\,000 L_\odot$ and masses range from ~ 330 to $\sim 9\,500 M_\odot$.

There is no associated value for either mass or luminosity for five of the fields from the ATLASGAL survey, as these regions either lay outside the survey’s coverage or due to a non-detection in the compact source catalogue.

3.2.5(a) UNCERTAINTIES IN EXTRACTED PARAMETERS

The distances that have been assigned to each field are kinematic and so have an associated uncertainty of ± 1 kpc. This uncertainty is mainly caused by peculiar motions of the clouds through the spiral arms of the Galaxy, which causes them to deviate from the rotation models. These are commonly referred to as “streaming motions” and can lead to perturbation from the expected radial velocities of $\pm 7 \text{ km s}^{-1}$ (Reid et al. 2009).

The ATLASGAL dust masses are estimated to be correct to within a factor of 2–3: this is mainly due to the fact that many of the parameters involved in the calculation are poorly constrained, such as the dust-to-gas ratio and the dust absorption coefficient (Urquhart et al. 2013). Two other parameters additionally affect the mass uncertainty: the kinetic or dust temperatures as derived from the spectral line analysis, with an approximate error of $\pm 1.5 \text{ K}$, and the uncertainty in the distance measurements as mentioned in the previous paragraph.

The main source of uncertainty for the luminosity values arises from the distance uncertainties and bolometric flux calculations which results from the fitting of the spectral energy distributions for each region: these are estimated to be no more than

Table 3.1: Extracted field parameters from the ATLASGAL survey.

Field id	Field name	$\text{Log}[L_{bol}]$ (L_{\odot})	$\text{Log}[M_{field}]$ (M_{\odot})	$\text{Log}[N(\text{H}_2)]$ (cm^{-2})
1	G261.6429-02.0922
2	G286.2086+00.1694
3	G305.2017+00.2072	5.139	3.527	23.362
4	G309.4230-00.6208	3.327	3.075	22.810
5	G312.5963+00.0479	4.827	3.175	22.836
6	G314.3197+00.1125	4.077	3.176	22.748
7	G318.9480-00.1969	3.871	2.523	23.092
8	G322.1729+00.6442	5.466	3.736	23.416
9	G323.4584-00.0787	5.074	3.106	22.873
10	G326.4755+00.6947	3.733	2.926	23.513
11	G326.7249+00.6159	4.545	2.686	23.079
12	G327.3941+00.1970	3.938	3.246	22.928
13	G327.4014+00.4454	4.761	3.587	23.321
14	G328.2523-00.5320	4.665	3.597	23.310
15	G328.3067+00.4308	5.828	3.705	23.076
16	G328.8074+00.6324	5.128	3.225	23.511
17	G330.9288-00.4070	3.371	2.816	22.894
18	G332.2944-00.0962	4.303	3.150	23.133
19	G332.9868-00.4871
20	G333.0058+00.7707	4.460	3.653	23.331
21	G333.0682-00.4461
22	G333.1075-00.5020	4.601	3.251	22.557
23	G336.3684-00.0033	4.794	3.736	23.072
24	G338.9196+00.5495	4.963	3.975	23.571
25	G338.9377-00.4890	3.475	2.863	22.668
26	G339.5836-00.1265	3.441	2.829	23.016
27	G339.9267-00.0837	3.605	3.064	22.900
28	G340.7455-01.0021	3.770	2.848	22.822
29	G341.2182-00.2136	4.030	2.775	22.933
30	G342.7057+00.1260	4.440	3.369	23.112
31	G343.5024-00.0145	4.466	3.050	23.016
32	G343.9033-00.6713	3.132	2.707	22.556
33	G344.4257+00.0451	5.389	3.619	22.857
34	G345.5043+00.3480

a factor of two.

While the uncertainties may be large for the absolute values for these parameters, the whole sample are uniformly affected and so the properties should provide statistically robust results.

3.3 OBSERVATIONAL DATA

3.3.1 ATCA OBSERVATIONS AND DATA REDUCTION

Observations were made of the NH_3 (1,1) and (2,2) inversion transitions towards 34 RMS identified MYSOs and HII regions (see Table 3.2 for details of observed fields). These observations were made between 15-22 February 2011 (Project Id: C2369; Urquhart et al. 2010). These observations were conducted using the Australia Telescope National Facilities' (ATNF) Australia Telescope Compact Array (ATCA). ATCA comprises of six 22 m diameter antennas, with five lying on a 3 km long east-west track with the sixth antenna being in a fixed position 3 km west of the track.

The array was set up in an east-west 352 configuration, utilising five of the antennae in a compact configuration with shortest and longest baselines of 31 and 352 metres respectively. The sixth antenna was not used for this study due to the large gap in uv -coverage. The observations were made with the ATCA Broad-band Backend (CABB; see Wilson et al. 2011 for details).

This provides a primary beam size of $\sim 2'$ (FWHM field of view) and a synthesised beam of $5\text{--}10''$ (FWHM resolution of the observations). A 64 MHz spectral window covering 23.6945 and 23.7226 GHz was used so as to include the NH_3 (1,1) and (2,2) transition in the same bandpass. Each source was observed for approximately 60 minutes, providing a velocity resolution of $0.4 \text{ km s}^{-1} \text{ channel}^{-1}$ and a sensitivity of $2.3 \text{ K channel}^{-1} \text{ beam}^{-1}$.

The sources 1934–638 and 1253–055 were observed once per day for absolute flux and bandpass calibration. The target sources were separated into groups of ~ 8 closely located sources to allow the sharing of phase calibrators and minimise observing overheads. An appropriate phase calibrator was selected for each group and the observations of the target sources were sandwiched in between observations of the phase calibrator. These observation blocks arranged to be less than an hour to allow the phase calibrators to be observed at regular intervals (typically 2-3 minutes every hour) throughout the observing session. These allow us to correct for fluctuations in the phase and amplitude of the data caused by atmospheric and instrumental effects throughout

Table 3.2: Observed field parameters. Distances appended with \star identify values obtained using the Bayesian distance estimator described in Reid et al. (2016).

Field id	Field name	RA (J2000)	Dec (J2000)	Number of clumps	v_{lsr} (km s $^{-1}$)	Distance (kpc)	rms noise (Jy beam $^{-1}$)	Beam $_{\text{maj}}$ (")	Beam $_{\text{min}}$ (")
1	G261.6429-02.0922	08h32m07.46s	-43d13m48.70s	1	14.5	2.0	0.25	9.36	5.57
2	G286.2086+00.1694	10h38m32.70s	-58d19m14.30s	2	-21.1	3.0	0.30	10.28	4.94
3	G305.2017+00.2072	13h11m10.45s	-62d34m38.60s	1	-42.4	3.8	0.45	6.74	5.97
4	G309.4230-00.6208	13h48m38.86s	-62d46m09.50s	1	-42.4	3.5	0.38	7.66	5.40
5	G312.5963+00.0479	14h13m14.12s	-61d16m48.90s	1	-63.7	6.0	0.32	8.70	5.07
6	G314.3197+00.1125	14h26m26.28s	-60d38m31.50s	2	-47.5	4.2	0.33	7.61	5.47
7	G318.9480-00.1969	15h00m55.10s	-58d59m06.00s	1	-34.4	2.1	0.41	6.88	5.83
8	G322.1729+00.6442	15h18m38.29s	-56d37m30.90s	1	-57.7	3.3	0.49	7.90	5.34
9	G323.4584-00.0787	15h29m19.36s	-56d31m21.70s	1	-66.8	4.0	0.29	7.72	6.19
10	G326.4755+00.6947	15h43m18.94s	-54d07m35.40s	1	-41.2	1.8	0.58	8.78	5.77
11	G326.7249+00.6159	15h44m59.39s	-54d02m19.60s	2	-41.7	1.8	0.33	8.95	5.74
12	G327.3941+00.1970	15h50m20.07s	-53d57m07.10s	1	-89.3	5.2	0.39	9.08	5.62
13	G327.4014+00.4454	15h49m19.36s	-53d45m14.40s	1	-78.4	5.0	0.52	8.80	5.66
14	G328.2523-00.5320	15h57m59.82s	-53d58m00.40s	3	-45.1	2.7	0.44	8.08	6.01
15	G328.3067+00.4308	15h54m06.34s	-53d11m39.20s	1	-93.2	5.8	0.33	8.44	5.93
16	G328.8074+00.6324	15h55m48.36s	-52d43m06.80s	2	-41.7	2.7	0.52	9.30	5.55
17	G330.9288-00.4070	16h10m45.07s	-52d05m50.20s	1	-41.2	2.6	0.30	9.22	5.40
18	G332.2944-00.0962	16h15m45.86s	-50d56m02.40s	1	-48.9	3.1	0.33	9.52	5.47
19	G332.9868-00.4871	16h20m37.81s	-50d43m49.60s	1	-52.8	3.6	0.42	9.66	5.44
20	G333.0058+00.7707	16h15m13.79s	-49d48m52.00s	1	-49.2	3.0	0.62	9.71	5.62

Table 3.3: Table 3.2 continued.

Field id	Field name	RA (J2000)	Dec (J2000)	Number of clumps	v_{lsr} (km s $^{-1}$)	Distance (kpc)	rms noise (Jy beam $^{-1}$)	Beam $_{\text{maj}}$ (")	Beam $_{\text{min}}$ (")
21	G333.0682-00.4461	16h20m48.95s	-50d38m40.30s	1	-53.3	3.6	0.59	9.37	5.50
22	G333.1075-00.5020	16h21m14.22s	-50d39m12.60s	2	-56.5	3.6	0.38	10.10	5.27
23	G336.3684-00.0033	16h32m56.46s	-47d57m52.30s	1	-126.7	6.7	0.54	10.48	5.74
24	G338.9196+00.5495	16h40m34.04s	-45d42m07.90s	1	-62.8	4.2	1.21	9.91	5.67
25	G338.9377-00.4890	16h45m08.80s	-46d22m17.00s	2	-36.6	2.9	0.36	10.08	5.64
26	G339.5836-00.1265	16h45m58.48s	-45d38m41.40s	1	-34.3	2.6	0.37	9.75	5.28
27	G339.9267-00.0837	16h47m03.94s	-45d21m20.50s	1	-52.8	3.6	0.34	9.90	5.56
28	G340.7455-01.0021	16h54m04.05s	-45d18m50.00s	1	-29.1	2.4	0.36	10.08	5.71
29	G341.2182-00.2136	16h52m17.93s	-44d26m53.00s	1	-42.9	3.3	0.50	9.84	5.45
30	G342.7057+00.1260	16h56m02.91s	-43d04m43.90s	1	-41.0	3.4	0.46	10.05	5.50
31	G343.5024-00.0145	16h59m20.90s	-42d32m38.40s	2	-27.9	2.6	0.45	10.20	5.57
32	G343.9033-00.6713	17h03m30.11s	-42d37m48.60s	1	-29.4	2.2	0.36	10.69	6.04
33	G344.4257+00.0451	17h02m09.35s	-41d46m44.30s	2	-66.6	4.9	0.45	10.61	5.35
34	G345.5043+00.3480	17h04m22.87s	-40d44m23.50s	1	-17.7	2.4	0.66	13.27	4.81

the observations.

The calibration and reduction of these data were performed using the MIRIAD reduction package (Sault et al. 1995) following standard ATCA procedures. Initially regions were imaged at twice the size of the primary beam, choosing a pixel size to provide ~ 10 pixels across the synthesised beam ($1''$ pixels). Sources were imaged with a velocity range of 120 km s^{-1} centred on the systemic velocity of the RMS source using the native velocity resolution of the spectrometer. This resulted in spectral line cubes of $256'' \times 256'' \times 300 \text{ km s}^{-1}$ for each transition.

These cubes were deconvolved using a robust weighting of 0.5 using a couple of hundred cleaning components per velocity channel, or until the first negative component was encountered. Weighting values less than -2 correspond to minimising sidelobe levels only (uniform weighting), whereas values greater than +2 minimise noise levels (natural weighting). A value of 0.5 gives nearly the same sensitivity as natural weighting, but with a significantly better beam. These cubes were inspected to identify bright ammonia peaks in the field, and when detected in a map, these were integrated along the velocity axis in order to produce a high signal-to-noise ratio (SNR) map of the ammonia emission. These maps allow the peak position of the emission (taken to be the centre of the clump) and morphology of the dense gas traced by the ammonia emission to be discerned and spatially compared with the position of their embedded MYSOs and/or HII regions.

The largest well-imaged structure possible at this frequency from these snapshot observations is limited to approximately $1'$ due to the limited uv -coverage and integration time. However, many of the maps displayed evidence of large-scale emission, which, when undersampled, can distort the processed images and lead to prominent imaging artifacts and confusion in the processed maps. This can reduce the SNR in the maps and over-resolve large-scale extended emission, breaking it up into irregular and/or multiple-component structures.

3.4 METHODS AND SOURCE IDENTIFICATION

3.4.1 SOURCE EXTRACTION

For each source NH_3 (1,1) and (2,2) emission intensity maps have been created by integrating the velocity channels between $\pm 25 \text{ km s}^{-1}$ of the peak above a 3σ threshold. These maps reveal the presence of high SNR clumps.

The `FellWalker` algorithm (Berry 2015; Moore et al. 2015) has been applied to

Table 3.4: Fe11Walker source catalogue for detected clumps. All parameters that have been derived in the table have been obtained using the NH₃ emission maps. Columns: (1) Field identification number; (2) Clump name derived from Galactic coordinates of the peak emission of the source; (3)-(4) Right ascension and declination of source in J2000 coordinates; (5)-(6) Semi-major and semi-minor axis of clumps; (7) Aspect ratio ($\sigma_{maj} / \sigma_{min}$); (8) Radius for each clump; (9)-(10) Sum and peak emission values; (11) Signal to noise ratio.

Field id	Clump name	RA (J2000)	Dec (J2000)	σ_{maj} (")	σ_{min} (")	Aspect Ratio	Radius (pc)	Sum (K km s ⁻¹)	Peak (K km s ⁻¹)	SNR
(1)	(2)	(3)	(4)	(5)	(6)	(7)	(8)	(9)	(10)	(11)
1	G261.6454-2.0884	08h32m09.00s	-43d13m47.57s	5.43	3.75	1.45	0.07	409.24	1.90	7.21
2	G286.2124+0.1697	10h38m34.18s	-58d19m17.65s	4.13	2.62	1.57	...	370.88	2.96	9.06
2	G286.2052+0.1706	10h38m31.49s	-58d19m01.99s	3.27	1.86	1.76	...	137.05	2.16	6.24
3	G305.2084+0.2061	13h11m13.80s	-62d34m41.23s	4.65	3.87	1.20	0.14	1423.72	10.29	22.03
4	G309.4208-0.6204	13h48m37.80s	-62d46m09.98s	7.45	6.57	1.13	0.26	950.19	2.58	6.63
5	G312.5987+0.0449	14h13m15.38s	-61d16m54.37s	3.64	2.25	1.62	...	231.04	2.33	6.53
6	G314.3214+0.1146	14h26m26.47s	-60d38m20.51s	4.31	3.37	1.28	0.12	262.18	2.11	6.18
6	G314.3197+0.1092	14h26m26.64s	-60d38m40.85s	2.33	1.45	1.61	0.09	53.54	1.64	4.08
7	G318.9477-0.1959	15h00m55.30s	-58d58m52.14s	5.94	4.99	1.19	0.12	1298.33	5.00	11.97
8	G322.1584+0.6361	15h18m34.63s	-56d38m24.79s	6.50	3.79	1.72	0.15	1096.10	5.67	11.18

Notes: Only a small portion of the data is provided here, the full table is presented in Appendix A.

the NH_3 (1,1) integrated emission maps due to their higher SNR since these are more likely to trace the full extent of individual NH_3 clumps and their associated emission peaks. The `FellWalker` algorithm was chosen as it has been widely used in recent studies (Urquhart et al. 2015a, Eden et al. 2017), and is robust against a wide choice of input parameters. It was required that all clumps be above a detection threshold of 3σ , where in this case σ refers to the image rms level as determined from emission-free regions of the maps. It was also required that clumps be larger than the beam size (~ 10 pixels) in order to avoid spurious detections. Detections towards the edges of the fields were also excluded due to lower SNRs, and because source parameters are likely to be poorly constrained; this did not prove to be a significant constraint, however, as emission is generally concentrated towards the centre of the fields. There appear to be ten fields which contain imaging artifacts that resulted from the poor sensitivity of the interferometric snapshot to large-scale extended emission (as mentioned in Sect. 3.3.1). This has been mitigated through the two thresholds required for a detected clump described above.

In total, `FellWalker` has identified 44 clumps in the 34 fields observed. The number of clumps detected in each field is given in Col. 5 of Table 3.2. The clump parameters determined by `FellWalker` are given in Table 3.4. The clump names are derived from the coordinates of the centre of the clump which can be found in Cols. 3 and 4 of this table. A total of 9 fields contain more than a single clump, with the maximum number of three clumps per field. Clumps lying within the same field have coherent velocities ($\delta v < 5 \text{ km s}^{-1}$), consistent with the hypothesis that they are all associated with the same giant molecular cloud (GMC), and many appear to be a part of the same mid-infrared structure within individual fields. Figure 3.1 presents a few examples of the NH_3 (1,1) inversion emission contours overlaid on $8 \mu\text{m}$ IRAC images of the same region along with the associated velocity maps.

The `FellWalker` algorithm also fits the semi-major and semi-minor axes of each clump, the ratio of which is used to find the corresponding aspect ratio: these are given in Cols. 5–7 of Table 3.4. Almost every clump is extended with respect to the beam and are typically elongated: the mean and standard deviation values of the aspect ratio are 1.66 and 0.58 respectively. The upper panel of Fig. 3.2 shows a histogram of the aspect ratios for the entire sample. One clump has an aspect ratio of 4.68 (G344.4279+0.0514). This particular source seems to be filamentary in nature as shown in Fig. 3.4. Due to the low aspect ratios, any projection elements are unlikely to impact on the morphologies of the NH_3 clumps.

The angular radius for each clump has been estimated from the geometric mean of the deconvolved major and minor axis of the NH_3 emission, multiplied by a factor η

Table 3.5: Table of RMS associations with corresponding angular offset values for all detected clumps. All RMS names appended with * relate to RMS objects embedded within the NH₃ clump shown.

Field id	Clump name	RMS name	RMS Type	Angular Offset (")
1	G261.6454−2.0884	G261.6429−02.0922	HII region	25
2	G286.2124+0.1697	G286.2086+00.1694	YSO	22
2	G286.2052+0.1706	G286.2086+00.1694	YSO	22
3	G305.2084+0.2061	G305.2017+00.2072A	YSO	49
4	G309.4208−0.6204	G309.4230−00.6208	YSO	7
5	G312.5987+0.0449	G312.5963+00.0479	HII region	21
6	G314.3214+0.1146	G314.3197+00.1125	YSO	11
6	G314.3197+0.1092	G314.3197+00.1125	YSO	14
7	G318.9477−0.1959	G318.9480−00.1969A*	YSO	0
8	G322.1584+0.6361	G322.1729+00.6442	YSO	79
9	G323.4537−0.0830	G323.4584−00.0787	HII region	27
10	G326.4753+0.7030	G326.4755+00.6947	YSO	43
11	G326.7270+0.6228	G326.7249+00.6159B	YSO	26
11	G326.7216+0.6166	G326.7249+00.6159A	HII region	18
12	G327.3933+0.1987	G327.3941+00.1970*	YSO	20
13	G327.4030+0.4447	G327.4014+00.4454*	HII region	3
14	G328.2544−0.5318	G328.2523−00.5320A*	YSO	0
14	G328.2610−0.5278	G328.2523−00.5320A	YSO	29
14	G328.2607−0.5206	G328.2523−00.5320B	YSO	46
15	G328.3021+0.4377	G328.3067+00.4308	HII region	48
16	G328.8057+0.6347	G328.8074+00.6324	HII region	18
17	G328.8109+0.6336	G328.8074+00.6324	HII region	17
18	G330.9259−0.4066	G330.9288−00.4070*	HII region	10
19	G332.2962−0.0927	G332.2944−00.0962	HII region	11
20	G332.9836−0.4885	G332.9868−00.4871*	YSO	9
21	G333.0179+0.7654	G333.0162+00.7615	HII region	12
22	G333.0674−0.4464	G333.0682−00.4461*	YSO	3
23	G333.1038−0.5026	G333.1075−00.5020	YSO	19
23	G333.1120−0.4996	G333.1075−00.5020	YSO	10
24	G336.3696−0.0045	G336.3684−00.0033A	HII region	9
25	G338.9231+0.5523	G338.9196+00.5495*	YSO	17
25	G338.9306−0.4948	G338.9377−00.4890B*	YSO	32
25	G338.9368−0.4889	G338.9377−00.4890B*	YSO	5
26	G339.5845−0.1267	G339.5836−00.1265*	YSO	15
27	G339.9257−0.0825	G339.9267−00.0837*	YSO	10
28	G340.7460−1.0005	G340.7455−01.0021*	YSO	14
29	G341.2166−0.2113	G341.2182−00.2136*	YSO	1
30	G342.7069+0.1250	G342.7057+00.1260B*	YSO	2
31	G343.5027−0.0133	G343.5024−00.0145*	HII region	1
31	G343.5058−0.0172	G343.5024−00.0145*	HII region	21
32	G343.9043−0.6705	G343.9033−00.6713*	YSO	2
33	G344.4279+0.0514	G344.4257+00.0451A	HII region	20
33	G344.4165+0.0455	G344.4257+00.0451C	YSO	12
34	G345.5044+0.3484	G345.5043+00.3480*	YSO	0

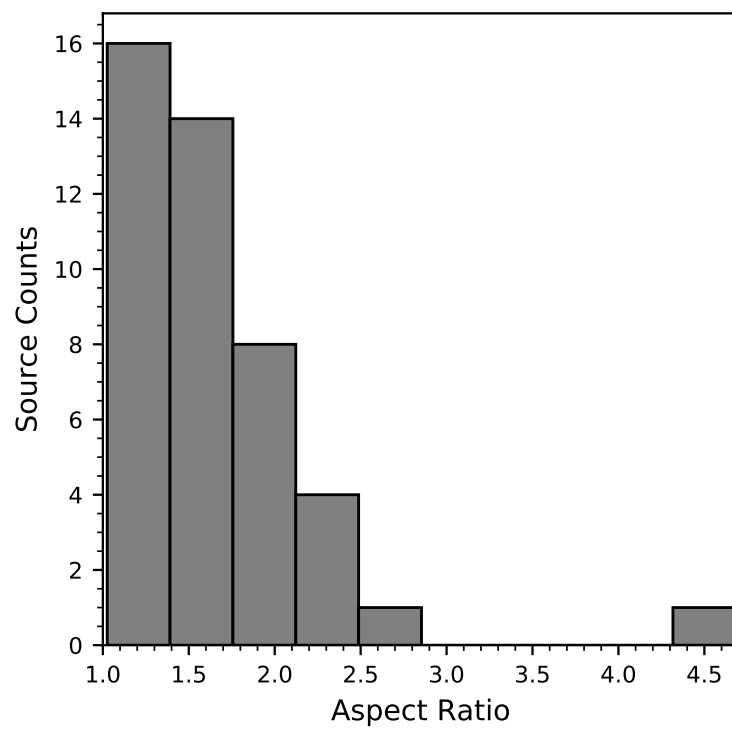


Figure 3.2: Histogram presenting the aspect ratios for all detected clumps (i.e. $\sigma_{\text{maj}} / \sigma_{\text{min}}$).

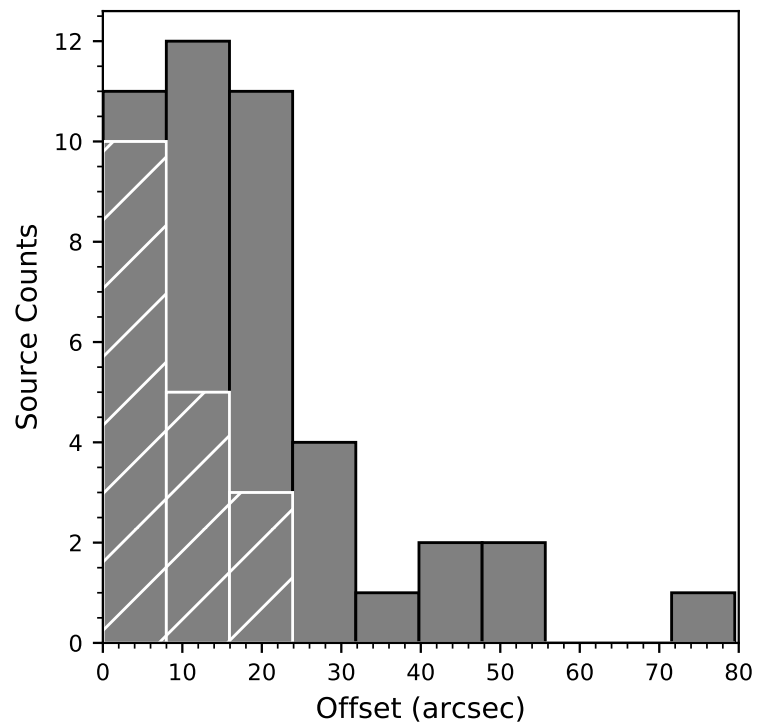


Figure 3.3: Histogram presenting the distribution of the angular offsets between associated RMS sources and peak clump positions, embedded sources are shown with hatched markings.

that relates the rms size of the emission distribution of the source to its angular radius (Eqn. 6 of Rosolowsky et al. 2010):

$$\theta_{\text{R}} = \eta \left[(\sigma_{\text{maj}}^2 - \sigma_{\text{bm}}^2) (\sigma_{\text{min}}^2 - \sigma_{\text{bm}}^2) \right]^{\frac{1}{4}} \quad (3.1)$$

where σ_{bm} is the rms size of the beam (i.e. $\sigma_{\text{bm}} = \frac{\theta_{\text{FWHM}}}{\sqrt{8 \ln 2}}$). The value of η is taken to be 2.4 following Rosolowsky et al. (2010). An angular size has been obtained for 31 out of the 44 clumps (70%): the remaining ten clumps have one axis smaller than the beam size and so a size cannot be accurately determined. This is an artifact of the detection threshold of the `FellWalker` algorithm; only NH_3 emission above this threshold is used for this analysis, although the NH_3 emission may be extended at levels below this threshold. This can result in the measured source sizes underestimating the size of the clumps and can result in sizes that are smaller than the beam (Rosolowsky et al., 2010). The obtained angular radius values range from 2.8'' to 19.4'' with a mean of 9.5''.

With the exception of one field not included in the ATLASGAL survey coverage (G261.6429–02.0922), all detected clumps in every field are enveloped by the thermal dust emission of the region, meaning that 43 of the 44 of the NH_3 clumps are associated with 32 dust sources. For the 32 ATLASGAL sources, 24 (75%) are associated with a single NH_3 clump, 6 (19%) with two NH_3 clumps, and 2 (6%) with three NH_3 clumps. The association of multiple ammonia clumps with a single dust clump, and the fact that ammonia is tracing high volume densities allows us to investigate the substructure of these regions.

3.4.2 RMS AND MASER ASSOCIATIONS

Each detected clump has been matched with a source from the RMS survey. RMS sources that lie towards the centre of the NH_3 (1,1) emission are classified as ‘embedded’, while sources located further are classified as ‘associated’. Every clump has at least one associated source due to the targeted nature of the observations. There are a total of 48 RMS sources in the sample, and there are only 20 RMS sources (49%) classified as either MYSO (15 sources) or HII region (5 sources) embedded with the clumps identified in the 34 fields.

There are therefore 14 MYSOs and 14 HII regions which are not embedded. The offsets between the RMS sources and each clump’s peak position can be found in Table 3.5, and a histogram plot of angular offsets is shown in the lower panel of Fig. 3.3. The angular offsets between the position of the targeted RMS sources and the centre

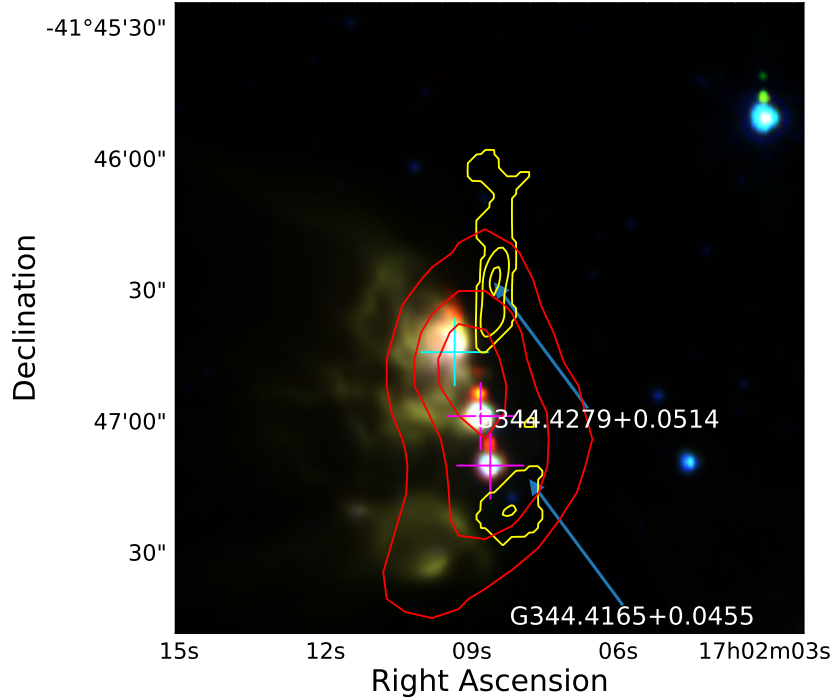


Figure 3.4: Example RGB GLIMPSE image of region (G344.4257+00.0451), overlaid with NH_3 and ATLASGAL contours in yellow and red respectively, the contours levels are equivalent to those in Fig. 3.1. This field contains two clumps, one of which (G344.4279+0.0514) presents the most elongated structure in the sample, with a filamentary morphology.

of the NH_3 emission for each clump ranges between $0.04''$ and $79.5''$ with a mean offset of $18.19''$. The maximum offset between the source and the NH_3 emission for deeply-embedded RMS sources is $21''$. These values are similar to those reported in previous studies (e.g. Urquhart et al. 2015a).

3.4.2(a) DISTANCES AND CLUMP RADII

Distances to the RMS sources in each field have been taken from Urquhart et al. (2014b), with only two fields (G261.6429−02.0922 and G286.2086+00.1694) having no reliable distance value. The Reid et al. (2016) model was used to estimate the distances for these two sources. This method uses a Bayesian approach to assign sources to a particular spiral arm based on their (l, b, v) coordinates while taking into account kinematic distances, displacement from the Galactic plane, and proximity to individual parallax sources. The distance to G261.6429−02.0922 was found to be 2.02 ± 0.78 kpc and 3.0 ± 1.23 kpc for G286.2086+00.1694. This additional information gives a complete list of distances for every observed field; these are given in the last

column of Table 1. Overall, the fields have a minimum and maximum distance of 1.80 and 6.70 kpc respectively, with a mean distance of 3.46 ± 1.22 kpc. There was no differences found between the distances towards MYSOs or HII regions. As mentioned in the previous section the angular radius for 31 out of the 44 (70%) detected clumps has been calculated, and with the determined distances, it is possible to calculate the physical clump size. The clumps have a mean radius of 0.15 pc with a range between 0.04 pc and 0.36 pc (see Table 3.4), which is on the size scale of individual cores or small stellar systems.

3.4.2(b) IMAGE ANALYSIS AND CLASSIFICATION

The GLIMPSE three-colour images provide a view into the infrared properties of the environments, and can be used to detect multiple phenomena as discussed in Sect. 3.2.1. Three-colour IRAC images of the observed regions are presented in Figs. 3.4, 3.5 and 3.6 (GLIMPSE images for all regions can be found in the appendix), and have overplotted contours of the ammonia and dust emission in order to examine the morphological correlation of molecular gas and mid-infrared emission and the embedded star formation.

A classification system was constructed based on the morphologies of the NH_3 emission and how it relates to the RMS sources and thermal dust emission from an inspection of these composite images. Fields which contain a single well-defined clump that is spatially coincident with the ATLASGAL emission and which have an RMS source located centrally towards the NH_3 emission are classified as *early star forming* (ESF). Fields that show a more unstructured and broken morphology, generally containing multiple NH_3 clumps and RMS sources that are not coincident with an NH_3 clump are classified as *late star forming* (LSF), as it is expected that the feedback from forming massive star has a significant disruptive impact on its surroundings. All regions show signs of ongoing star formation processes, and Figs. 3.5 and 3.6 show some examples of regions that are classified as ESF and LSF, respectively.

Three of the fields in this sample were classified as ‘quiescent’ as they shown no signs of current star formation. These quiescent clumps are well aligned with the dust emission in the area but show no signs of having undergone any star formation (i.e. no evidence of an embedded mid-infrared point source, which is usually taken as evidence of the presence of a embedded stellar object). While all observations were targeted towards RMS sources, the offset between the NH_3 emission and the nearest RMS object for these three regions is sufficiently large (at least 3 times the beam size) to conclude that they are not associated. An example of a quiescent clump is shown in the left panel of Figure 3.1 (G326.7270+0.6228).

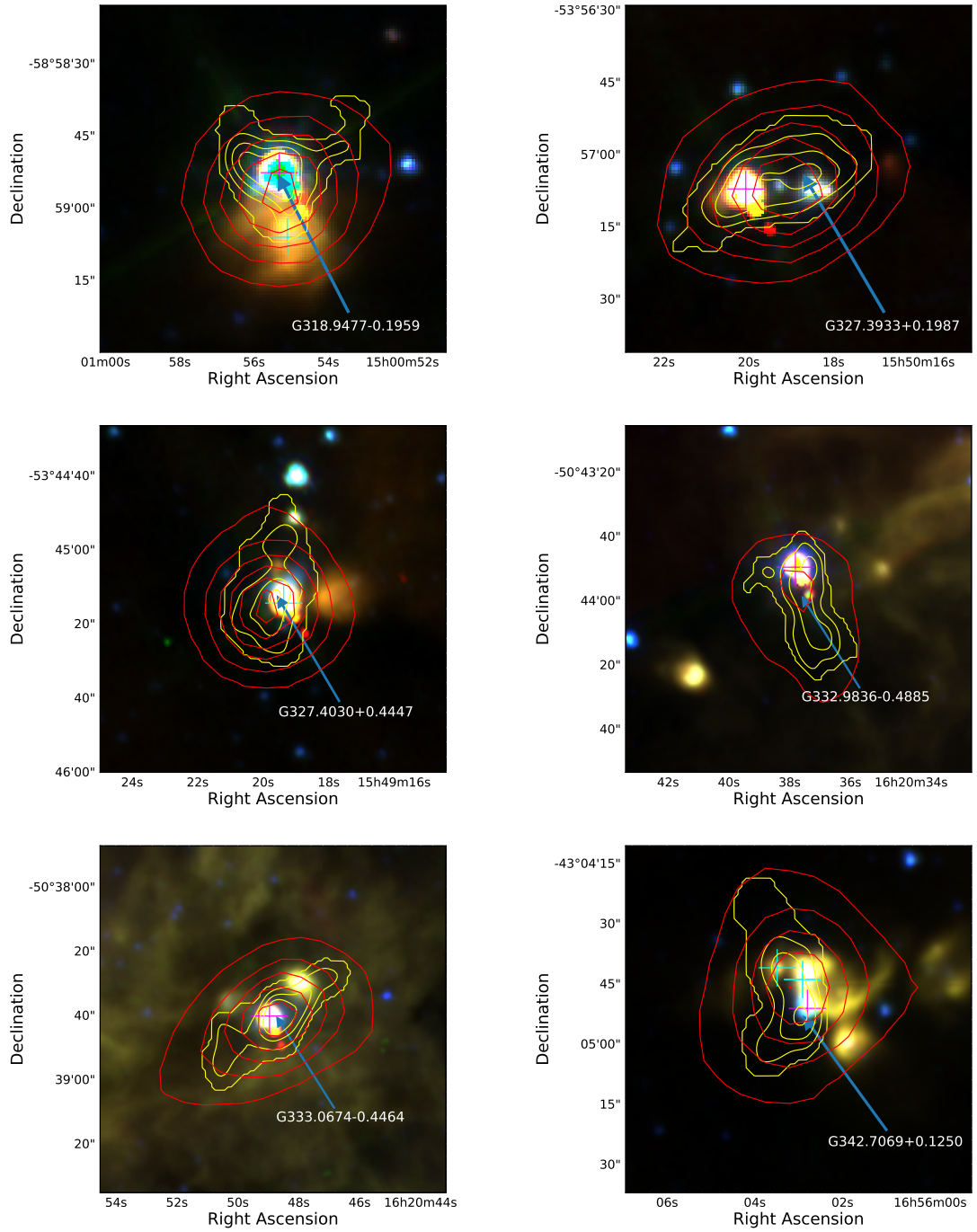


Figure 3.5: Example maps of early star forming regions, presented in each panel is a three-colour GLIMPSE image overlaid with NH₃ emission and ATLASGAL dust emission contours in yellow and red respectively, the contours levels are equivalent to those in Fig 3.1. The wavelengths for the RGB channels are 8, 4.5 and 3.4 μm respectively. MYSOs and HII regions identified by the RMS survey are shown with magenta and cyan crosses respectively. Clump positions and names are shown with blue arrows and white labels. GLIMPSE images for the remaining 12 ESF fields can be found in the appendix.

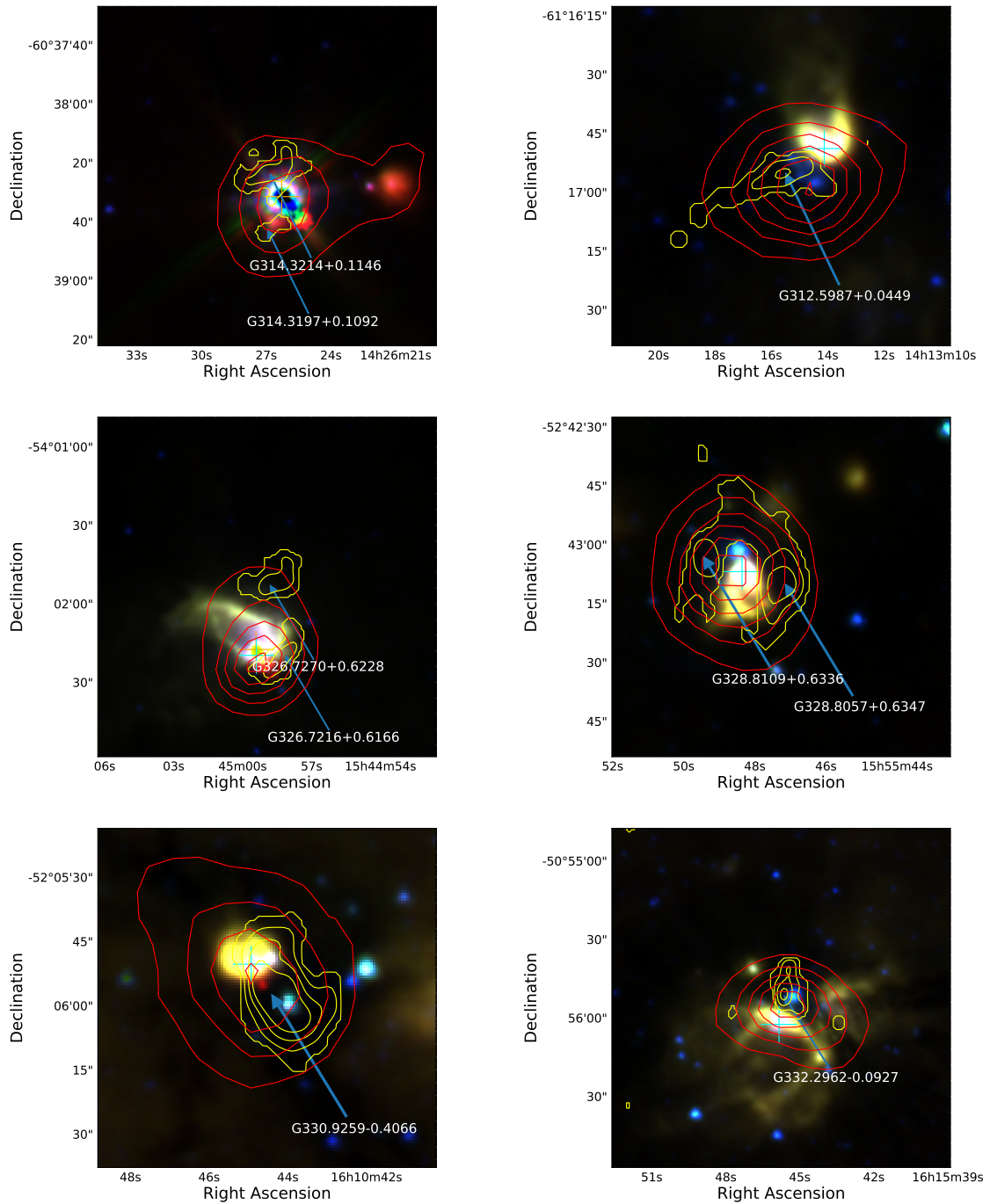


Figure 3.6: Image details are the same as for Fig. 3.5, but for a sample of late star forming regions. GLIMPSE images for the remaining 10 LSF regions can be found in the appendix.

If a field contains both an embedded MYSO and an HII region (or multiple of either), then the most centrally-located source is taken as the primary association (10 fields, 6 of which are ESF and 4 are LSF). There are 15 fields in the sample that have been classified as ESF fields. Of these fifteen, 13 are associated with MYSOs (as defined by the RMS survey), with the remaining two associated with an HII region. Sixteen fields have been classified as LSF. Only six of these fields contain an embedded MYSO, while the majority of fields are associated with an HII region. An inspection of the images indicates that the majority of early star forming regions are associated with MYSOs (87%), while later regions are dominated by HII regions (63%). MYSOs, therefore, appear to be still very embedded, while the majority of the HII regions appear to be actively disrupting their natal clump and breaking out of their dust cocoons (as shown in Fig.3.1). This is not obvious in the ATLASGAL data (which is sensitive to the whole column of gas along the line of sight, and also has lower spatial resolution than the NH₃ observations) but can clearly be seen by the NH₃ emission, which has a critical density of $n \sim 1.8 \times 10^3 \text{ cm}^{-3}$ and so only traces the high volume density substructure within the clumps.

Our visual examination of the dust- and ammonia-overlaid three-colour IRAC maps has resulted in the identification of three visually distinct stages (quiescent, ESF and LSF). It was necessary to demonstrate that this sequence is reliable, and one such approach is to compare the physical properties of these different types of regions and determine whether there are any physical trends that support the visual classification undertaken. It is worth noting that the classification parameters depend on the line of sight towards each individual source. It may be that sources which have been classified as ESF may alternatively be classed as LSF if they were view from a different angle, furthermore, the sensitivity of the observations may also cause a misinterpretation of which class a source belongs to and with greater sensitivity it could be potentially be shown that certain LSF fields are in fact ESF. In this sense, the classification system may not be wholly robust, however, this effect could be tested by employing the use of NH₃ modelling and simulations techniques to statistically estimate the variation in a source's classification when viewed from different angles. These techniques are beyond the subject of this Thesis, and for the data present in this Chapter, the system is assumed to be a good measure of classification.

Data from the MMB survey and HOPS has been used in order to provide more information on the regions presented in this study. Overall, 52 H₂O and 31 methanol masers are found to be associated with the 34 fields. A breakdown of this sample is presented in Table 3.6 for each classification and central RMS object.

GLIMPSE 8 μm images have been used to provide context for the maser distribu-

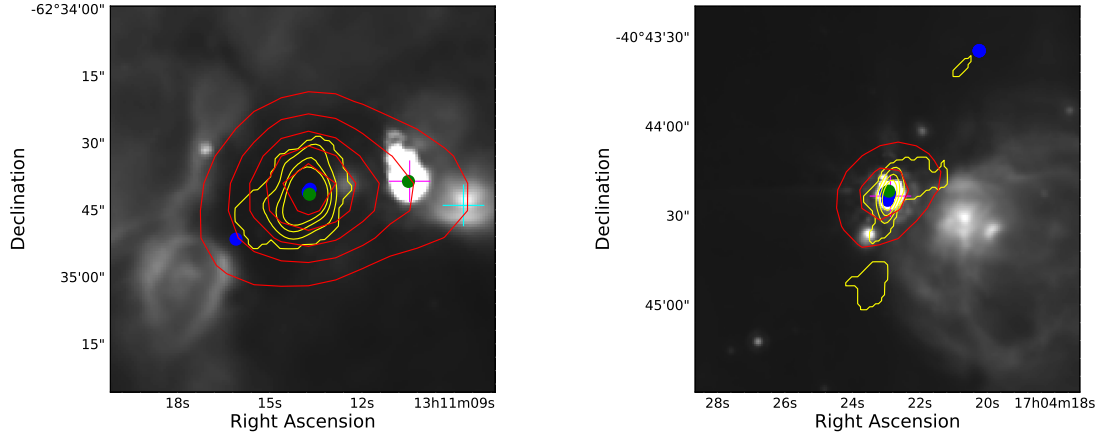


Figure 3.7: GLIMPSE $8\mu\text{m}$ images showing two regions from the sample (G305.2017+00.2072 and G345.5043+00.3480). The red contours outline the ATLASGAL dust emission and the yellow contours outline the NH_3 emission, while the green and blue filled circles represent the methanol and H_2O maser detections respectively, the contours levels are equivalent to those in Fig. 3.1. Magenta markers represents the position of identified MYSOs, while cyan markers show the positions of HII regions.

Table 3.6: Distribution of masers across the sample.

Classification	Methanol	H_2O
	Masers	Masers
ESF	20	41
LSF	11	11
YSO	23	32
HII region	8	15

tion with NH_3 and ATLASGAL contours: two example maps of these can be found in Fig. 3.7. The image shown in the left panel shows a region which has been defined as quiescent with an MYSO and HII region in close proximity to the west; however, there are also coincident masers (8 water and 1 methanol) towards the centre of the gas and dust emission. Therefore, this region is unlikely to be quiescent and is probably in an early protostellar stage of star formation, as the presence of maser emission indicates that a central core is likely to have already developed. This is the case for all three regions which have been identified as quiescent (G305.2017+00.2072, G322.1729+00.6442 & G326.4755+00.6947), all of which have at least one methanol maser towards the centre of the field. These quiescent fields have been reclassified as early star forming, leaving no quiescent regions in the sample. Therefore, 18 fields have been classified as being ESF and 16 fields as LSF. The right panel of Fig. 3.7 presents another region with a relatively high number of maser detections. This field is classified as early star forming and is associated with a total of 12 masers (10 water and 2 methanol). All of these are found towards the central RMS object. This source appears to be located on the edge of an evolved HII region and so this may be an example of triggered star formation (see further discussion in Sect. 5.4.4).

3.5 DETERMINATION OF PHYSICAL PROPERTIES

3.5.1 AMMONIA LINE FITTING

A spectral line analysis has been conducted for all 44 clumps which have been identified by `FellWalker`. The theory for the calculation of physical parameters using the inversion transitions of ammonia can be found in Sect. 2.4.

This study makes use of the method presented in Rosolowsky et al. (2008) for estimating physical parameters from ammonia spectra, using a nonlinear least-squares minimisation code to determine the optimal fit to the observed spectra. This technique simultaneously fits observed the NH_3 inversion transitions (in this case, the (1,1) & (2,2) transitions) using the physical parameters (such as rotational temperature and optical depth) as fitting parameters. This avoids potential systematic errors that may be encountered when transitions are fitted independently and automatically determines uncertainties for the physical parameters of the system.

A `Python` implementation of this method, called `pyspeckit` (Ginsburg and Mirocha, 2011), was used to fit the eighteen individual (1,1) and twenty-one (2,2) hyperfine transitions simultaneously, determining the free parameters which include the rotational

(T_{rot}) and excitation (T_{ex}) temperatures, FWHM line-width (Δv), radial velocity (v_{LSR}) and the NH_3 column density. While the satellite lines of the (2,2) emission are generally undetected in the observations, a well-detected (2,2) main line sufficiently constrains the solution allowing for good determinations of the free parameters (see Sect. 2.4). This model assumes that the kinetic temperature is less than $T_0 = 41.5$ K, which is the energy difference associated with these lowest two inversion transitions, implying that only these first two energy states are significantly populated.

For each of the data cubes, a pixel-by-pixel line analysis has been performed in order to extract spectra which can then be fit using the aforementioned technique. The moment maps of the ammonia spectra were used to provide initial guesses at the velocity and line-width parameters, which were then refined by a pixel-by-pixel fitting process. Only pixels above a 3σ threshold were fitted to avoid contamination of the results due to the inclusion of pixels with low SNRs. The observed maps have been spatially smoothed to twice the size of the original beam ($\sim 20''$) in order to improve the SNR of individual spectra. The derived peak and median values for the fitted parameters for all of the clumps are given in Table 3.7.

3.5.1(a) THERMAL AND NON-THERMAL LINE-WIDTHS

The observed FWHM line-width (Δv_{obs} , a free parameter determined by the fitting procedure) is a convolution of the intrinsic line-width of the source (Δv_{int}) and the velocity resolution of the observations. The 0.4 km s^{-1} spectrometer channel width was removed by subtracting this value from the measured FWHM line-width in quadrature:

$$\Delta v_{\text{int}} = \sqrt{(\Delta v_{\text{obs}}^2 - (0.4)^2)}. \quad (3.2)$$

The peak intrinsic line-widths have mean and median values of 3.85 ± 0.3 and 3.28 km s^{-1} respectively. These values are similar to values found in previous studies (Sridharan et al., 2002; Wielen et al., 2012).

The line-widths of the ammonia spectra consist of thermal and non-thermal components where the thermal component can be estimated, as shown in Sect. 2.2.5:

$$\Delta v_{\text{th}} = \sqrt{\left(\frac{8 \ln 2 k_{\text{B}} T_{\text{kin}}}{m_{\text{NH}_3}}\right)}, \quad (3.3)$$

where $8 \ln 2$ is the conversion between the velocity dispersion Δv and the FWHM line-width Δv , k_{B} is the Boltzmann constant, and m_{NH_3} is the mass of an ammonia molecule (17.03 AMU). The measured line-widths themselves are significantly broader than this estimation (for gas temperatures of 20 K, Δv_{th} is $\sim 0.22 \text{ km s}^{-1}$), meaning there is a

large contribution from non-thermal components such as supersonic turbulent motions, outflows, shocks and magnetic fields (Elmegreen and Scalo 2004). The impact on the data from these mechanisms can be derived by subtracting the thermal component in quadrature:

$$\Delta v_{\text{nt}} = \sqrt{\left(\Delta v_{\text{int}}^2 - \frac{8 \ln 2 k_{\text{B}} T_{\text{kin}}}{m_{\text{NH}_3}} \right)}. \quad (3.4)$$

The gas pressure ratio can be estimated from the ratio of the thermal and non-thermal line-widths, which are equivalent to the thermal and non-thermal pressures within the gas:

$$R_p = \left(\frac{\Delta v_{\text{th}}^2}{\Delta v_{\text{nt}}^2} \right). \quad (3.5)$$

These ratio values are quite low (the mean and median values of the mean pressure for each clump is 0.012 and 0.01 respectively, with a range of 0.002 to 0.03, see Table 3.8), indicating that the pressure in the gas is dominated by non-thermal motion.

3.5.1(b) BEAM FILLING FACTOR

The previously-mentioned assumption of kinetic temperature limit mentioned above ($T_{\text{kin}} < T_0 = 41.5 \text{ K}$) provides a significant restriction on this study.

For $T_{\text{kin}} < T_0$, the calculation of the rotation temperature can be completed using the following equation (see Sect. 2.4; Walmsley and Ungerechts 1983; Swift et al. 2005):

$$T_{\text{rot}} = T_{\text{kin}} \left\{ 1 + \frac{T_{\text{kin}}}{T_0} \ln [1 + 0.6 \exp(-15.7 T_{\text{kin}})] \right\}^{-1}. \quad (3.6)$$

The calculated values of rotational temperature have been used in order to determine the beam filling factor for the entire sample (see Sect. 2.4):

$$B_{\text{ff}} = \frac{T_{\text{ex}}}{T_{\text{rot}}}. \quad (3.7)$$

The calculated excitation temperatures (2.77 to 7.10 K) and beam filling factors are relatively low (0.09 to 0.21 with a mean value of 0.15), which is similar to other studies (Friesen et al. 2009, Urquhart et al. 2011, Urquhart et al. 2015a). The less-than-unity values of the filling factor suggest that although the emission is extended with respect to the beam, clumps are likely to consist of a significant number of smaller dense substructures (cores), which when convolved with the beam results in the appearance of an extended emission region.

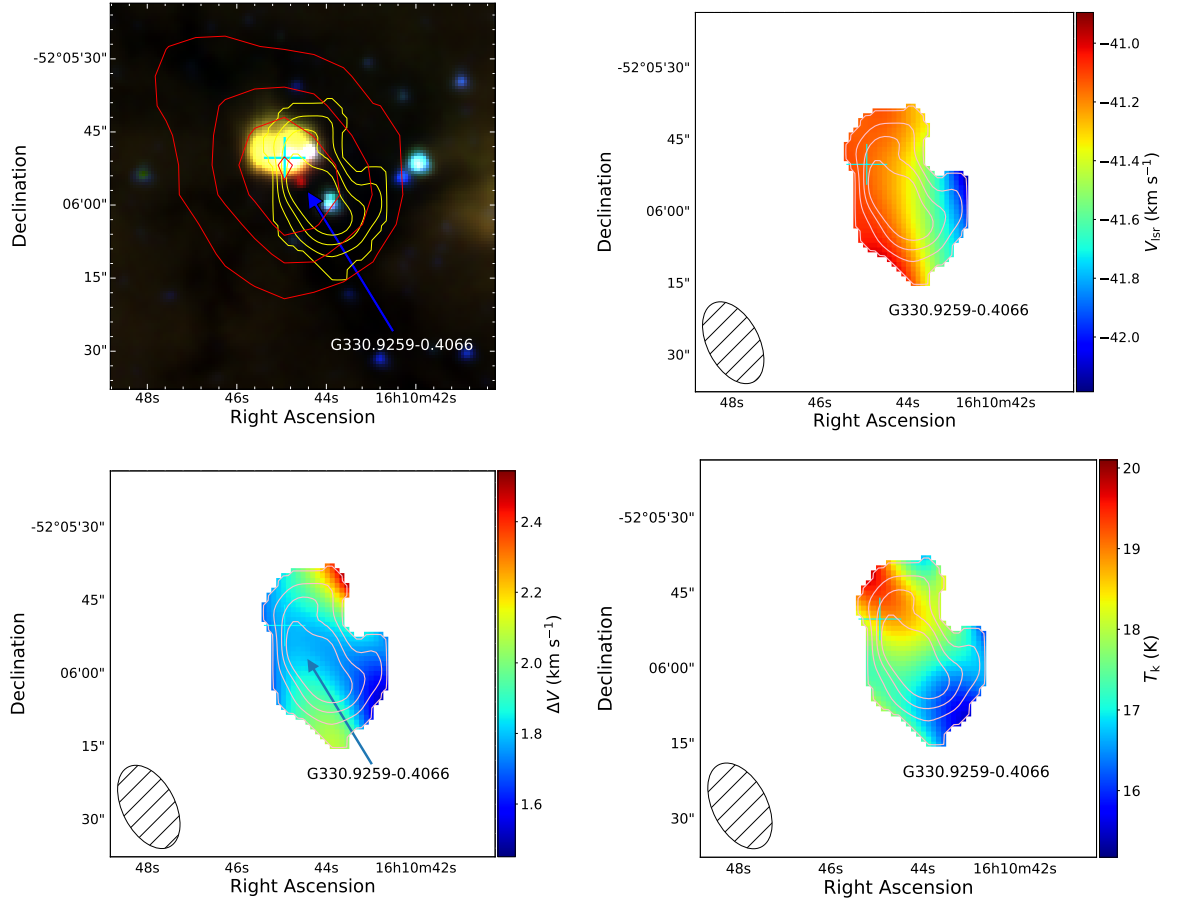


Figure 3.8: Sample maps of the various parameters described in Sects. 3.4 and 3.5.1 for region G330.9288-00.4070. The upper left panel presents a three-colour RGB image created from the GLIMPSE data, overplotted with the NH₃ and ATLASGAL emission in yellow and red contours respectively. The contours levels are equivalent to those in Fig. 3.1. From the upper right clockwise to the bottom left, the maps presented are the velocity, velocity dispersion, and the kinetic temperature. The blue arrows and black labels identify ammonia clumps identified using the `FellWalker` algorithm. Orange and cyan markers identify the positions of any MYSOs or HII regions respectively. Beam sizes are shown as a hatched black ellipsoids in the lower right corner of each plot.

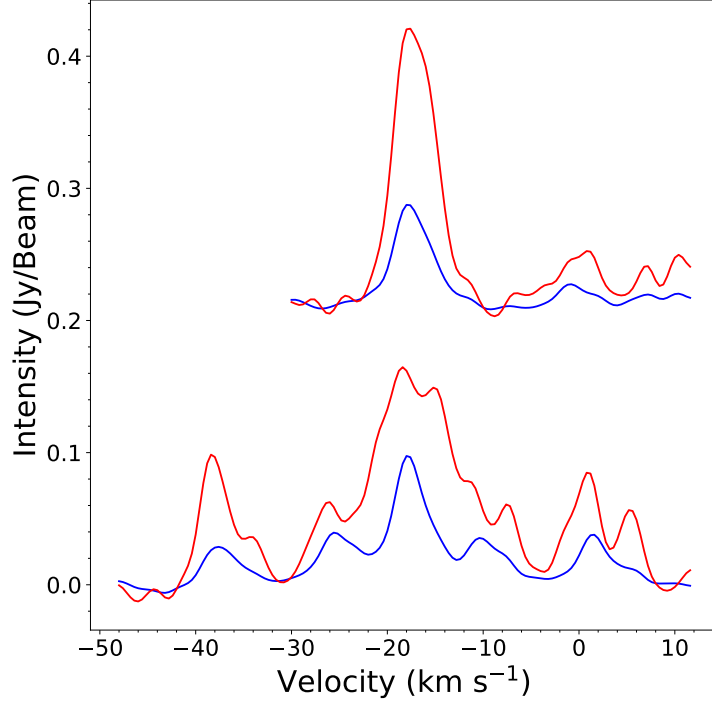


Figure 3.9: Example NH_3 spectra of field G345.5043+00.3480. The peak and average spectra across the clump are shown in red and blue respectively. The spectra have been smoothed with a 1D Gaussian kernel ($\sigma = 2 \text{ km s}^{-1}$).

3.5.1(c) COLUMN DENSITIES

The NH_3 column density is calculated as a free parameter using the inversion transition hyperfine structure. This essentially uses the derived rotation temperature, and so has already taken into account the beam filling factor. The optical depth is calculated from the ratio between the observed brightness of the main and inner satellite lines, but low signal-to-noise ratios for the satellite lines produced large uncertainties in this ratio, resulting in a very poorly constrained optical depth for weakly-detected pixels. As the column density of the NH_3 gas is directly derived from the optical depth, the majority of column density values are also unreliable. Pixels with this feature were located based on their high relative errors ($> 100\%$) from the associated column density error maps produced by the fitting routine and removed from the analysis.

The statistical values for each parameter is given in Table 3.7 and a summary of these for the whole sample is given in Table 3.8.

Table 3.7: Detected NH₃ clump parameters. The columns are as follows: (1) Field ID given in Table 1; (2) Name of clump derived from Galactic coordinates of peak emission of each clump; (3)-(4) Radial velocity and intrinsic FWHM line width; (5-7) Different calculated temperatures for each clump; (8) Beam filling factor ($T_{\text{ex}}/T_{\text{rot}}$); (10) NH₃ column density. (For each cell, initial values are peak values, with median values shown in parenthesis for the pixel by pixel fitting routine.) Regions appended with * identified regions with contain dual spectra components.

Field id	Clump name	$v_{\text{l sr}}$ (km s ⁻¹)	Δv (km s ⁻¹)	T_{ex} (K)	T_{rot} (K)	T_{kin} (K)	B_{ff}	log(column density) (cm ⁻²)
(1)	(2)	(3)	(4)	(5)	(6)	(7)	(8)	(9)
1	G261.6454-2.0884	14.55	2.97 (2.45)	3.15 (2.82)	23.89 (21.07)	28.86 (24.49)	0.15 (0.13)	16.41 (15.96)
2	G286.2124+0.1697	-21.15	2.84 (1.53)	2.86 (2.83)	17.28 (16.50)	19.15 (18.12)	0.17 (0.17)	15.94 (14.79)
2	G286.2052+0.1706	-18.09	2.91 (2.13)	2.94 (2.81)	23.98 (19.43)	29.00 (22.10)	0.17 (0.15)	14.70 (14.35)
3	G305.2084+0.2061	-41.94	8.69 (6.50)	2.93 (2.82)	27.81 (25.20)	35.60 (31.01)	0.14 (0.11)	17.60 (15.45)
4	G309.4208-0.6204	-42.51	1.66 (1.46)	2.84 (2.81)	17.88 (15.90)	19.96 (17.34)	0.22 (0.18)	18.87 (17.42)
5	G312.5987+0.0449	-63.55	3.08 (2.69)	2.85 (2.82)	24.09 (20.97)	29.18 (24.34)	0.15 (0.13)	15.27 (14.74)
6	G314.3214+0.1146	-47.44	1.74 (1.62)	2.81 (2.80)	18.85 (16.95)	21.29 (18.71)	0.20 (0.16)	18.78 (15.95)
6	G314.3197+0.1092	-48.26	2.11 (1.85)	2.77 (2.77)	17.15 (16.31)	18.98 (17.88)	0.19 (0.17)	17.42 (17.11)
7	G318.9477-0.1959	-34.54	3.98 (2.82)	2.88 (2.83)	22.26 (19.99)	26.29 (22.91)	0.17 (0.14)	18.57 (17.41)
8	G322.1584+0.6361	-57.91	4.47 (3.83)	2.87 (2.81)	29.43 (23.28)	38.65 (27.87)	0.14 (0.12)	19.02 (16.69)

Notes: Only a small portion of the data is provided here, the full table is presented in Appendix A.

Table 3.8: Statistical properties for the whole sample.

Parameter	Number	Mean	Standard Error	Standard Deviation	Median	Min	Max
Aspect Ratio	44	1.66	0.09	0.60	1.57	1.03	4.68
Angular Offset	44	18.19	2.41	15.97	15.32	0.04	79.5
Distance (kpc) (fields)	34	3.46	0.21	1.22	3.30	1.80	6.70
Radius (pc) (fields)	34	0.15	0.01	0.09	0.12	0.04	0.36
Tkin (Mean) (K)	44	22.31	0.74	4.90	21.47	14.43	36.67
FWHM line width (Mean) (km s^{-1})	44	2.69	0.17	1.15	2.47	1.28	6.09
Pressure Ratio (Mean)	44	0.01	0.001	0.01	0.01	0.002	0.02
Beam filling factor (Mean)	44	0.15	0.004	0.02	0.15	0.09	0.21
N(NH_3) (Mean)	44	16.72	0.26	1.71	16.58	14.33	22.36
Log[Field mass] (M_\odot)	29	3.21	3.18	0.07	3.18	2.52	3.98
Log[Field luminosity] (L_\odot)	29	4.37	0.13	0.72	4.46	3.13	5.83

3.5.1(d) UNCERTAINTIES ON THE FITTED PARAMETERS

The `FellWalker` algorithm provides no estimation of the uncertainties for the position or size of the detected clumps (which is a function of beam size and SNR), although the mean error of this is calculated to be $\sim 3.7''$ (beam size/ \sqrt{SNR}).

The procedure used during the fitting process automatically computes error maps for each individual free parameter which is derived from the ammonia spectra, the uncertainties for which are the derived uncertainties from the nonlinear least-squares fitting using the covariance matrix. These uncertainties include statistical and systematic errors arising from the model and also error propagation, a detailed explanation of the errors for this fitting routine can be found in (Rosolowsky et al., 2008). Uncertainties for the temperatures (T_{kin} , T_{ex} , T_{rot}) and velocity are relatively small, typically less than 0.5 K and 0.1 km s⁻¹, respectively. The errors for the beam filling factor are also relatively low as the values are calculated from the ratio of the excitation and rotational temperatures. As mentioned in Sect 3.5.1(c), errors for the majority of optical depth and column density calculations cause these values to be unreliable.

A number of fields within the sample show signs of multiple components: visual inspection indicates that five fields have at least two spectral components in either the NH₃ (1,1) or (2,2) transitions, as there is a clear difference between the average and peak spectra as shown in Fig. 3.9. The NH₃ (1,1) average spectrum appears coherent, whereas the peak spectrum shows an indication of multiple components at different velocities, which are unresolved, as the FWHM of each NH₃ spectral line component is not separated. Multiple components tend to increase the measured line-widths, and it is difficult to resolve both individual components without higher spectral and angular resolution. Affected regions can be found labeled with a star (*) in Table 3.7.

The statistical values for the luminosity and mass of all dust clumps can be found in Table 3.8, while the values for individual sources are given in Table 3.1. Fitted parameter maps for all of the regions, along with the corresponding GLIMPSE images, can be found in the appendix.

3.6 DISCUSSION OF PHYSICAL PARAMETERS

3.6.1 OVERVIEW OF DERIVED PROPERTIES

Multiple properties have been derived from the NH₃ spectral line analysis (kinetic temperatures, FWHM line-widths, beam filling factors and pressure ratios), which

have been supplemented with parameters from the ATLASGAL survey (luminosities and masses). Values for the temperatures and beam filling factors, which range between 10–40 K and 0.09–0.21, along with the measured FWHM line-widths, are similar to previous studies (Sridharan et al., 2002; Wielen et al., 2012).

3.6.2 EVOLUTIONARY SEQUENCE

As outlined in the introduction, the main purpose of this study is to investigate the physical conditions of the environments of high-mass star formation in order to better understand where they form and how their feedback in turn affects their environments. The morphology of the molecular gas with respect to the different types of embedded objects has been investigated to see how they are affecting their local environment. The accumulated ATLASGAL survey data has aided in the understanding of these regions and the larger structure in the local environment and how it relates to the dense gas as mapped by the NH_3 emission.

It is possible to construct a rudimentary evolutionary track by incorporating all of this information and the three types of classifications for each field. An example of how this can be visualised is shown in Fig. 3.10. A region begins in the quiescent/protostellar state with no observable ongoing formation and no visible embedded objects at the infrared wavelengths of the GLIMPSE survey (3.6, 4.5 & 8 μm). These initial regions are already associated with methanol masers, and are therefore harbouring massive protostars (upper panel of Fig. 3.10). The morphology of these clumps is relatively unbroken with only a single clump of emission. As accretion processes drive the embedded objects into the MYSO stage, the environments increase in temperature and turbulence as the MYSOs feed back into their local environment. These early-stage clumps have high signal-to-noise and a well-defined structure with at least one RMS object embedded towards the centre of the emission (middle panel of Fig. 3.10). Once the MYSO has reached maturity and it begins to produce an HII region, it will disrupt its environment, fragmenting any dense material which could be observed via NH_3 emission (lower panel of Fig. 3.10).

This proposed sequence of events is similar in nature to previous studies (e.g. Zinnecker and Yorke 2007; Chambers et al. 2009; Battersby et al. 2014), where similar evolutionary sequences are presented using a number of different tracers. Chambers et al. (2009) proposed an evolutionary sequence for infrared dark clumps (IRDCs), this begins with a quiescent clump transitioning into an active clump and finally into a more evolved “red” clump. These classifications were based solely on IR emission, 24 μm point sources and enhanced 8 μm emission. That evolutionary model is similar in nature to what is presented in this study, although the main focus for this work is

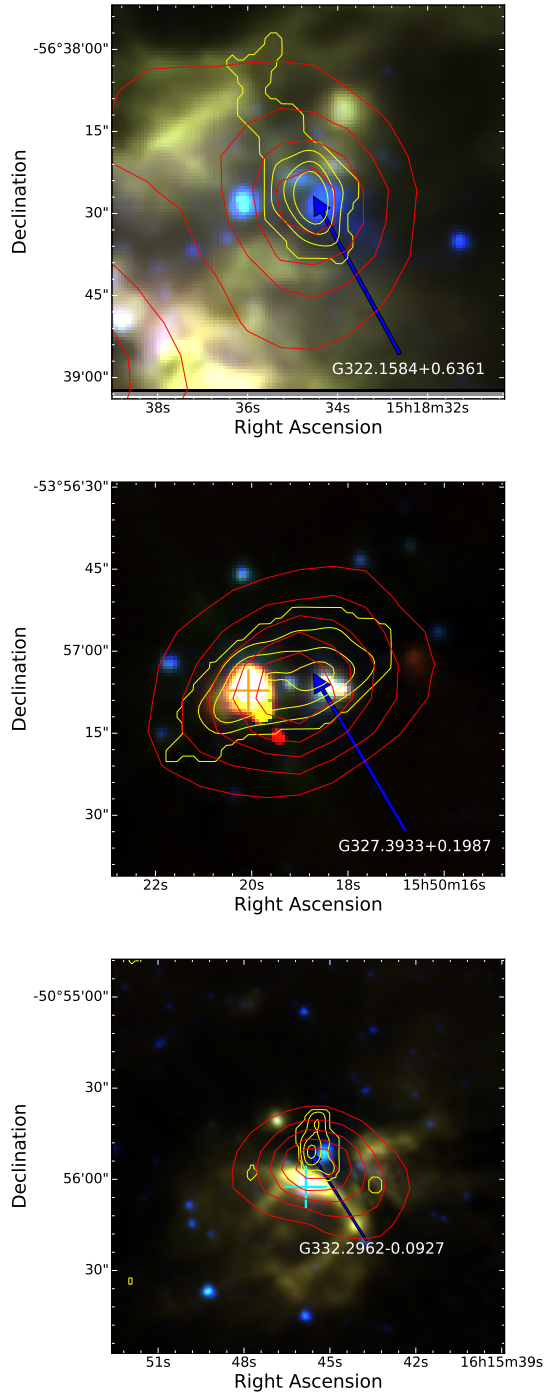


Figure 3.10: Example GLIMPSE three-colour images of the morphological structure and differences between the three evolutionary stages outlined in this study. The upper panel presents a quiescent clump with no embedded or nearby RMS source, the middle panel presents an ESF field, with an embedded MYSOs, while the lower panel presents an LSF field, where a HII region has developed and started to disrupt its environment. NH₃ (1,1) contours are shown in yellow starting at 3σ increasing in steps of 0.5σ , equivalent to those in Fig. 3.1. RMS objects are marked with magenta and cyan crosses for MYSOs and HII regions respectively.

on the distribution and offsets of NH_3 and $870\ \mu\text{m}$ emission, relative to the positions of RMS sources. This work also gives a physical view to other large sample studies, such as Urquhart et al. (2014; Fig. 21), which includes ATLASGAL compact source catalogue data and shows two distinct phases, accretion and dispersion, which can clearly be seen in the observations. While this may not be a robust evolutionary sequence model for massive star formation, this data does nicely highlight differences between each evolutionary stage identified here.

3.6.3 COMPARISON OF PHYSICAL PARAMETERS

The statistical properties for the entire sample are given in Table 3.8, and a complete set of maps for each individual field can be found in the appendix.

Throughout this study each individual source has been classified as either early-phase star-forming (ESF) or late-phase star-forming (LSF), and here, differences between the two classes will be investigated. The principle basis for this classification system is the difference in morphologies as shown in Fig. 3.5 and 3.6. The use of maser emission data has additionally allowed the reclassification of regions which appear to be quiescent but are likely to be in a protostellar stage, and therefore are in an early stage of star formation. The quiescent clumps are each associated with at least one methanol maser, which are almost exclusively associated with high-mass star formation (e.g. Breen et al. 2011) and are therefore harbouring a protostar, and so it is appropriate to classify these clumps as ESF.

Analysis of the various fitted and derived parameters from the NH_3 observations, GLIMPSE and ATLASGAL emissions was undertaken. ESF and LSF region cumulative distributions were analysed for six of the parameters (luminosity, mass, column density, clump volume and clump velocity dispersion) in an effort to identify any significant differences and to compare the properties of the two evolutionary samples identified. The use of a two-sample KS-test has been employed for each distribution. The KS-test is used for calculating the probability that two samples are drawn from the same population, and produces a p -value which can be used to reject the null hypothesis. A 3σ confidence threshold ($\alpha < 0.0013$) was used to reject the null hypothesis that any two distributions are drawn from the same parent population. All associated p -values were found to be greater than this confidence value, and so no statistical difference can be seen between the ESF and LSF fields/clumps for any of these parameters.

Temperature and velocity dispersion gradients are common across the sample, ranging from ~ 10 to ~ 40 K. The peak kinetic temperature measurements of star-forming clumps are in general coincident with an embedded object and decrease towards the

edges for the ESF clumps. Many clumps located near LSF sources that have recently broken out of their natal clumps exhibit gradients, with values that peak at the edge closest to the RMS source and decrease with increasing distance from that source. Examples of these two gradient cases seen towards the ESF and LSF clumps are shown in Figs. 3.11 and 3.12, respectively. These regions will be discussed in the following section.

Feedback from the RMS sources is therefore having a significant impact on the temperature and dynamics of their natal clumps regardless of whether they are still deeply embedded (ESF) or have already started to disrupt their local environment and are starting to emerge from their dust cocoons (LSF). Both classifications have similar median temperatures across the sample, so while the temperature gradients may differ as described above, the absolute values are similar (15–35 K).

Region-wide parameter distributions (luminosity, masses and column densities) between the two classifications were also investigated for significant differences. It might be expected that the luminosity for LSF regions should be naturally higher as the embedded objects are more luminous whereas ESF clumps are likely to show higher masses and column densities since the natal environments have not started to be dispersed. However, as previously noted, no statistical difference are found between the mass and luminosities of the two classifications in KS-tests. The sizes of individual clumps has also been compared, and younger clumps are tend found to be larger than the more evolved material in terms of pixel area (arcsecond²). The mean luminosity-to-mass (L/M) ratio for ESF sample is 1.33 with a standard error of 0.03, while the mean LSF ratio is found to be 1.4, with a standard error of 0.05. The median values do also differ by a similar amount. The L/M ratios are a good indicator of evolutionary stage (increasing L/M indicates more evolved regions), therefore, from this analysis, it appears that the entire sample covers a narrow evolutionary time scale. However, analysis of the morphological distribution of the dense gas (as traced by the ammonia) do reveal significant differences between the two evolutionary groups that are not observed in the dust emission maps, which is due to the relatively low spatial resolution of the ATLASGAL survey. The dust emission traces the total column density, rather than just the high-density regions, and so may smooth out any clumpy substructure that is present in the sources.

Urquhart et al. (2014a) found the L/M ratio to be similar for a large sample of MYSOs and HII regions identified by the RMS survey and concluded that both evolutionary samples were towards the end of the main accretion phase, which is consistent with the finding here. It is also clear that although the HII regions are having a significant impact on the internal structure of their natal clumps and so properties derived

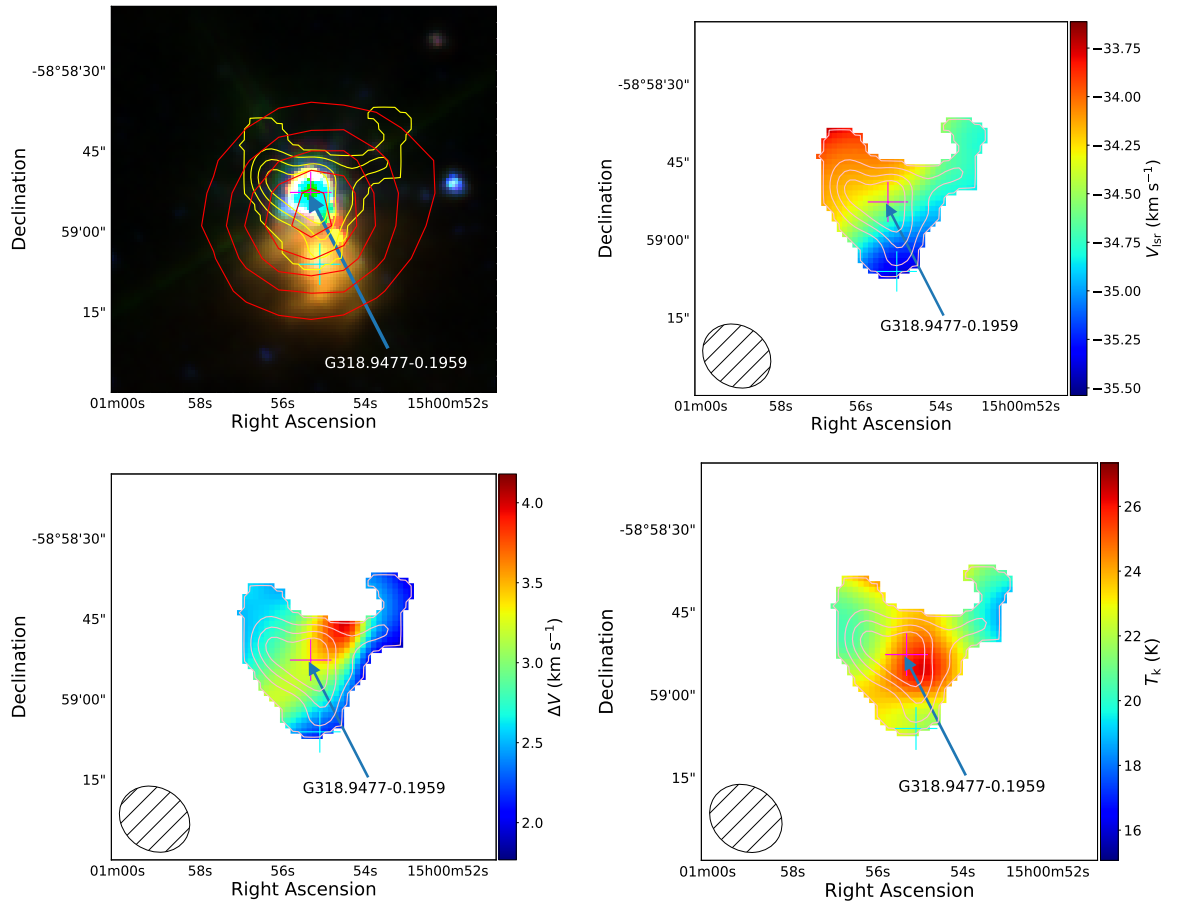


Figure 3.11: Example maps showing field G318.9480-00.1969. Each panel presents, clockwise from the upper left, three-colour RGB GLIMPSE image overlaid with NH_3 (1,1) and ATLASGAL dust emission contours in yellow and red respectively, velocity, kinetic temperature and velocity dispersion. The contours levels are equivalent to those in Fig. 3.1. Magenta and cyan crosses mark MYSOs and HII regions respectively.

from dust emission alone are not very useful to investigate the evolution of these two stages.

3.6.4 INTERESTING SOURCES

In the following subsections three case studies of interesting regions are presented, along with the associated three-colour RGB GLIMPSE image and parameter maps.

3.6.4(a) G318.9477–0.1959

Figure 3.11 shows a selection of parameter maps for a single star forming region (G318.9480–00.1969). This particular region has a NH_3 (1,1) SNR of 11.97 and is associated with two sources identified from the RMS survey, one of which is a MYSO (G318.9480–00.1969A) that is clearly embedded towards the peak of the ammonia emission. The second is an HII region (G318.9480–00.1969B) located towards the southern edge of the NH_3 clump. A single clump (G318.9477–0.1959) has been identified in this region by the `FellWalker` algorithm with an aspect ratio of 1.19, and so has a morphology that is fairly circular as seen by the NH_3 (1,1) emission contours. This clump is located towards the centre of the ATLASGAL dust emission, as expected for an embedded region in the early stages of star formation.

The GLIMPSE RGB image shows a central bright saturated source corresponding to the position of the MYSO, as well as revealing the presence of some diffuse MIR emission coincident with the HII region. Given that the HII region is not associated with any ammonia and is associated with diffuse MIR emission it would appear that the HII region is quite evolved and has started to disperse its surroundings. These two sources dominate the mid-infrared emission in the map. The position of the central object is correlated with an increase in kinetic temperature as expected for an embedded MYSO (see lower right panel of Fig. 3.11); however, the HII region to the south does not appear to be correlated with a locally elevated gas temperature. This also indicates that it has already dispersed its natal material and is located either slightly in the foreground or background with respect to the clump hosting the MYSO. The line-width maximum is not coincident with either object (see lower left panel of Fig. 3.11), although the peak values do seem to form an elongated structure running north-west to south-east through the clump roughly centred on the position of the MYSO (see lower left panel of Fig. 3.11). This is somewhat suggestive of the presence of a bipolar molecular outflow. Similar types of this kind of structure were seen in Urquhart et al. (2015a) in multiple fields (e.g. G010.47+00.03, G011.11–00.40, G013.33–00.03 and G014.61+00.02).

This source was studied as G318.9477–0.1959 by Navarete et al. (2015) as part of

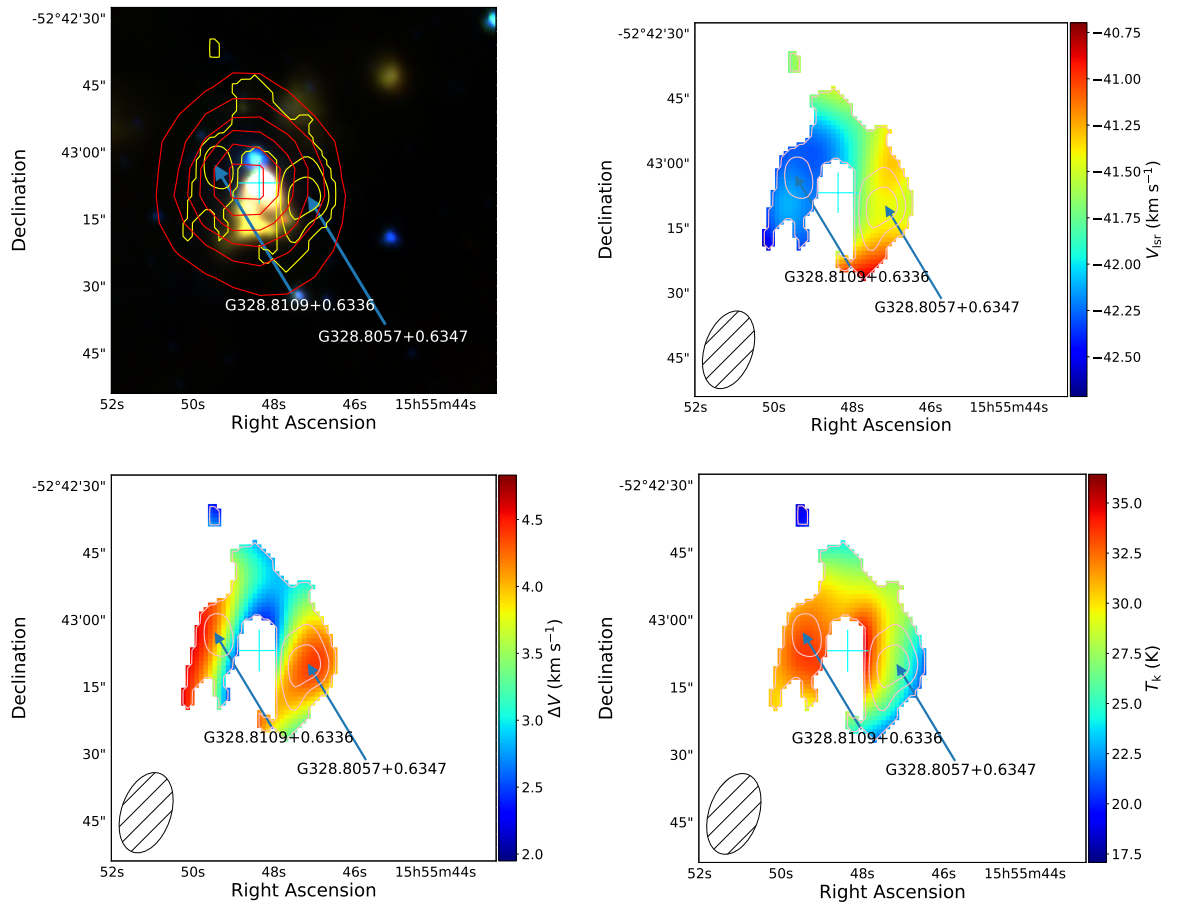


Figure 3.12: Examples maps showing field G328.8074+00.6324. Each panel presented is the same as Fig. 3.11.

an investigation of the accretion processes in a sample of 353 MYSOs selected from the RMS survey. The study revealed that extended H₂ emission is a good tracer of outflow activity, which is itself a signpost of ongoing accretion processes.

A comparison of this H₂ emission in Figure A296 from Navarete et al. (2015), to the NH₃ maps presented in this study, shows that the outflow is directed towards the excavated cavity indicated towards the north west in Fig. 3.11; this is also in the direction of the maximum FWHM line width. Closer inspection indicates that there are in fact multiple outflows in this region, likely to be driven by a central cluster. None of these outflows is directly aligned with the FWHM maxima or the excavated cavity, however.

This field is also associated with one methanol and four water masers, all of which are offset less than 0.05'' from the central RMS object (G318.9480–00.1969A). The presence of the methanol maser confirms that this region is indeed undergoing high-mass star formation, as these masers are thought to be excited in dense material in an accretion disk by mid-IR pumping from the central source (e.g. De Buizer et al. 2000).

3.6.4(b) G328.8074+00.6324

A second morphologically interesting example is region G328.8074+00.6324, shown in Fig. 3.12. This particular field involves two NH₃ detected clumps which are connected via weaker NH₃ emission, forming a ‘horseshoe’ shape. These clumps (G328.8057+0.6347 & G328.8109+0.6336) have NH₃ (1,1) SNR values of 7.98 and 5.94, respectively, and aspect ratios of 1.96 and 1.78, so both clumps are fairly elongated in shape. Only one RMS source has been detected in this region (G328.8074+00.6324). This object has been classified as an HII region by the RMS survey, and lies at the centre of the complex but appears to be removed from any NH₃ emission above the detection threshold. The ATLASGAL dust emission, as with the previous example, is well-correlated with the spatial position of the gas emission and completely encompasses it, with the position of the RMS source approximately coincident with the dust emission. The GLIMPSE image shows multiple evolved stars in the region and a large central IR object corresponding to the HII region, which appears to be somewhat compact with a more diffuse, less intense, envelope. This region is defined as LSF, as the HII region at the centre of the emission is disrupting its environment, and dispersing the dense gas.

The kinetic temperature map shown in Fig. 3.12 suggests central heating by the RMS source. The kinetic temperature is highest directly around the central HII region and within the central area of the field, while the western edge of G328.8057+0.6347 is approximately 10 K cooler, suggesting the feedback from the RMS source is not yet

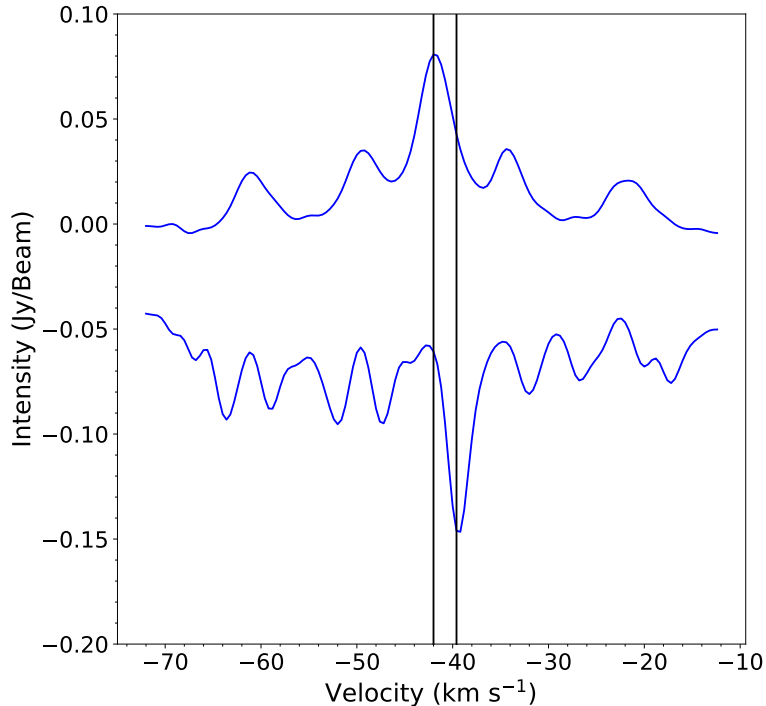


Figure 3.13: Absorption and emission spectra from field: G328.8074+00.6324. The absorption spectrum has been offset by -0.05 Jy/beam. The black lines represent the peaks from the two spectra. The spectra have been smoothed with a 1D Gaussian kernel ($\sigma = 2 \text{ km s}^{-1}$).

affecting this sector of gas.

The line-width maxima do not correspond well with the temperature distribution: line-widths are dominated by non-thermal motions concentrated on the east-west extremities. As with G318.9480–00.1969, there appears to be a velocity gradient across the complex, however, a more detailed look at the NH_3 (1,1) data cube shows that there is NH_3 gas in front of the HII region which is currently in absorption against the bright free-free continuum. Therefore, the HII region is likely to be still enveloped in a shell of dense gas.

Figure 3.13 presents two spectra from this region, the first is the average emission spectrum for the NH_3 emission above the 3σ threshold, while the second presents the average absorption averaged over the central nine pixels towards the embedded HII region. The spectral peak velocities are offset by -2.4 km s^{-1} , which indicates that the material in front of the HII region is moving towards us slower than the systemic velocity of the natal clump. This infall motion of material suggests that the clump is still undergoing gravitational collapse. By assuming that the material surrounding the central object is a shell with an average density of $92.5 \text{ M}_\odot \text{ pc}^{-3} \left(\frac{\text{Mass}_{\text{ATLASGAL}}}{\text{Volume}_{\text{ATLASGAL}}} \right)$, the infall rate for this particular source has been calculated to be $9.6 \times 10^{-3} \text{ M}_\odot \text{ yr}^{-1}$.

Wyrowski et al. (2016) observed nine massive molecular clumps to search for infall signatures. The mean infall rate was found to be $6.33 \times 10^{-3} M_{\odot} \text{yr}^{-1}$ with a standard deviation of $5.95 \times 10^{-3} M_{\odot} \text{yr}^{-1}$. The value found for G328.8074+00.6324 is similar to this distribution.

The stability of the clumps can be investigated using the virial parameter, which is the ratio of virial mass (the mass that can be supported by the internal energy of the clump) and the actual mass of the clump. This is defined as:

$$\alpha = \frac{M_{\text{vir}}}{M_{\text{clump}}}, \quad (3.8)$$

where

$$\left(\frac{M_{\text{vir}}}{M_{\odot}} \right) = 161 \left(\frac{R}{\text{pc}} \right) \left(\frac{\Delta v}{\text{km s}^{-1}} \right)^2, \quad (3.9)$$

where R is the radius of the clump and Δv is the line-width (see Sect. 2.5).

An isothermal sphere in hydrostatic equilibrium, supported by equipartition of thermal and magnetic energy, has a critical value of $\alpha_{\text{cr}} = 2$ (Kauffmann et al., 2013). Clumps with a value above this are subcritical and will undergo expansion if not pressure-confined by their local environments. Clumps with values below α_{cr} are supercritical; they are gravitationally unstable, and should be in a state of free-fall unless supported by strong magnetic fields. This particular region has a virial parameter of $\alpha = 2.04$, placing it in the subcritical regime. The error in this value for α is dominated by the ATLASGAL clump mass uncertainty, which is $\sim 20\%$ (Urquhart et al., 2018). The virial mass also depends on the source distance to calculate the spatial radius of the clump; the error in this distance is $\sim 17\%$, obtained from the Reid et al. (2016) model. The difference between α and α_{cr} is relatively small and due to the large errors associated with the virial parameter, the clump could either be sub or supercritical. As the region shows signs of global infall, this potentially means that the central object is beginning to stabilise the inner section of the clump, but the outer layers are undergoing collapse.

3.6.4(c) G345.5043+00.3480

Figure 3.14 presents 4 panels similar to the previous two examples. This source is classified as early star forming, and contains a single MYSO (G345.5043+00.3480), offset by less than one arcsecond (one pixel) from the centre of the NH_3 emission. Line-width and temperature maps have similar distributions, with the maxima located towards the centroid of the clump, with ranges of $\sim 15\text{--}35 \text{ K}$ and $\sim 1.2\text{--}5.6 \text{ km s}^{-1}$,

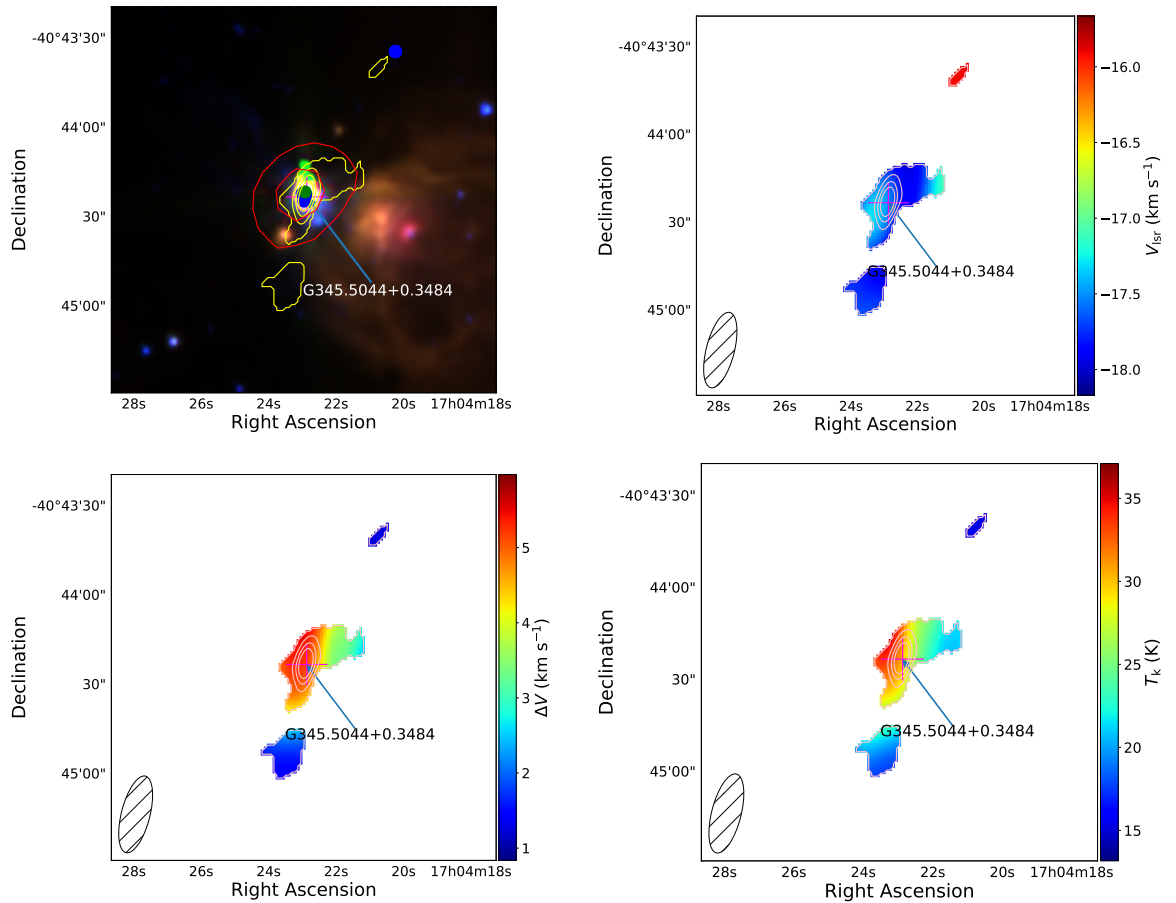


Figure 3.14: Examples maps showing field G345.5043+00.3480. Methanol and water masers have been included in the three-colour GLIMPSE image in with green and blue filled circles respectively, otherwise each panel presented is the same as Fig. 3.11.

respectively.

One NH_3 clump has been detected through `FellWalker`, and although another two sources have been detected in the observations, both are smaller than the beam size. The lack of ATLASGAL emission from around these two smaller sources suggests that these are therefore likely to be image artifacts (see Sect. 3.3.1). However, while there is no dust emission in this region beyond the main detected clump toward the centre of the field, the NH_3 emission to the north west of the main clump is coincident with a water maser which can be seen in upper left panel of Fig. 3.14 and so this source may in fact be a genuine detection.

The GLIMPSE image reveals a bright, evolved HII region that lies to the southwest of the main portion of gas emission (see upper left panel of Fig. 3.14). This HII region has been identified as IRAS 15520-5234 (Walsh et al., 1998; Garay et al., 2006) and is a known radio source. The shape of the clump would imply that the HII region has compressed the dense gas, and subsequently a new star-forming region has been formed on the edge of the region, suggesting an instance of triggered star formation.

This region has the expected temperature and FWHM line-width peaks toward the embedded MYSO, and there is also a very small velocity difference across the central clump, with the smaller source to the north-west having a lower velocity. There appears to be no overlapping infrared or radio emission between these two clumps, although all of the emission appears to be coincident with the edge of the evolved HII region and has similar velocities, and so is likely to be associated.

3.6.5 TRIGGERED STAR FORMATION

Elmegreen (1992) proposed a model of triggered star formation, wherein an ionization shock front produced by the expansion of HII regions created by one group of massive stars provides the external pressure to compress adjacent material in a molecular clouds, thereby inducing subsequent generations of massive stars to form. This mechanism may play a significant role in the evolution of massive star forming regions (e.g. Thompson et al. 2012).

As discussed previously, methanol masers are located at the sites of high-mass star formation, while water masers are sensitive to shocked material. By using maser positions and the likely presence of an HII region (which can be inferred through the morphology of extended $8\mu\text{m}$ emission), multiple regions presented in this study are consistent with triggered star formation. As HII regions expand into nearby molecular material, they begin to compress this matter which could form future generations of high-mass stars. The incorporated maser emission data helps to refine this picture as both methanol and water maser emission is known to be coincident with star formation.

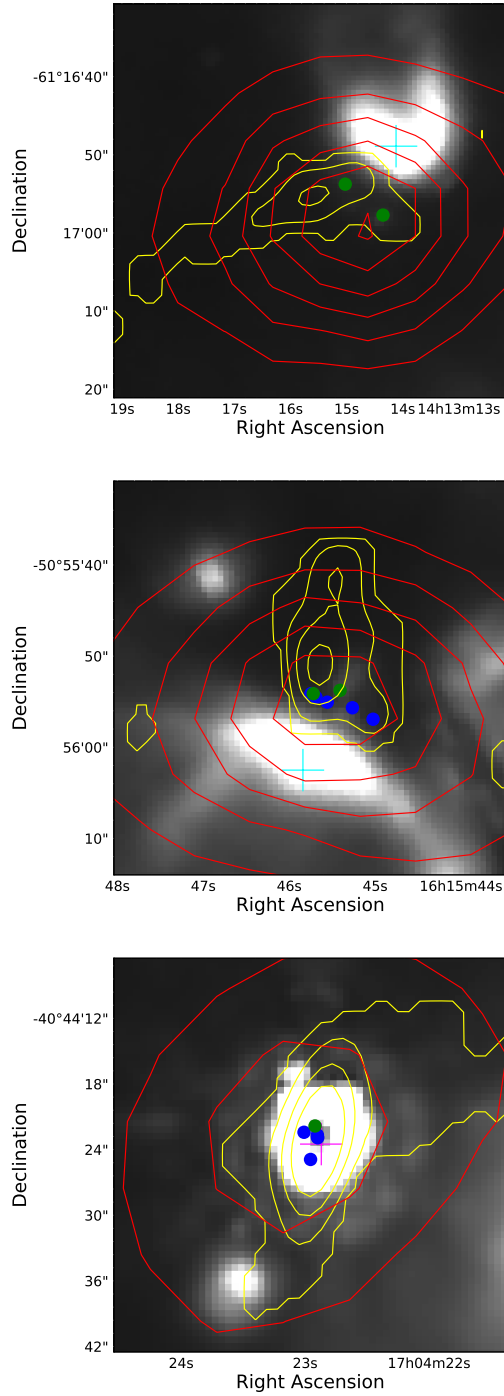


Figure 3.15: Three GLIMPSE 8 μm images presenting regions of possible triggered star formation. Each panel presents an 8 μm image overlaid with NH₃ and ATLASGAL emission contours in yellow and red respectively. The contours levels are equivalent to those in Fig. 3.1. MYSOs and HII regions identified by the RMS survey are shown with magenta and cyan crosses respectively. Methanol and water maser positions are marked with green and blue filled circles respectively.

Figure 3.15 presents three regions which appear to contain examples of triggered star formation at different stages. The top panel of Fig. 3.15 shows a relatively early and compact HII region to the north-west of the NH_3 emission. It can be seen that two methanol masers are present within the dense material traced by the NH_3 in different locations, implying two protostellar cores are embedded within the environment. This is potentially due to the influence of the nearby HII region which suggests that this material is undergoing shocks. The middle panel of Fig. 3.15 presents the same effect more conclusively. The HII region towards the south is clearly having an impact on the dense material and is dispersing its environment, indicated by the appearance of multiple NH_3 clumps on the edges of the radiation. The central clump also has a string of water masers along this boundary, which suggests that this material is undergoing shock. Two methanol masers are located behind these water masers, again implying the presence of high-mass protostellar cores, which may have formed due to the compression of gas as the HII region expands towards it. The lower panel of Fig. 3.15 presents a more diffuse HII region in the south-west which seems to be in a later evolutionary stage. A MYSO has already formed within the gas and dust emission, which has been subjected to the effects of the nearby HII region. This MYSO is associated with two methanol masers and 10 water masers.

These three regions show the effect that HII regions have on their local environment and the likelihood that they can cause triggered star formation and produce future generations of stars. The use of the classification system presented in this study creates a difficulty in assigning these types of regions, as they display both qualities of ESF and LSF fields. While HII regions are present and are impacting on their local environment, the presence of a large number of maser detections implies protostellar objects in an initial stage of formation.

3.7 CONCLUSIONS

The NH_3 (1,1) and (2,2) inversion transitions have been used to map 34 fields. The `FellWalker` algorithm has been used with a threshold value of 3σ to identify 44 clumps distributed among these regions. No statistical differences are found between clumps classified as early star-forming or late star-forming when using a two sample KS-test. The early star formation (ESF) star forming clumps do generally exhibit elevated temperatures, while the late star formation (LSF) counterparts have larger line-widths. Most ESF clumps have been previously identified by as MYSOs while the majority of LSF clumps are associated with HII regions. Physical parameters have been

extracted from complementary surveys such as ATLASGAL and GLIMPSE legacy surveys. Masses for the fields range between a few hundred to over $10\,000 M_{\odot}$ and luminosities range between $\sim 10^3$ to $\sim 10^6 L_{\odot}$.

These data have been used to construct a rudimentary evolutionary sequence of proposed massive star formation based on the morphology of their associated high density gas. ESF fields generally have RMS objects which are found towards the centre of centrally condensed coherent clumps, while the embedded objects within LSF regions are not coincident with dense gas but are generally found to be surrounded by multiple fragments. The higher level of fragmentation seen towards the LSF clumps is consistent with an expectation of association with more evolved and more luminous HII regions that are disrupting and “burning out from” their natal clumps. The clump-averaged physical properties of these two samples are not statistically different from each other (mass, luminosity, temperatures and line-widths), although the structure of the dense gas is very different, which may indicate that the formation of the HII region has a much more significant impact on the overall structure of natal clump than on its physical properties.

It was found that 31 methanol masers associated with 34 fields and 52 water masers are associated 21 fields. The majority of both types of masers are found towards ESF fields. The detection rate for water masers for the ESF and LSF field are 89% and 25% respectively, with a similar average number of spots detected in both ESF and LSF fields. The detection rates for methanol masers are 72 and 44% for the ESF and LSF fields, respectively. The reason for the significantly lower detection rates towards the LSF clumps is likely to be linked to the disruption of natal clumps by the expansion of the HII regions.

Triggered star formation appears to be present in three of the observed regions. The $8\ \mu\text{m}$ images of these sources all show the presence of nearby HII regions that show evidence of affecting the dense gas as traced by NH_3 emission seen towards these sources. A large number of methanol and water masers are found to be coincident with these regions revealing that these nearby HII regions are not only having a significant impact on their local environments but also appear to be having an influence on star formation in the surrounding dense gas.

CHAPTER 4

THE PHYSICAL PARAMETERS OF DUST CLUMPS ASSOCIATED WITH 6.7 GHz METHANOL MASERS

4.1 INTRODUCTION

This Chapter aims to investigate the relationship between the 6.7 GHz methanol masers and Galactic dust clumps. A comparison between the MMB survey catalogue and the ATLASGAL compact source catalogue (CSC) was presented in Urquhart et al. (2013). This was accompanied by a set of dedicated follow-up dust continuum observations, which targeted MMB sources located within the ATLASGAL region not associated with an ATLASGAL counterpart and MMB sources not covered by ATLASGAL (i.e. $|b| > 1.5^\circ$ or $280^\circ \geq \ell \geq 186^\circ$; Urquhart et al. 2015b). Combined, these studies associated 99% of all MMB methanol masers with dense star forming clumps. These two studies focused on the 707 methanol masers identified at the time ($20^\circ \geq \ell \geq 186^\circ$). The environment, physical properties and Galactic distribution of maser associated dust clumps were investigated with the methanol masers being preferentially associated with more massive and luminous dust clumps.

Previous studies have found that there is a relationship among the different maser transitions and species in these regions. Ellingsen et al. (2007) presented a “straw man” model for the evolutionary sequence of masers in star formation regions. This model has been refined by more recent studies (e.g. Breen et al. 2010). However, how this model relates to the surrounding material and environment has not yet been fully developed. This model will be developed by looking at the statistical lifetimes of methanol masers, similar to previous works (Van Der Walt, 2005), albeit with a larger and more complete sample of masers.

In this Chapter, the methanol masers reported in the most recent MMB catalogue (265 sources; Breen et al. 2015) are matched with dense clumps identified by the ATLASGAL and JPS (JCMT Plane Survey; Moore et al. 2015; Eden et al. 2017) surveys, to produce the largest and most complete census of the physical environments where high-mass stars are forming across the Milky Way. This particular study will focus on expanding these previous works by taking advantage of the availability of integrated maser fluxes (Breen et al., 2015), distances and bolometric luminosities that were not available in the two previous studies conducted (Urquhart et al. 2013, 2015b). The physical parameters of this methanol maser associated sample of clumps is compared with the properties of the general population of clumps to investigate when this stage begins and ends, and how the properties differ as the clumps evolve. This large sample is also to critically test and refine correlations between the physical properties of the host clumps and the methanol masers that have been previously reported in the literature (Hill et al., 2005; Breen et al., 2010).

4.2 SURVEY DESCRIPTIONS

In order to determine the dust properties of associated dense clumps both the JPS and ATLASGAL surveys have been used. ATLASGAL has produced a complete sample of clump properties across the inner Galactic plane, however, the JPS catalogue is used to help refine these properties for a select number of clumps. An overview of the ATLASGAL survey is given in Sect 3.2.2 while information on the JCMT plane survey is provided below. The MMB survey has been described in Sect. 3.2.3, however, in the following paragraphs, more relevant information is given which relates to the work presented in this Chapter.

Table 4.1: Summary of the different longitude ranges covered in the various MMB survey papers and the number of 6.7 GHz methanol maser sites detected in each range.

Longitude range	# of maser sites	Reference
$6^\circ \geq \ell \geq 345^\circ$	183	Caswell et al. (2010)
$20^\circ \geq \ell \geq 6^\circ$	119	Green et al. (2010)
$345^\circ \geq \ell \geq 330^\circ$	198	Caswell et al. (2011)
$330^\circ \geq \ell \geq 186^\circ$	207	Green et al. (2012)
$60^\circ \geq \ell \geq 20^\circ$	265	Breen et al. (2015)
$60^\circ \geq \ell \geq 186^\circ$	972	

4.2.1 THE METHANOL MULTIBEAM (MMB) SURVEY

The MMB survey has detected 972 masers in total and these have been reported in a series of papers, each of which has focused on a specific range of Galactic longitude. Table 4.1 presents a summary of the longitude ranges, number of masers detected and the publication where these are reported. It is likely that the entire MMB survey accounts for the majority of 6.7 GHz methanol maser sources across the Galaxy, as it has been shown that away from the Galactic plane, methanol maser emission is rare (Yang et al., 2017, 2019).

Until recently, the integrated flux density for methanol maser sources has been unavailable in the literature, and previous studies have used the peak maser fluxes in order to estimate the corresponding maser luminosities. The integrated flux densities are now available (Breen et al., 2015) and shall be used in this work to derive the maser luminosities. Figure 4.1 presents the distribution of the maser peak fluxes against the maser integrated fluxes for the entire MMB catalogue (Breen et al., 2015). The two flux samples are similar above 1 Jy, however, below this value the peak flux densities are found to be systematically larger. A consequence of this is that studies that have used the peak flux density to estimate the luminosities will have systematically overestimated the luminosities for the weaker masers (Urquhart et al., 2015b). This effect was also noted by Breen et al. (2016) for the 12.2 GHz methanol maser transition (see Fig. 2 of Breen et al. 2016). They determined that this deviation is due to weaker masers exhibiting fewer spectral features, and therefore, having lower integrated flux densities than their stronger counterparts.

4.2.2 THE JCMT PLANE SURVEY (JPS)

The JCMT Plane Survey (JPS; Moore et al. 2015) is an 850 μm continuum survey of six fields in the northern inner Galactic plane with a longitude range of $63^\circ \geq \ell \geq 7^\circ$.

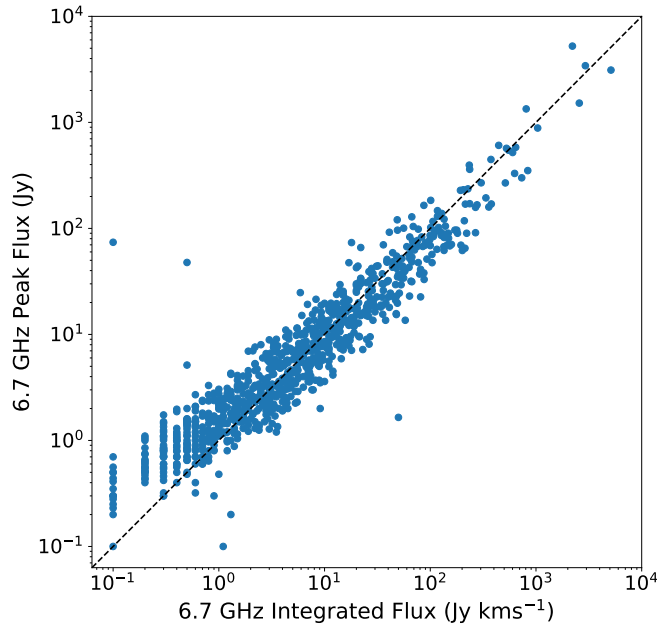


Figure 4.1: Distribution of methanol maser peak flux densities versus the maser integrated flux densities for the entire MMB catalogue (Breen et al., 2015). The 1:1 line is also shown.

Each field covers approximately 12 sq. degrees (with $|b| < 1^\circ$ and ℓ centred at 10° , 20° , 30° , 40° , 50° and 60°). The survey was conducted using the Submillimetre Common-User Bolometer Array 2 (SCUBA2; Holland et al. 2013) on the James Clerk Maxwell Telescope. The JPS survey has produced a compact source catalogue of $\sim 8\,000$ sources (Eden et al., 2017) that has a completeness of 95% at $0.04 \text{ Jy beam}^{-1}$ and 0.3 Jy for the peak and integrated fluxes respectively. The JCMT has a dish size of 15 m with an angular resolution (FWHM) of $14.4''$ at $850 \mu\text{m}$.

The JCMT survey provides a useful complementary data set to the ATLASGAL survey due to the similar wavelength range, modestly better resolution than ATLASGAL ($14.4''$ compared to $19.2''$) and significantly better sensitivity (~ 8 times improved). These factors mean that the JPS data are better able to identify substructure within larger ATLASGAL clumps. Two examples are shown in Fig. 4.2 to illustrate this point. In both of these examples the ATLASGAL contours (blue) hint at the presence of multiple components, however, the difference in peak flux was not sufficient (i.e. $\Delta\text{SNR} < 3$) for the extraction algorithm to be able to separate them into distinct objects. The improved sensitivity of JPS means that although the fluxes for the different components are similar, the difference in the signal to noise ratio is sufficient (i.e. $\Delta\text{SNR} > 3$) for source extraction to identify them as individual structures.

Eden et al. (2017) compared the peak and integrated fluxes between the detected

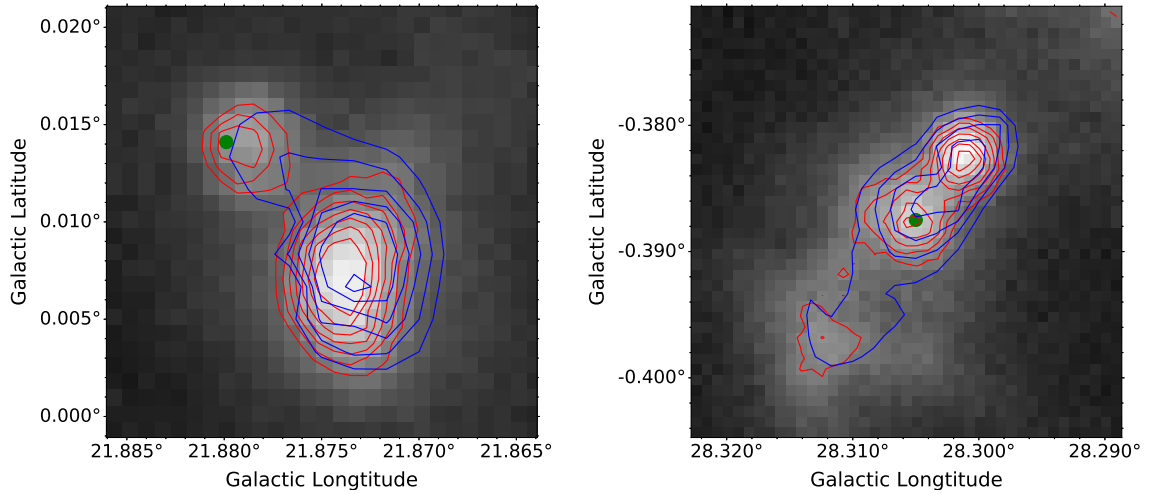


Figure 4.2: Example maps of JPS $850\ \mu\text{m}$ emission from two regions, AGAL021.873+00.007 & AGAL028.301–00.382. The red and blue contours trace the dust emission detected by the JPS and ATLASGAL emission respectively, the contours start at 3σ and increase in steps of 0.5σ . The position of the methanol masers are indicated by filled green circles. These maps illustrate how the higher sensitivity and resolution of the JPS data is better able to trace the structure of the clumps compared to ATLASGAL.

ATLASGAL and JPS sources, and found them to be linearly correlated. They reported a small systematic offset with lower JPS peak flux densities, which was shown by Moore et al. (2015) to be due to the smaller beam size of the JCMT.

4.3 MMB ASSOCIATIONS

This Section discusses the attempt to associate each of the 265 masers listed in the latest methanol maser catalogue published by the MMB survey (Breen et al. 2015), with either an ATLASGAL or JPS detection from their respective catalogues. This was done by identifying any methanol maser that is within the 3σ boundary of a dense clump found in the ATLASGAL and JPS catalogues (Urquhart et al. 2014b; Eden et al. 2017, respectively). Images have been created of every region so that each match could be confirmed visually. This has resulted in 232 methanol masers being matched to ATLASGAL sources and 146 to JPS sources, with 131 masers having associated emission in both ATLASGAL and JPS. There are 11 masers which are associated with emission seen in JPS with no counterpart in ATLASGAL. Matches between the MMB survey and ATLASGAL/JPS can be found in Table 4.2.

Table 4.2: Matched MMB sources with the ATLASGAL and JPS catalogues; maser offsets and continuum fluxes are shown for each survey. Maser names appended with a * are where the measured JPS flux has been used preferentially over the ATLASGAL counterparts.

MMB name	ATLASGAL CSC name	ATLASGAL- MMB offset ($''$)	ATLASGAL- peak flux (Jy beam $^{-1}$)	ATLASGAL int flux (Jy)	JPS catalogue name	JPS- MMB offset ($''$)	JPS peak flux (Jy beam $^{-1}$)	JPS int flux (Jy)
G020.081-00.135	AGAL020.081-00.136	1.76	7.68	18.43	JPSG020.080-00.135	3.88	6.2	14.64
G020.237+00.065	AGAL020.236+00.064	6.31	1.45	5.1	JPSG020.237+00.066	2.16	1.1	4.24
G020.239+00.065	AGAL020.236+00.064	12.83	—	—	JPSG020.237+00.066	2.16	1.1	4.24
G020.364-00.013	AGAL020.362-00.012	5.3	1.95	4.84	JPSG020.362-00.013	6.99	1.65	3.92
G020.733-00.059	AGAL020.731-00.059	9.87	2.81	19.19	JPSG020.732-00.060	12.32	2.41	8.57
G020.926-00.050	—	—	—	—	JPSG020.926-00.050	5.63	0.18	0.34
G020.963-00.075	AGAL020.962-00.074	4.42	0.42	1.4	JPSG020.963-00.074	8.56	0.41	1.33
G021.023-00.063*	AGAL021.000-00.057	83.52	0.48	2.32	JPSG021.023-00.063	4.9	0.33	0.71
G021.407-00.254	AGAL021.406-00.252	7.17	0.55	1.2	JPSG021.407-00.255	5.35	0.43	0.88
G021.562-00.033	AGAL021.561-00.032	6.38	1.03	4.04	JPSG021.562-00.032	3.83	0.78	2.15

Notes: Only a small portion of the data is provided here, the full table is only available in electronic format.

Table 4.3: Detected sources from the MMB survey which have no corresponding dust continuum emission at 850 or 870 μm . Note the last two entries in this table are not covered by either the JPS or ATLASGAL surveys and so are only included in this table for completeness. Maser names appended with * are where the lower submillimetre limits are derived from the JPS 850 μm emission.

MMB Name	$S_{\text{peak},6.7\text{ GHz}}$ (Jy)	$S_{\text{int},6.7\text{ GHz}}$ (Jy km s $^{-1}$)	$S_{\text{peak,submm}}$ (Jy beam $^{-1}$)
MMB005.677−00.027	0.79	0.4	< 0.12
MMB014.521+00.155	1.40	2.4	< 0.12
MMB023.126+00.395	1.10	1.0	< 0.04
MMB029.993-00.282*	1.70	0.9	< 0.03
MMB032.516+00.323*	1.60	0.5	< 0.03
MMB033.486+00.040	3.30	3.7	< 0.06
MMB044.644-00.516	0.50	0.1	< 0.05
MMB059.833+00.672*	0.00	17.7	< 0.03
MMB303.869+00.194	0.90	0.6	< 0.12
MMB337.517−00.348	1.50	0.3	< 0.10
MMB350.470+00.029	1.44	0.2	< 0.08
MMB356.054−00.095	0.52	0.2	< 0.14
MMB026.422+01.685	3.80	2.6	−
MMB035.200-01.736	519.90	601.3	−

4.3.1 ANGULAR CORRELATION OF THE $60^\circ \geq \ell \geq 20^\circ$ MASERS

The initial matches were identified using a search radius of $50''$ and this was sufficient to match $\sim 90\%$ of the methanol masers. Visual inspection of the submm emission maps identified another four masers that are located within the boundary of extended ATLASGAL clumps; these matched masers lie further away from the peak of the thermal dust emission. The left panel of Fig. 4.3 shows the 2-dimensional angular offsets between the methanol masers and the peak submillimetre (submm) positions given in the JPS and ATLASGAL catalogues. It is clear from this plot that the positions of the vast majority of the masers are tightly correlated with the peak of the submm emission. The right panel of Fig. 4.3 shows the cumulative distribution functions (CDFs) of the MMB-JPS and MMB-ATLASGAL offsets; this clearly shows that the offsets between the MMB and JPS sources are smaller than the offsets between MMB and ATLASGAL. Comparing these two distributions using a KS test gives a p -value $\ll 0.0013$ confirming that the differences in maser offsets between the two submillimetre surveys is statistically significant.

The difference in the angular offset between the MMB-JPS and MMB-ATLASGAL associations is likely to be due to the increased resolution and sensitivity of JPS (as discussed in Sect. 4.2.2). To verify this all sources where there is a significant offset

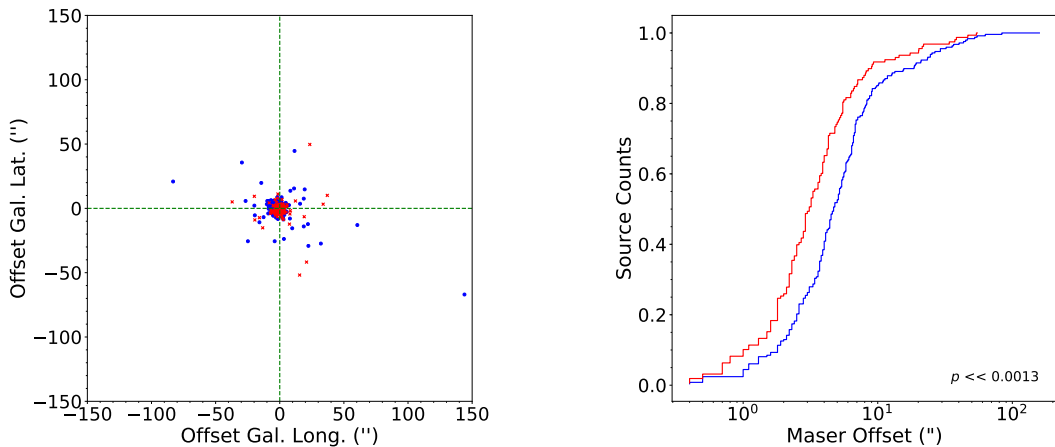


Figure 4.3: Offset distributions of the matching statistic for the latest addition of the MMB survey ($60^\circ > \ell > 20^\circ$). The left panel presents the 2D offsets between methanol maser detections and the ATLASGAL and JPS source catalogues. The right panel shows the cumulative distribution functions of the MMB-JPS and MMB-ATLASGAL offsets. The p -value from a KS test is shown in the lower right of the plot. In both plots the distribution of the MMB-JPS and MMB-ATLASGAL offsets are shown in red and blue respectively.

between the ATLASGAL and JPS peak emission were visually inspected (see Fig. 4.2 for examples). In cases where the JPS data has resolved an ATLASGAL clump into multiple components, and where one component provides a significantly smaller offset ($< 16.7''$; this corresponds to three times the median of the offset distribution), the maser has been associated to the JPS source as these values are likely to be more reliable in determining the clump properties associated with nearby maser emission. This is the case for 10 methanol maser sources. Inspecting these matches it appears that for 2 of the methanol maser sources (G048.902–00.273 & G049.482–00.402), the respective source extraction algorithms employed to create the ATLASGAL and JPS catalogues, have chosen different centroid positions for the same dust emission. For these two cases the ATLASGAL parameters have been chosen for consistency. Table 4.2 identifies the 8 methanol masers that are matched to both the ATLASGAL and JPS catalogues but where the JPS parameters are preferentially used (MMB names have been appended with *).

The ATLASGAL and JPS maps for every maser that was not matched in either catalogue have been visually inspected. This was to identify emission coincident with methanol maser positions that were below the detection threshold used for the automatic source extraction algorithms ($\text{SNR} > 5$). This process has identified a further 14 masers found to be associated with ATLASGAL (10) and JPS (4) emission. For these regions the SAOImage DS9 software has been used to place an aperture over the

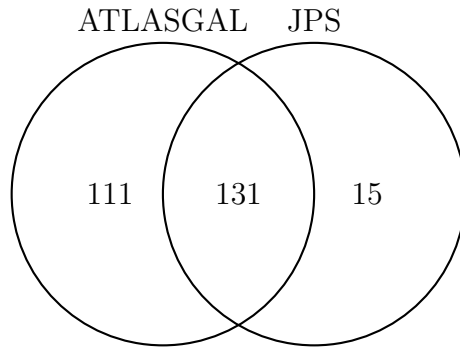


Figure 4.4: Venn diagram presenting the matching statistics for detected masers in the region $l = 20^\circ - 60^\circ$. The total sample of methanol masers in this region is 265, for which a match has been found to either ATLASGAL or JPS for 257 of these. Manual extraction has been used for 10 of the ATLASGAL matches and 4 of the JPS matches. For the 6 sources with no corresponding detection in ATLASGAL and for a further 8 sources where JPS better describes the clump distribution, the JPS flux values have been preferentially used.

emission to extract the peak and integrated fluxes. Therefore, in total 257 methanol masers have been matched to thermal dust emission with 242 of these maser being associated with ATLASGAL emission and 146 to JPS emission, Fig. 4.4 presents a Venn diagram of the matching statistics.

No dust continuum emission was detected for 8 of the 265 masers in this region. However, 2 of these lie beyond the Galactic latitude coverage of JPS and ATLASGAL and so no information is available; these are MMB026.422+01.685 and MMB035.200-01.736. Therefore, only 6 methanol masers have not been matched to a submillimetre counterpart. The MMB names, maser fluxes and an upper limit for the submillimetre emission are provided in Table 4.3 for these 8 masers and the 7 masers that were unassociated with submillimetre emission in the previous studies (Urquhart et al. 2013, 2015b). It is likely that these maser sources are associated with submillimetre emission, however, the sensitivity of the data used in this Thesis has not detected any within the vicinity of these masers.

4.3.2 VELOCITY CORRELATION OF THE $60^\circ \geq \ell \geq 20^\circ$ MASERS

Maser velocity information is available for all 265 sources in the latest addition of the MMB survey catalogue. Velocity values are also available for 219 dense clumps in this region, taken from the ATLASGAL catalogue (Urquhart et al. 2018). The velocities of the new methanol masers with the corresponding molecular line velocities have been compared to confirm maser associations in velocity space as well as positional space. The left panel of Fig. 4.5 presents these clump velocities against the corresponding

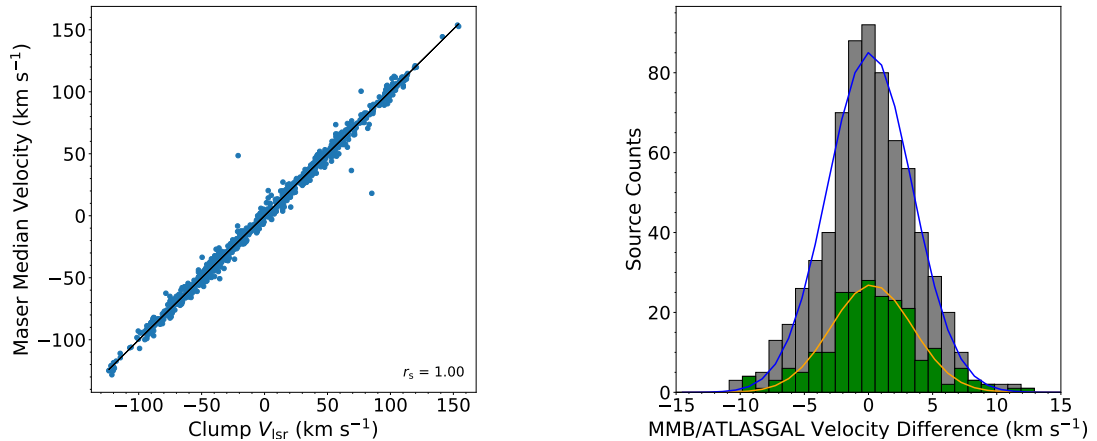


Figure 4.5: The left panel presents the distribution of the median maser velocities against the clump velocities for the entire matched sample ($60^\circ \geq \ell \geq 186^\circ$), with a best fit line shown. The results from a Spearman’s rank correlation test is shown in the lower right of the plot. The right panel presents histograms of the offsets between the median maser velocities and the molecular line velocities for every match in the MMB survey is shown in grey with the matches for the latest addition to the MMB survey shown in green. Gaussian curves have been fitted to the data to determine the mean and standard deviations of the distributions.

spatially matched maser velocities. The majority of masers have small offsets in velocity space and so it is likely that these sources are in fact associated with the dust continuum emission. The velocity differences between the latest addition of the MMB survey with previously matched maser sources (Urquhart et al., 2015b) have been compared using a KS test. This produces a p -value much higher than the significance threshold and so there is likely no difference between these two samples.

The histograms presented in the right panel of Fig. 4.5 show the velocity difference distributions of both the previous and latest matches of the MMB survey. Both histograms have been fitted using a Gaussian model. As there appears to be no difference between these two samples the statistics of the full sample have been used in order to identify any outliers in velocity space. The mean and median velocity difference in this sample is 0.17 km s^{-1} and 0.15 km s^{-1} respectively, with a standard error of 0.15 km s^{-1} . The standard deviation of this model is 4.5 km s^{-1} and set a confidence threshold of 3σ (13.5 km s^{-1}) to identify outliers in this distribution. All of the maser sources within the new sample ($60^\circ > \ell > 20^\circ$) have a velocity difference of less than this value and no outliers were identified in this distribution.

4.3.3 MATCHING STATISTICS FOR THE WHOLE MMB CATALOGUE

In the previous section 257 methanol masers were matched with dust emission. Combining these new matches with those identified in the previous studies has resulted in 958 of the 972 masers within the MMB catalogue being associated with dust emission; this is an association statistic of 98.5%. There are 14 of the 972 maser sources that have not been matched to any corresponding dust continuum emission. All of these non-matches can be found in Table 4.3. The majority of these simply have no associated dust emission, likely due to the sensitivity of the JPS and ATLASGAL surveys.

Figure 4.6 shows the source angular surface density distribution of all matched MMB sources (958) as a function of the angular offset. For comparison this plot also shows the distribution for the masers matched in this work. The distributions look indistinguishable from each other and this is confirmed by a KS test (p -value = 0.11). The mean of this distribution is $7.6''$, with a standard deviation of $10.9''$. There are 33 associations with a higher offset than three times this standard deviation. Although it is likely that all detected associations are real, objects that are at a considerable angular or physical distance from the peak continuum emission are very likely to be embedded in regions of enhanced density, however, are unlikely to be resolved as discrete clumps within JPS or the ATLASGAL survey. Therefore, this study shall only consider sources which have an angular offset of less than this 3σ ($32.7''$), ensuring that the derived physical parameters are representative of the material which is actually associated with methanol maser emission.

Figure 4.5 presents the velocity offset distribution of the maser associations, for both the newest addition to the MMB survey and for every match in the entire MMB survey. There are 922 maser sources in the entire sample that have a radial velocity measurement and for which a velocity difference using the median maser velocity can be determined. As with the angular offsets, only those sources that have a velocity offset of less than 3σ (13.5 km s^{-1}) have been included in the sample; 11 sources within the entire matched sample (958 masers) have velocity offsets larger than this value and so are excluded from the statistical analysis of physical properties.

The velocity ranges of the maser sources from this sample have a mean and standard deviation of 7.10 and 5.50 km s^{-1} respectively. The maximum velocity range is found to be 28.5 km s^{-1} . Sridharan et al. (2002) found that velocity ranges were confined to 15 km s^{-1} , although this is likely due to their smaller sample size. The velocity ranges found are much more consistent with Caswell (2009). In general, it is found that the more luminous masers also have larger velocity ranges, which has been noted in previous studies (e.g. Breen et al. 2011), this relationship is described further in

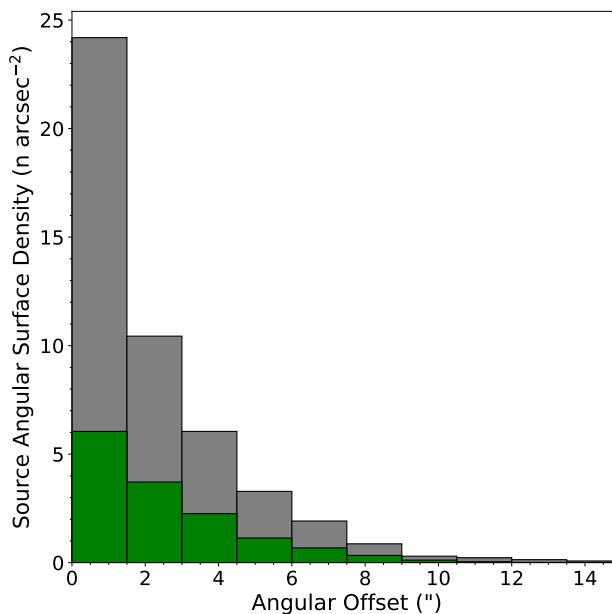


Figure 4.6: Source angular surface density as a function of angular offset between the methanol masers and the peak of the submm clumps for all the whole matched sample (Urquhart et al. 2013, 2015b and this work). Surface densities for the newest addition to the MMB survey ($60^\circ > \ell > 20^\circ$) are shown in green with the rest of the Galactic sample presented in grey. There are 15 maser associations beyond the limits of this histogram.

Sect. 4.4.5.

Therefore, taking into account the conditions above, along with the number of non associations, the sample consists of 839 matched masers, all of which have an angular and velocity offset of less than 3σ ($32.7''$ and 13.5 km s^{-1}). Table 4.4 presents the matches between the MMB survey and corresponding dust emission for the newest addition to the MMB survey and Table 4.5 presents these matches for the entire MMB survey.

4.4 PHYSICAL PARAMETERS OF MASER CLUMPS

This section will compare the physical parameters of the masers with those of their host clumps and also compare the properties of these host clumps themselves with the properties of the full population of dense clumps that encompass the whole range of evolutionary stages, as identified by the ATLASGAL survey. The physical parameters for the vast majority of clumps located have been determined in a previous study Urquhart

Table 4.4: Matches between MMB and ATLASGAL for the newest addition to the MMB survey, with corresponding ATLASGAL catalogue parameters. Columns: (1) MMB defined maser name; (2) ATLASGAL CSC name; (3)-(4) Maser peak and integrated flux densities; (5) Molecular line velocities; (6)-(7) Maser peak and median velocities; (8) Maser velocity range; (9) ATLASGAL-MMB Offset.

MMB name	Clump name	MMB peak flux (Jy)	MMB integrated flux (Jy km s ⁻¹)	v_{lsr} (km s ⁻¹)	v_{peak} (km s ⁻¹)	v_{median} (km s ⁻¹)	v_{range} (km s ⁻¹)	MMB offset (")
G020.081-00.135	AGAL020.081-00.136	1.7	0.7	41.1	43.5	43.05	1.70	1.76
G020.237+00.065	AGAL020.236+00.064	84.9	-1.0	70.8	71.9	73.00	9.80	6.31
G020.239+00.065	AGAL020.236+00.064	6.9	-1.0	—	70.4	65.30	11.40	12.83
G020.364-00.013	AGAL020.362-00.012	2.9	5.3	52.2	55.9	54.55	9.50	5.3
G020.733-00.059	AGAL020.731-00.059	1.3	1.4	56	60.7	59.40	8.80	9.87
G020.926-00.050	—	4.1	6.8	—	27.4	26.60	6.20	—
G020.963-00.075	AGAL020.962-00.074	2.2	1.0	30.9	34.6	34.20	1.20	4.42
G021.023-00.063	AGAL021.000-00.057	2.2	1.1	31.1	31.1	31.85	5.70	83.52
G021.407-00.254	AGAL021.406-00.252	14.5	14.2	91.1	89.0	89.00	12.60	7.17
G021.562-00.033	AGAL021.561-00.032	13	18.3	113.6	117.2	114.75	11.90	6.38

Notes: Only a small portion of the data is provided here, the full table is presented in Appendix B.

Table 4.5: Matches between MMB and ATLASGAL for the entire MMB catalogue, with corresponding ATLASGAL source parameters.

MMB name	Clump name	Dust temp (K)	Distance (kpc)	Radius (pc)	Maser luminosity (L_{\odot})	Surface density ($\log[M_{\odot} \text{pc}^{-2}]$)	Volume density ($\log[\text{cm}^{-3}]$)	Clump luminosity ($\log[L_{\odot}]$)	Clump mass ($\log[M_{\odot}]$)	$L_{\text{bol}}/M_{\text{fwhm}}$ ratio ($\log[L_{\odot} M_{\odot}^{-1}]$)
G005.618-00.082	AGAL005.617-00.082	15.05	16.2	0.79	-5.07	2.76	4.65	4.38	3.81	0.58
G005.630-00.294	AGAL005.629-00.294	28	3	0.12	-6.73	2.77	5.06	3.16	1.75	1.41
G005.657+00.416	G005.656+00.417	—	—	—	—	—	—	—	—	—
G005.677-00.027	—	—	—	—	—	—	—	—	—	—
G005.885-00.393	AGAL005.884-00.392	34.54	3	0.11	-7.2	2.49	6.15	5.33	2.72	2.61
G005.900-00.430	AGAL005.899-00.429	25.48	3	0.15	-6.42	2.9	5.69	4.75	2.71	2.04
G006.189-00.358	AGAL006.188-00.357	22.86	—	—	—	2.73	—	—	—	—
G006.368-00.052	AGAL006.368-00.051	24.33	14.3	0.77	-5.41	2.08	4.2	4.7	3.32	1.38
G006.539-00.108	AGAL006.551-00.097	25.45	3	0.25	-7.36	2.33	4.77	4.41	2.44	1.96
G006.588-00.192	AGAL006.588-00.192*	—	—	—	—	—	—	—	—	—

Notes: Only a small portion of the data is provided here, the full table is presented in Appendix B.

et al. (2018), and a detailed derivation of these parameters is given in Sect. 2.5. This study is concentrated on ~ 8000 clumps located away from the Galactic centre (GC; $60^\circ > \ell > 5^\circ$ and $355^\circ > \ell > 300^\circ$).

Maser emission is detected in 866 sources of the entire ATLASGAL catalogue (8.5%). There are 25 maser emission sites which have been associated with either JPS emission only or where the dust continuum fluxes have been manually extracted (as described in Sect. 4.3.1), these have not been included in the sample due to the lack of distance measurements and therefore poorly constrained physical parameters. Distances are available to 660 methanol maser associated clumps, which have been obtained from Urquhart et al. (2018). Figure 4.7 presents a histogram of the distribution of clump heliocentric distances, the entire ATLASGAL sample is shown in grey with the MMB associated clumps shown in green.

Therefore, the maser associated sample presented in this study includes 660 dust clumps across the Galactic plane not including the central 10° (i.e. $5^\circ > \ell > 355^\circ$). Also, throughout this study a distance limited sample (2 to 4 kpc; a total of 222 clumps) has been employed, along side the full sample of clumps, to test for any distance bias affecting the statistical results.

In addition to the physical properties that will be described in the following subsections, the $L_{\text{bol}}/M_{\text{fwhm}}$ ratio is also defined, which will be described in Sect. 4.4.3. It has been shown in previous studies that the luminosity-to-mass ratio is a good statistical indicator of evolutionary stage (Molinari et al., 2008) and this ratio will be used throughout the remainder of this study to investigate the properties of the clumps with respect to their evolutionary stage. This parameter also has the advantage of being distance independent, and so eliminates an important source of uncertainty, but can also be determined for clumps where a distance is not yet available. The $L_{\text{bol}}/M_{\text{fwhm}}$ ratio is calculated from the luminosities given in Urquhart et al. (2018) and the M_{fwhm} , with units of $L_\odot M_\odot^{-1}$. In the following subsections the methods used to derive the physical parameters are described and a summary of the statistical physical properties of the dense clumps are provided in Table 4.6.

4.4.1 SPECTRAL ENERGY DISTRIBUTIONS

The physical parameters used in this study are taken from Urquhart et al. (2018) as mentioned in Sect. 4.4, which covers the longitude range $60^\circ \geq \ell \geq 300^\circ$. To determine the environmental properties for the maser sources within the MMB survey which lie beyond this longitude range (i.e. $300^\circ \geq \ell \geq 186^\circ$), aperture photometry has been performed to reconstruct the dust continuum spectral energy distributions (SEDs; for a more detailed description of this method please see Sect. 2.5 or Sect. 3 of König et al.

Table 4.6: Total statistical parameters for all maser associated clumps, determined within the matching criteria, within the Galactic longitude range $60^\circ > \ell > -60^\circ$, excluding the central 10° towards the Galactic centre. The values in brackets show the statistics from a distance limited sample (2 to 4kpc).

Parameter	No.	Mean	Standard error	σ	Median	Min	Max
Distance (kpc)	660 (222)	5.85 (3.07)	0.15 (0.03)	3.82 (0.48)	4.70 (3.10)	0.10 (2.10)	24.20 (3.90)
FWHM Radius (pc)	631 (212)	0.36 (0.20)	0.01 (0.01)	0.27 (0.08)	0.26 (0.18)	0.01 (0.08)	1.85 (0.53)
Temperature (K)	642 (210)	24.16 (24.06)	0.19 (0.36)	4.88 (5.23)	23.66 (23.35)	13.41 (13.41)	46.41 (46.41)
Log[Maser Luminosity (L_\odot)]	634 (220)	-6.01 (-6.34)	0.04 (0.06)	0.99 (0.87)	-5.97 (-6.29)	-9.25 (-8.09)	-3.40 (-3.49)
Log[Luminosity (L_\odot)]	642 (210)	4.03 (3.69)	0.04 (0.06)	0.96 (0.81)	4.02 (3.57)	-0.22 (1.74)	6.91 (5.83)
Log[Clump Mass (M_\odot)]	632 (208)	2.65 (2.30)	0.03 (0.03)	0.66 (0.41)	2.72 (2.31)	-1.05 (1.23)	4.40 (3.28)
Log[$L_{\text{bol}}/M_{\text{fwhm}}(L_\odot/M_\odot)$]	632 (208)	1.39 (1.40)	0.02 (0.04)	0.59 (0.61)	1.37 (1.35)	-0.07 (0.12)	3.17 (3.17)
Log[$n(\text{H}_2)$](cm^{-3})	613 (200)	4.86 (5.07)	0.02 (0.03)	0.56 (0.44)	4.82 (5.02)	3.40 (4.11)	6.90 (6.90)
Free Fall Time (Myr)	613 (200)	0.22 (0.16)	0.01 (0.01)	0.14 (0.08)	0.19 (0.15)	0.02 (0.02)	1.00 (0.44)

2017). SED fitting has been used to provide information for 10 sources beyond the longitude range covered by Urquhart et al. (2018). This method has also been used for a further 34 maser sources, which were either beyond the ATLASGAL survey coverage or were not detected within the survey itself. An example SED and corresponding fit is shown in Fig. 4.8.

4.4.2 CLUMP SIZES

In order to circumvent an observational bias when measuring the radius of clumps, which is discussed below, the current sizes of clumps as found in Urquhart et al. (2018) have not been used. Instead the sizes of clumps is determined using the FWHM of the dust continuum emission, assuming that the flux from each clump is Gaussian in nature.

The clump FWHM angular radius is determined from the number of pixels, $\text{npix}_{\text{fwhm}}$, with fluxes above the 50% peak flux contour:

$$R_{\text{fwhm}} = \sqrt{\frac{A}{\pi}}, \quad (4.1)$$

where A is $\text{npix}_{\text{fwhm}}$ multiplied by the square of the pixel size in arcseconds (i.e. 36 sq.""). The 50% flux level is below the detection threshold for sources with a SNR below 6σ , and consequently the $\text{npix}_{\text{fwhm}}$ and R_{fwhm} for these sources are unreliable and are therefore excluded from this calculation. Clumps with fewer pixels than the beam integral are excluded ($\Theta_{\text{fwhm}}^2 \times 1.133 = 11.3$ pixels, where Θ_{fwhm} is 19.2") as the flux measurements will be overestimated. The R_{fwhm} that satisfy these two conditions are deconvolved from the ATLASGAL beam using:

$$R_{\text{fwhm,decon}} = \sqrt{R_{\text{fwhm}}^2 - \left(\frac{\Theta_{\text{fwhm}}}{2}\right)^2}, \quad (4.2)$$

The distances given in Urquhart et al. (2018) are used to convert the deconvolved radius into a physical radius, $R_{\text{fwhm,pc}}$.

Figure 4.9 presents two distributions of clump radii versus evolutionary stages as determined by the clump $L_{\text{bol}}/M_{\text{fwhm}}$ ratios. The left panel shows previously calculated effective radii values ($2.4 \times \sigma_{\text{radius}}$; Rosolowsky et al. 2010) for dense clumps as taken from Urquhart et al. (2018), with the right panel showing the FWHM derived radii values from this study. The results from a Spearman's test are shown in the lower left corner of each panel. Urquhart et al. (2018) noted a correlation between the increasing size and decreasing surface density of clumps, and their evolutionary stage; the increase in radius is clearly seen in the upper panel of Fig. 4.9. This distribution has

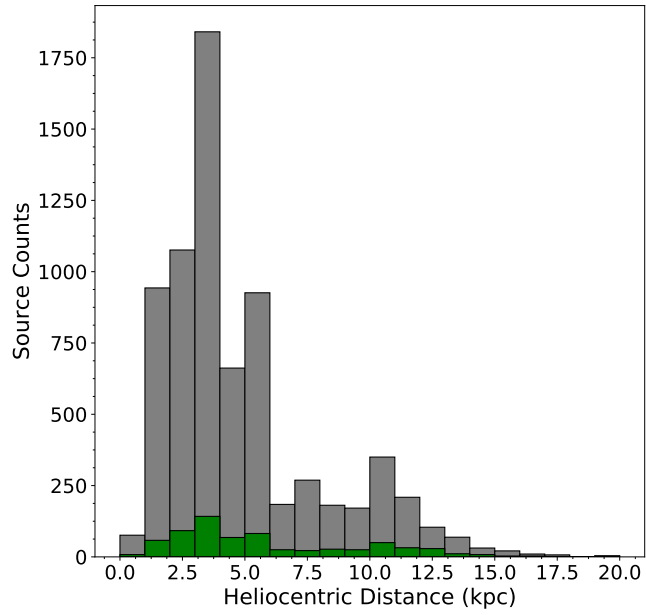


Figure 4.7: Histogram presenting the distribution of clump heliocentric distances. The entire ATLASGAL sample is shown in grey, with the MMB associated clumps shown in green. The bin size used is 1 kpc. There are two sources that have a heliocentric distance beyond 20 kpc.

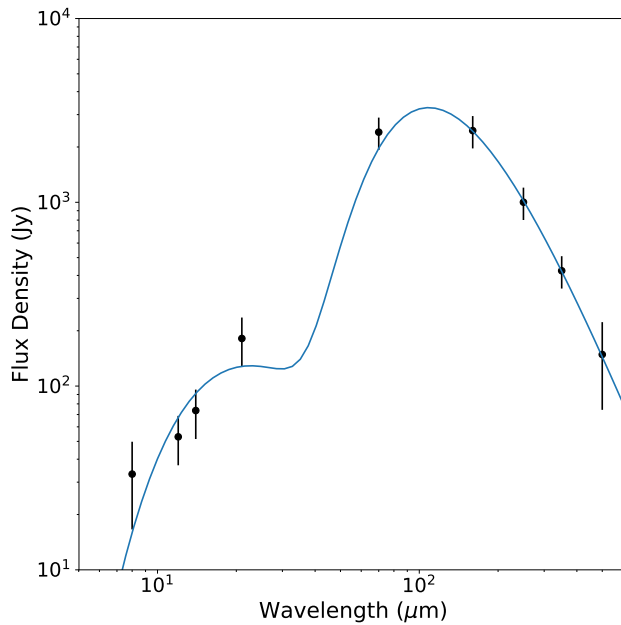


Figure 4.8: A spectral energy distribution and corresponding fit for an example region (G189.030+00.783). Flux density error bars are shown.

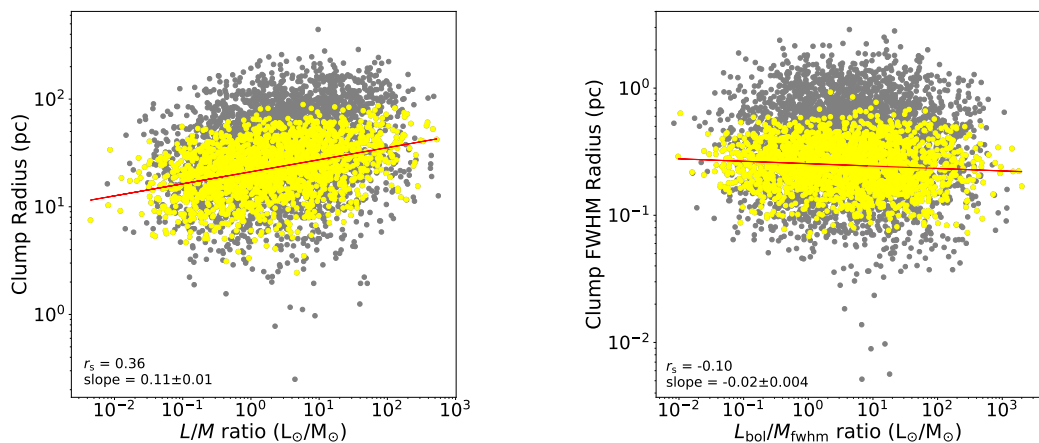


Figure 4.9: The left panel presents the clump radius vs clump L/M ratio for previously calculated values of radius, luminosity and mass within the ATLASGAL survey. The right panel presents clump FWHM radius against clump $L_{\text{bol}}/M_{\text{fwhm}}$ ratio, for the newly derived clump sizes (see Sect. 4.4.2). Both plots present the entire ATLASGAL sample and a distance limited sample (2 to 4 kpc) in grey and yellow respectively. The results from a Spearman’s rank correlation coefficient test for the distance limited samples (2 to 4 kpc) is shown in the lower left of each panel, the p -value for both distributions is below the significance threshold.

a Spearman’s results of 0.36 and p -value of much less than the significance threshold with a best fit slope of 0.11 ± 0.01 . Similar trends for increasing radii and decreasing volume density as a function of evolution have been reported in a number of submm dust continuum studies (e.g. Hill et al. 2005; Breen et al. 2010; Contreras et al. 2017). These trends are generally explained as the expansion of the clumps towards the end of their evolution and although plausible for the final stages, due to mechanical and radiative feedback, this cannot explain the very smooth increase in radius throughout their evolution. Particularly given that at the earliest states it is expected that they are collapsing and accreting material onto the evolving protostellar objects.

Urquhart et al. (2018) determined that this was due to an observational bias where the increasing average temperature of the clumps results in more of the extended envelope becoming bright enough to be detected by ATLASGAL, resulting in an apparent increase in the source sizes as the clumps evolve. In an effort to eliminate this bias the sizes and physical parameters have been recalculated using only the $870 \mu\text{m}$ emission above the FWHM flux contour. The right panel of Fig. 4.9 shows the relationship between the R_{fwhm} and the evolutionary tracer; this clearly demonstrates that the observational bias as been corrected for, as the corrected slope for this distribution is -0.02 ± 0.004 . Also the result from a Spearman’s test gives a r_s statistic of -0.10 , while this is significant (as shown by a corresponding p -value of less than the confidence

threshold), it shows a poor correlation.

The distribution of these new radius values, for the entire ATLASGAL sample, can be found in the upper panels of Fig. 4.10, along with the distribution of maser associated clumps. The upper right panel of Fig. 4.10 presents the cumulative distribution function of the radii values for a distance limited sample (2 to 4 kpc), for both of these samples. It is clear from the CDF shown in the right panel that the methanol maser associated clumps are significantly more compact than the rest of the population (p -value $\ll 0.0013$). It appears that maser associated clumps have statistically significantly smaller FWHM radii values when compared to the full ATLASGAL sample. Therefore, dense clumps associated with a methanol maser are generally much more compact than those without this high-mass star formation signpost.

4.4.3 CLUMP MASSES AND VOLUME DENSITIES

The mass within the 50% contour, M_{fwhm} , is scaled from the total mass calculated in Urquhart et al. (2018) using the ratio of flux within the FWHM and the total flux of the clump. Figure 4.11 presents the distribution of the clump M_{fwhm} for the entire ATLASGAL sample and a distance limited sample (2 to 4 kpc), it can be seen that the M_{fwhm} is independent of the evolution of a clump. The new mass distribution for the full sample and maser associated sample of clumps is shown in the middle panels of Fig. 4.10. The middle right panel of Fig. 4.10 presents the distance limited sample CDF of these distributions. It can be seen that there is no overall difference in the masses of clumps associated with methanol maser emission and the general population of clumps, as confirmed by the results of a KS test (p -value = 0.387). This suggests that clump mass alone is not an important factor in determining whether a particular clump is likely to form a high-mass star.

The volume density is calculated, within the FWHM contour, by dividing the M_{fwhm} by the volume:

$$n(\text{H}_2) = \frac{3}{4\pi} \frac{M_{\text{fwhm}}}{\mu m_{\text{p}} R_{\text{fwhm}}^3}, \quad (4.3)$$

where $n(\text{H}_2)$ is the hydrogen particle density per cm^{-3} , μ is the mean molecular weight per hydrogen atom (taken as 2.8; Kauffmann et al. 2008) and m_{p} is the mean proton mass, and M_{fwhm} and R_{fwhm} are as previously defined. It is assumed that each clump is generally spherical and not extended along the line of sight. Volume densities are available for 81% of the clump sample presented in this study, the distribution of this parameter can be seen in the lower panels of Fig. 4.10. Inspection of these plots reveals that clumps hosting methanol masers have a significantly higher volume density.

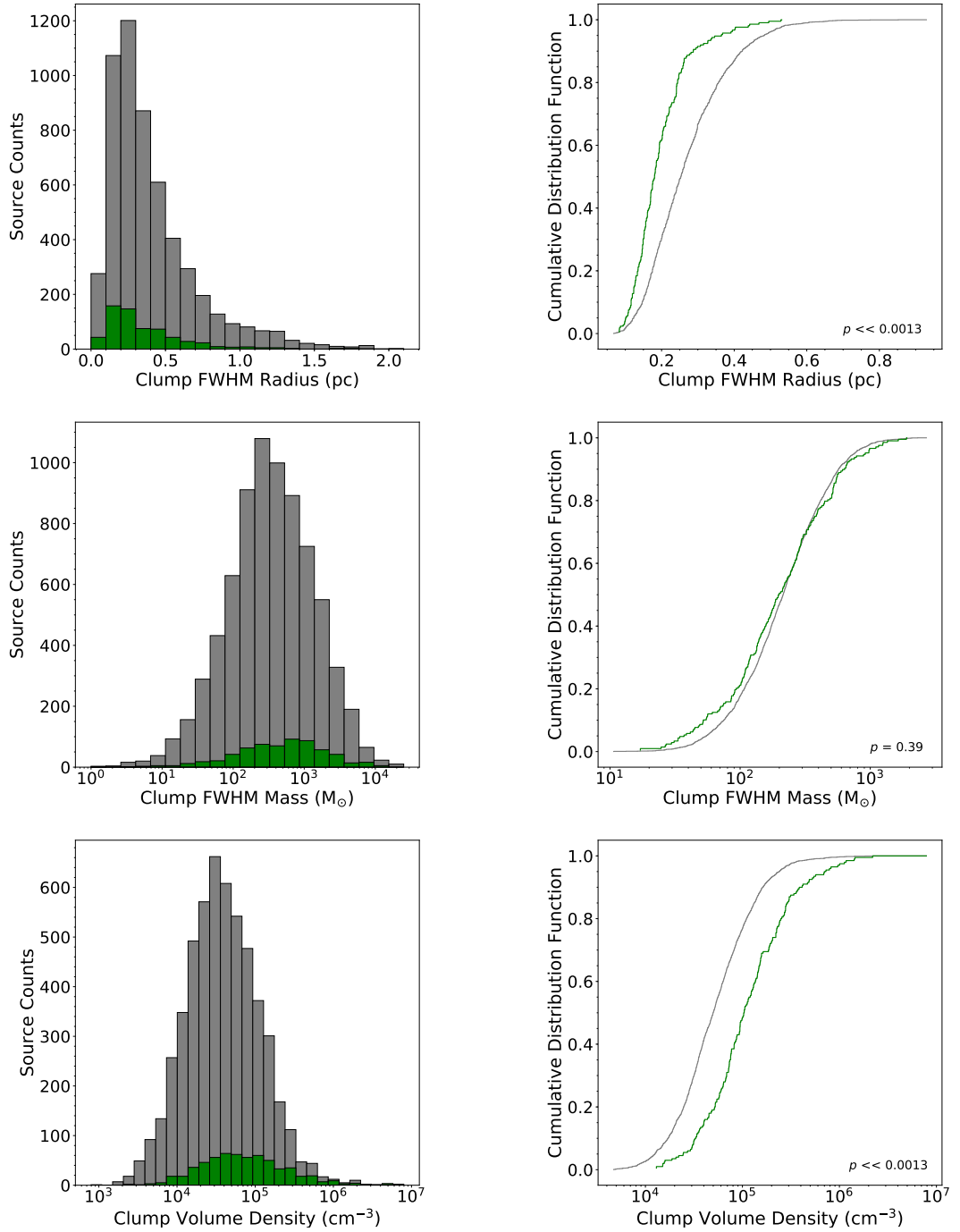


Figure 4.10: Radius, mass and volume density parameter distributions are presented in the upper, middle and lower panels respectively. The histograms in the left panels present the entire distributions of the maser associated clumps and ATLASGAL sample in green and grey respectively, whereas the cumulative distribution functions in the right panels present a distance limited sample. The p -value results from a KS test are shown in the lower right of the CDF panels.

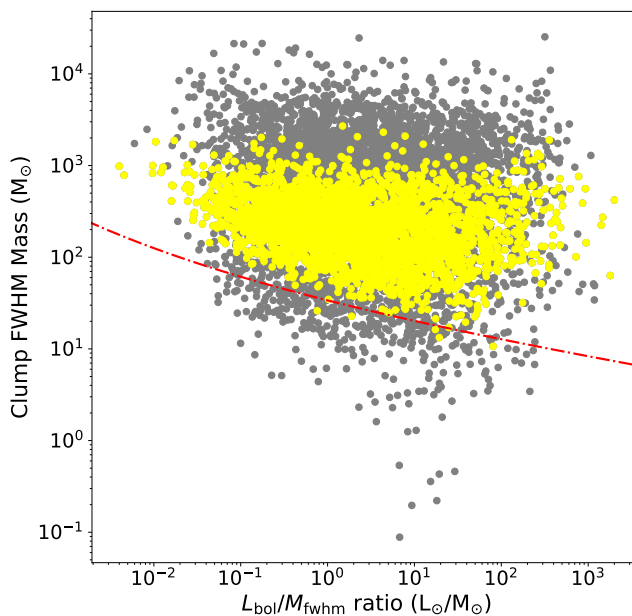


Figure 4.11: Clump FWHM mass vs. $L_{\text{bol}}/M_{\text{fwhm}}$ ratio. A distance limited sample (2 to 4 kpc) is shown in yellow with the full ATLASGAL sample shown in grey. The red dash-dotted line presents the 5σ observational sensitivity limit of the ATLASGAL survey.

4.4.4 STABILITY AND FREE-FALL COLLAPSE

In order to estimate the gravitational stability of the sample of clumps, the virial parameter for each source have been derived. This parameter is a measure of the balance between internal energy and gravitational collapse (see Sect. 2.5) and is defined as:

$$\alpha_{\text{vir}} = \frac{5\sigma_v^2 R_{\text{fwhm}}}{GM_{\text{fwhm}}}, \quad (4.4)$$

where σ_v is the velocity dispersion, which is calculated from NH_3 (1,1) inversion transition observations (e.g. Dunham et al. 2011; Urquhart et al. 2011; Wienen et al. 2012, 2018), G is the gravitational constant and all other parameters are as previously defined. The virial parameters for 216 sources in the sample have been calculated, with a mean and median of 0.84 and 0.61 respectively with a standard deviation of 1.02. A clump with a virial parameter of less than 2 indicates that it is unstable and will undergo global collapse in the absence of a supporting magnetic field (Kauffmann et al. 2013); 203 clumps (94%) have a values of less than 2 and given that the majority of clumps are already associated with star formation (Urquhart et al. 2018) it is safe to assume that the majority of these clumps are collapsing. Figure 4.12 presents the dis-

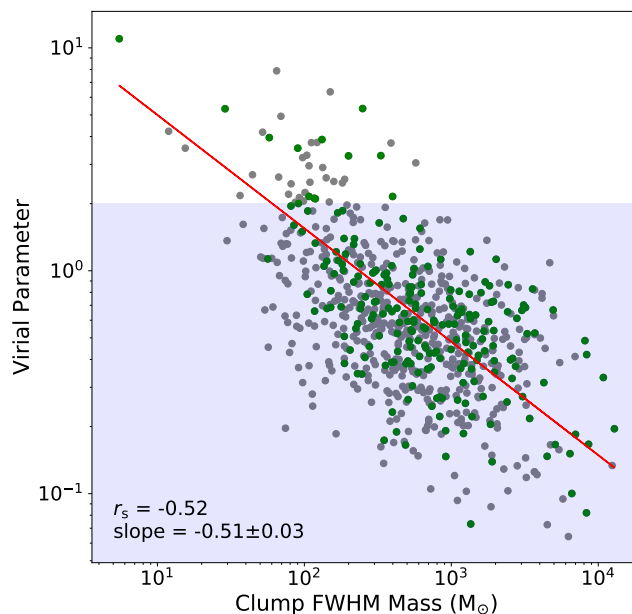


Figure 4.12: Virial parameter (α_{vir}) against clump FWHM mass. The maser associated clumps and full ATLASGAL sample are shown in green and grey respectively. The solid red line shows the results from an orthogonal distance regression of the maser associated sample, where $\alpha_{\text{vir}} \propto M_{\text{fwhm}}^{-0.5 \pm 0.03}$. The shaded region indicates unstable clumps where $\alpha_{\text{vir}} < 2$.

tribution of the virial parameter against the clump FWHM mass; this reveals a trend for the most massive clumps being the most gravitationally unstable. Fitting the data it is found that $\alpha_{\text{vir}} \propto M_{\text{fwhm}}^{-0.5 \pm 0.03}$, which is consistent with the relations derived by Larson (1981).

Free fall times (derivation given in Sect. 2.5) have been derived from the calculated volume densities:

$$t_{\text{ff}} = \sqrt{\frac{3\pi}{32G\rho}}, \quad (4.5)$$

where $\rho = \frac{3M_{\text{fwhm}}}{4\pi R_{\text{fwhm}}^3}$ is the mean density of the clump. A free fall time has been derived for every clump with a corresponding density measurement, these values range from 2×10^4 and 1×10^6 years. Thermodynamical changes the clump undergoes or any support mechanisms that might impede the global collapse have not been taken into account. However, the change in temperature of the clumps during the embedded evolution stages is quite modest (~ 15 K) and given the low virial parameters for the majority of the sample and the fact that all of the high density clumps are already associated with star formation it is unlikely any support mechanism is sufficient to counteract the global collapse on clump scales.

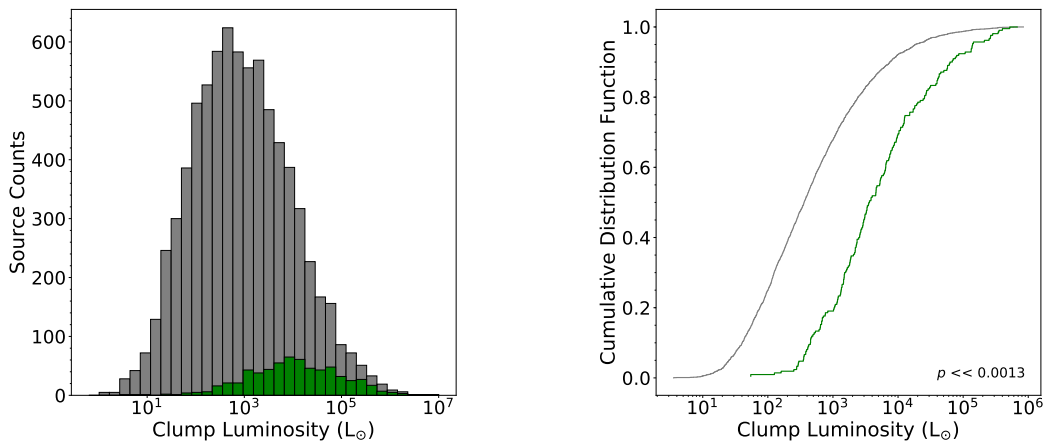


Figure 4.13: Clump luminosity parameter distributions. The histograms in the upper panel present the entire distribution of the maser associated clumps and ATLASGAL sample in green and grey respectively, whereas the cumulative distribution functions in the lower panels present a distance limited sample. The p -value result from a KS test are shown in the lower right of the lower panel.

4.4.5 BOLOMETRIC AND MASER LUMINOSITIES

The clump bolometric luminosities are taken unchanged from Urquhart et al. (2018). The distribution of clump luminosity can be found in Fig. 4.13. It can be seen from the upper panel of this figure that the luminosity values for maser associated clumps are, on average, increased when compared to the full ATLASGAL sample. This is expected as the 6.7 GHz methanol maser is thought to be produced in the dense envelopes surrounding high-mass protostellar objects and YSOs. Naturally, the majority of a clump’s luminosity will be due to any associated high-mass embedded object. Lower luminosity clumps, especially those that are quiescent, with no known embedded objects, are unlikely to produced maser emission, which is supported by the analysis presented here.

The difference between clumps with and without maser emission can be more clearly seen in the lower panel of Fig. 4.13. This panel presents a cumulative distribution function of luminosity and shows both distance limited samples of the full ATLASGAL sample and maser associated clumps. There is a clear difference between these two samples, as confirmed by a KS test ($p \ll 0.0013$).

The maser luminosities have been calculated using (see Sect. 2.5):

$$L = 4 \pi D^2 S_{\text{int},6.7 \text{ GHz}}, \quad (4.6)$$

where $S_{\text{int},6.7 \text{ GHz}}$ is the integrated maser flux and D is the heliocentric distance to the host clump. Maser emission from any particular source is assumed to be isotropic and the flux of maser sources decreases following an inverse square law. The units of this

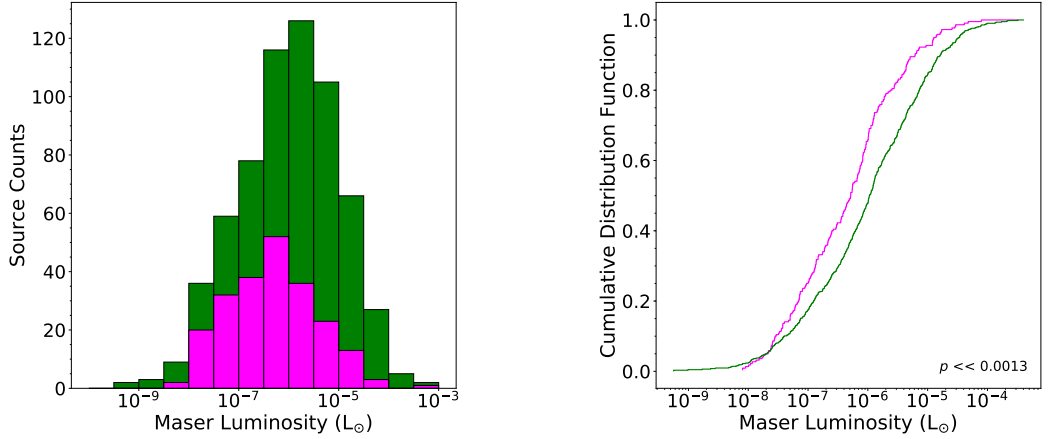


Figure 4.14: The left presents a histogram of the methanol maser luminosities. A distance limited sample is shown overplotted in magenta, the bin size is 0.5 dex. The right panel presents the CDF of the same distribution.

parameter are $\text{Jy km s}^{-1} \text{kpc}^2$ and are, therefore, somewhat arbitrary. A conversion factor has been derived to convert the maser luminosities from $\text{Jy km s}^{-1} \text{kpc}^2$ into L_{\odot} :

$$\Delta f = \frac{f \Delta v}{c} = \frac{6.7 \text{ GHz} \times 1 \text{ km s}^{-1}}{3 \times 10^5 \text{ km s}^{-1}} = 22.3 \text{ kHz}, \quad (4.7)$$

where f is the base frequency of the maser emission (6.7 GHz) and c is the speed of light. This shows that a change in velocity of 1 km s^{-1} is proportional to a frequency change of 22.3 kHz. Figure 4.14 presents a histogram of the methanol maser integrated luminosities along with the corresponding CDF, both the full and distance limited sample are shown. The difference in maser luminosity between the full and distance limited sample (2 to 4 kpc) are found to be significant (p -value $\ll 0.0013$) as shown by the result from a KS test.

Figure 4.15 shows how maser velocity ranges change depending on the maser luminosity. It can be seen that as maser luminosity increases, the velocity range also increases, the results from a Spearman's rank test indicate there is a reasonable positive correlation between these two variables ($r_s = 0.43$). It is likely that the increase in velocity range can be attributed to an increase in individual spots within the maser spectra, this has also been stated in previous studies (e.g. Green et al. 2017), and with other maser species (e.g. Anglada et al. 2002). There appears to be a large amount of scatter in Fig. 4.15, and so it is not necessarily true that the most luminous masers also have the largest velocity ranges.

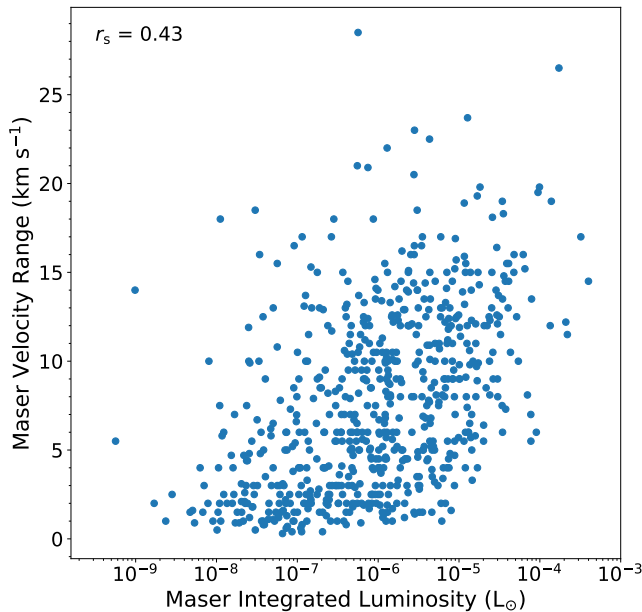


Figure 4.15: Scatter plot presenting the distribution of maser integrated luminosity against the maser velocity ranges. The result from a Spearman’s rank correlation test is shown in the upper left, with a p -value of $\ll 0.0013$.

4.4.6 UNCERTAINTIES IN THE PHYSICAL PARAMETERS

Dust temperature values are obtained through the fitting of the spectral energy distributions with a mean error of $\sim 10\%$. The uncertainties in the distances are estimated from the Bayesian distance algorithm presented in Reid et al. (2016) and are of order ± 0.5 kpc and the fractional uncertainty in the radius will be the same as for the distance as these are linearly related ($\sim 30\%$ at 1 kpc, but only a few per cent at distances greater than 10 kpc). The fractional uncertainty in the maser luminosity is $\sqrt{2}$ times the fractional uncertainty in the distance, however, in calculating this quantity it is assumed that the maser emission is isotropic and so the uncertainty on these measurements is hard to estimate. The error on the bolometric fluxes are approximately 50% but when combined with the uncertainty in the distance the total uncertainty is estimate to be approximately a factor of 2. The uncertainty in the mass, surface and volume density calculations are likely to be dominated by the uncertainty in the dust to mass ratio and the value of κ_v (dust absorption coefficient; taken as $1.85 \text{ cm}^2 \text{ g}^{-1}$ interpolated from Schuller et al. 2009) both of which are poorly constrained and therefore the uncertainties for these is likely to be a factor of 2–3. However, while the uncertainties associated with the physical parameters may be quite large, these affect the entire sample uniformly and will increase the scatter in distributions but will still allow statistical trends to be identified and robustly analysed, especially when considering a

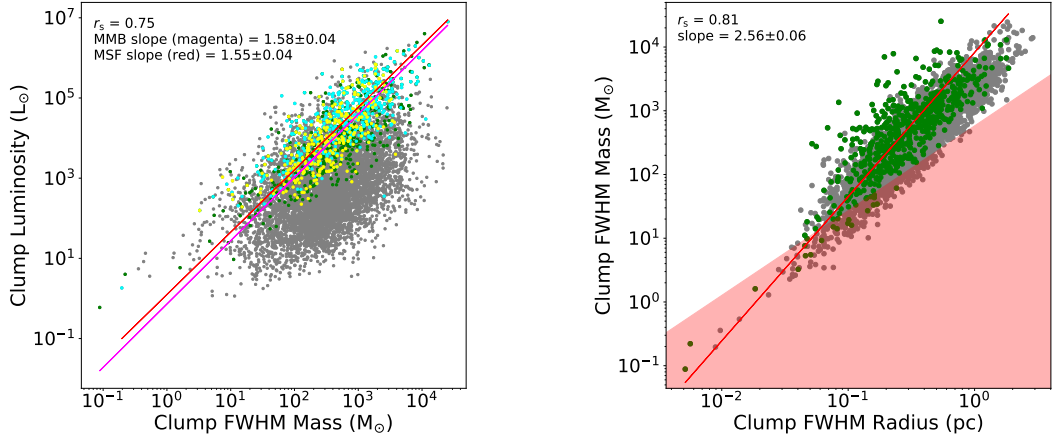


Figure 4.16: The upper panel presents the distribution of clump bolometric luminosity versus clump FWHM mass, maser associated clumps, YSO associated clumps, HII region associated clumps and the full ATLASGAL sample are shown in green, yellow, cyan and green respectively. The lower panel presents clump FWHM mass versus clump FWHM radius with maser associated clumps and the full ATLASGAL sample in green and grey respectively. Orthogonal distance regression has been used with the clump samples to produce best fit lines, shown in red and magenta. The slope of the best fit lines and the corresponding Spearman’s coefficient are shown in the upper left of each panel, the p -values for both distributions is less than the significance threshold. The shaded area in the lower panel shows the area devoid of massive star formation as derived by Kauffmann et al. (2010).

distance limited sample.

4.5 DISCUSSION

The sample presented in this study is the largest and most representative of maser associated dense clumps to date. Our statistical analysis will focus on the central 80% of sources in each parameter space, this will remove any potential outliers arising from incorrect distance measurements or due to extreme sources that might skew the results.

4.5.1 LUMINOSITY, MASS AND RADIUS CORRELATIONS

Figure 4.16 presents plots showing the relationship between luminosity, mass and radius for the ATLASGAL clumps. These are similar to plots presented in Urquhart et al. (2018) but have been updated using the FWHM clump masses and radii in order to remove any bias due to evolution. The overall correlations between these parameters

are actually very similar, but the slopes are significantly steeper. The previous slope for L_{bol} vs. M_{clump} was 1.31 ± 0.02 compared to L_{bol} vs. M_{fwhm} which is 1.55 ± 0.04 for the full sample of massive star forming clumps (i.e. those hosting massive (M)YSOs and HII regions; Urquhart et al. 2014a) and so the smaller FWHM masses have resulted in a modestly steeper relationship. The slope of the clumps associated with methanol masers is 1.58 ± 0.04 and so is not significantly different to that of the massive star forming clumps. The slopes, however, for the distance limited sample of clumps and clumps associated with a methanol maser are significantly steeper at 2.58 ± 0.17 and 2.35 ± 0.19 , respectively. This is likely due to the fact that clouds are being mapped at larger distances rather than clumps and so capturing more mass that is not actually contributing to the star formation process.

The right panel of Fig. 4.16 shows the mass-radius relationship of the clumps. Comparing the results again with those given in Urquhart et al. (2018), the slope found of 2.12 ± 0.01 for the M_{fwhm} vs. R_{fwhm} for the whole sample is significantly larger than the slope of 1.65 ± 0.01 derived from the M_{clump} vs. R_{eff} (where R_{eff} is the effective radius of the clump). The change in the slope is because a modest increase in temperature has a much more significant influence on the radius (a change in temperature between 12 to 45 K can result in change in radius by a factor of 4.2; as discussed in Sect. 8 of Urquhart et al. 2018). For comparison the slope of clumps determined by a set of targeted recent high-resolution $350 \mu\text{m}$ observations towards ATLASGAL clumps selected from the GaussClump catalogue (Csengeri et al. 2014) reported a mass-radius slope between 2 and 2.3 (Lin et al. 2019, *subm.*). Analysis of the CHIMPS ^{13}CO (3-2) survey (Rigby et al. 2016) finds the mass-radius slope to be 2.47 ± 0.02 (Rigby et al. 2019, *subm.*), while Roman-Duval et al. (2010) reported a slope of 2.36 ± 0.04 from analysis of ^{13}CO (1-0) emission drawn from the Galactic Ring Survey (GRS; Jackson et al. 2006). There is, therefore, a significant amount of variation in the measured slope of the relationship between the mass and radius in the literature, which is probably due to differences in the way the radius is determined ($R_{\text{eff}} = \eta R_{\sigma}$, η is a multiplication factor (between 1.9-2.4) that scales the R_{σ} , which is the standard deviation of the intensity-weighted emission profile), the tracer (CO or dust), and the assumptions used to determine the clump masses (dust emissivity, dust-to-gas ratio and H_2 to CO ratio) and the method used to fit the data (least-square fitting, orthogonal distance regression etc.).

The slope for the mass-radius relation for the maser associated clumps is significantly steeper than found for the full sample of clumps (2.56 ± 0.06). This is to be expected given that the methanol maser associated clumps are, while having a similar mass to the general population of clumps, significantly smaller and have, on aver-

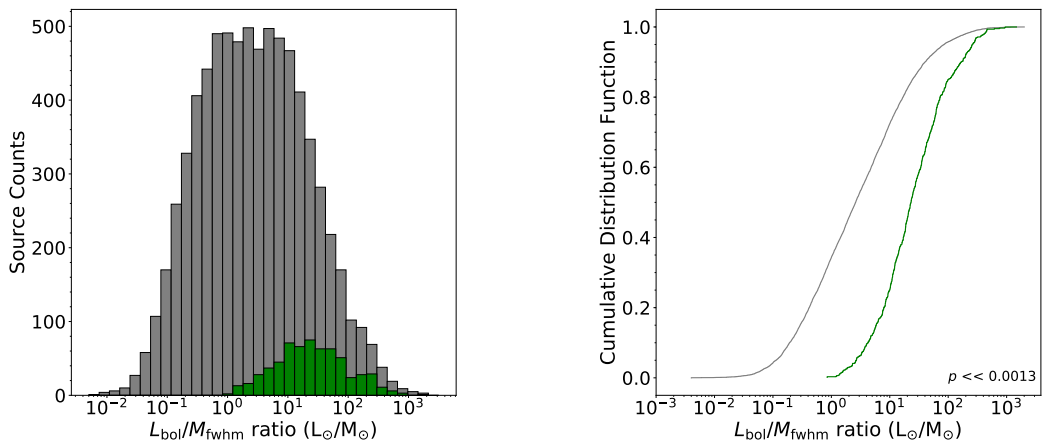


Figure 4.17: $L_{\text{bol}}/M_{\text{fwhm}}$ ratio distributions. The histograms in the upper panel presents the entire distribution of the maser associated clumps and ATLASGAL sample in green and grey respectively, with the corresponding cumulative distribution function shown in the lower panel. The p -value results from a KS test is shown in the lower right of the CDF panel.

age, higher volume densities. The slope for the distance limited samples of clumps and maser associated clumps are both significantly larger but also have much larger uncertainties; they are 2.56 ± 0.06 and 4.37 ± 0.48 , respectively.

4.5.2 $L_{\text{bol}}/M_{\text{fwhm}}$ RATIO CORRELATIONS

Luminosity-mass ratios have proven to be an effective indicator of the evolutionary stages of dense Galactic clumps, as mentioned in Sect. 4.4. As with the previous physical parameters, Fig. 4.17 presents the histogram and distance limited CDF of the $L_{\text{bol}}/M_{\text{fwhm}}$ ratios of the maser associated clumps and the entire ATLASGAL sample. The clumps associated with a maser appear to occupy a distinct region of the parameter space, from $\sim 10^{0.6}$ to $10^{2.2} L_{\odot} M_{\odot}^{-1}$ (central 80%). Therefore, masers are associated with a specific part towards the end, of the evolutionary process of star formation within dense clumps.

As $L_{\text{bol}}/M_{\text{fwhm}}$ ratios can be used to study the evolutionary stages of clumps, the derived parameters can be used to test current theories of maser evolutionary stages. Previous studies have related the luminosity of different maser species with specific stages in the ongoing evolution. The upper panel of Fig. 4.18 presents the distribution of methanol maser luminosity against the parent clump $L_{\text{bol}}/M_{\text{fwhm}}$ ratio with the maser velocity range being shown as a third parameter. There is no significant correlation between the integrated luminosity of methanol masers and evolutionary stage of their corresponding clumps, and there is a large amount of scatter in this distribution. This

scatter may be due to a number of reasons, such as the viewing angle of individual maser sources or their intrinsic periodic variability (approximately an order of magnitude; e.g. Goedhart et al. 2003; Van Der Walt et al. 2009; Durjasz et al. 2019), flux variations of pumping sources, variations in density, abundance and temperature, or the fact that the methanol masers are only present over a very limited range of the protostar’s evolution.

The middle panel of Fig. 4.18 shows how the clump luminosity changes with increasing $L_{\text{bol}}/M_{\text{fwhm}}$ ratio. The expected strong correlation is seen ($L_{\text{bol}} \propto L_{\text{bol}}/M_{\text{fwhm}}^{1.39 \pm 0.08}$, $r_s = 0.85$) as the luminosity of evolving clumps generally determines the $L_{\text{bol}}/M_{\text{fwhm}}$ ratio, due to the mass being relatively constant over the lifetime of a clump. The right panel of Fig. 4.18 presents the distribution of maser and clump luminosities for the distance limited sample (2 to 4 kpc). It can be seen that as the luminosity of a clump evolves, the strength of corresponding maser emission increases.

It is found that $L_{\text{bol}} \propto L_{\text{maser}}^{0.86 \pm 0.09}$ with a Spearman’s rank coefficient of 0.28, this is consistent with the slope reported in Urquhart et al. (2015b) ($L_{\text{bol}} \propto L_{\text{maser}}^{0.93 \pm 0.08}$) that was determined from the peak flux. So there is no significant difference between estimating the maser luminosity from the peak or integrated flux. This relationship is also true for the non-distance limited sample ($L_{\text{bol}} \propto L_{\text{maser}}^{0.90 \pm 0.04}$). The maser and bolometric luminosity are almost linearly correlated, this is consistent with the hypothesis that methanol masers are radiatively pumped (Sobolev et al., 1997). If, as expected, the methanol maser is exclusively associated with massive stars, the linear correlation would suggest that the majority of the bolometric luminosity is the result of a single star within a clump (Walsh et al., 2001).

The distribution found in the lower panel of Fig. 4.18 has also been colour-coded based on clump FWHM mass. As it has been shown in Fig. 4.11 that the mass of clumps does not change during evolution, the lower panel of Fig. 4.18 shows that the most intense masers are associated with the most massive clumps. It is found that $L_{\text{maser}} \propto M_{\text{fwhm}}^{0.50 \pm 0.02}$. It is clear that maser strength is dependent on clump mass, however, this correlation is less significant than the maser dependence on bolometric luminosity. Therefore, it follows that the brightness of masers is affected more by the luminosities of embedded central objects rather than the mass of the surrounding material.

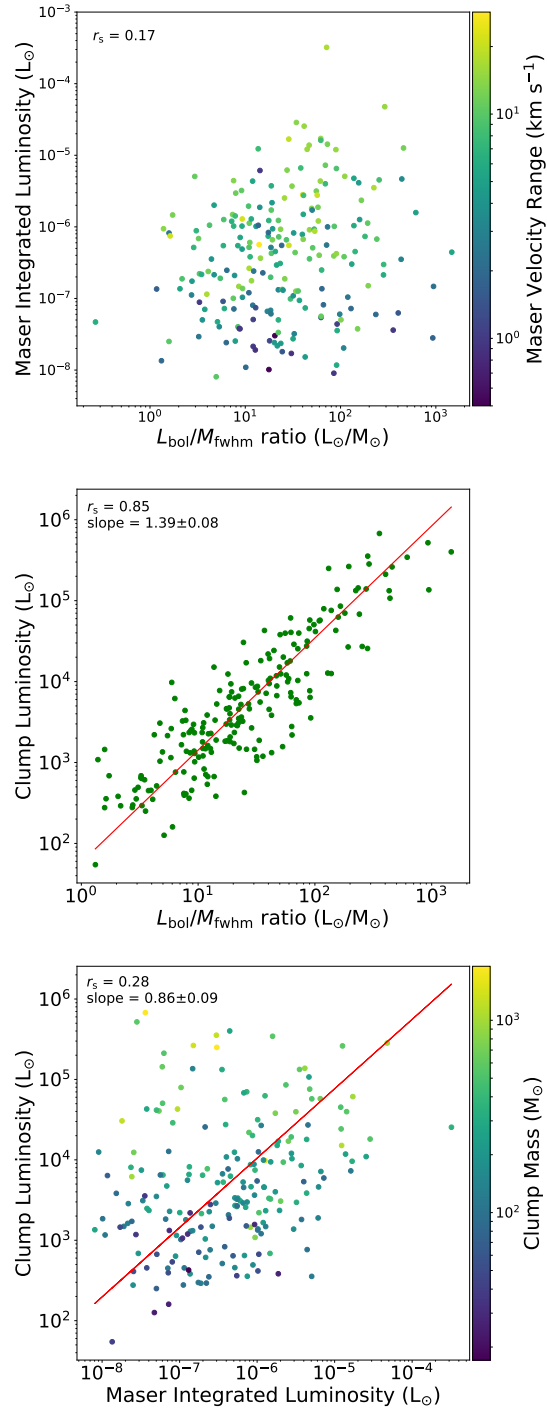


Figure 4.18: The upper panel presents the maser integrated luminosity distribution against clump $L_{\text{bol}}/M_{\text{fwhm}}$ ratio with maser velocity range as a third parameter. The middle panel presents the clump bolometric luminosity distributed against $L_{\text{bol}}/M_{\text{fwhm}}$ ratio. The lower panel presents the clump bolometric luminosity versus the maser integrated luminosity, with clump FWHM mass as a third parameter. All three plots have been fitted using orthogonal distance regression, shown as solid red lines. The corresponding Spearman's rank coefficients are shown in the upper left of each panel, and all associated p -values are less than the confidence threshold ($p < 0.0013$).

4.5.3 LOWER LIMITS ON PHYSICAL CONDITIONS

4.5.3(a) STELLAR AND CLUMP MASS

It has been shown in previous studies that the class II 6.7 GHz maser emission is only associated with intermediate to high mass stars (Minier et al., 2003). These authors performed a search for the class II 6.7 GHz methanol maser towards 123 low-mass young stellar objects and protostellar condensations. The study failed to find any strong methanol masers associated with low-mass star formation, and found a lower protostellar mass limit of $\sim 3 M_{\odot}$, leading them to conclude that methanol masers are exclusively associated with intermediate and high-mass protostellar objects.

The minimum mass of embedded objects in the sample is estimated using the clump luminosity measurements that are mainly attributed to these central objects. Luminosity can be approximated from the mass of a star ($L \sim M^{3.5}$; Kuiper 1938). This minimum luminosity is found to be $10^{2.77} L_{\odot}$ ($590 L_{\odot}$). Using this value the corresponding minimum mass of an embedded object is estimated to be $\sim 6 M_{\odot}$, assuming that the luminosity is primarily coming from a single source (Walsh et al., 2001). The uncertainty in this value is dominated by the error in the derived bolometric luminosities, a value of $\sim 42\%$ (see Sect. 4.4.6). Therefore, the uncertainty on the lower mass limit is found to be $\sim 2.5 M_{\odot}$. These results strongly support the finding of Minier et al. (2003).

4.5.3(b) VOLUME DENSITY

Section 4.4 describes how the radii and masses of clumps have been recalculated in order to remove any temperature bias that may be present within the observations. Furthermore, new values for volume density have also been calculated to align with these new radius and mass values. In general, volume densities for maser associated clumps lie between 10^4 and 10^6 particles per cm^3 as seen in the lower left panel of Fig. 4.10. Figure 4.19 presents the distribution of clump volume density against the corresponding $L_{\text{bol}}/M_{\text{fwhm}}$ ratios for the distance limited sample, with the entire ATLASGAL and the maser associated samples shown in grey and green respectively. Given that both the mass and radius of the clumps have been shown to be constant during evolution, it should follow that volume density is also constant. There is a small negative correlation between these two parameters, as confirmed by a Spearman's rank coefficient test, with an r_s value of -0.14 . However, this is likely due to an observational bias as the observations are less sensitive to low volume densities at low temperatures (the sensitivity limit is shown but the dash-dotted curve in Fig. 4.19). As a consequence,

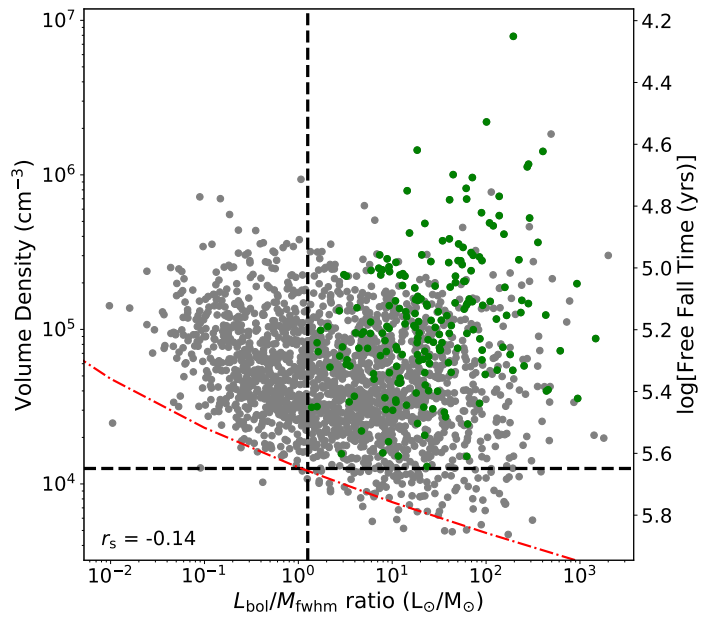


Figure 4.19: Distance limited sample of volume density versus $L_{\text{bol}}/M_{\text{fwhm}}$ ratio. The entire ATLASGAL sample is shown in grey with the maser associated sample shown in green, the lower limits of each parameter (calculated from the central 80% of the data) are shown as dotted black lines, with the observational sensitivity limit of ATLASGAL shown as a red dash-dotted line. The results from a Spearman’s correlation test for the full ATLASGAL sample is shown in the lower left of the panel, and the corresponding p -value is less than the significance threshold.

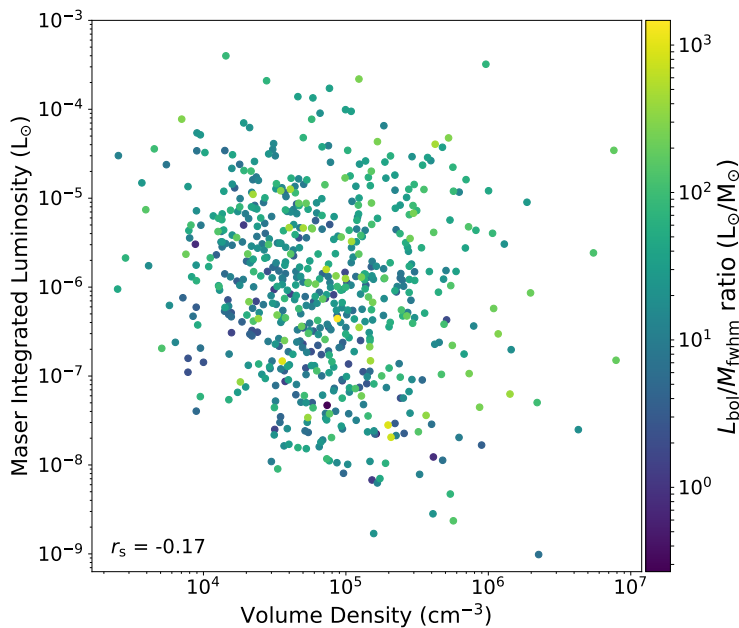


Figure 4.20: Distance limited sample of methanol maser luminosity versus volume density with the data coloured based on the $L_{\text{bol}}/M_{\text{fwhm}}$ ratios. The results from a Spearman’s correlation test is shown in the lower left of the panel.

ATLASGAL is more sensitive to more evolved sources.

It appears that the maser associated clumps occupy a well defined region in this parameter space, $L_{\text{bol}}/M_{\text{fwhm}}$ ratio values of $\geq 1 L_{\odot} M_{\odot}^{-1}$, as discussed above (see Sect. 4.5.2), and volume densities above $\sim 10^{4.1} \text{ cm}^{-3}$. This suggests that there is a lower density limit for the production of maser emission and that there is a clear maser turn on stage during protostellar evolution. It may be that the measured mass of a clump is not as important in the production of maser emission as the volume density, as shown by the middle right panel of Fig. 4.10. This lower limit on volume density is found to be $10^{4.1} \text{ cm}^{-3}$, and any clump with a value lower than this, is unlikely to produce maser emission. Masers associated with compact, dense clumps have a specific turn-on point and must be driven by an intermediate to high-mass protostar.

The maser luminosities have also been tested against the corresponding volume densities. Figure 4.20 shows the relationship between volume density and the integrated maser luminosity. It can be seen from the distribution of these parameters that there is a weak correlation between them ($r_s = -0.17$; p -value $\ll 0.0013$); this is consistent with the findings of Urquhart et al. (2013) and Urquhart et al. (2015b). Breen et al. (2010) and Breen et al. (2011) also investigated the correlation between the peak and integrated luminosities of the 6.7 GHz methanol maser transition and reported trends of decreasing volume density with increasing maser luminosity ($r_s = -0.46$ and -0.39

for the peak and integrated luminosities for samples sizes of 113 and 46 respectively). While these previous studies and the work presented here both find negative correlations within this distribution, the result determined here is likely to be more robust due to the significantly larger sample (613 sources).

4.5.4 MASER LIFETIMES

The lifetime of the methanol maser phase has been investigated in a number of previous studies (e.g. Codella et al. 2004; Van Der Walt 2005). In this subsection the much larger sample is used in an effort to provide a more concrete estimate on this maser lifetime. It is likely that the maser lifetime is not a constant across every single star forming region of the Galaxy and is dependent on a number of factors, including the mass of the central object, clump volume density, methanol abundance and the amount of ionising radiation over time, although this large sample should provide strong statistics to calculate a firm lifetime for maser emission.

Free fall times have been derived for each clump in the sample with a corresponding volume density measurement (see Sect. 4.4). These free fall times range from $\sim 2 \times 10^4$ to 10^6 yrs, and masers will exist for a portion of these time scales. It is likely that maser emission is seen once a relatively efficient pumping mechanism is formed and will continue to exist until an UC HII region forms and begins to disrupt the local environment. Therefore, to calculate how long this maser phase lasts, the ratio of the number of maser clumps against the total number of dense clumps within the ATLASGAL sample has been taken to derive a clump ratio at free fall time intervals. These ratios can then be multiplied by the clump free fall times to give an absolute value for statistical lifetime for the maser phase at specific clump volume densities (i.e. $t_{\text{stat}} = \frac{N_{\text{maser}}}{N_{\text{all}}} \times t_{\text{ff}}$).

Figure 4.21 presents how these lifetimes change through the volume density parameter space, the errors on this plot are derived using Poisson statistics ($\sim 1/\sqrt{N}$). Volume densities appear to be complete above $10^{4.5} \text{ cm}^{-3}$ (see Fig. 4.20), and therefore, only the clumps with a density value above this threshold are considered.

The lifetimes range between 3×10^4 and 3.6×10^4 years, with a mean error of $\sim 10\%$. The average maser statistical lifetime is found to be $\sim 3.3 \times 10^4$ years, with a standard deviation of 0.23×10^4 years. While volume density is dependent on distance, because the statistical lifetimes depend on the ratio between two volume density samples, the overall calculation for these lifetimes is distance independent.

As the radii of dust clumps are constant across their lifetime, volume density is dependent on the clump mass, these results show that the most dense clumps, and therefore, the most massive will have associated maser emission with the shortest life-

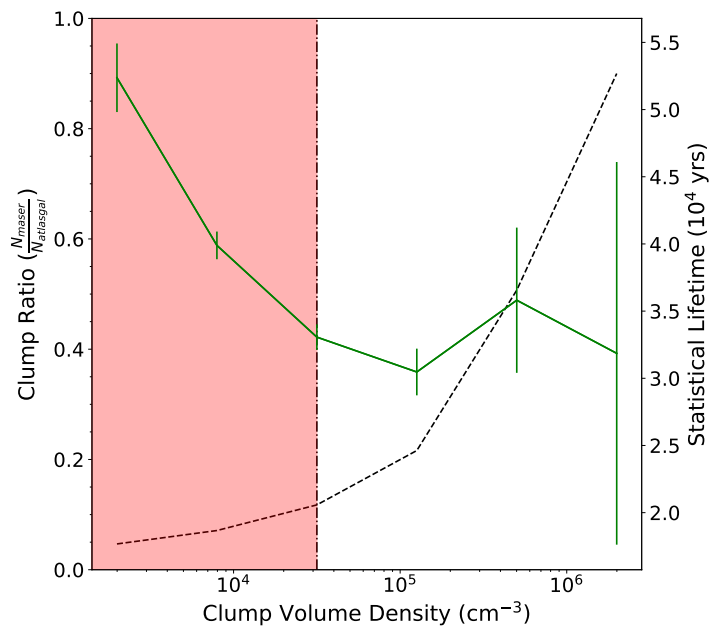


Figure 4.21: Plot presenting the clump ratio ($\frac{N_{\text{maser}}}{N_{\text{all}}}$), and statistical lifetime as a function of clump volume density. The black dotted line shows the increasing number of maser associated clumps with respect to volume density, whereas the solid green line presents the drop in statistical lifetime as volume density increases. The shaded region represents the parameter space where the sample is incomplete. Errors shown are derived from Poisson statistics.

times. This falls within the currently accepted theory whereby denser clumps will evolve on much shorter timescales and will quickly produce HII regions, disrupting masing material much faster than lower density clumps. The least dense and massive clumps take longer to produce HII regions and so, potentially, the conditions for maser emission lasts for a greater period of time. The proportion of clumps with maser emission increases significantly with density (see dashed line in Fig. 4.21), and the majority of masers are associated with YSOs (63%). Therefore, it is likely that pre-stellar and protostellar stages are extremely short-lived in high-density clumps and so are less observed, resulting in a low association rate between protostellar objects and methanol maser sources.

Van Der Walt (2005) undertook a statistical study to estimate the lifetimes of the class II 6.7 GHz methanol masers. This estimate was based on the current known number of masers at the time. This work applied a completeness correction to this number to estimate the potential number of maser detections that should exist within the Galaxy. At the time only 519 methanol masers sources were known, and he estimated that the minimum number of maser detections present across the Galaxy should be 850, this value is slightly lower than the number of maser sites detected within the MMB survey. Van Der Walt (2005) found that the maser lifetimes should lie between 2.5×10^4 and 4.5×10^4 years, the variation within this result was mainly due to the different initial mass functions used in the analysis.

The lifetimes determined from the ratio of maser associated and unassociated clumps, and the free-fall times lie within the range calculated by Van Der Walt (2005). Our results, therefore, provide strong observational support for theoretical predictions of the class II 6.7 GHz methanol maser lifetimes.

4.5.5 EMBEDDED EVOLUTIONARY STAGES

We have already found that the methanol maser phase covers a relatively narrow range in the evolution of clumps (see Fig. 4.17). It is likely that the masers are associated with nearby young massive embedded objects (Norris et al., 1993, 1998; Lee et al., 2001) that themselves cover a range of evolutionary stages. The ATLASGAL catalogue of dense clumps is likely to include the full range of evolutionary stages and comparing the properties of the full ATLASGAL sample with those associated with methanol masers can provide a way to observe how the physical parameters of dense clumps change during the “maser phase”.

The ATLASGAL survey has classified each detected clump based on the most likely associated embedded object. Clumps have been classified as one of the following: quiescent, protostellar, young stellar object and HII region (see Sect. 4.1 Urquhart

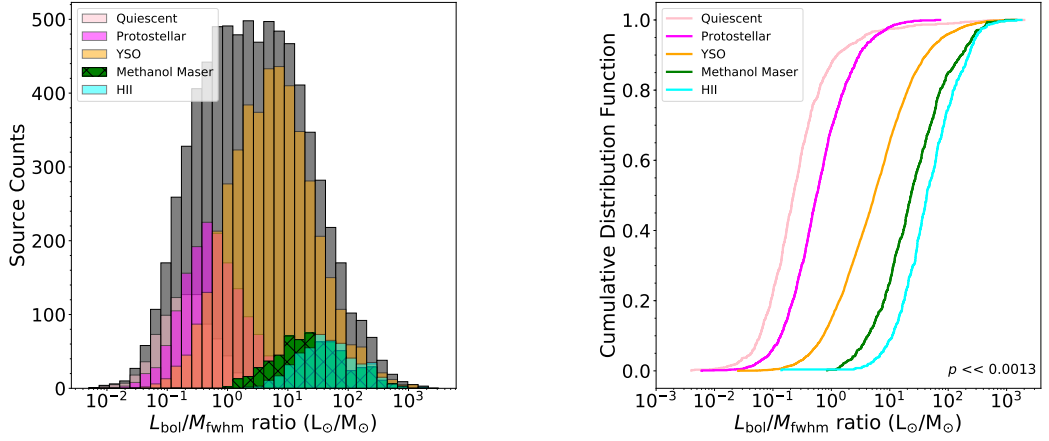


Figure 4.22: The left panel presents a histogram of $L_{\text{bol}}/M_{\text{fwhm}}$ ratios for each evolutionary stage defined by the ATLASGAL survey, with the entire ATLASGAL sample being shown in grey. Maser associated clumps are shown with black hatching to clearly show where these objects lie within this parameter space. The right panel presents the cumulative distribution function for this histogram, for a distance limited sample (2 to 4 kpc). Legends with evolutionary classification are shown in the upper left of each panel.

et al. 2018 for a complete description of the evolutionary sequence). One of the aims is to evaluate where sources with maser emission fit within this classification scheme. Figure 4.22 presents a histogram and cumulative distribution function of $L_{\text{bol}}/M_{\text{fwhm}}$ ratios based on the clumps' evolutionary classification. The expected distribution is seen for the different classifications; quiescent clumps have the lowest $L_{\text{bol}}/M_{\text{fwhm}}$ ratios, which increase when the protostellar object forms and continue to increase as more material is accreted onto the protostar and its luminosity increases. As the bolometric luminosities increase the peak of the SED shifts to shorter wavelengths and when it becomes detectable at mid-infrared wavelengths they are classified as young stellar objects (YSO). The highest $L_{\text{bol}}/M_{\text{fwhm}}$ ratios are attributed to HII regions, which are signposts of the final embedded stages in the formation of the highest-mass stars ($> 10 M_{\odot}$). This distribution can be more clearly seen in the CDF (see right panel of Fig. 4.22).

The “maser phase” can be defined using the luminosity-mass ratios of the dense dust clumps. The methanol masers are associated with $L_{\text{bol}}/M_{\text{fwhm}}$ ratios of between $10^{0.6}$ and $10^{2.2} L_{\odot} M_{\odot}^{-1}$ and therefore occupy a distinct part of this parameter space as discussed in Sect. 4.5.2. The maser $L_{\text{bol}}/M_{\text{fwhm}}$ distribution also indicated (green histogram and curves in the plots shown in Fig. 4.22). Generally, the maser associated clump $L_{\text{bol}}/M_{\text{fwhm}}$ ratios overlap with those of protostellar and YSO stages but are most similar to that of the HII region associated clumps. This is expected, as masers

are thought to turn on once a protostellar source of sufficient mass has been formed ($\gtrsim 6 M_{\odot}$; Minier et al. 2003 and Sect. 4.5.3(a) of this study), and continue until the physical conditions required are disrupted when the feedback from the central source (i.e. expanding HII regions and dispersion of the host clump). This hypothesis is supported by the results reported by a number of studies that have investigated the association between methanol masers and UC HII regions (e.g. Walsh et al. 1997, 1998; Van Der Walt et al. 2003). The CDF of the $L_{\text{bol}}/M_{\text{fwhm}}$ methanol maser associated clumps (shown in the right panel of Fig. 4.22) further provides strong evidence for this hypothesis.

Walsh et al. (1998) found that there was a $\sim 20\text{--}25\%$ coincidence of 6.7 GHz masers and radio continuum emission, which would suggest that the conditions required for the masers emission persist for a short period after the formation of the UC HII region. A similar association rate has also been reported in other studies (i.e. Hu et al. 2016). Where there is an association, it is likely that the HII region is not yet developed enough to disrupt the masing material. Given the mean lifetime of the methanol maser is $\sim 3 \times 10^4$ yrs this period is likely to be ~ 7500 yrs.

Excluding the Galactic centre region ($5^{\circ} > \ell > 355^{\circ}$), the full sample of matched masers presented in this study, 855 maser emission sources, has been used to evaluate the association rate between methanol masers and HII regions. For the 855 maser sources, 252 are associated with a clump that harbours a HII region, either ultra compact or extended, as identified by the ATLASGAL survey follow up observations. Within the ATLASGAL survey, 875 dust continuum sources are found to be associated with a HII region and therefore 29% of HII regions are also associated with a methanol maser. Figure 4.23 presents a Venn diagram of the maser - HII region matches from Walsh et al. (1998) and this work. The association rate between masers and HII regions found in this study (30%) is slightly higher than that found by Walsh et al. (1998) (20-25%), and more similar to the association rate presented in Hu et al. (2016).

Breen et al. (2010) defined an evolutionary sequence based on 1.2 mm emission, 6.7 GHz methanol maser emission and 8 GHz radio continuum emission. The results presented in this work support the Breen et al. (2010) model and, using the $L_{\text{bol}}/M_{\text{fwhm}}$ ratio, it is possible to put a quantitative result to their sequence: (i) Clumps initially begin with no detectable maser or radio continuum emission, (ii) once a clump has an $L_{\text{bol}}/M_{\text{fwhm}}$ ratio of $\sim 10^{0.6} L_{\odot} M_{\odot}^{-1}$, 6.7 GHz maser emission turns on and these clumps must also have a protostellar core of $> 6 M_{\odot}$ (Sect. 4.5.3) and volume density above $10^{4.1} \text{ cm}^{-3}$, (iii) as the $L_{\text{bol}}/M_{\text{fwhm}}$ ratio approaches a value of $\sim 10^{0.65} L_{\odot} M_{\odot}^{-1}$, radio continuum emission produced from HII regions is seen in conjunction with maser

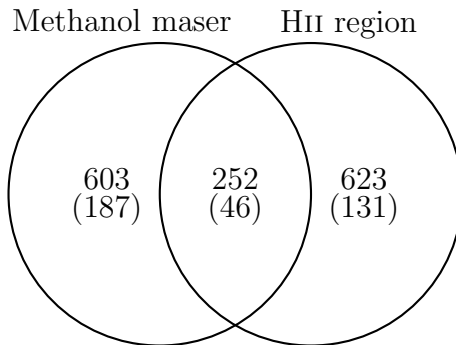


Figure 4.23: Venn diagram presenting the overlap between methanol masers and HII regions. Values determined by Walsh et al. (1998) are shown in brackets and they find 20% of methanol masers are coincident with HIIs while a larger proportion (25%) of HIIs are associated with methanol masers. Results from this study show these values to be 30% and 29% respectively.

emission, (iv) as $L_{\text{bol}}/M_{\text{fwhm}}$ ratios increase towards $10^{2.2} L_{\odot} M_{\odot}^{-1}$, maser emission begins to decline as the effects of HII regions begin to disrupt the local environment, and the HII regions themselves become extended. Breen et al. (2011) demonstrated that, during this evolutionary sequence, the integrated luminosity and velocity ranges of the 6.7 GHz methanol maser increase, which is supported by this work. However, due to the amount of scatter in these distributions, the maser luminosity and velocity range is not a particularly useful indicator of evolution.

4.6 CONCLUSIONS

This work has compiled the largest and most representative sample of class II 6.7 GHz methanol maser associated dust clumps to date. In this latest study, 257 out of 265 methanol maser sources in the region $60^{\circ} > l > 20^{\circ}$ have been matched to submm emission in either JPS or ATLASGAL. In total, 958 out of 972 methanol maser sources identified by the MMB survey across the Galactic plane have been matched to submm dust emission, an association rate of 98.6%. Two of the unmatched masers lie beyond the coverage of both JPS and ATLASGAL, with the remaining 12 appearing to have no corresponding submillimetre emission.

Physical parameters (sizes, masses, densities, luminosities, virial parameters, statistical lifetimes) have been derived for each maser associated clump for which a distance measurement is available and correlations have been investigated. A summary of the main findings of this study are listed below:

1. The radii, masses and volume densities of clumps within the ATLASGAL survey have been recalculated, and it is found that previous effects seen during the evolution of star-forming clumps (increasing radius, mass and density) can be attributed to an observational bias. By using the FWHM values for these parameters, this bias has been removed and these physical properties are found to remain constant across the lifetime of individual clumps. Therefore, the mass and radius of clumps, and by extension density, are independent of evolutionary stage and these properties are determined at the earliest stages in the formation of these dense clumps.
2. There is an almost ubiquitous association between the 6.7 GHz methanol maser and dust continuum sources, with 958 (99%) of sources within the MMB survey catalogue being matched to either 850 or 870 μm emission across the Galactic plane ($60^\circ \geq \ell \geq 186^\circ$). This is strong evidence for masers being tightly associated with star formation, and in nearly all cases the clumps show evidence of being in an advanced stage of star formation, due to their associations with either a YSO or HII region ($\sim 95\%$).
3. The bolometric luminosities of clumps has been found to be proportional to the luminosities of associated maser sources with a power-law exponent of order unity ($L_{\text{bol}} \propto L_{\text{maser}}^{0.86 \pm 0.09}$). This provides strong support for the currently accepted theory that the 6.7 GHz methanol maser transition is radiatively pumped. Furthermore, the linear correlation would also suggest that most of the bolometric luminosity can be attributed to a single star that is driving the methanol maser.
4. Using the bolometric luminosities of embedded objects associated with maser emission, a minimum mass for stellar objects associated with methanol maser emission has been derived. This limit is found to be $\geq 6 M_\odot$, which is consistent with previous studies that have concluded that these masers are exclusively associated with intermediate and high-mass star formation (Minier et al. 2003).
5. The distribution of the masses of clumps associated with methanol masers is indistinguishable from the general population of dense clumps and so mass alone is not an important parameter in determining the current or future occurrence of a methanol maser. However, the radius and density of maser associated clumps are

significantly different from the values determined for the full sample of clumps, but as radius is shown not to alter during evolution, it is likely that the density of clumps is the most significant indicator of current or future maser emission. Our results suggest that there is a lower density threshold below which no masers are found ($n(\text{H}_2) \geq 10^{4.1} \text{ cm}^{-3}$), and could indicate that intermediate and high-mass star formation, and maser emission, is inefficient below this threshold.

6. The evolutionary sequence for clumps spans over five orders of magnitude of the $L_{\text{bol}}/M_{\text{fwhm}}$ ratio parameter space (0.01 to $10^3 L_{\odot} M_{\odot}^{-1}$). The maser associated clumps occupy a relatively narrow region (~ 1.5 orders of magnitude) within this parameter space. Therefore, there is a well defined maser turn-on and turn-off stage in the evolutionary process of high-mass star formation. The low association rates with protostellar objects is likely to be linked to the minimum stellar mass required to drive the maser and the time needed to accrete sufficient material to attain this mass.

7. The free-fall times and the fraction of clumps associated with a methanol maser have been used to estimate a statistical lifetime of $\sim 3.3 \times 10^4$ years for the maser phase. There is a 30% coincidence between masers and HII regions, and maser emission persists for a short time after the creation of an HII region, this time period is found to be ~ 7500 years. The $L_{\text{bol}}/M_{\text{fwhm}}$ ratios of maser associated clumps, and HII region associated clumps supports previous work in the development of an evolutionary sequence based on maser and radio continuum emission in the Galactic plane (Breen et al., 2010).

Overall, these results support previous works in developing an evolutionary sequence for methanol maser emission by using the physical parameters of associated clump material. The distinct region occupied by maser associated clumps in various parameter spaces, ($L_{\text{bol}}/M_{\text{fwhm}}$ ratio, volume density and lifetime) provide a more concrete basis for the maser evolutionary "straw model" outlined by Ellingsen (2007) and refined by Breen et al. (2010).

CHAPTER 5

INVESTIGATING THE EVOLUTIONARY STAGES OF STAR FORMATION THROUGH VARIOUS MASER SPECIES

This Chapter aims to directly continue the work presented in Chap. 4. This work will investigate the relationships between further maser species and the ATLASGAL catalogue as presented in Urquhart et al. (2018). The maser species of interest are that of the 12.2 GHz methanol maser, the 22.2 GHz water maser and the four hydroxyl maser emission lines at 1612, 1665, 1667, 1720 MHz. This will also be combined with the results of the 6.7 GHz methanol maser study as found in Chap. 4.

While it is known that the 6.7 GHz methanol maser is exclusively associated with massive star formation, there also exist other maser species that are known to be associated with regions of star formation, such as the class II 12.2 GHz methanol maser, the 22.2 GHz maser emission produced by water (H_2O ; Cheung et al. 1969), and the four base transitions of hydroxyl (OH ; Weinreb et al. 1963) at 1612, 1665, 1667 and 1720 MHz (see Sect. 1.5.3).

Observations of water maser indicate that these are found in outflows as well as circumstellar disks of both low- and high-mass young stellar objects (Claussen et al., 1996; Codella et al., 2004; Titmarsh et al., 2014, 2016) and so are associated with regions of ongoing star formation. Hydroxyl masers are known to trace a number of

different environments, such as expanding shells of evolved stars (Wilson and Barrett, 1968; Elitzur et al., 1976), star formation regions (Argon et al., 2000; Qiao et al., 2014, 2016) and supernovae remnants (Claussen et al., 1999; Caswell, 2004), as mentioned in Sect. 1.5.3.

As these three maser species are capable of tracing different physical conditions and processes, studies have been undertaken to investigate the relationship between the masers and environments where high-mass stars born (e.g. Beuther et al. 2002; Breen et al. 2010; Breen and Ellingsen 2011; Urquhart et al. 2013, 2015b). As mentioned in Sect. 4.1, Ellingsen (2007) presented a “straw man” model for the evolution and relative timescales of different maser species (water, methanol, hydroxyl) within regions of star formation. This model was further refined by Breen et al. (2010) who estimated relative lifetimes for each of the maser species. The sequence of events as described by this model state that during star formation, class I (collisionally pumped) methanol masers occur first, likely found in accretion disks around young stellar objects, followed by the appearance of water masers, produced in the post-shocked gas due to outflows associated with these objects. Class II (radiatively pumped) masers are then produced in accretion disks due to the thermal output of the natal star and finally, hydroxyl masers are seen towards developing HII regions, and as these HII regions evolve, they disrupt and disperse their environments, destroying the conditions necessary for any type of maser emission to exist, as indicated by the decreased detection rate of all maser types in the late evolutionary phases.

This Chapter will extend the work of Chap. 4 by investigating the physical properties of dense Galactic clumps associated with each maser species, for which catalogues have been produced from a number of Galactic surveys. Breen et al. have produced a number of MMB follow-up observations towards sites of the 6.7 GHz masers, searching for the class II 12.2 GHz methanol maser transition (Breen et al., 2012a,b, 2014, 2016), and catalogues of water and hydroxyl masers have been produced by the H₂O southern Galactic Plane Survey (HOPS; Walsh et al. 2011) and The HI/OH/Recombination line survey (THOR; Beuther et al. 2016b) respectively. Along with investigating the physical properties of maser associated clumps, statistical lifetimes for each of the masers species will be derived and their positions in the evolutionary timescales of star formation will be identified.

5.1 SURVEY DESCRIPTIONS

Descriptions of the ATLASGAL, HOPS and MMB surveys are given in Chaps. 3 and 4. While the HOPS and ATLASGAL surveys will not be explained further, extra context on the MMB survey is given, specifically information that pertains to the 12.2 GHz methanol maser follow-up observations. The THOR survey catalogue is also utilised in this study and is described here.

5.1.1 THE HI/OH/RECOMBINATION (THOR) LINE SURVEY

The HI/OH/Recombination line survey of the inner Milky Way (Beuther et al., 2016a) has surveyed $66.8^\circ \leq \ell \leq 14.5^\circ$ and $|b| < 1.25^\circ$ of the Galactic plane using the Karl Jansky Very Large Array (VLA) in its C-array configuration. The THOR survey has observed a number of different spectral lines, including the HI 21 cm and nineteen of the $Hn\alpha$ radio recombination lines, as well as continuum emission between 1 and 2 GHz (Bihr et al., 2016). The survey has spatial resolutions of ~ 12.5 to $19''$, with a spectral resolution of 1.5 km s^{-1} .

Most recently, THOR has produced an unbiased catalogue of the four OH maser emission lines at 1612, 1665, 1667 and 1720 MHz (Beuther et al., 2019). The catalogue comprises of OH maser sources in the northern hemisphere, tracing a number of different astronomical phenomena. The 1612 MHz are associated with evolved stars, whereas the 1665 and 1667 MHz emission are seen towards regions of star formation. The 1720 MHz maser line is generally found towards supernova remnants. However, it can be seen that none of these associations are exclusive and all four transitions can be found within different environments and even toward the same region (Caswell et al., 2013; Walsh et al., 2016).

5.1.2 THE METHANOL MULTIBEAM (MMB) SURVEY

Breen et al. (Breen et al., 2012a,b, 2014, 2016) have produced a number of MMB follow-up observations towards sites of the 6.7 GHz masers, searching for the class II 12.2 GHz methanol maser transition. The 12.2 GHz maser is the strongest and most widespread methanol maser line after the 6.7 GHz transition, and over the same coverage as the MMB survey ($60^\circ \geq \ell \geq 186^\circ$), 431 12.2 GHz masers have been detected. Breen et al. concluded that the 12.2 GHz maser occurs within star-formation regions at a slightly later stage of evolution than regions that are only associated with the 6.7 GHz transition and estimated the lifetime of this maser emission to be between 11 300 and

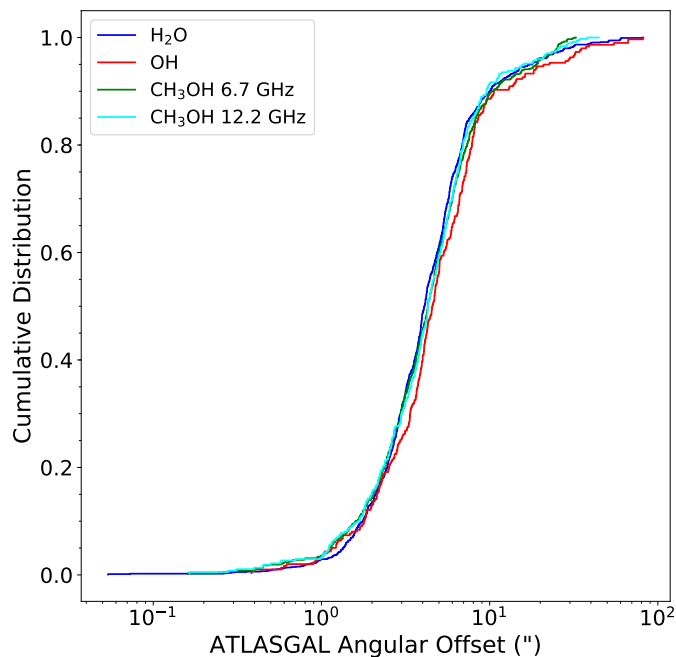


Figure 5.1: A cumulative distribution function of the maser-ATLASGAL angular offsets. Each coloured line represents a different maser species as shown by the legend in the top left of the plot.

20 400 years. It is worth noting that as the 12.2 GHz maser observations are targeted towards known positions of 6.7 GHz masers, this sample may not be regarded as an independent sample.

5.2 MASER ASSOCIATIONS

This study will only focus on the Galactic coverage between $60^\circ > |\ell| > 5^\circ$ and $|b| < 1.5^\circ$, the same coverage as Urquhart et al. (2018), and therefore, this study will have accurate determinations on the physical properties of clumps associated with any maser transition.

By using the catalogues of the surveys mentioned in the previous section, this work has attempted to associate multiple maser transitions to dense clumps as found in the ATLASGAL survey. These maser transitions are the 6.7 GHz & 12.2 GHz methanol maser, 22.2 GHz water maser and the four hydroxyl maser emission lines at 1612, 1665, 1667 and 1720 MHz. The matching results already provided in Urquhart et al. (2013, 2015b) and Chap. 4 are used for the 6.7 GHz methanol maser emission.

When mentioning a specific maser species or transition in this study, the corre-

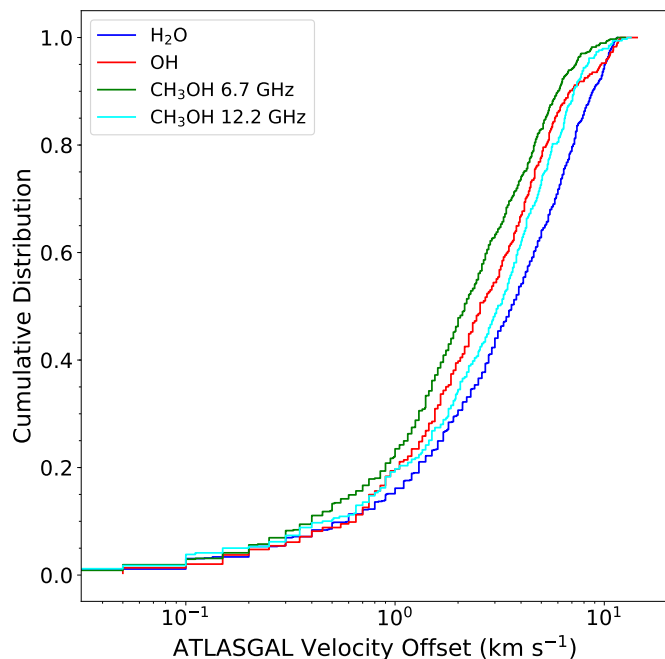


Figure 5.2: A cumulative distribution function of the maser-ATLASGAL velocity offsets. Each coloured line represents a different maser species as shown by the legend in the top left of the plot.

sponding frequency of that maser will always be given, and the term “maser” used independently will refer to all the maser transitions.

5.2.1 SPATIAL MATCHING

Initial matches were identified by using a $90''$ radius between maser emission and the $870\ \mu\text{m}$ peak dust emission. This radius is the 3σ value of the effective radius distribution for ATLASGAL sources and so 99.7% of dust continuum sources have a radius of less than this size. Images have been created from the ATLASGAL $870\ \mu\text{m}$ emission maps, so that each match could be confirmed visually. A match was confirmed if the maser source was within the 3σ boundary of the $870\ \mu\text{m}$ emission and all masers found beyond this boundary have been removed from any further analysis as these are unlikely to be associated with star formation. It is found that 429 OH, 359 water and 392 12.2 GHz masers sites are spatially coincident with dust emission. A cumulative distribution function of the angular offsets for each of the maser species can be found in Fig. 5.1. It can be seen from this figure that the majority of masers ($\sim 90\%$) lie within $10''$ of a dust continuum peak, and since the majority of star formation is concentrated towards the highest column density regions in the centre of clumps this provides further confirmation that the masers are associated with star formation.

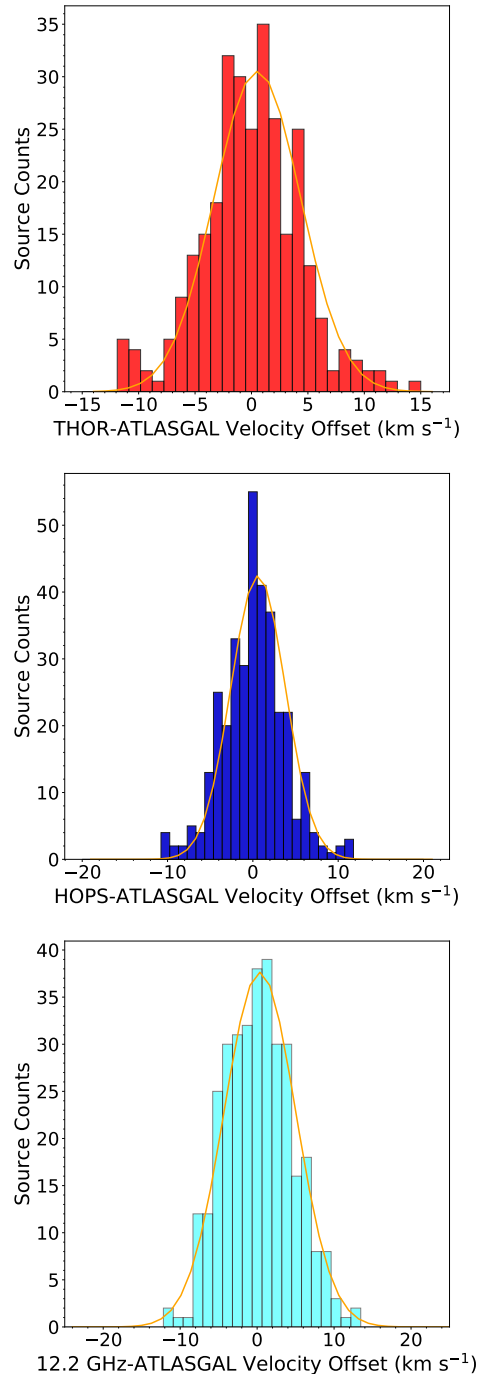


Figure 5.3: Histograms presenting the velocity offsets between the median maser velocities and the ATLASGAL molecular line velocities. The panels present the hydroxyl, water and 12.2 GHz methanol maser velocity distributions in the upper, middle and lower panels respectively. A Gaussian fit has been found for each histogram and is shown as the solid yellow lines in each panel.

Table 5.1: Total matches for each maser species and the ATLASGAL catalogue between Galactic longitudes $60^\circ > \ell > -60^\circ$, where all matches are below the 3σ threshold in both positional and velocity space. The percentage of associated dust clumps with each survey coverage is also given. Errors have been calculated using Poisson statistics ($\sim 1/\sqrt{N}$).

Maser Transition	Maser-Dust Associations	Percentage of associated dust clumps
CH ₃ OH 6.7 GHz	839/918 ($91 \pm 0.9\%$)	8.5%
CH ₃ OH 12.2 GHz	340/414 ($82 \pm 1.9\%$)	3.2%
H ₂ O 22.2 GHz	345/614 ($56 \pm 2.0\%$)	2.9%
OH 1612 MHz	38/1065 ($4 \pm 0.6\%$)	0.3%
OH 1665 MHz	175/306 ($57 \pm 2.8\%$)	1.2%
OH 1667 MHz	53/142 ($37 \pm 4.1\%$)	0.3%
OH 1720 MHz	28/53 ($53 \pm 6.9\%$)	0.2%

5.2.2 VELOCITY OFFSETS

Molecular line velocities of the dense clumps are available for the majority of masers and for a large portion of the ATLASGAL survey. These measurements are used to examine the correlation between the masers and the dense clumps to confirm their associations. The difference between maser median velocity and clump median velocity have been calculated for all of the maser species that are spatially coincident and the histograms of these distributions can be found in Fig. 5.3. To confirm this maser associated sample, only clumps with a maser source that has a velocity difference of less than 3σ have been included, which is calculated by fitting the velocity difference distributions with a Gaussian model. The Gaussian fits appear to be a reasonable model for all of the velocity distributions.

The 3σ values for the different distributions are 11.56, 11.92 and 13.89 km s⁻¹ for the H₂O, OH and 12.2 GHz methanol masers respectively. These values, for each maser class, are used to constrain this sample selection further, as masers with a high velocity offset to the spatial coincident clumps may be unassociated with the clumps themselves and the star formation processes.

5.2.3 TOTAL MATCHED SAMPLE

This study has matched a number of different maser species to dense clumps across the Galaxy as identified by the ATLASGAL survey. The sample has been constrained using the positional and velocity offsets as previously described. The number of maser associations for each maser transition can be found in Table 5.1.

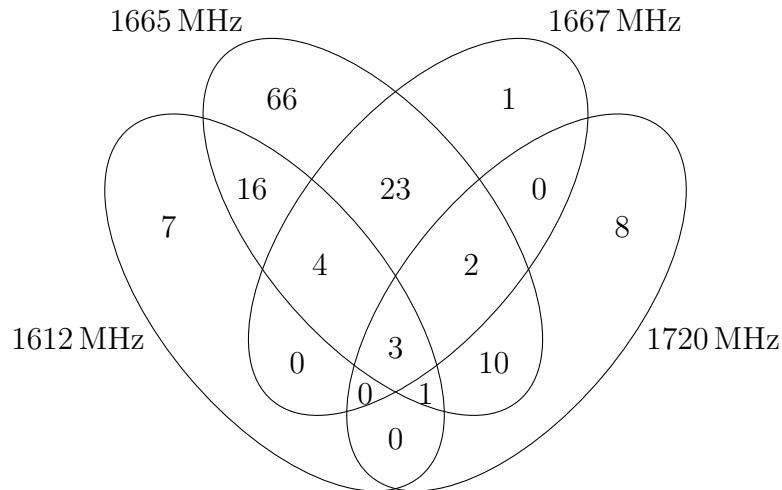


Figure 5.4: A Venn diagram presenting the associations between the different transition lines of the hydroxyl masers and the ATLASGAL catalogue.

There are no differences found between the spatial offsets between each maser species and the average offset between any maser species and the peak dust emission is $\sim 6''$ with the 90% range of the maser samples having offsets between $1.7''$ and $10.3''$. The absolute velocity differences for all of the maser species range between $2.8\text{--}4.3\text{ km s}^{-1}$ with the 6.7 GHz maser species having the smallest average velocity offset of 2.8 km s^{-1} .

Out of the 807 hydroxyl maser sites, 294 have been matched to 141 individual dense clumps identified by the ATLASGAL survey, that are likely to be associated with high-mass star formation. This is an association rate of 19% with 2.1 maser spots per clump on average. The majority of clumps contain only 1 maser source (66/141) and with 67 clumps containing between 2 and 4 sources. However, there exists 4 clumps with 5 maser sources and also another 4 which contain more than 5 maser sources. As the average number of masers per clumps is 2.1, only 3 of these 8 sources have a significantly large number of masers (AGAL030.703-00.067 & AGAL031.412+00.307 with 9 and AGAL030.823-00.156 with 8; these 3 regions are associated with the W43 star forming complex) which could be of interest.

As the THOR survey covers all four hydroxyl emission lines, the 1612, 1665, 1667 and 1720 MHz transitions are found to have corresponding association rates with 141 dust clumps of 4, 57, 37, 53% respectively. Figure 5.4 presents a Venn diagram of the matches between clumps and the four different hydroxyl transition lines. Out of the 141 dust continuum sources, 125 are associated with a 1665 MHz maser, with only 24 dense clumps containing a 1720 MHz maser. ATLASGAL sources that are only associated with a hydroxyl maser are also only associated with either the 1612

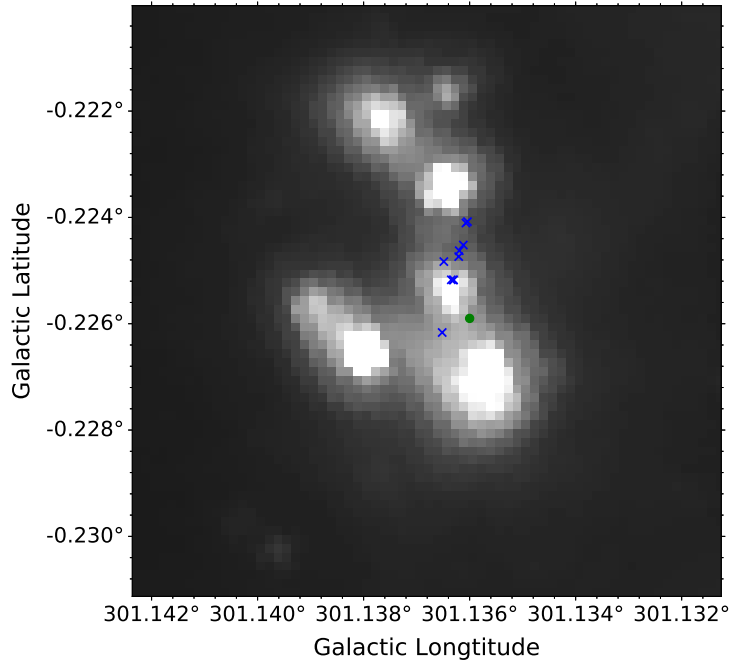


Figure 5.5: An example GLIMPSE $8\ \mu\text{m}$ image of the region G301.136-00.226. The positions of water masers have been overplotted as blue crosses and methanol masers as green filled circles.

or 1665 MHz transitions. Furthermore, the majority of hydroxyl masers (96%) to be associated with either a YSO or HII region as identified by the ATLASGAL survey, there exists 8 clumps which are coincident with a hydroxyl maser (1665 or 1667 MHz) and a protostellar object.

This study has matched 978 of water maser spots (345 maser sites), presented in Walsh et al. (2014), to 291 dust continuum sources, an association rate of 55% with a mean maser number of spots per clump of 3.4, which is higher than found for the hydroxyl masers. It is found that out of the 298 matched continuum sources, there is one source with 10 maser spots (G301.136-00.226), a significant number of maser spots, which is also associated with a 6.7 GHz methanol maser. An $8\ \mu\text{m}$ infrared GLIMPSE legacy survey image of this regions is presented in Fig. 5.5. A spatial linear correlation between the water masers can be seen, likely due to an outflow originating in the region.

For the 432 emission sites of the 12.2 GHz, as identified by Breen et al., 340 are found to be associated with 330 individual ATLASGAL sources. An association rate of 79% and with an average of 1 maser site per clump. Matching statistics for the 6.7 GHz methanol masers are taken unchanged from Chap. 4. Using the same matching procedure, Chap. 4 produced a sample of 839 6.7 GHz masers, identified by the MMB survey, that are associated with dust continuum emission. The percentage of the

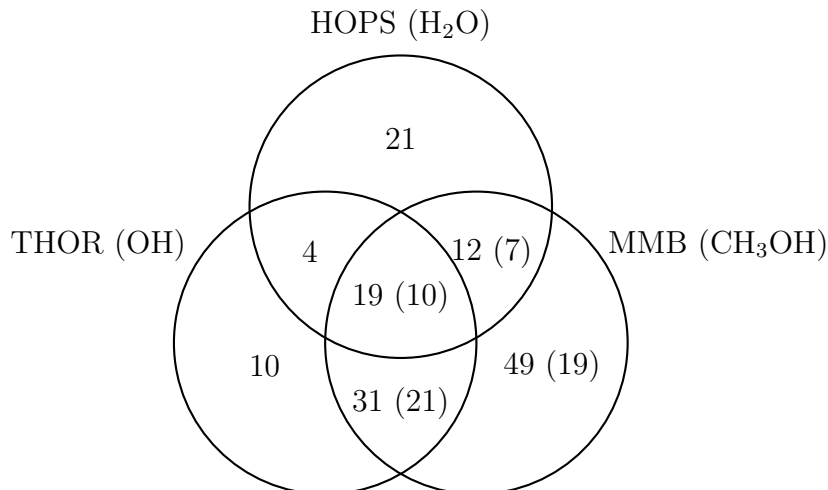


Figure 5.6: A Venn diagram presenting the number of ATLASGAL sources and the corresponding associated masers between Galactic longitudes, $30^\circ > \ell > 14.5^\circ$, and Galactic latitudes, $|b| < 0.5^\circ$. The values in brackets are the values for the 12.2 GHz methanol masers, which are always associated with a 6.7 GHz maser counterpart.

number of dust clumps associated with each maser species can be found in Table 5.1.

5.2.4 COMBINED WINDOW

Each of the surveys presented in this study have differing Galactic coverages and while this has no impact on the fractional associations between individual masers species and the dust emission, to be able to compare associations rates for different sources, it is necessary to investigate a common region. Fortunately, due to the coverages of the presented surveys, there exists a window where they all overlap. This window is positioned between Galactic longitudes of $30^\circ > \ell > 14.5^\circ$ and Galactic latitudes of $|b| < 0.5^\circ$. This portion of the Galaxy can be used to investigate the relationships between the maser species themselves and how they relate to the dust continuum.

Within this window it is found that there are 1 263 ATLASGAL sources with only 146 (12%) of these being associated with maser emission. The matches between this subsample of clumps and the various maser transitions are shown in Fig. 5.6 in the form of a Venn diagram. As all of the 12.2 GHz masers will have a 6.7 GHz counterpart, due to the nature of the observations, they are included in brackets with the 6.7 GHz matching values. Within this overlapping coverage window there are 64, 47, 58 and 111 associated hydroxyl, water, 12.2 GHz methanol and 6.7 GHz methanol masers respectively.

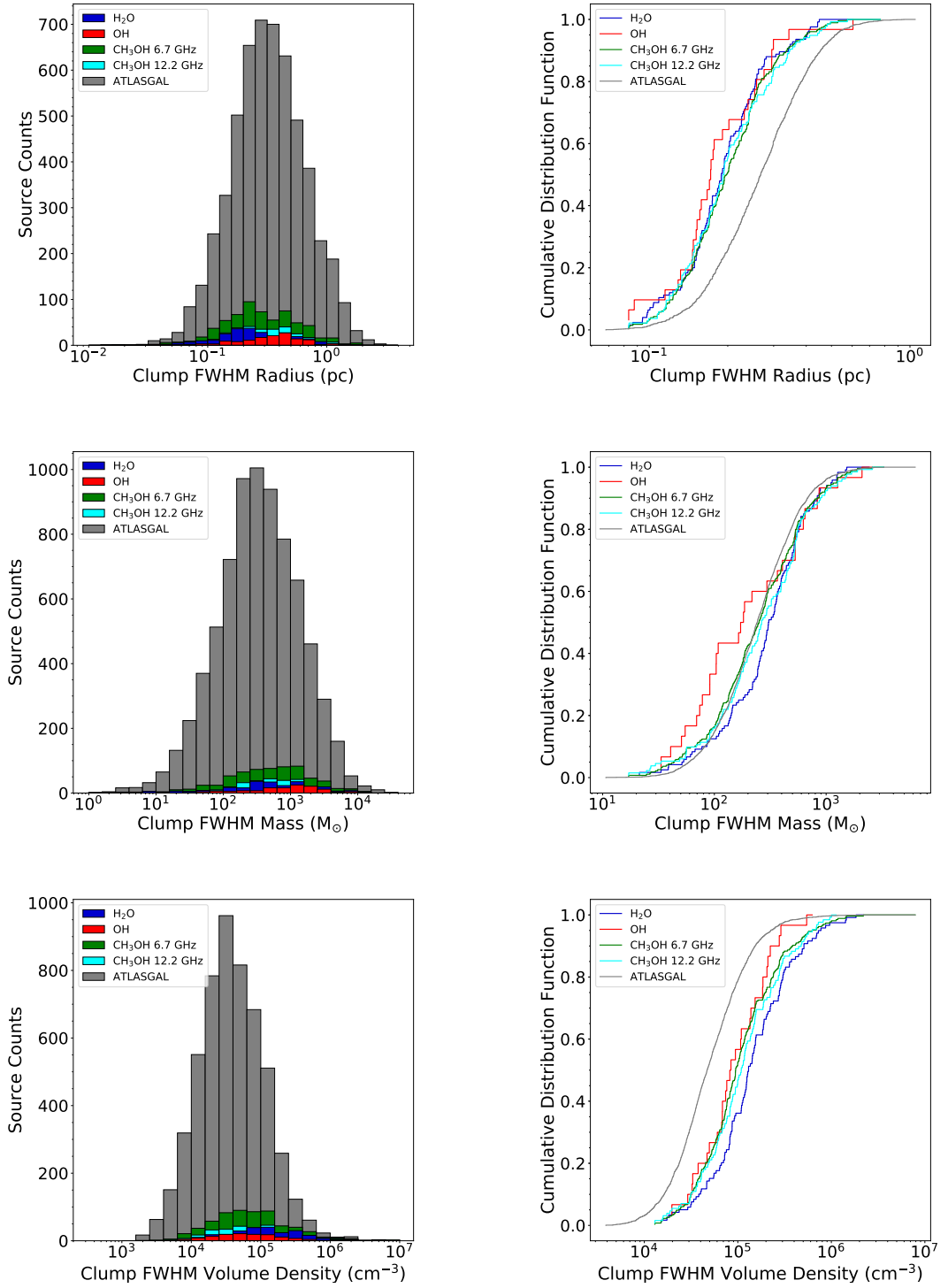


Figure 5.7: Radius, mass and volume density parameter distributions are presented in the upper, middle and lower panels respectively. The histograms in the left panels present the entire distributions of the maser associated clumps and the ATLASGAL clumps, whereas the cumulative distribution functions in the right panels present a distance limited sample (2 to 5 kpc). The bin sizes used for the histograms are 0.1 dex for the radius and 0.2 dex for the masses and volume densities.

Table 5.2: Total statistical parameters for all maser associated clumps, determined within the matching criteria, within the Galactic longitude range $60^\circ > |\ell| > 5^\circ$. The values in brackets show the statistics from a distance limited sample between 2 and 5 kpc.

Parameter	Number	Mean	Standard Deviation	Standard Error	Median	Min	Max
Distance (kpc)							
Maser sample	804 (273)	5.80 (3.07)	3.84 (0.48)	0.14 (0.03)	4.60 (3.10)	0.10 (2.10)	24.20 (3.90)
ATLASGAL	7743 (3014)	4.90 (3.10)	3.31 (0.46)	0.04 (0.01)	3.60 (3.10)	0.00 (2.10)	24.20 (3.90)
Radius (pc)							
Maser sample	768 (263)	0.35 (0.20)	0.27 (0.08)	0.01 (0.00)	0.26 (0.18)	0.01 (0.08)	1.85 (0.53)
ATLASGAL	5478 (2108)	0.41 (0.27)	0.31 (0.11)	0.00 (0.00)	0.32 (0.25)	0.00 (0.07)	2.89 (0.93)
Temperature (K)							
Maser sample	830 (258)	23.91 (23.78)	5.26 (5.66)	0.18 (0.35)	23.42 (23.16)	11.76 (12.13)	51.23 (51.23)
ATLASGAL	9928 (2952)	19.40 (18.93)	5.72 (5.89)	0.06 (0.11)	18.44 (17.76)	5.87 (7.89)	59.96 (51.23)
log[Luminosity (L_\odot)]							
Maser sample	780 (258)	3.99 (3.65)	1.00 (0.84)	0.04 (0.05)	4.00 (3.53)	-0.22 (1.74)	6.91 (5.83)
ATLASGAL	7601 (2952)	2.95 (2.66)	1.03 (0.89)	0.01 (0.02)	2.89 (2.56)	-0.28 (0.55)	6.91 (5.93)
log[Clump Mass (M_\odot)]							
Maser sample	768 (256)	2.63 (2.30)	0.68 (0.41)	0.02 (0.03)	2.71 (2.32)	-1.05 (1.23)	4.40 (3.28)
ATLASGAL	7460 (2909)	2.52 (2.32)	0.61 (0.34)	0.01 (0.01)	2.53 (2.33)	-1.05 (1.03)	4.40 (3.43)
log[L/M Ratio ($L_\odot M_\odot^{-1}$)]							
Maser sample	768 (256)	1.38 (1.36)	0.63 (0.65)	0.02 (0.04)	1.35 (1.30)	-0.43 (-0.43)	3.25 (3.25)
ATLASGAL	7460 (2909)	0.44 (0.34)	0.89 (0.91)	0.01 (0.02)	0.42 (0.29)	-2.40 (-2.40)	3.30 (3.30)
log[Volume Density (cm^{-3})]							
Maser sample	744 (248)	4.86 (5.06)	0.54 (0.43)	0.02 (0.03)	4.83 (5.02)	3.40 (4.11)	6.90 (6.90)
ATLASGAL	5354 (2052)	4.59 (4.72)	0.48 (0.39)	0.01 (0.01)	4.56 (4.70)	2.95 (3.67)	6.90 (6.90)
log[Free-Fall Time (yrs)]							
Maser sample	744 (248)	5.27 (5.17)	0.27 (0.22)	0.01 (0.01)	5.28 (5.19)	4.25 (4.25)	6.00 (5.64)
ATLASGAL	5354 (2052)	5.41 (5.34)	0.24 (0.20)	0.00 (0.00)	5.42 (5.35)	4.25 (4.25)	6.22 (5.86)

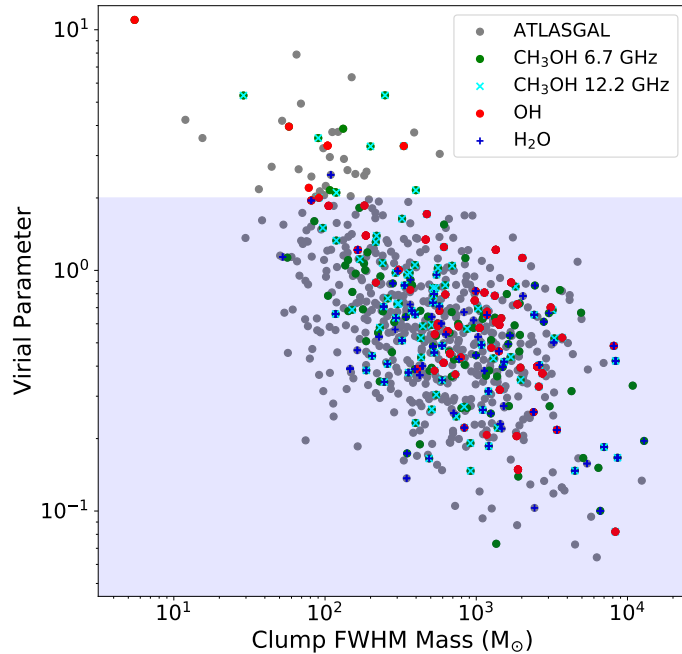


Figure 5.8: Virial parameters versus clump mass for maser associated clumps. A distance limited sample is shown (2 to 5 kpc). The blue shaded area indicates then region of parameter space where clumps are gravitationally unstable and would be in global collapse with a supporting magnetic field.

5.3 PHYSICAL PARAMETER CALCULATIONS

In the following subsections, a description of how the physical parameters of the sample are derived and a full table of statistics for each property is presented in Table 5.2. All of the following parameters have been discussed in Sect. 2.5 and 4.4, but are included here for completeness. The ATLASGAL catalogue gives an effective radius for each clump larger than the beam size of the survey; this radius is the intensity weighted flux density distribution (Contreras et al., 2013) scaled by a value of 2.4, which gives a reasonable approximation of the observed clump size (Rosolowsky et al., 2010). However, it was shown by Urquhart et al. (2018) that evolving clumps appeared to be associated with increasing radius, mass and volume density measurements, and they determined that this was due to an observational bias. As Galactic clumps evolve their average temperature increases, which in turn, results in the extended envelope of these regions becoming bright enough to be detected by the ATLASGAL survey. Therefore, the apparent size and mass of sources appeared to increase (and density decreasing proportionally) during evolution. Chapter 4 eliminated this bias by only considering

the flux from within the full-width half-maximum (FWHM) contour of each $870\ \mu\text{m}$ source. It was shown that this technique effectively removed the observational bias (see Fig. 4.9). Throughout this study a distance limited sample will also be used, from 2 to 5 kpc, to test for any distance biases that may exist within the sample.

5.3.1 FWHM RADIUS AND CLUMP MASS

The FWHM radius and mass values used in this study are taken directly from Chap. 4 and are scaled from the values found in Urquhart et al. (2018) by using the ratio between the FWHM flux and the total flux of each clump. A more detail description of this analysis is given in Sect. 4.4.2. The CDFs of radius and mass for maser associated clumps can be found in upper and middle panels of Fig. 5.7.

The FWHM volume densities have also been calculated using the scaled radii and masses in the same way as described in Sect. 4.4.3:

$$n(\text{H}_2) = \frac{3}{4\pi} \frac{M_{\text{fwhm}}}{\mu m_p R_{\text{fwhm,pc}}^3}, \quad (5.1)$$

where $n(\text{H}_2)$ is the hydrogen number density of clumps, μ is the mean molecular weight of hydrogen, taken here to be 2.8, and m_p is the mean proton mass. M_{fwhm} and R_{fwhm} are the FWHM mass and radius respectively. Here the clumps are assumed to be spherical and not extended along the line of sight. The lower panels of Fig. 5.7 present the distributions of clump volume density; these reveal that all of the maser species have similar densities, which are significantly higher compared to the full ATLASGAL sample.

5.3.2 STABILITY AND FREE-FALL TIMES

To test the stability of individual clumps the virial parameter can be derived, which is defined as (Bertoldi and McKee, 1992):

$$\alpha_{\text{vir}} = \frac{5\sigma_v^2 R_{\text{fwhm,pc}}}{GM_{\text{fwhm}}}, \quad (5.2)$$

where σ_v^2 is the velocity dispersion of the NH_3 inversion transition emission observations (e.g. Urquhart et al. 2011; Wienen et al. 2012, 2018) and the other parameters are as previously defined. The virial parameter is a measure of the balance between gravitational collapse and internal energy that can counteract this collapse. A value of less than 2 is generally indicates that an individual clump is unstable and is likely to be undergoing global gravitational collapse in the absence of any supporting magnetic fields.

Table 5.3: Factors for converting the maser luminosities into units of L_{\odot} .

Maser Transition Frequency	Conversion Factor (kHz)
22.235 GHz	74.1
1612 MHz	5.4
1665 MHz	5.6
1667 MHz	5.6
1720 MHz	5.7
6.7 GHz	22.3
12.2 GHz	40.7

The virial parameter has been calculated for 741 ATLASGAL clumps Urquhart et al. (2018). Fig. 5.8 present the distributions of these virial parameters against clump FWHM mass for all clumps; clumps associated with masers are identified by different symbols and colours. The majority of the clumps in this sample have a value lower than 2 and so are likely to be unstable to gravitational collapse.

Free-fall timescales (derivation given in Sect. 2.5) can be derived for each clump that have a corresponding FWHM volume density measurement:

$$t_{\text{ff}} = \sqrt{\frac{3\pi}{32G\rho}}, \quad (5.3)$$

where ρ is the mean volume density of a clump and G is the gravitational constant. The free-fall times for sources detected in ATLASGAL range between $\sim 2 \times 10^4$ and 2×10^6 yrs. These free-fall times will be used to derive the statistical lifetime for each maser species in Sect. 5.4.2(b). When calculating the free-fall times of clumps, it is assumed that the dominant force is gravity and have not taken into account any support mechanisms that may impede the global collapse of clumps. However, given that $\sim 90\%$ of ATLASGAL clumps are associated with star formation it is safe to assume they are collapsing locally if not globally.

5.3.3 MASER AND BOLOMETRIC LUMINOSITIES

Maser luminosities have been calculated using the determined flux values from the respective maser surveys and distance measurements taken from Urquhart et al. (2018). For consistency, the peak maser fluxes have been used rather than the integrated fluxes to determine the maser luminosities, as the Walsh et al. (2014) HOPS catalogue does not contain integrated fluxes due to the nature of the observations in looking for individual maser spots. In Sect. 4.2.2, it is shown that the differences between the peak and integrated fluxes for maser emission are insignificant above 1 Jy. These maser luminosities have units of Jy kpc km s^{-1} and are, therefore, somewhat arbitrary. As in

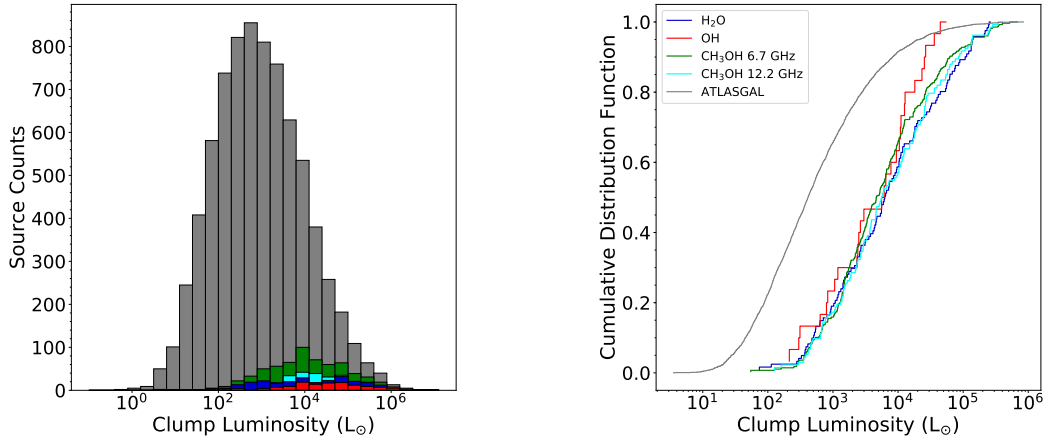


Figure 5.9: Luminosity parameter distributions. The histogram in the upper panel presents the entire distribution of the maser associated clumps and ATLASGAL sample, whereas the cumulative distribution function in the lower panel presents a distance limited sample (2 to 5 kpc). The bin size used for the histogram is 0.3 dex.

Chap. 4, conversion factors have been used to convert the maser luminosities into solar units, a list of these factors can be found in Table 5.3. It is found that the methanol and water masers have similar luminosities whereas the hydroxyl masers are significantly less luminous; this could be due to the typical associations between hydroxyl masers and HII regions. As HII regions disperse their environment, less material is available for pumping, reducing the intensity of the masers.

Bolometric luminosities have been taken unchanged from Urquhart et al. (2018). These luminosities have been calculated by reconstructing each sources' spectral energy distribution (SED; Sect. 2.5). Each luminosity measurement derived from the fitting of the SEDs has been scaled based using the distances to sources to provide an accurate value for the clump luminosities. Figure 5.9 presents the distribution of luminosities as a histogram and cumulative distribution function. There appears to be no significant trends or differences between clumps associated with the different types of masers, although, they do appear to be quite different when compared to the full sample of clumps, this will be discussed in detail in Sect. 5.4.2.

5.3.4 $L_{\text{bol}}/M_{\text{fwhm}}$ RATIOS

Along with the physical parameters that have been derived in the previous subsections, the $L_{\text{bol}}/M_{\text{fwhm}}$ ratio is also defined, the ratio between the bolometric luminosity of clumps and their corresponding FWHM mass. Previous works have shown that this ratio is a good indicator of evolutionary stage (Molinari et al., 2008), and so for the

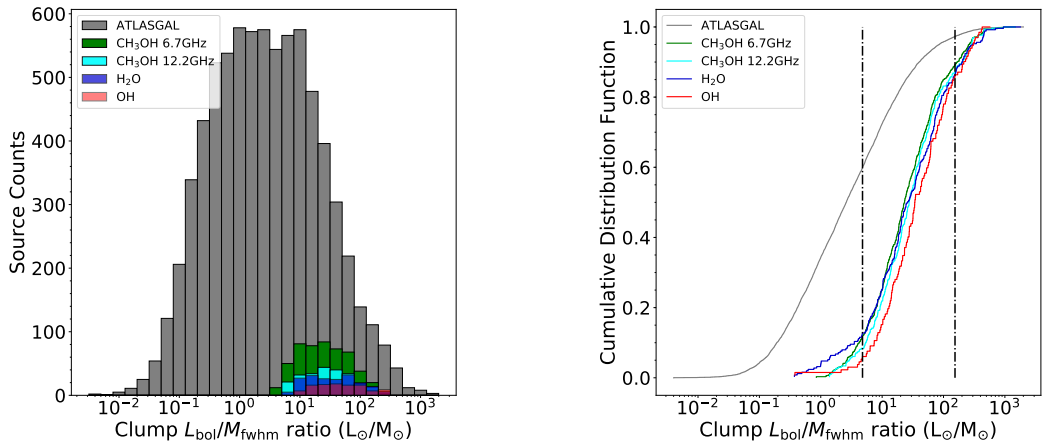


Figure 5.10: $L_{\text{bol}}/M_{\text{fwhm}}$ ratio parameter distribution. The left panel presents a histogram of the $L_{\text{bol}}/M_{\text{fwhm}}$ ratio distribution for each of the maser associated clumps while the right panel presents a cumulative distribution function of these data. The vertical dash-dotted lines shown on the right panel represent the $L_{\text{bol}}/M_{\text{fwhm}}$ ratio range for MSF clumps as identified by the ATLASGAL survey (Urquhart et al., 2014b).

analysis within this study the $L_{\text{bol}}/M_{\text{fwhm}}$ ratios of clumps is used to determine the global evolutionary phase of these star formation regions. Figure 5.10 presents the $L_{\text{bol}}/M_{\text{fwhm}}$ ratio distributions as a histogram and cumulative distribution function, which will be further discussed in Sect. 5.4.2(a).

5.3.5 UNCERTAINTIES IN PHYSICAL PARAMETERS

The uncertainties in the distance measurements towards clumps are on the order of ± 0.5 kpc and are estimated from the Bayesian distance algorithm presented in Reid et al. (2016). The uncertainty for radius is linearly correlated with the distance errors and this uncertainty is $\sim 30\%$ at 1 kpc but only a few percent at distances larger than 10 kpc. The mean error found when determining the dust temperature values from the spectral energy distributions is $\sim 10\%$. The fractional uncertainty for the maser luminosities is roughly $\sqrt{2}$ times the fractional uncertainty in the distance measurements, however, in calculating this quantity it is assumed the maser sources are emitting isotropically and so the uncertainty on these measurements are hard to estimate. As for the physical properties of the clumps, the error on the bolometric luminosities is a factor of a few due to the uncertainty on the bolometric flux values and the distance errors. The uncertainty on the mass and volume density are likely dominated by the uncertainty in the value for the dust absorption coefficient (interpolated from Schuller et al. 2009 and taken to be $1.85 \text{ cm}^2 \text{ g}^{-1}$) and the estimation of the dust-to-gas ratio (taken to be 100). While the uncertainties on the physical parameters may be quite

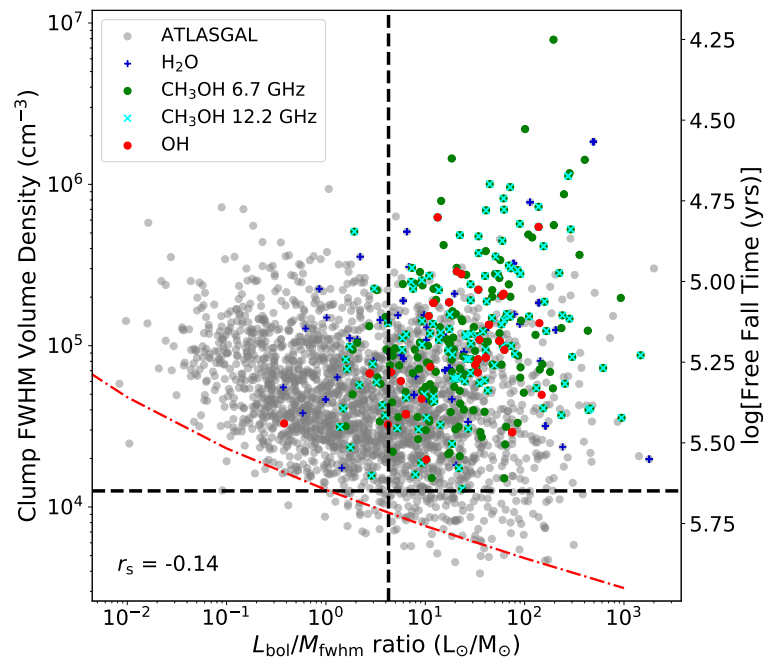


Figure 5.11: Distance limited sample of volume density versus $L_{\text{bol}}/M_{\text{fwhm}}$ ratio. The entire ATLASGAL sample is shown in grey with the various maser species denoted by the legend in the upper right of the plot. The black dashed lines represent the 10% threshold in each parameter space. The sensitivity limits of the ATLASGAL survey is shown as the red dash-dotted line.

large, they affect the entire sample uniformly and will increase the scatter in the distributions, however, this will still allow for statistical trends to be identified and analysed, especially when considering a distance limited sample.

5.4 DISCUSSION

As in Chap. 4, only the central 80% of parameter values within any given distribution is used, this will remove any potential errors or biases resulting from outliers due to inaccurate distance measurements or extreme sources.

5.4.1 COMBINED WINDOW

Section 5.2.4 described a overlapping window between the survey coverages that are used in this study, between $30^\circ > \ell > 14.5^\circ$ and $|b| < 0.5^\circ$. The associations rates for each maser species in shown in Table 5.1. Figure 5.6 presents a Venn diagram of the associated masers with 146 clumps in this window, 47% of these are associated with multiple maser species. This study finds that 76% of the clumps are associated with a 6.7 GHz methanol maser, significantly higher than the number of clumps associated with water (38%) and hydroxyl masers (44%). It can also be seen that 12.2 GHz methanol masers are present in 39% of clumps, showing that only approximately half of 6.7 GHz maser have a 12.2 GHz counterpart, a result found in the 12.2 GHz maser follow-up catalogues (e.g. Breen et al. 2012a) but which differs from previous studies of this association rate (Błaszkiwicz and Kus 2004; 19%). The 6.7 GHz masers also account for the majority of masers that are found in isolation at 58%, while the water and hydroxyl masers are only found in isolation 25% and 12% of the time respectively.

It appears to be quite rare to find both a water maser and hydroxyl maser to be associated with the same source (only 4 out of 146 clumps), whereas the majority of these masers are always found with a methanol maser counterpart. Beuther et al. (2002) found that $\sim 38\%$ of methanol masers do not show water emission and that $\sim 35\%$ of water masers are not associated with a methanol maser. These results differ slightly in that $28 \pm 6\%$ methanol masers are associated with water emission, and $55 \pm 7\%$ of water masers are associated with methanol emission. Breen et al. (2018) presented a comparisons between the MMB and HOPS catalogues, and while they also found that 28% of methanol masers have a water counterpart, they only found that 40% of water masers are seen coincident with methanol masers, although this disparity is likely due to the matching parameters used in each study. Furthermore, studies were

conducted by Titmarsh et al. (Titmarsh et al., 2014, 2016) towards known positions of the 6.7 GHz maser and they found $\sim 46\%$ and $\sim 50\%$ of methanol masers have a water emission counterpart. It is likely that the high variability of water masers plays a role in the differences between the coincident percentage along with the sensitivity of the corresponding studies.

No differences are found between the physical properties of clumps that are associated with different maser species or a combination of the various species. The $L_{\text{bol}}/M_{\text{fwhm}}$ ratios of this samples also have no significant trends, although, it is found that clumps with multiple maser species generally have larger $L_{\text{bol}}/M_{\text{fwhm}}$ ratios than those associated with only a single maser transition. As the majority of clumps harbour multiple maser species, this indicates that the physical conditions required for maser emission to be produced are similar for all of the maser species.

5.4.2 PHYSICAL PARAMETERS

Figure 5.7 presents the histograms and distance limited cumulative distribution functions of clump FWHM radius, mass and volume density. It can be seen that the clumps associated with a maser are more compact than the full ATLASGAL sample, as presented in the upper right panel of Fig. 5.7. A Kolmogorov-Smirnov (KS) test has been applied to the radii of clumps associated with a maser source and the ATLASGAL sample to identify whether the difference in radii between the two samples is statistically significant; this has revealed that all of the maser associated clumps are significantly more compact than the rest of the dust clump sample ($p \ll 0.0013$). The masses of maser associated clumps are similar to the average mass of dense clumps and there are no significant differences. As the clumps containing a maser are significantly more compact than the ATLASGAL sample, while having similar masses, the calculated volume densities are naturally increased, showing that masers are only associated with those clumps above a certain density threshold ($n(\text{H}_2) > 10^{4.1} \text{ cm}^{-3}$); this density limit is consistent with the result found in Sect. 4.5.3. Figure 5.9 presents the distribution of clump luminosity for the various samples and all of the maser clumps are found to be more luminous when compared to the average clump luminosity. This implies that a certain protostellar mass is required ($\sim 6 M_{\odot}$), and therefore luminosity ($\sim 500 L_{\odot}$), in order to drive sufficient radiative and mechanical energy into the circumstellar environment to effectively pump the various maser species.

The physical parameters that have been discussed above are all similar for each of the clumps associated with a different maser species, and all appear to be significantly increased when compared to the full ATLASGAL sample. These results do not completely conform with previous studies, for example, Breen and Ellingsen (2011) found

Table 5.4: The central 80% of the $L_{\text{bol}}/M_{\text{fwhm}}$ ratio, volume density and luminosities parameters for each maser species.

Maser Species	$L_{\text{bol}}/M_{\text{fwhm}}$ ratio ranges	Volume density ranges (cm^{-3})	Luminosity ranges (L_{\odot})
Water	$10^{0.80} - 10^{2.35}$	$10^{4.4} - 10^{5.8}$	$10^{2.7} - 10^{5.4}$
Hydroxyl	$10^{0.98} - 10^{2.43}$	$10^{4.2} - 10^{5.7}$	$10^{3.6} - 10^{5.9}$
Methanol 12.2 GHz	$10^{0.75} - 10^{2.33}$	$10^{4.3} - 10^{5.7}$	$10^{3.0} - 10^{5.4}$
Methanol 6.7 GHz	$10^{0.63} - 10^{2.23}$	$10^{4.1} - 10^{5.6}$	$10^{2.8} - 10^{5.3}$

that water masers are typically found towards clumps with larger radii, increased mass and increased luminosity. While masers are associated with the brightest clumps, there is no difference between any other physical property (radius, mass or density) and the larger ATLASGAL clump sample. This conflict is likely due to the source sample used in Breen et al. (2010), which originates from Hill et al. (2005). This millimetre study presented observations of 131 star-forming complexes suspected of harbouring massive star formation. The differences between the samples presented in this study and Hill et al. (2005) can be attributed to the method of calculating the radii and masses of individual sources, the radii of millimetre sources in Hill et al. (2005) is highly dependent on the temperature of each region, an observational bias that is described in Sect. 4.4.2, and instead the sizes of sources in this study are calculated based on the FWHM flux distribution. Also Hill et al. (2005) used a constant temperature of 20 K to determine the mass of each clump, whereas the ATLASGAL temperatures are based on the results of spectral energy distribution fitting analysis.

5.4.2(a) EVOLUTIONARY STAGE - $L_{\text{bol}}/M_{\text{fwhm}}$ RATIOS

Figure 5.10 presents the histograms for the $L_{\text{bol}}/M_{\text{fwhm}}$ ratios of all the maser species and the full ATLASGAL sample, along with the corresponding cumulative distribution function for these data. It can be seen from the left panel of this figure, that all the maser species occupy approximately the same distinct part of the parameter space, between $\sim 10^{0.6}$ and $10^{2.5} L_{\odot} M_{\odot}^{-1}$. The exact ranges of $L_{\text{bol}}/M_{\text{fwhm}}$ ratios for each maser species can be found in Table 5.4. Since the $L_{\text{bol}}/M_{\text{fwhm}}$ ratios of all of the maser associated clumps are similar (as confirmed by a KS test), it could be assumed that the mechanisms required for the production of any maser emission only occurs at a set stage in the evolution of star formation and then only for protostellar sources above a certain luminosity ($\sim 500 L_{\odot}$).

Figure 5.11 presents clump FWHM volume density versus clump $L_{\text{bol}}/M_{\text{fwhm}}$ ratio. It can be seen that there is a slight negative correlation between these two parameters, although, this is likely due to the sensitivity limit of the ATLASGAL survey, which is also shown in the figure. In Chap. 4, a lower limit of volume density for maser associated clumps was found to be $10^{4.1} \text{ cm}^{-3}$. This limit seems to hold true for all of the maser species presented in this study, as shown in Fig 5.11 and Table 5.4. Overall, these results show that certain physical conditions are necessary for the global presence on any type of maser; this conditions are $L_{\text{bol}}/M_{\text{fwhm}}$ of between $10^{0.6}$ and $10^{2.5} L_{\odot} M_{\odot}^{-1}$, volume densities of above $10^{4.1} \text{ cm}^{-3}$, and luminosities of $\sim 500 L_{\odot}$, which corresponds to a protostellar mass of $\sim 6 M_{\odot}$ ($L \sim M^{3.5}$; Kuiper 1938). Naturally, these conditions are only required for masers present in star formation regions and may not hold true

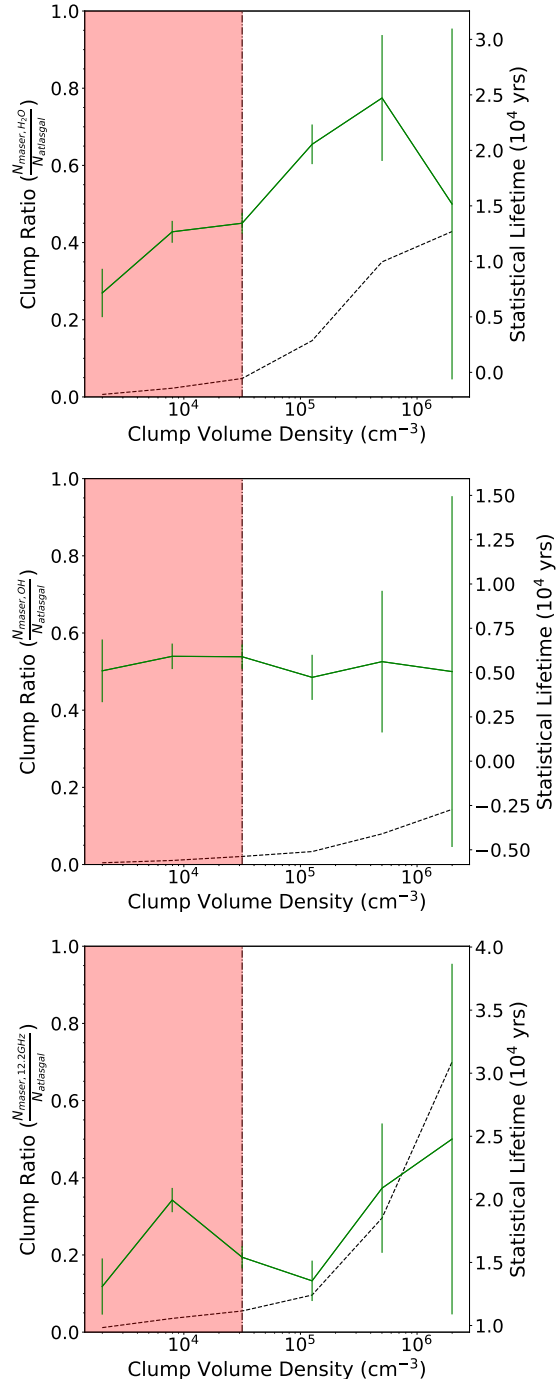


Figure 5.12: Plots presenting the clump ratios for each maser species and the statistical lifetimes as a function of clump FWHM volume density. The upper, middle and lower panels present the lifetimes for the water, hydroxyl and 12.2 GHz methanol masers respectively. The black dotted lines shows the increasing number of maser associated clumps with respect the volume density, whereas the solid green line presents the change in statistical lifetime for each volume density range. The shaded regions represents the parameter space where the sample is incomplete. Errors shown are derived from Poisson statistics.

for the same maser species associated with other celestial objects.

5.4.2(b) STATISTICAL LIFETIMES

Chapter 4 presented the calculation of the statistical lifetime of the 6.7 GHz methanol maser by finding the ratio of maser associated clumps at specific density intervals and multiplying these by the free fall times at these intervals. The mean statistical lifetime for this maser transition was found to be $\sim 3.3 \times 10^4$ yrs, which was in very good agreement with theoretical predictions (Van Der Walt, 2005). This derivation has been repeated for the maser species presented in this study. Free fall times have been calculated for each clump within the sample that has a corresponding volume density measurement. These free fall times range from $\sim 20\,000$ yrs to $\sim 750\,000$ yrs. It is likely that any maser emission will only be present for a fraction of these timescales and so by multiplying these times by the fraction of clumps associated with a particular kind of maser emission at specific volume density intervals, the statistical lifetime for maser emission can be found. Figure 5.12 presents the clump ratios and statistical lifetimes for each maser species as a function of volume density. It can be seen from this figure that the number of maser associated clumps increases with increase clump volume density. For the calculation of the statistical lifetimes, only clumps which have volume densities above the completeness limited for this parameter are included, $n > 10^{4.5} \text{ cm}^{-3}$ (Sect. 4.5.4). The mean lifetimes of maser emission are found to be 1.6, 0.5 and 2.0×10^4 yrs for the water, hydroxyl and 12.2 GHz methanol masers respectively. The statistical lifetime for the 6.7 GHz maser is taken from Chap. 4 as 3.3×10^4 yrs. The uncertainty on these calculations has been calculated using Poisson statistics and is shown in Fig. 5.12, with the mean error being found to be $\sim 10\%$.

5.4.3 “STRAW MAN” MODEL COMPARISON

One of the main aims of this study was to investigate the Ellingsen (2007) “straw man” model using the physical properties presented in the ATLASGAL catalogue. This model is based on maser observations within regions of ongoing star formation and that, in short, methanol masers (class I & II) are associated with a very early stage of formation, followed by water masers, hydroxyl masers are then seen coincident with ultra-compact HII regions. Section 5.4.2(a) shows that all of the maser associated clumps have similar $L_{\text{bol}}/M_{\text{fwhm}}$ ratios, which is used as the gauge of protostellar evolution, albeit with some small differences ($\sim 10^{0.1} - 10^{0.3} L_{\odot} M_{\odot}^{-1}$). These differences between the $L_{\text{bol}}/M_{\text{fwhm}}$ ratios of the maser species could be used to establish a similar model to the “straw man” model and it can be seen that these values do

support the majority of the predicted maser phases with the exception of the 12.2 GHz maser, which is found to begin before the presence of water emission. However, due to the errors on the $L_{\text{bol}}/M_{\text{fwhm}}$ ratios, these differences are insignificant and so the confirmation of the Ellingsen (2007) cannot be completed using the $L_{\text{bol}}/M_{\text{fwhm}}$ ratios of associated clumps.

The sample presented here can also attempt to test the “straw man” model using the calculated statistical lifetimes for each maser phases. Breen et al. (2010) predicted that the lifetime of the 12.2 GHz methanol maser to be between 1.5×10^4 yrs and 2.7×10^4 yrs, and the statistical lifetime which is calculated for this maser does lie towards the centre of this range at $\sim 2 \times 10^4$ yrs, and so these results are in good agreement with Breen et al. (2010). Along with the statistical lifetime for the 6.7 GHz maser found in Chap. 4, ($\sim 3.3 \times 10^4$ yrs) these results support the “straw man” model in terms of the methanol masers. The model presented by Breen et al. (2010) also shows that the hydroxyl maser has a lifetime of $\sim 20\,000$ yrs and the value found here is only a quarter of that prediction ($\sim 0.5 \times 10^4$ yrs). Finally, water masers are predicted to have relative lifetimes of $\sim 30\,000$ yrs, while a lifetime of approximately one half of this at only $16\,000$ yrs is found in this study. While these measurements give a good indication of lifetimes for each maser species, it is difficult to secure where these lifetimes lie in relation to one another as the $L_{\text{bol}}/M_{\text{fwhm}}$ ratios show no significant trends. Overall, a good agreement is found with the “straw man” model in terms of the methanol masers having employed a different method to previous studies to calculate the maser lifetimes, however, reduced values for lifetimes of the water and hydroxyl emission are found.

5.5 CONCLUSIONS

This study has investigated the correlations between the ATLASGAL catalogue and dense Galactic clumps that are associated with methanol, water and hydroxyl maser emission. Catalogues from the HOPS, THOR, MMB and ATLASGAL surveys, along with 12.2 GHz MMB follow-up observations, have been used to match maser emission to dense clumps located in the Galactic mid-plane ($|\ell| < 60^\circ$ & $|b| < 1.5^\circ$). Association rates for the water, hydroxyl and 12.2 GHz masers are found to be 56, 38, 82% respectively. Physical parameters for the maser associated clumps and the full ATLASGAL sample are taken from Urquhart et al. (2018) and Chap 4.

1. The majority of methanol and water maser emission across the Galactic plane are associated with dense clumps, as identified by the ATLASGAL survey. Where a

maser match has been found, they appear to have tightly correlated systematic velocities as those found for their counterpart clumps. The majority of masers ($\sim 90\%$) are also found to be tightly correlated with the peak of the dust emission ($< 10''$), where the highest densities are found, implying that they are at least coincident if not directly associated with embedded star formation.

2. It is common to find clumps coincident with multiple maser species ($\sim 45\%$), but the majority of maser species are found in isolation ($\sim 55\%$). The communality of multiple species being found in a large fraction of clumps may be due to multiple evolutionary stages being present in each clump or that the various maser species require similar physical conditions. This is supported by the fact that all maser associated clumps, regardless of the corresponding maser species, have similar properties (no statistical differences are found between the clumps that are associated with different maser emissions).
3. There appears to be a similar density threshold required for the production of maser emission as found in Chap. 4, maser emission of any type is only found with associated clump densities of greater than $10^{4.1} \text{ cm}^{-3}$, further justifying that volume density is likely an important factor for maser emission. Furthermore, the fraction of clumps with associated maser emission increases alongside increasing density as shown in Fig. 5.12.
4. The $L_{\text{bol}}/M_{\text{fwhm}}$ ratios of maser associated clumps, regardless of the associated maser emission, are shown to occupy the same distinct region of the parameter space, and so all maser emission can be seen to have a well defined turning on and turning off points in the evolutionary sequence. The “straw man” model predicts that the different maser species turn on and off at different times, however, these results are not consistent with these predictions.
5. The physical properties required for maser emission have been constrained and it is shown that masers only exist in clumps with volume densities above $10^{4.1} \text{ cm}^{-3}$, luminosities greater than $\sim 500 L_{\odot}$ and also require a minimum protostellar mass, estimated to be $\sim 6 M_{\odot}$. Maser species also have a well defined turn-on point ($\sim 10^{0.6} L_{\odot} M_{\odot}^{-1}$), which is independent of the type of maser.
6. Statistical lifetimes are calculated for the water, hydroxyl and 12.2 GHz methanol masers, and these lifetimes are found to be $\sim 1.6, 0.5$ and 2.0×10^4 yrs respectively. The lifetimes for the 6.7 GHz (as found in Chap. 4) and 12.2 GHz methanol masers are found to be in good agreement with the values predicted by Breen et al. (2010), whereas the statistical lifetimes determined for the water and hydroxyl

masers are considerably shorter than those predicted, by one quarter and one half respectively.

CHAPTER 6

SUMMARY AND CONCLUSIONS

This Chapter summarises each chapter by providing the main conclusions. Overall conclusions are then given along with possible future work.

6.1 SUMMARY

INTRODUCTION (Chapter 1)

This Chapter includes a background of radio astronomy and star formation. Different types of Galactic emission are also explained and a description of the ISM is given. Radio astronomy is a useful tool that can be used to study continuum and spectral line emission in a range of environments that relate to the processes of star formation. A discussion of the current theories of massive star formation are presented along with the generalised method that aims to explain the initial stages of the formation. It is shown that while massive stars play an important role in the evolution of the Galaxy, our knowledge of their formation is limited due to issues with detection, rarity and observational limitations. Thesis aims and structure are then provided.

THEORY AND OBSERVATIONS (Chapter 2)

In this Chapter, the relevant theory of radiative transfer, spectral line emission and telescope detection systems are provided. The equations and methods used for measuring physical properties of star formation regions are derived along with a framework of molecular line emission that is required for an understanding of the work presented in

the chapters that follow. Specific focus is given to the inversion transitions of the ammonia molecule and the spectral energy distributions derived from the measurements of thermal dust emission across a number of different wavelengths.

AMMONIA MAPPING OF THE ENVIRONMENT OF YOUNG MASSIVE STELLAR OBJECTS (Chapter 3)

This Chapter investigates the morphological differences between the gas and dust towards 34 regions of star formation. The dense gas within these star forming regions is mapped using the first two inversion transitions of the ammonia molecule, while the dust is identified by the ATLASGAL survey. These data were used to construct a rudimentary evolutionary sequence based of the morphologies of the associated dense gas. The 34 regions of interest were classified into early star-forming (ESF) and late star-forming (LSF); environments in the early stages of star formation showed that embedded objects (identified by the RMS survey), dense gas and dust were all coincident in clumps with relatively simple morphologies. The late star-forming class of regions had coincident RMS objects and dust, but the dense gas appeared to be in a state of disruption, showing fragmented morphologies where the gas has begun to disperse.

Urquhart et al. (2018) provides a catalogue of over 8 000 dust clumps with measured physical parameters, which were utilised in this study. The parameters between the two identified classes were not significantly different, implying that the morphology and coincidence of the gas and dust changes more rapidly than the global properties of star forming regions. It was found that the masses of the presented clumps range between a few hundred to over 10 000 M_{\odot} , with luminosities ranging between $\sim 10^3$ to $\sim 10^6 L_{\odot}$.

Catalogues from the HOPS and MMB surveys were also employed to investigate any differences in maser associations between the early and late star-forming regions. It is seen that the majority of masers, both water and methanol, are seen towards ESF fields, with detection rates of 89 and 72% respectively. The reason for the significantly lower detection rates towards LSF regions is likely linked to the disruption of natal clumps by the expansion of HII regions, and for the LSF regions, 63% are associated with a HII region.

A number of interesting sources are also presented that show potential outflows, molecular infall and possible triggered star formation. Triggered star formation appears to be present in three of the observed regions, GLIMPSE images show these sources to be in the presence of nearby HII regions that show evidence of affecting the dense gas within these fields. The coincident of maser emission in these regions reveal that the HII regions are not only having a significant impact on their environments but also

potentially having an influence on star formation. As developing HII regions disrupt natal material, it is likely the masers highlighted are predominantly associated with a limited part of the evolutionary sequence, which is explored in Chaps. 4 and 5.

THE PHYSICAL PARAMETERS OF DUST CLUMPS ASSOCIATED WITH 6.7 GHz METHANOL MASERS (Chapter 4)

This Chapter presents a study of the associations between Galactic dust clumps, as identified by the JPS and ATLASGAL surveys, and the class II 6.7 GHz methanol maser, as identified by the MMB survey. The largest and most complete sample of 6.7 GHz methanol masers to date is used in order to investigate where this maser species lies in the evolutionary stages of high-mass star formation. It is found that the 6.7 GHz masers have an almost ubiquitous association with dust emission across the Galactic plane ($\sim 99\%$) and the majority of masers associated ($\sim 95\%$) clumps show evidence of being in an advanced stage of star formation as they are also associated with young stellar objects and/or HII regions.

The physical parameters of clumps associated with methanol masers have been tested against the full sample of ATLASGAL sources; this revealed that the bolometric luminosity of a clump is linearly proportional to the maser luminosities ($L_{\text{bol}} \propto L_{\text{maser}}^{0.86 \pm 0.09}$), and this relation provides strong evidence that the 6.7 GHz maser is radiatively pumped. There is also no difference in mass between the maser associated sample and the full ATLASGAL catalogue, implying that the mass of a clump is imprinted during its formation and does not change until natal material begins to disperse on global scales.

The 6.7 GHz methanol maser occupies a distinct range within the $L_{\text{bol}}/M_{\text{fwhm}}$ ratio parameter space ($10^{0.6} - 10^{2.2} L_{\odot} M_{\odot}^{-1}$), showing that these maser are associated with a well defined stage in the evolutionary of star formation. This study also constrains the physical parameters necessary for maser emission to take place, with a required minimum mass of $\geq 6 M_{\odot}$ and a volume density threshold of $n(\text{H}_2) \geq 10^{4.1} \text{ cm}^{-3}$. Intermediate- and high-mass star formation is likely to be inefficient below these limits. A statistical lifetime for the 6.7 GHz maser is calculated to be $\sim 3.3 \times 10^4$ yrs, which is consistent with theoretical predictions (Van Der Walt, 2005).

This work has expanded on previous studies and confirmed that the 6.7 GHz methanol masers are exclusively associated with dense dust. The physical parameters for maser associated clumps have been constrained and their presence during the formation of high-mass stars has been isolated to a well defined phase. These results are consistent with the “straw man” model presented in Ellingsen (2007) & Breen et al. (2010), and with the theoretical predictions reported in the literature (Van Der Walt, 2005). In

the following chapter, these results are expanded on but considering additional maser species to further constrain these models and predictions.

INVESTIGATING THE EVOLUTIONARY STAGES OF STAR FORMATION THROUGH VARIOUS MASER SPECIES (Chapter 5)

This Chapter directly follows the work presented in Chap. 4 and investigates the associations between further maser species and dense Galactic clumps. The maser species of interest are the class II 12.2 GHz methanol maser, the 22.2 GHz water maser and the four base transitions of the hydroxyl maser at 1612, 1665, 1667 and 1720 MHz. Catalogues from the HOPS and THOR surveys, along with MMB follow-up observations, have been used to match these maser species to dense dust clumps, as identified by the ATLASGAL survey.

Association rates for the water, hydroxyl and 12.2 GHz methanol masers are found to be 56, 38 and 82% respectively. The majority of masers ($\sim 90\%$) are found to be within $10''$ from the peak of dust emission, implying that matched masers are likely associated with embedded star formation. The majority of masers species are found in isolation (55%), however, it is common to find multiple maser species associated with the same clump (45%), suggesting a large overlap in the physical conditions.

The physical parameters of maser associated clumps are found to be statistically different to the full ATLASGAL sample, although, there is no difference in the properties for clumps that are coincident with different maser species. Clumps associated with a maser are generally more compact, more dense and with higher luminosities.

The $L_{\text{bol}}/M_{\text{fwhm}}$ ratios of maser associated clumps show that, all appear to occupy the same distinct area of the parameter space ($10^{0.6} - 10^{2.5} L_{\odot} M_{\odot}^{-1}$), implying that all masers have the same turn-on and turn-off points, regardless of the corresponding maser type. It is also shown that masers require clump densities of above $10^{4.1} \text{ cm}^{-3}$ and clump luminosities of above $\sim 500 L_{\odot}$, which corresponds to a protostellar mass of $\sim 6 M_{\odot}$. Using the $L_{\text{bol}}/M_{\text{fwhm}}$ ratios, the data presented cannot support the “straw man” evolutionary model laid out by Ellingsen (2007) and Breen et al. (2010).

Statistical lifetimes are derived for the water, hydroxyl and 12.2 GHz methanol masers. The lifetime of the 12.2 GHz maser is found to be 2×10^4 yrs, consistent with the results of Breen et al. (2010), however, the lifetimes found the water and hydroxyl masers are less than predicted by one half (1.6×10^4 yrs) and one quarter (0.5×10^4 yrs) respectively.

6.2 OVERALL CONCLUSIONS

A range of radio wavelength molecular line and maser transitions, with archival submillimetre and infrared surveys, have been used to investigate the proposed evolutionary sequence for massive star formation. The physical conditions towards a sample of MYSOs and HII regions have been investigated and while the dust derived properties appear similar, the molecular line data reveals significant differences. Regions of possible triggered star formation have also been identified through the use of interstellar maser emission.

The results presented throughout this Thesis show that the processes that govern the formation of massive stars and their associated evolutionary stages are intricate and complex, and therefore, required a large number of in-depth studies into the various mechanisms and associated emissions. Interstellar molecular emission can be used to investigate the initial stages of how massive stars form, either through pinpointing various evolutionary stages or by presenting the morphological differences between dense gas, dust and embedded objects, and provide insight into how environmental conditions can impact star formation.

Maser emission is shown to be an effective and useful tool in the study of star formation, by providing insight into regions of possible triggered star formation and as a tool to identify young massive stars. Different maser species are likely to require different conditions in order for their production but the results found in Chaps. 4 and 5 show that the different potential production mechanisms must all be effective at the same time during the evolutionary timescales of massive star formation.

One of the primary results from this Thesis is that the physical properties of dense dust clumps across the Galactic plane are ingrained at their formation. This is shown in Chap. 3 where it is determined that there are no observed changes in the morphology of the dust emission, however, changes are observed in the morphology of the molecular line emission, which is sensitive to high densities. The regions of interest in this study are classified into early and late star forming and no statistical differences are seen between the physical properties of the two classifications. The work in Chap. 4 finds that the radii and masses of clumps do not change during their evolution. It is likely that the physical properties at clump scales do not change until after a HII region has developed sufficiently in order to significantly disperse the natal environments.

A main aim of the studies presented in Chaps. 4 and 5 is to investigate the “straw man” evolutionary model presented in Ellingsen (2007), and developed in Breen et al. (2010), by using the physical properties of dense clumps as identified by the ATLAS-

GAL survey. The statistical lifetimes for the 6.7 GHz ($\sim 3.3 \times 10^4$ yrs) and 12.2 GHz ($\sim 2.0 \times 10^4$ yrs) methanol masers derived in this Thesis are consistent with the predicted values from Breen et al. (2010), and as these lifetimes have been measured independently using different methods, are likely to be accurate. However, the lifetimes for the water and hydroxyl masers are much shorter than predicted by Breen et al. (2010). These results cast doubt on the validity of the “straw man” model as similar physical conditions are found for all the investigated maser species, however, further work is required to identify differences in the way the previous studies have measured the physical properties of maser regions and any potential biases that might explain the differences between the two studies.

6.3 FUTURE WORK

The work presented in this Thesis has shown the usefulness of molecular emission in the study of massive star formation, and has identified some interesting sources (potential trigger star formation found in Chap. 3 and regions with a significant number of masers found in Chap. 5). However, the observations presented are not of the highest possible resolution or signal-to-noise, and so with improved observations, a more detailed and in-depth analysis of high-mass star formation regions could be undertaken. There are already many studies underway, utilising the Atacama Large Millimeter Array (ALMA), but these samples can only be put into context by understanding the properties of the whole population.

Recently, the Green Bank Observatory has undertaken two large scale surveys, the Radio Ammonia Mid-Plane Survey (RAMPS; Hogge et al. 2018) and the Green Bank Ammonia Survey (GAS; Friesen et al. 2017), which has mapped a much larger portion of the Milky Way than the observations in Chap. 3. Such observations could be used to refine the results presented here and provide a fuller overview of the morphologies of star formation regions. Potential observations could also be extended to include multiple molecular tracers, providing a multi-wavelength analysis and further improving our understanding of massive stars. Furthermore, molecular line surveys (CHIMPS/SEDIGISM) can be used to study the kinematics and temperature distributions of large-scale structures, along with radio surveys (THOR) which can map out regions of ionised gas, providing more insight into the distribution and necessary conditions for the formation of high-mass stars throughout the Galaxy.

While Chaps. 4 and 5 use a number of maser species to investigate a possible model of formation based on maser emission, this work could be extended to include further

maser transitions and species to refine the evolutionary “straw man” model. An important issue could be developing an unbiased class II 12.2 GHz methanol maser survey across the Galactic plane, in order to investigate the proposed exclusive association with the 6.7 GHz methanol maser. It might also be possible to undertake high resolution observations, perhaps using ALMA, to investigate the positioning of masers and their source material around young massive stars and HII regions.

BIBLIOGRAPHY

- G. Anglada, R. Estalella, J. Pastor, L. F. Rodriguez, and A. D. Haschick. A CS and NH 3 Survey of Regions with H 2O Maser Emission. *Astrophys. J.*, 463:205–223, 2002. ISSN 0004-637X. doi: 10.1086/177235.
- A. L. Argon, M. J. Reid, and Karl M. Menten. Interstellar Hydroxyl Masers in the Galaxy. I. The VLA Survey. *The Astrophysical Journal Supplement Series*, 129: 159–227, Jul 2000. doi: 10.1086/313406.
- C. Battersby, A. Ginsburg, J. Bally, S. Longmore, M. Dunham, and J. Darling. The Onset of Massive Star Formation: the Evolution of Temperature and Density Structure in an Infrared Dark Cloud. *ApJ*, 787(2007):113, 2014. ISSN 0004-637X. doi: 10.1088/0004-637X/787/2/113.
- M. B. Bell and H. E. Matthews. Detection of HC11N in the cold dust cloud TMC-1. *Astrophys. J.*, 483:L61, 1997. ISSN 0004-637X. doi: 10.1086/184460.
- R. A. Benjamin, E Churchwell, B. L. Babler, T. M. Bania, D. P. Clemens, M. Cohen, J. M. Dickey, R. Indebetouw, J. M. Jackson, H. A. Kobulnicky, A. Lazarian, A. P. Marston, J. S. Mathis, M. R. Meade, S. Seager, S. R. Stolovy, C Watson, B. A. Whitney, M. J. Wolff, and M. G. Wolfire. GLIMPSE. I. An SIRTf Legacy Project to Map the Inner Galaxy. *Publ. Astron. Soc. Pacific*, 115(810):953–964, 2003. ISSN 0004-6280. doi: 10.1086/376696.
- E. A. Bergin and M. Tafalla. Cold Dark Clouds: The Initial Conditions for Star Formation. *Annu. Rev. Astron. Astrophys.*, 45:339–96, 2007. doi: 10.1146/annurev.astro.45.071206.100404.
- D. S. Berry. FellWalker-A clump identification algorithm. *Astronomy and Computing*, 10:22–31, Apr 2015. doi: 10.1016/j.ascom.2014.11.004.

- F. Bertoldi and C. F. McKee. Pressure-confined clumps in magnetized molecular clouds. *Astrophys. J.*, 395:140, 1992. ISSN 0004-637X. doi: 10.1086/171638.
- H. Beuther, A. Walsh, P. Schilke, T. K. Sridharan, K. M. Menten, and F. Wyrowski. CH₃OH and H₂O masers in high-mass star-forming regions. *Astron. Astrophys.*, 390: 289–298, 2002. doi: 10.1051/0004-6361:20020710.
- H. Beuther, S. Bühr, M. Rugel, K. Johnston, Y. Wang, F. Walter, A. Brunthaler, A. J. Walsh, J. Ott, J. Stil, Th Henning, T Schierhuber, J Kainulainen, M Heyer, P F Goldsmith, L D Anderson, and S N Longmore. The HI / OH / Recombination line survey of the inner Milky Way (THOR) - Survey overview and data release 1. *A&A*, 595:A32, 2016a.
- H. Beuther, S. Meidt, E. Schinnerer, R. Paladino, and A. Leroy. Galactic Bar/Spiral Arm Interactions in NGC3627. *A&A*, pages 1–14, 2016b. ISSN 0004-6361. doi: 10.1051/0004-6361/201526749.
- H. Beuther, A. Walsh, Y. Wang, M. Rugel, J. Soler, H. Linz, R. S. Klessen, L. D. Anderson, J. S. Urquhart, S. C. O. Glover, S. J. Billington, J. Kainulainen, K. M. Menten, N. Roy, S. N. Longmore, and F. Bigiel. OH maser emission in the THOR survey of the northern Milky Way. *A&A*, 628:A90, August 2019. doi: 10.1051/0004-6361/201935936.
- S. Bühr, K. G. Johnston, H. Beuther, L. D. Anderson, J. Ott, M. Rugel, F. Bigiel, A. Brunthaler, S. C. O. Glover, T. Henning, M. H. Heyer, R. S. Klessen, H. Linz, S. N. Longmore, N. M. McClure-Griffiths, K. M. Menten, R. Plume, T. Schierhuber, R. Shanahan, J. M. Stil, J. S. Urquhart, and A. J. Walsh. Continuum sources from the THOR survey between 1 and 2 GHz. *A&A*, 588:A97, 2016. ISSN 0004-6361. doi: 10.1051/0004-6361/201527697.
- S. J. Billington, J. S. Urquhart, C. Figura, D. J. Eden, and T. J. T. Moore. The RMS survey: Ammonia mapping of the environment of massive young stellar objects -II. *MNRAS*, 483:3146–3167, 2019a. doi: 10.1093/mnras/sty3053.
- S J Billington, J S Urquhart, C König, T J T Moore, D J Eden, S L Breen, W-J Kim, M A Thompson, S P Ellingsen, K M Menten, F Wyrowski, and S Leurini. ATLASGAL physical parameters of dust clumps associated with 6.7 GHz methanol masers. *Mon. Not. R. Astron. Soc.*, 490:2779–2798, 2019b. ISSN 0035-8711. doi: 10.1093/mnras/stz2691.
- L. Błazzkiewicz and A J Kus. 12.2 GHz survey towards 6.7 GHz methanol masers. *A&A*, 413(1):233–240, 2004. ISSN 0004-6361. doi: 10.1051/0004-6361:20031451.

- B. J. Bok and E. F. Reilly. Small Dark Nebulae. *Astrophys. J.*, 105:255, 1947. ISSN 0004-637X. doi: 10.1086/144901.
- I. A. Bonnell and M. R. Bate. Accretion in stellar clusters and the collisional formation of massive stars. *MNRAS*, 336(2):659–669, 2002. ISSN 00358711. doi: 10.1046/j.1365-8711.2002.05794.x.
- I. A. Bonnell, M. R. Bate, C. J. Clarke, and J. E. Pringle. Accretion and the stellar mass spectrum in small clusters. *MNRAS*, 285(1):201–208, 1997. ISSN 1098-6596. doi: 10.1017/CBO9781107415324.004.
- I. A. Bonnell, M. R. Bate, C. J. Clarke, and J. E. Pringle. Competitive accretion in embedded stellar clusters. *MNRAS*, 323(4):785–794, 2001. ISSN 00358711. doi: 10.1046/j.1365-8711.2001.04270.x.
- S. L. Breen and S. P. Ellingsen. Constraining the properties of 1.2-mm dust clumps that contain luminous water masers. *MNRAS*, 416(1):178–204, 2011. ISSN 00358711. doi: 10.1111/j.1365-2966.2011.19020.x.
- S. L. Breen, S. P. Ellingsen, J. L. Caswell, and B. E. Lewis. 12.2-GHz methanol masers towards 1.2-mm dust clumps: Quantifying high-mass star formation evolutionary schemes. *MNRAS*, 401(4):2219–2244, 2010. ISSN 00358711. doi: 10.1111/j.1365-2966.2009.15831.x.
- S. L. Breen, S. P. Ellingsen, J. L. Caswell, J. A. Green, G. A. Fuller, M. A. Voronkov, L. J. Quinn, and A. Avison. Statistical properties of 12.2GHz methanol masers associated with a complete sample of 6.7GHz methanol masers. *ApJ*, 733(2), 2011. ISSN 15384357. doi: 10.1088/0004-637X/733/2/80.
- S. L. Breen, S. P. Ellingsen, J. L. Caswell, J. A. Green, M. A. Voronkov, A. Avison, G. A. Fuller, and L. J. Quinn. 12.2-GHz methanol maser MMB follow-up catalogue - I. Longitude range 330-10. *MNRAS*, 421:1703–1735, 2012a. ISSN 13652966. doi: 10.1093/mnras/stw965.
- S. L. Breen, S. P. Ellingsen, J. L. Caswell, J. A. Green, M. A. Voronkov, G. A. Fuller, L. J. Quinn, and A. Avison. 12.2-GHz methanol maser methanol multibeam follow-up catalogue - II. Longitude range 186-330. *MNRAS*, 426(3):2189–2207, 2012b. ISSN 00358711. doi: 10.1111/j.1365-2966.2012.21759.x.
- S. L. Breen, S. P. Ellingsen, Y. Contreras, J. A. Green, J. L. Caswell, J. B. Stevens, J. R. Dawson, and M. A. Voronkov. Confirmation of the exclusive association between

- 6.7-GHz methanol masers and high-mass star formation regions. *MNRAS*, 435(1): 524–530, 2013. ISSN 00358711. doi: 10.1093/mnras/stt1315.
- S. L. Breen, S. P. Ellingsen, J. L. Caswell, J. A. Green, M. A. Voronkov, A. Avison, G. A. Fuller, L. J. Quinn, and A. Titmarsh. 12.2-GHz methanol maser MMB follow-up catalogue - III. Longitude range 10 to 20. *MNRAS*, 438(4):3368–3382, 2014. ISSN 00358711. doi: 10.1093/mnras/stt2447.
- S. L. Breen, G. A. Fuller, J. L. Caswell, J. A. Green, A. Avison, S. P. Ellingsen, M. D. Gray, M. Pestalozzi, L. J. Quinn, A. M.S. Richards, M. A. Thompson, and M. A. Voronkov. The 6-GHz methanol multibeam maser catalogue-V. Galactic longitudes 20-60. *MNRAS*, 450(4):4109–4136, 2015. ISSN 13652966. doi: 10.1093/mnras/stv847.
- S. L. Breen, S. P. Ellingsen, J. L. Caswell, J. A. Green, M. A. Voronkov, A. Avison, G. A. Fuller, and L. J. Quinn. 12.2-GHz methanol maser MMB follow-up catalogue - IV. Longitude range 20-60. *MNRAS*, 459(4):4066–4087, 2016. ISSN 13652966. doi: 10.1093/mnras/stw965.
- S. L. Breen, Y. Contreras, S. P. Ellingsen, J. A. Green, A. J. Walsh, A. Avison, S. N. Longmore, G. A. Fuller, M. A. Voronkov, J. Horton, and A. Kroon. The 6-GHz Multibeam Maser Survey - III. Comparison between the MMB and HOPS. *MNRAS*, 474(3):3898–3911, 2018. ISSN 13652966. doi: 10.1093/mnras/stx3051.
- J. Cami, J. Bernard-Salas, E. Peeters, and S. E. Malek. Fullerenes in Circumstellar and Interstellar Environments. In José Cernicharo and Rafael Bachiller, editors, *The Molecular Universe*, volume 280 of *IAU Symposium*, pages 216–227, Dec 2011. doi: 10.1017/S1743921311024999.
- J. L. Caswell. OH 1720-MHz masers in southern star-forming regions. *Monthly Notices of the Royal Astronomical Society*, 349(1):99–114, Mar 2004. doi: 10.1111/j.1365-2966.2004.07472.x.
- J. L. Caswell. Precise Positions of Methanol Masers. *Publ. Astron. Soc. Aust.*, 26(04): 454–467, 2009. ISSN 1323-3580. doi: 10.1071/as09013.
- J L Caswell, G A Fuller, J A Green, A Avison, S L Breen, K J Brooks, M G Burton, A Chrysostomou, J Cox, P J Diamond, S P Ellingsen, M D Gray, M G Hoare, M. R.W. Mashed, N. M. McClure-Griffiths, M R Pestalozzi, C J Phillips, L Quinn, M A Thompson, M A Voronkov, A J Walsh, D. Ward-Thompson, D. Wong-McSweeney, J A Yates, and R J Cohen. The 6-GHz methanol multibeam maser cat-

- alogue - I. Galactic Centre region, longitudes 345 to 6. *MNRAS*, 404(2):1029–1060, 2010. ISSN 00358711. doi: 10.1111/j.1365-2966.2010.16339.x.
- J. L. Caswell, G. A. Fuller, J. A. Green, A. Avison, S. L. Breen, S. P. Ellingsen, M. D. Gray, M. R. Pestalozzi, L. Quinn, M. A. Thompson, and M. A. Voronkov. The 6-GHz methanol multibeam maser catalogue - III. Galactic longitudes 330 to 345. *MNRAS*, 417(3):1964–1995, 2011. ISSN 00358711. doi: 10.1111/j.1365-2966.2011.19383.x.
- J. L. Caswell, J. A. Green, and C. J. Phillips. Parkes full polarization spectra of OH masers - I. galactic longitudes 350 through the galactic centre to 41. *MNRAS*, 431(2):1180–1219, 2013. ISSN 00358711. doi: 10.1093/mnras/stt239.
- S. Cazaux and A. G. G. M. Tielens. Molecular Hydrogen Formation in the Interstellar Medium. *Astrophys. J.*, 575(1):L29–L32, 2002. ISSN 0004637X. doi: 10.1086/342607.
- E. T. Chambers, J. M. Jackson, J. M. Rathborne, and R. Simon. Star formation activity of cores within infrared dark clouds. *Astrophys. Journal, Suppl. Ser.*, 181(2):360–390, 2009. ISSN 00670049. doi: 10.1088/0067-0049/181/2/360.
- A. C. Cheung, D. M. Rank, C. H. Townes, D. D. Thornton, and W. J. Welch. Detection of NH₃ Molecules in the Interstellar Medium by Their Microwave Emission. *Phys. Rev. Lett.*, 21(25):1701–1705, Dec 1968. doi: 10.1103/PhysRevLett.21.1701.
- A. C. Cheung, D. M. Rank, C. H. Townes, D. D. Thornton, and W. J. Welch. Detection of Water in Interstellar Regions by its Microwave Radiation. *Nature*, 221(5181):626–628, Feb 1969. doi: 10.1038/221626a0.
- R.-A. Chira, H. Beuther, H. Linz, F. Schuller, C. M. Walmsley, K. M. Menten, and L. Bronfman. Characterization of infrared dark clouds. *Astron. Astrophys.*, 552:A40, 2013. ISSN 0004-6361. doi: 10.1051/0004-6361/201219567.
- E. Churchwell, B. L. Babler, M. R. Meade, B. A. Whitney, R. Benjamin, R. Indebetouw, C. Cyganowski, T. P. Robitaille, M. Povich, C. Watson, and S. Bracker. The Spitzer/GLIMPSE Surveys: A New View of the Milky Way. *Publ. Astron. Soc. Pacific*, 121(877):213–230, 2009. ISSN 0004-6280. doi: 10.1086/597811.
- M. J. Claussen, B. A. Wilking, P. J. Benson, A. Wootten, P. C. Myers, and S. Terebey. A Monthly Survey of Water Masers Associated with Low-Mass Stars. *Astrophys. J. Suppl. v.106*, 106:111, 1996. ISSN 00670049. doi: 10.1086/192330.
- M. J. Claussen, W. M. Goss, D. A. Frail, and K. Desai. The Sizes of 1720 MHz OH Masers: VLBA and MERLIN Observations of the Supernova Remnants W44 and W28. *The Astrophysical Journal*, 522(1):349–356, Sep 1999. doi: 10.1086/307641.

- D. P. Clemens, J. Lin Yun, and M. H. Heyer. Bok Globules and Small Molecular Clouds: Deep IRAS Photometry and 12CO Spectroscopy. *Astrophys. J. Suppl. Ser.*, 75:877–904, 1991.
- C. Codella, A. Lorenzani, A. T. Gallego, R. Cesaroni, and L. Moscadelli. The association between masers and outflows in massive star forming regions. *A&A*, 417(2): 615–624, 2004. ISSN 0004-6361. doi: 10.1051/0004-6361:20035608.
- Y. Contreras, F. Schuller, J. S. Urquhart, T. Csengeri, F. Wyrowski, H. Beuther, S. Bontemps, L. Bronfman, T. Henning, K. M. Menten, P. Schilke, C. M. Walmsley, M. Wienen, J. Tackenberg, and H. Linz. ATLASGAL compact source catalogue: 330 < < 21. *A&A*, 549:A45, 2013. ISSN 0004-6361. doi: 10.1051/0004-6361/201220155.
- Y. Contreras, J. M. Rathborne, A. Guzman, J. Jackson, S. Whitaker, P. Sanhueza, and J. Foster. Characterizing the properties of cluster precursors in the MALT90 survey. *MNRAS*, 466(1):340–354, 2017. ISSN 13652966. doi: 10.1093/mnras/stw3110.
- H. D.B. Cooper, S. L. Lumsden, R. D. Oudmaijer, M. G. Hoare, A. J. Clarke, J. S. Urquhart, J. C. Mottram, T. J.T. Moore, and B. Davies. The RMS survey: Near-IR spectroscopy of massive young stellar objects. *Mon. Not. R. Astron. Soc.*, 430(2): 1125–1157, 2013. ISSN 00358711. doi: 10.1093/mnras/sts681.
- P. A. Crowther, O. Schnurr, R. Hirschi, N. Yusof, R. J. Parker, S. P. Goodwin, and H. A. Kassim. The R136 star cluster hosts several stars whose individual masses greatly exceed the accepted 150 M. stellar mass limit. *Mon. Not. R. Astron. Soc.*, 408(2):731–751, 2010. ISSN 00358711. doi: 10.1111/j.1365-2966.2010.17167.x.
- T. Csengeri, J. S. Urquhart, F. Schuller, F. Motte, S. Bontemps, F. Wyrowski, K. M. Menten, L. Bronfman, H. Beuther, Th. Henning, L. Testi, A. Zavagno, and M. Walmsley. The ATLASGAL survey: a catalog of dust condensations in the Galactic plane. *A&A*, 565:A75, 2014. ISSN 0004-6361. doi: 10.1051/0004-6361/201322434.
- T. Csengeri, S. Leurini, F. Wyrowski, J. S. Urquhart, K. M. Menten, and Et Al. ATLASGAL-selected massive clumps in the inner Galaxy: II. Characterisation of different evolutionary stages and their SiO emission. *A&A*, 586:149, 2016. ISSN 14320746. doi: 10.1051/0004-6361/201526841.
- R. M. Cutri, M. F. Skrutskie, S. van Dyk, C. A. Beichman, J. M. Carpenter, T. Chester, L. Cambresy, T. Evans, J. Fowler, J. Gizis, E. Howard, J. Huchra, T. Jarrett, E. L. Kopan, J. D. Kirkpatrick, R. M. Light, K. A. Marsh, H. McCallon, S. Schneider, R. Stiening, M. Sykes, M. Weinberg, W. A. Wheaton, S. Wheelock, and N. Zacarias. *2MASS All Sky Catalog of point sources*. 2003.

- C. J. Cyganowski, B. A. Whitney, E. Holden, E. Braden, C. L. Brogan, E. Churchwell, R. Indebetouw, D. F. Watson, B. L. Babler, R. Benjamin, M. Gomez, M. R. Meade, M. S. Povich, T. P. Robitaille, and C. Watson. A catalog of extended green objects in the glimpse survey: A new sample of massive young stellar object outflow candidates. *Astron. J.*, 136(6):2391–2412, 2008. ISSN 00046256. doi: 10.1088/0004-6256/136/6/2391.
- E. Dartois. Observations of Interstellar Carbon Compounds. In C. Joblin and A. G. G. M. Tielens, editors, *EAS Publications Series*, volume 46, pages 381–391, Mar 2011. doi: 10.1051/eas/1146039.
- J. M. De Buizer, R. K. Pina, and C. M. Telesco. MidInfrared Imaging of Starforming Regions Containing Methanol Masers. *Astrophys. J. Suppl. Ser.*, 130(1993):437–461, 2000. ISSN 0067-0049. doi: 10.1086/317351.
- F. Dell’Agli, P. Ventura, R. Schneider, M. Di Criscienzo, D. A. García-Hernández, C. Rossi, and E. Brocato. Asymptotic giant branch stars in the Large Magellanic Cloud: evolution of dust in circumstellar envelopes. *MNRAS*, 447(4):2992–3015, Mar 2015. doi: 10.1093/mnras/stu2559.
- D. F. Dickinson. Water emission from infrared dark stars. *Astrophys. J. Suppl. Ser.*, 30:259–271, 1976.
- M. K. Dunham, E. Rosolowsky, Neal J. Evans, C. Cyganowski, and J. S. Urquhart. The Bolocam Galactic Plane Survey. VII. Characterizing the properties of massive star-forming regions. *Astrophys. J.*, 741(2), 2011. ISSN 15384357. doi: 10.1088/0004-637X/741/2/110.
- L. Dunne, S. Eales, R. Ivison, H. Morgan, and M. Edmunds. The origin of cosmic dust. *Nature*, 424:285, 2003. ISSN 00167029.
- M. Durjasz, M. Szymczak, and M. Olech. A highly variable methanol maser in G111.2560.770. *MNRAS*, 485(1):777–783, 2019. ISSN 0035-8711. doi: 10.1093/mnras/stz472.
- D. J. Eden, T. J. T. Moore, R. Plume, J. S. Urquhart, M. A. Thompson, H. Parsons, J. T. Dempsey, A. J. Rigby, L. K. Morgan, H. S. Thomas, D. Berry, J. Buckle, C. M. Brunt, H. M. Butner, D. Carretero, A. Chrysostomou, M. J. Currie, H. M. DeVilliers, M. Fich, A. G. Gibb, M. G. Hoare, T. Jenness, G. Manser, J. C. Mottram, C. Natario, F. Olguin, N. Peretto, M. Pestalozzi, D. Polychroni, R. O. Redman, C. Salji, L. J. Summers, K. Tahani, A. Traficante, J. DiFrancesco, A. Evans, G. A.

- Fuller, D. Johnstone, G. Joncas, S. N. Longmore, P. G. Martin, J. S. Richer, B. Wierling, G. J. White, and M. Zhu. The JCMT Plane Survey: First complete data release - emission maps and compact source catalogue. *MNRAS*, 469:2163–2183, 2017. ISSN 0035-8711. doi: 10.1093/mnras/stx874.
- M. P. Egan, S. D. Price, and K. E. Kraemer. The Midcourse Space Experiment Point Source Catalog Version 2.3. In *American Astronomical Society Meeting Abstracts*, volume 203, page 57.08, Dec 2003.
- M. Elitzur, P. Goldreich, and N. Scoville. OH-IR stars. II. A model for the 1612 MHz masers. *The Astrophysical Journal*, 205:384–396, Apr 1976. doi: 10.1086/154289.
- M. Elitzur, D. J. Hollenbach, and C. F. McKee. H₂O masers in star-forming regions. *ApJ*, 346:983–990, 1989.
- S. P. Ellingsen. A GLIMPSE -based search for 6 . 7-GHz methanol masers and the lifetime of their spectral features. *MNRAS*, 377:571–583, 2007. doi: 10.1111/j.1365-2966.2007.11615.x.
- S. P. Ellingsen, M. A. Voronkov, D. M. Cragg, and A. M. Sobolev. Investigating high-mass star formation through maser surveys. *Proc. Int. Astron. Union*, 242:213–217, 2007. doi: 10.1017/S1743921307012999.
- B. Elmegreen. Triggered Star Formation. In G. Tenorio-Tagle, M. Prieto, and F. Sanchez, editors, *Star Formation in Stellar Systems*, page 381, Jan 1992.
- B. G. Elmegreen. Triggering the Formation of Young Clusters. In Douglas Paul Geisler, Eva K. Grebel, and Dante Minniti, editors, *Extragalactic Star Clusters*, volume 207 of *IAU Symposium*, page 390, Jan 2002.
- B. G. Elmegreen and C. J. Lada. Sequential formation of subgroups in OB associations. *ApJ*, 214:725–741, Jun 1977. doi: 10.1086/155302.
- B. G. Elmegreen and J. Scalo. Interstellar Turbulence I: Observations and Processes. *Annu. Rev. Astron. Astrophys*, 42:211, 2004. ISSN 0066-4146. doi: 10.1146/annurev.astro.41.011802.094859.
- H. I. Ewen and E. M. Purcell. Observation of a line in the galactic radio spectrum: Radiation from galactic hydrogen at 1,420 Mc./sec. *Nature*, 168:365, 1951. ISSN 00280836. doi: 10.1038/168356a0.

- G. G. Fazio, J. L. Hora, S. P. Willner, J. R. Stauffer, M. L. Ashby, Z. Wang, E. V. Tollestrup, J. L. Pipher, W. J. Forrest, C. R. McCreight, S. H. Moseley, W. F. Hoffmann, P. Eisenhardt, and E. L. Wright. Infrared array camera (IRAC) for the Space Infrared Telescope Facility (SIRTF). In Albert M. Fowler, editor, *Proc. SPIE*, volume 3354 of *Society of Photo-Optical Instrumentation Engineers (SPIE) Conference Series*, pages 1024–1031, Aug 1998. doi: 10.1117/12.317225.
- K. M. Ferrière. The interstellar environment of our galaxy. *Rev. Mod. Phys.*, 73(4): 1031–1066, 2001. ISSN 00346861. doi: 10.1103/RevModPhys.73.1031.
- J. R. Forster and J. L. Caswell. OH and H₂O masers in 74 star-forming regions. *Astron. Astrophys. Suppl. Ser.*, 137:43–49, 1999. ISSN 03650138. doi: 10.1051/aas:1999479.
- R. K. Friesen, J. Di Francesco, Y. L. Shirley, and P. C. Myers. The initial conditions of clustered star formation. I. NH₃ observations of dense cores in ophiuchus. *Astrophys. J.*, 697(2):1457–1480, 2009. ISSN 15384357. doi: 10.1088/0004-637X/697/2/1457.
- R. K. Friesen, J. E. Pineda, co-PIs, E. Rosolowsky, F. Alves, A. Chacón-Tanarro, H. How-Huan Chen, M. Chun-Yuan Chen, J. Di Francesco, J. Keown, H. Kirk, A. Punanova, Y. Seo, Yancy Shirley, A. Ginsburg, C. Hall, S. S. R. Offner, A. Singh, H. G. Arce, P. Caselli, A. A. Goodman, P. G. Martin, C. Matzner, P. C. Myers, E. Redaelli, and GAS Collaboration. The Green Bank Ammonia Survey: First Results of NH₃ Mapping of the Gould Belt. *ApJ*, 843(1):63, Jul 2017. doi: 10.3847/1538-4357/aa6d58.
- D. Fulvio, S. Góbi, C. Jäger, Á. Kereszturi, and T. Henning. Laboratory Experiments on the Low-temperature Formation of Carbonaceous Grains in the ISM. *Astrophys. J. Suppl. Ser.*, 233(1):14, 2017. ISSN 1538-4365. doi: 10.3847/1538-4365/aa9224.
- G. Garay and S. Lizano. Massive Stars: Their Environment and Formation. *Publ. Astron. Soc. Pacific*, 111:1049–1087, 1999. ISSN 0004-6280. doi: 10.1086/316416.
- G. Garay, K. J. Brooks, D. Mardones, and R. P. Norris. A Multiwavelength Study of Young Massive Star-Forming Regions . I . The Ionized Gas Content. *ApJ*, 651: 914–932, 2006.
- R. Genzel, D. Dowell, P. T. P. Ho, and J. Bieging. NH₃ in Orion-KL: A New Interpretation. *ApJ*, 259:L103, 1982.
- A. Ginsburg and J. Mirocha. PySpecKit: Python Spectroscopic Toolkit, Sep 2011.
- S. Goedhart, M. J. Gaylard, and D. J. Van Der Walt. Periodic flares in the methanol maser source G9.62+0.20E. *MNRAS*, 339:L33–L36, 2003.

- J. A. Green, J. L. Caswell, G. A. Fuller, A. Avison, S. L. Breen, K. Brooks, M. G. Burton, A. Chrysostomou, J. Cox, P. J. Diamond, S. P. Ellingsen, M. D. Gray, M. G. Hoare, M. R.W. Masheder, N. M. McClure-Griffiths, M. Pestalozzi, C. Phillips, L. Quinn, M. A. Thompson, M. A. Voronkov, A. Walsh, D. Ward-Thompson, D. Wong-McSweeney, J. A. Yates, and R. J. Cohen. The 6-GHz multibeam maser survey - I. Techniques. *MNRAS*, 392(2):783–794, 2009. ISSN 00358711. doi: 10.1111/j.1365-2966.2008.14091.x.
- J. A. Green, J. L. Caswell, G. A. Fuller, A. Avison, S. L. Breen, S. P. Ellingsen, M. D. Gray, M. Pestalozzi, L. Quinn, M. A. Thompson, and M. A. Voronkov. The 6-GHz methanol multibeam maser catalogue - II. Galactic longitudes 6 to 20. *MNRAS*, 409(3):913–935, dec 2010. ISSN 00358711. doi: 10.1111/j.1365-2966.2010.17376.x.
- J. A. Green, J. L. Caswell, G. A. Fuller, A. Avison, S. L. Breen, S. P. Ellingsen, M. D. Gray, M. Pestalozzi, L. Quinn, M. A. Thompson, and M. A. Voronkov. The 6-GHz methanol multibeam maser catalogue - IV. Galactic longitudes 186-330 including the Orion-Monoceros region. *MNRAS*, 420(4):3108–3125, 2012. ISSN 00358711. doi: 10.1111/j.1365-2966.2011.20229.x.
- J. A. Green, S. L. Breen, G. A. Fuller, N. M. McClure-Griffiths, S. P. Ellingsen, M. A. Voronkov, A. Avison, K. Brooks, M. G. Burton, A. Chrysostomou, J. Cox, P. J. Diamond, M. D. Gray, M. G. Hoare, M. R.W. Masheder, M. Pestalozzi, C. Phillips, L. J. Quinn, A. M.S. Richards, M. A. Thompson, A. J. Walsh, D. Ward-Thompson, D. Wong-McSweeney, and J. A. Yates. The 6-GHz multibeam maser survey - II. Statistical analysis and Galactic distribution of 6668-MHz methanol masers. *MNRAS*, 469(2):1383–1402, 2017. ISSN 13652966. doi: 10.1093/mnras/stx887.
- M. Griffin, A. Abergel, and A. Abreu. The Herschel-SPIRE instrument and its in-flight performance. *A&A*, 518:L3, 2010.
- A. E. Guzmán, P. Sanhueza, Y. Contreras, H. A. Smith, J. M. Jackson, S. Hoq, and J. M. Rathborne. Far-infrared dust temperatures and column densities of the MALT90 molecular clump sample. *Astrophys. J.*, 815(2):130, 2015. ISSN 15384357. doi: 10.1088/0004-637X/815/2/130.
- Eric Herbst and William Klemperer. The Formation and Depletion of Molecules in Dense Interstellar Clouds. *ApJ*, 185:505–534, October 1973. doi: 10.1086/152436.
- A. Hewish, S. J. Bell, J. D H Pilkington, P. F. Scott, and R. A. Collins. Observation of a rapidly pulsating radio source. *Nature*, 217:709H, 1968. ISSN 00280836. doi: 10.1038/217709a0.

- T Hill, M G Burton, V Minier, M A Thompson, A J Walsh, M. Hunt-Cunningham, and G Garay. Millimetre continuum observations of southern massive star formation regions - I. SIMBA observations of cold cores. *MNRAS*, 363(2):405–451, 2005. ISSN 00358711. doi: 10.1111/j.1365-2966.2005.09347.x.
- P.T. P. Ho and C. H. Townes. Interstellar Ammonia. *Annu. Rev. Astron. Astrophys.*, 21(1):239–270, 1983. ISSN 0066-4146. doi: 10.1146/annurev.aa.21.090183.001323.
- T. Hogge, J. Jackson, I. Stephens, S. Whitaker, J. Foster, M. Camarata, D. Anish Roshi, J. Di Francesco, S. Longmore, R. Loughnane, T. Moore, J. Rathborne, P. Sanchez, and A. Walsh. The Radio Ammonia Mid-plane Survey (RAMPS) Pilot Survey. *ApJS*, 237(2):27, Aug 2018. doi: 10.3847/1538-4365/aacf94.
- W. S. Holland, D. Bintley, E. L. Chapain, A. Chrysostomou, G. R. Davis, J. T. Dempsey, W. D. Duncan, M. Fich, P. Friberg, M. Halpern, K. D. Irwin, T. Jenness, B. D. Kelly, M. J. MacIntosh, E. I. Robson, D. Scott, and P. A. R. Ade. SCUBA-2: the 10 000 pixel bolometer camera on the James Clerk Maxwell Telescope. *MNRAS*, 430(4):2513–2533, 2013. ISSN 0035-8711. doi: 10.1093/mnras/sts612.
- D. Hollenbach and C. F. McKee. Molecule Formation and Infrared Emission in Fast Interstellar Shocks. III. Results for J Shocks in Molecular Clouds. *The Astrophysical Journal*, 342:306, Jul 1989. doi: 10.1086/167595.
- J. M. Hollis, P. R. Jewell, F. J. Lovas, A. Remijan, and H. Møllendal. Green Bank Telescope Detection of New Interstellar Aldehydes: Propenal and Propanal. *The Astrophysical Journal*, 610(1):L21–L24, Jul 2004. doi: 10.1086/423200.
- B. Hu, K. M. Menten, Y. Wu, A. Bartkiewicz, K. Rygl, M. J. Reid, J. S. Urquhart, and X. Zheng. On the relationship of UCHII regions and class II methanol masers. I. Source catalogs. *Astrophys. J.*, 833(1):18, 2016. doi: 10.3847/0004-637x/833/1/18.
- C. Indrani and A. A. Deshpande. The large scale structure of the Galactic magnetic field. *New A*, 4(1):33–40, Feb 1999. doi: 10.1016/S1384-1076(98)00038-4.
- J. M. Jackson, J. M. Rathborne, R. Y. Shah, R. Simon, T. M. Bania, D. P. Clemens, E. T. Chambers, A. M. Johnson, M. Dormody, R. Lavoie, and M. H. Heyer. The Boston UniversityFive College Radio Astronomy Observatory Galactic Ring Survey. *Astrophys. J. Suppl. Ser.*, 163(1):145–159, 2006. ISSN 0067-0049. doi: 10.1086/500091.
- K. G. Jansky. Radio waves from outside the solar system [9]. *Nature*, 132(3323):66, 1933a. ISSN 00280836. doi: 10.1038/132066a0.

- K. G. Jansky. Electrical Phenomena that apparently are of Interstellar Origin. *Pop. Astron.*, 41:548, 1933b.
- R. C. Jones. The general theory of bolometer performance. *Journal of the Optical Society of America (1917-1983)*, 43(1):1–10, Jan 1953.
- P. M.W. Kalberla and J. Kerp. The HI Distribution of the Milky Way. *Annu. Rev. Astron. Astrophys.*, 47(1):27–61, 2009. ISSN 0066-4146. doi: 10.1146/annurev-astro-082708-101823.
- J. Kauffmann, F. Bertoldi, T. L. Bourke, N. J. Evans, and C. W. Lee. MAMBO mapping of Spitzer c2d small clouds and cores. *A&A*, 487(3):993–1017, 2008. ISSN 0004-6361. doi: 10.1051/0004-6361:200809481.
- J. Kauffmann, T. Pillai, R. Shetty, P. C. Myers, and A. A. Goodman. The mass-size relation from clouds to cores. I. A new probe of structure in molecular clouds. *ApJ*, 712(2):1137–1146, 2010. ISSN 15384357. doi: 10.1088/0004-637X/712/2/1137.
- J. Kauffmann, T. Pillai, and P. F. Goldsmith. Low virial parameters in molecular clouds: Implications for high-mass star formation and magnetic fields. *Astrophys. J.*, 779(2), 2013. ISSN 15384357. doi: 10.1088/0004-637X/779/2/185.
- R. C. Kennicutt. The role of massive stars in astrophysics. *Proc. Int. Astron. Union*, 1(S227):3–11, 2005. ISSN 17439221. doi: 10.1017/S1743921305004308.
- R. S. Klessen and S. C.O. Glover. Physical Processes in the Interstellar Medium. *Astrochem. Astrobiol.*, 43:85, 2016. doi: 10.1007/978-3-642-31730-9_3.
- R. F. Knacke. Carbonaceous compounds in interstellar dust. *Nature*, 269(5624):132–134, Sep 1977. doi: 10.1038/269132a0.
- C. Koen. On the upper limit on stellar masses in the Large Magellanic Cloud cluster R136. *Mon. Not. R. Astron. Soc.*, 365(2):590–594, 2006. ISSN 00358711. doi: 10.1111/j.1365-2966.2005.09739.x.
- C. König, J. S. Urquhart, T. Csengeri, S. Leurini, F. Wyrowski, A. Giannetti, M. Wienen, T. Pillai, J. Kauffmann, K. M. Menten, and F. Schuller. ATLASGAL-selected massive clumps in the inner Galaxy III. Dust Continuum Characterization of an Evolutionary Sample. *A&A*, 599(A139):1–33, 2017. ISSN 14320746. doi: 10.1051/0004-6361/201526841.

- M. R. Krumholz and B. Burkhart. Is turbulence in the interstellar medium driven by feedback or gravity? An observational test. *Mon. Not. R. Astron. Soc.*, 458(2): 1671–1677, 2016. ISSN 13652966. doi: 10.1093/mnras/stw434.
- G. P. Kuiper. The empirical mass-luminosity relation g. p. kuiper. *ApJ*, 88:472, 1938.
- S. Kurtz. Hypercompact HII regions. *Proc. Int. Astron. Union*, 227:111–119, 2005.
- J. H. Lacy, R. Knacke, T. R. Geballe, and A. T. Tokunaga. Detection of absorption by H₂ in molecular clouds: A direct measurement of the H₂:CO ratio. *Astrophys. J.*, 428:L69, 1994. ISSN 0004-637X. doi: 10.1086/187395.
- W. Langer. The carbon monoxide abundance in interstellar clouds. *Astrophys. J.*, 206: 699, 1976. ISSN 0004-637X. doi: 10.1086/154430.
- R. B Larson. Turbulence and star formation in molecular clouds. *Mon. Not. R. Astron. Soc.*, 194:809–826, 1981. ISSN 0035-8711. doi: 10.1093/mnras/194.4.809.
- J. K. Lee, A. J. Walsh, M. G. Burton, and M. C B Ashley. Discovery of molecular hydrogen line emission associated with methanol maser emission. *MNRAS*, 324(4): 1102–1108, 2001. ISSN 00358711. doi: 10.1046/j.1365-8711.2001.04396.x.
- A. Leger and J. L. Puget. Identification of the “unidentified” IR emission features of interstellar dust ? *A&A*, 500:279–282, Aug 1984.
- S. N. Longmore, M. G. Burton, P. J. Barnes, T. Wong, C. R. Purcell, and J. Ott. Multiwavelength observations of southern hot molecular cores traced by methanol masers - I. Ammonia and 24-GHz continuum data. *MNRAS*, 379(2):535–572, Aug 2007. doi: 10.1111/j.1365-2966.2007.11850.x.
- S. N. Longmore, A. J. Walsh, C. R. Purcell, D. J. Burke, J. Henshaw, D. Walker, J. Urquhart, A. T. Barnes, M. Whiting, M. G. Burton, S. L. Breen, T. Britton, K. J. Brooks, M. R. Cunningham, J. A. Green, L. Harvey-Smith, L. Hindson, M. G. Hoare, B. Indermuehle, P. A. Jones, N. Lo, V. Lowe, T. J.T. Moore, M. A. Thompson, and M. A. Voronkov. H₂O Southern Galactic Plane Survey (HOPS): Paper III - properties of dense molecular gas across the inner Milky Way. *Mon. Not. R. Astron. Soc.*, 470(2):1462–1490, 2017. ISSN 13652966. doi: 10.1093/mnras/stx1226.
- S. L. Lumsden, M. G. Hoare, J. S. Urquhart, R. D. Oudmaijer, B. Davies, J. C. Mottram, H. D.B. Cooper, and T. J.T. Moore. The red MSX source survey: The massive young stellar population of our galaxy. *Astrophys. Journal, Suppl. Ser.*, 208 (1), 2013. ISSN 00670049. doi: 10.1088/0067-0049/208/1/11.

- M.-M. Mac Low and R. S. Klessen. Control of star formation by supersonic turbulence. *Reviews of Modern Physics*, 76(1):125–194, Jan 2004. doi: 10.1103/RevModPhys.76.125.
- J. G. Mangum, A. Wootten, and L. G. Mundy. Synthesis imaging of the DR 21 (OH) cluster. II - Thermal ammonia and water maser emission. *Astrophys. J.*, 388:467, 1992. ISSN 0004-637X. doi: 10.1086/171167.
- J. S. Mathis and G. Whiffen. Composite Interstellar Grains. *ApJ*, 341:808–822, 1989.
- T. A. Matthews and A. R. Sandage. Optical Identification of 3c 48, 3c 196, and 3c 286 with Stellar Objects. *Astrophys. J.*, 138:30M, 1963. ISSN 0004-637X. doi: 10.1086/147615.
- C. F. McKee and J. C. Tan. The Formation of Massive Stars from Turbulent Cores. *Astrophys. J.*, 585(2):850–871, 2003. ISSN 0004-637X. doi: 10.1086/346149.
- A. McKellar. Molecular Lines from the Lowest States of Diatomic Molecules Composed of Atoms Probably Present in Interstellar Space. *Publications of the Dominion Astrophysical Observatory Victoria*, 7:251, Jan 1941.
- K. M. Menten. The discovery of a new, very strong, and widespread interstellar methanol maser line. *ApJ*, 380:L75–L78, 1991. ISSN 0004-637X. doi: 10.1086/186177.
- D. Mihalas and J. Binney. *Galactic astronomy. Structure and kinematics*. 1981.
- T. J. Millar, P. D. Brown, H. Olofsson, and A. Hjalmarsen. The detection of ethanol in W 51M. *Astronomy and Astrophysics*, 205:L5–L7, Oct 1988.
- T. Minamidani, N. Mizuno, Y. Mizuno, A. Kawamura, T. Onishi, T. Hasegawa, K. Tatematsu, M. Ikeda, Y. Moriguchi, N. Yamaguchi, J. Ott, T. Wong, E. Muller, J. L. Pineda, A. Hughes, L. Staveley-Smith, U. Klein, A. Mizuno, S. Nikolić, R. S. Booth, A. Heikkilä, L. Nyman, M. Lerner, G. Garay, S. Kim, M. Fujishita, T. Kawase, M. Rubio, and Y. Fukui. Submillimeter Observations of Giant Molecular Clouds in the Large Magellanic Cloud: Temperature and Density as Determined from $J = 3-2$ and $J = 1-0$ Transitions of CO. *ApJS*, 175(2):485–508, Apr 2008. doi: 10.1086/524038.
- V. Minier, S. P. Ellingsen, R. P. Norris, and R. S. Booth. The protostellar mass limit for 6.7 GHz methanol masers. *A&A*, 403(3):1095–1100, 2003. ISSN 0004-6361. doi: 10.1051/0004-6361:20030465.

- L. F. Miranda, Y. Gómez, G. Anglada, and J. M. Torrelles. Water-maser emission from a planetary nebula with a magnetized torus. *Nature*, 414(6861):284–286, Nov 2001. doi: 10.1038/35104518.
- S. Molinari, S. Pezzuto, R. Cesaroni, J. Brand, F. Faustini, and L. Testi. The evolution of the spectral energy distribution in massive young stellar objects. *A&A*, 481:345–365, 2008. doi: 10.1051/0004-6361:20078661.
- S. Molinari, B. M. Swinyard, J. Bally, M. J. Barlow, J.-P. Bernard, P. G. Martin, T. J. T. Moore, A. Noriega-Crespo, and the Hi-GAL Consortium. Hi-GAL: the Herschel infrared Galactic Plane Survey. *Publ. Astron. Soc. Pacific*, 122:314–325, 2010. doi: 10.1086/651314.
- S. Molinari, E. Schisano, D. Elia, M. Pestalozzi, A. Traficante, S. Pezzuto, B. M. Swinyard, A. Noriega-Crespo, J. Bally, T. J. T. Moore, R. Plume, A. Zavagno, A. M. di Giorgio, S. J. Liu, G. L. Pilbratt, J. C. Mottram, D. Russeil, L. Piazzo, M. Veneziani, M. Benedettini, L. Calzoletti, F. Faustini, P. Natoli, F. Piacentini, M. Merello, A. Palmese, R. Del Grande, D. Polychroni, K. L. J. Rygl, G. Polenta, M. J. Barlow, J.-P. Bernard, P. G. Martin, L. Testi, B. Ali, P. André, M. T. Beltrán, N. Billot, S. Carey, R. Cesaroni, M. Compiègne, D. Eden, Y. Fukui, P. Garcia-Lario, M. G. Hoare, M. Huang, G. Joncas, T. L. Lim, S. D. Lord, S. Martinavarro-Armengol, F. Motte, R. Paladini, D. Paradis, N. Peretto, T. Robitaille, P. Schilke, N. Schneider, B. Schulz, B. Sibthorpe, F. Strafella, M. A. Thompson, G. Umana, D. Ward-Thompson, and F. Wyrowski. Hi-GAL, the Herschel infrared Galactic Plane Survey: photometric maps and compact source catalogues. *Astron. Astrophys.*, 591:A149, 2016. ISSN 0004-6361. doi: 10.1051/0004-6361/201526380.
- T. J.T. Moore, R. Plume, M. A. Thompson, H. Parsons, J. S. Urquhart, D. J. Eden, J. T. Dempsey, L. K. Morgan, H. S. Thomas, J. Buckle, C. M. Brunt, H. Butner, D. Carretero, A. Chrysostomou, H. M. DeVilliers, M. Fich, M. G. Hoare, G. Manser, J. C. Mottram, C. Nataro, F. Olguin, N. Peretto, D. Polychroni, R. O. Redman, A. J. Rigby, C. Salji, L. J. Summers, D. Berry, M. J. Currie, T. Jenness, M. Pestalozzi, A. Traficante, P. Bastien, J. DiFrancesco, C. J. Davis, A. Evans, P. Friberg, G. A. Fuller, A. G. Gibb, S. Gibson, T. Hill, D. Johnstone, G. Joncas, S. N. Longmore, S. L. Lumsden, P. G. Martin, Q. Nguyn Lu’o’ng, J. E. Pineda, C. Purcell, J. S. Richer, G. H. Schieven, R. Shipman, M. Spaans, A. R. Taylor, S. Viti, B. Weferling, G. J. White, and M. Zhu. The JCMT Plane Survey: Early results from the = 30 field. *MNRAS*, 453(4):4264–4277, 2015. ISSN 13652966. doi: 10.1093/mnras/stv1833.
- J. C. Mottram, M. G. Hoare, S. L. Lumsden, R. D. Oudmaijer, J. S. Urquhart, T.L.

- Sheret, A. J. Clarke, and J Allsopp. The RMS survey: mid-infrared observations of candidate massive YSOs in the southern hemisphere. *Astron. Astrophys.*, 476: 1019–1112, 2007.
- J. C. Mottram, M. G. Hoare, B. Davies, S. L. Lumsden, R. D. Oudmaijer, J. Urquhart, T. J. T. Moore, H. D.B. Cooper, and J. J. Stead. The RMS survey: The luminosity functions and timescales of massive young stellar objects and compact H II regions. *Astrophys. J. Lett.*, 730(2 PART II):6–11, 2011a. ISSN 20418213. doi: 10.1088/2041-8205/730/2/L33.
- J. C. Mottram, M. G. Hoare, J. S. Urquhart, S. L. Lumsden, R. D. Oudmaijer, T. P. Robitaille, T. J.T. Moore, B. Davies, and J. Stead. The Red MSX Source survey: The bolometric fluxes and luminosity distributions of young massive stars. *Astron. Astrophys.*, 525(9):1–12, 2011b. ISSN 14320746. doi: 10.1051/0004-6361/201014479.
- G. Mulas, G. Mallocci, C. Joblin, and C. Cecchi-Pestellini. Polycyclic aromatic hydrocarbons and the extinction curve. volume 46, pages 327–340, 03 2011. doi: 10.1051/eas/1146034.
- F. Navarete, A. Daminieli, C. L. Barbosa, and R. D. Blum. A survey of extended H₂ emission from massive YSOs. *Mon. Not. R. Astron. Soc.*, 450(4):4364–4398, 2015. ISSN 13652966. doi: 10.1093/mnras/stv914.
- R. P. Norris, J. B. Whiteoak, J. L. Caswell, M. H. Wieringa, and R. G. Gough. Synthesis images og 6.7 GHz methanol masers. *ApJ*, 412:222–232, 1993.
- R. P. Norris, S. E. Byleveld, P. J. Diamond, S. P. Ellingsen, R. H. Ferris, R. G. Gough, M. J. Kesteven, P. M. McCulloch, C. J. Phillips, J. E. Reynolds, A. K. Tzioumis, Y. Takahashi, E. R. Troup, and K. J. Wellington. Methanol Masers as Tracers of Circumstellar Disks. *ApJ*, 508(1):275–285, 1998. ISSN 0004-637X. doi: 10.1086/306373.
- M. S. Oey and C. J. Clarke. Statistical Confirmation of a Stellar Upper Mass Limit. *Astrophys. J.*, 620(1):L43–L46, 2005. ISSN 0004-637X. doi: 10.1086/428396.
- A. A. Penzias and R. W. Wilson. A Measurement of Excess Antenna Temperature at 4080 Mc/s. *Astrophys. J.*, 142:419P, 1965. ISSN 0004-637X. doi: 10.1086/148307.
- M. Péroult, A. Omont, G. Simon, P. Séguin, D. Ojha, J. Blommaert, M. Felli, G. Gilmore, F. Guglielmo, H. Habing, S. Price, A. Robin, B. De Batz, C. Cesarsky, D. Elbaz, N. Epchtein, P. Fouqué, S. Guest, D. Levine, A. Pollock, T. Prusti,

- R. Siebenmorgen, L. Testi, and D. Tiphène. First ISOCAM images of the Milky Way. *Astron. Astrophys.*, 315(2):L165–L168, 1996. ISSN 00046361.
- N. Peretto, G. A. Fuller, R. Plume, L. D Anderson, J. Bally, C. Battersby, M. T. Beltran, J.-P. Bernard, L. Calzoletti, A. M. DiGiorgio, F. Faustini, J. M. Kirk, C. Lenfestey, D. Marshall, P. Martin, S. Molinari, L. Montier, F. Motte, I. Ristorcelli, J. A. Rodón, H. A. Smith, A. Traficante, M. Veneziani, D. Ward-Thompson, and L. Wilcock. Mapping the column density and dust temperature structure of IRDCs with Herschel. *Astron. Astrophys.*, 518:L98, 2010. ISSN 0004-6361. doi: 10.1051/0004-6361/201014652.
- G. L. Pilbratt, J. R. Riedinger, and T. Passvogel. An ESA facility for far-infrared and submillimetre astronomy. *A&A*, 518:L1, 2010.
- T. Pillai, F. Wyrowski, S. J. Carey, and K. M. Menten. Ammonia in infrared dark clouds. *A&A*, 450:569–583, 2006. ISSN 0004-6361. doi: 10.1051/0004-6361.
- A. Poglitsch, C. Waelkens, O. H. Bauer, J. Cepa, T. Henning, C. Van Hoof, R. Katterloher, F. Kerschbaum, D. Lemke, E. Renotte, L. Rodriguez, P. Royer, and P. Saraceno. The Photodetector Array Camera & Spectrometer (PACS) for the Herschel space observatory. *Eur. Sp. Agency, (Special Publ. ESA SP, 2(577):11–16*, 2010. ISSN 03796566. doi: 10.1117/12.670654.
- S. D. Price, M. P. Egan, S. J. Carey, D. R. Mizuno, and T. A. Kuchar. MIDCOURSE SPACE EXPERIMENT survey of the Galactic plane. *Astron. J.*, 121(5):2819–2842, 2001. ISSN 00046256. doi: 10.1086/320404.
- C. R. Purcell, S. N. Longmore, A. J. Walsh, M. T. Whiting, S. L. Breen, T. Britton, K. J. Brooks, M. G. Burton, M. R. Cunningham, J. A. Green, L. Harvey-Smith, L. Hindson, M. G. Hoare, B. Indermuehle, P. A. Jones, N. Lo, V. Lowe, C. J. Phillips, M. A. Thompson, J. S. Urquhart, M. A. Voronkov, and G. L. White. The H 2O southern galactic plane survey: NH 3 (1,1) and (2,2) catalogues. *Mon. Not. R. Astron. Soc.*, 426(3):1972–1991, 2012. ISSN 00358711. doi: 10.1111/j.1365-2966.2012.21800.x.
- H. Qiao, J. Li, Z. Shen, X. Chen, and X. Zheng. The catalogues and mid-infrared environment of interstellar OH masers. *Monthly Notices of the Royal Astronomical Society*, 441(4):3137–3147, Jul 2014. doi: 10.1093/mnras/stu776.
- H.-H. Qiao, A. J. Walsh, J. A. Green, S. L. Breen, J. R. Dawson, S. P. Ellingsen, J. F. Gómez, C. H. Jordan, Z.-Q. Shen, V. Lowe, and P. A. Jones. Accurate OH Maser

- Positions from the SPLASH Pilot Region. *The Astrophysical Journal Supplement Series*, 227(2):26, Dec 2016. doi: 10.3847/1538-4365/227/2/26.
- S. E. Ragan, E. A. Bergin, and D. Wilner. Very large array observations of ammonia in infrared-dark clouds. I. Column density and temperature structure. *Astrophys. J.*, 736(2), 2011. ISSN 15384357. doi: 10.1088/0004-637X/736/2/163.
- G. Reber. Cosmic Static. *Proc. IRE*, 28:68, 1940. ISSN 00968390. doi: 10.1109/JRPROC.1942.231700.
- M. J. Reid, K. M. Menten, X. W. Zheng, A. Brunthaler, and Y. Xu. A trigonometric parallax of sgr b2. *Astrophys. J.*, 705(2):1548–1553, 2009. ISSN 15384357. doi: 10.1088/0004-637X/705/2/1548.
- M. J. Reid, T. M. Dame, K. M. Menten, and A. Brunthaler. A Parallax-based Distance Estimator for Spiral Arm Sources. *Astrophys. J.*, 823(2):1–11, 2016. ISSN 0004-637X. doi: 10.3847/0004-637X/823/2/77.
- D. Riebel, S. Srinivasan, B. Sargent, and M. Meixner. The Mass-loss Return from Evolved Stars to the Large Magellanic Cloud. VI. Luminosities and Mass-loss Rates on Population Scales. *ApJ*, 753(1):71, Jul 2012. doi: 10.1088/0004-637X/753/1/71.
- A. J. Rigby, T. J.T. Moore, R. Plume, D. J. Eden, J. S. Urquhart, M. A. Thompson, J. C. Mottram, C. M. Brunt, H. M. Butner, J. T. Dempsey, S. J. Gibson, J. Hatchell, T. Jenness, N. Kuno, S. N. Longmore, L. K. Morgan, D. Polychroni, H. Thomas, G. J. White, and M. Zhu. CHIMPS: The $^{13}\text{CO}/\text{C}^{18}\text{O}$ ($J = 3 - 2$) Heterodyne Inner Milky Way Plane Survey. *Mon. Not. R. Astron. Soc.*, 456(3):2885–2899, 2016. ISSN 13652966. doi: 10.1093/mnras/stv2808.
- J. Roman-Duval, J. M. Jackson, M. Heyer, J. Rathborne, and R. Simon. Physical properties and galactic distribution of molecular clouds identified in the galactic ring survey. *Astrophys. J.*, 723(1):492–507, 2010. ISSN 15384357. doi: 10.1088/0004-637X/723/1/492.
- J. Roman-Duval, J. M. Jackson, M. Heyer, J. Rathborne, and R. Simon. Physical Properties and Galactic Distribution of Molecular Clouds Identified in the Galactic Ring Survey. *ApJ*, 723(1):492–507, Nov 2010. doi: 10.1088/0004-637X/723/1/492.
- E. Rosolowsky, M. K. Dunham, A. Ginsburg, E. T. Bradley, J. Aguirre, J. Bally, C. Battersby, C. Cyganowski, D. Dowell, M. Drosback, N. J. Evans, J. Glenn, P. Harvey, G. S. Stringfellow, J. Walawender, and J. P. Williams. The bolocam galactic plane

- survey. II. Catalog of the image data. *Astrophys. Journal, Suppl. Ser.*, 188(1):123–138, 2010. ISSN 00670049. doi: 10.1088/0067-0049/188/1/123.
- E. W. Rosolowsky, J. E. Pineda, J. B. Foster, M. A. Borkin, J. Kauffmann, P. Caselli, P. C. Myers, and A. A. Goodman. An Ammonia Spectral Atlas of Dense Cores in Perseus. *Astrophys. J. Suppl. Ser.*, 175(2):509–521, 2008. ISSN 0067-0049. doi: 10.1086/524299.
- R. J. Sault, P. J. Teuben, and M. C. H. Wright. A Retrospective View of MIRIAD. In R. A. Shaw, H. E. Payne, and J. J. E. Hayes, editors, *Astronomical Data Analysis Software and Systems IV*, volume 77 of *Astronomical Society of the Pacific Conference Series*, page 433, Jan 1995.
- B. D. Savage and J. S. Mathis. Observed properties of interstellar dust. *Annu. Rev. Astron. Astrophys.*, 17:73, 1979.
- F. Schuller, K. M. Menten, Y. Contreras, F. Wyrowski, P. Schilke, L. Bronfman, T. Henning, C. M. Walmsley, H. Beuther, S. Bontemps, R. Cesaroni, L. Deharveng, G. Garay, F. Herpin, B. Lefloch, H. Linz, D. Mardones, V. Minier, S. Molinari, F. Motte, L.-Å. Nyman, V. Reveret, C. Risacher, D. Russeil, N. Schneider, L. Testi, T. Troost, T. Vasyunina, M. Wienen, A. Zavagno, A. Kovacs, E. Kreysa, G. Siringo, and A. Weiß. ATLASGAL The APEX telescope large area survey of the galaxy at 870um. *A&A*, 504(2):415–427, 2009. ISSN 0004-6361. doi: 10.1051/0004-6361/200811568.
- F. Schuller, T. Csengeri, J. S. Urquhart, A. Duarte-Cabral, P. J. Barnes, A. Giannetti, A. K. Hernandez, S. Leurini, M. Mattern, S. N.X. Medina, C. Agurto, F. Azagra, L. D. Anderson, M. T. Beltrán, H. Beuther, S. Bontemps, L. Bronfman, C. L. Dobbs, M. Dumke, R. Finger, A. Ginsburg, E. Gonzalez, T. Henning, J. Kauffmann, F. Mac-Auliffe, K. M. Menten, F. M. Montenegro-Montes, T. J.T. Moore, E. Muller, R. Parra, J. P. Perez-Beaupuits, A. Pettitt, D. Russeil, A. Sánchez-Monge, P. Schilke, E. Schisano, S. Suri, L. Testi, K. Torstensson, P. Venegas, K. Wang, M. Wienen, F. Wyrowski, and A. Zavagno. SEDIGISM: Structure, excitation, and dynamics of the inner Galactic interstellar medium. *Astron. Astrophys.*, 601(January), 2017. ISSN 14320746. doi: 10.1051/0004-6361/201628933.
- Graham B. I. Scott, Colin G. Freeman, and Murray J. McEwan. The interstellar synthesis of ammonia. *MNRAS*, 290(4):636–638, October 1997. doi: 10.1093/mnras/290.4.636.

- F. H. Shu. Self-similar collapse of isothermal spheres and star formation. *1ApJ*, 214: 488–497, 1977.
- F. H. Shu, F. Adams, and S. Lizano. Star Formation in Molecular Clouds: Observations and Theory. *ARA&A*, 25:23–81, 1987.
- G. Siringo, E. Kreysa, A. Kovacs, F. Schuller, A. Weiß, W. Esch, H.-P. Gemünd, N. Jethava, G. Lundershausen, R. Güsten, K. M. Menten, A. Beelen, F. Bertoldi, J. W. Beeman, E. E. Haller, and A. Colin. The large APEX bolometer camera LABOCA. *A&A*, 497:945–962, 2009. doi: 10.1117/12.787981.
- M. D. Smith. *The Origin of Stars*. 2004. doi: 10.1142/p353.
- L. E. Snyder, D. Buhl, B. Zuckerman, and P. Palmer. Microwave Detection of Interstellar Formaldehyde. *Phys. Rev. Lett.*, 22(13):679–681, Mar 1969. doi: 10.1103/PhysRevLett.22.679.
- A. M. Sobolev, D. M. Cragg, and P. D. Godfrey. Pumping of Class II methanol masers II. The 5₁-6₀ A⁺ transition. *A&A*, 324:211–220, 1997.
- P. M. Solomon, D. B. Sanders, and N. Z. Scoville. Giant Molecular Clouds in the Galaxy: Distribution, Mass, Size and Age. *IAUS*, 84:35S, 1979.
- L. Spitzer. *Physical processes in the interstellar medium*. 1978. doi: 10.1002/9783527617722.
- T. K. Sridharan, H. Beuther, P. Schilke, K. M. Menten, and F. Wyrowski. High-Mass Proto-Stellar Candidates - I : The Sample and Initial Results. *ApJ*, 566:931, 2002. ISSN 0004-637X. doi: 10.1086/338332.
- Theodore P. Stecher. Interstellar Ectinction in the Ultraviolet. *ApJ*, 142:1683, November 1965. doi: 10.1086/148462.
- J. J. Swift, W. J. Welch, and J. Di Francesco. A PreProtostellar Core in L1551. *Astrophys. J.*, 620(2):823–834, 2005. ISSN 0004-637X. doi: 10.1086/427257.
- T. Temim, E. Dwek, K. Tchernyshyov, M. L. Boyer, M. Meixner, C. Gall, and J. Roman-Duval. Dust destruction rates and lifetimes in the magellanic clouds. *Astrophys. J.*, 799:158, 2015. ISSN 15384357. doi: 10.1088/0004-637X/799/2/158.
- P. Thomasson. MERLIN. *Q. J. R. Astron. Soc.*, 27:413–431, 1986.

- M. A. Thompson, J. S. Urquhart, T. J.T. Moore, and L. K. Morgan. The statistics of triggered star formation: An overdensity of massive young stellar objects around Spitzer bubbles. *Mon. Not. R. Astron. Soc.*, 421(1):408–418, 2012. ISSN 00358711. doi: 10.1111/j.1365-2966.2011.20315.x.
- A. G. G. M. Tielens. *The Physics and Chemistry of the Interstellar Medium*. 2005.
- A. M. Titmarsh, S. P. Ellingsen, S. L. Breen, J. L. Caswell, and M. A. Voronkov. A search for water masers associated with class II methanol masers - I. Longitude range 6 to 20. *MNRAS*, 443:2923–2939, 2014. ISSN 13652966. doi: 10.1093/mnras/stw636.
- A. M. Titmarsh, S. P. Ellingsen, S. L. Breen, J. L. Caswell, and M. A. Voronkov. A search for water masers associated with class II methanol masers - II. Longitude range 341 to 6. *MNRAS*, 459(1):157–170, 2016. ISSN 13652966. doi: 10.1093/mnras/stw636.
- C. H. Townes. Microwave and radio-frequency resonance lines of interest to radio astronomy. In Hendrik Christoffel van de Hulst, editor, *Radio astronomy*, volume 4 of *IAU Symposium*, page 92, Jan 1957.
- C. H. Townes and A. L. Schawlow. *Microwave Spectroscopy*. 1955.
- H. Ungerechts, C. M. Walmsley, and G. Winnewisser. Ammonia and Cyanoacetylene Observations of the High Density Core of L183 (L134N). *A&A*, 88:259, 1980.
- J. S. Urquhart, A. L. Busfield, M. G. Hoare, S. L. Lumsden, A. J. Clarke, T. J. T. Moore, J. C. Mottram, and R. D. Oudmaijer. The RMS survey - Radio observations of candidate massive YSOs in the southern hemisphere. *A&A*, 461(1):11–23, 2007a. ISSN 0004-6361. doi: 10.1051/0004-6361:20065837.
- J. S. Urquhart, A. L. Busfield, M. G. Hoare, S. L. Lumsden, R. D. Oudmaijer, T. J. T. Moore, A. G. Gibb, C. R. Purcell, M. G. Burton, and L. J. L. Marechal. The RMS Survey: 13CO observations of candidate massive YSOs in the southern Galactic plane. *A&A*, 474:891–901, 2007b. ISSN 00046361.
- J. S. Urquhart, M. A. Thompson, L. K. Morgan, M. R. Pestalozzi, Glenn J. White, and D. N. Muna. A tale of two cores: triggered massive star formation in the bright-rimmed cloud SFO 75. *A&A*, 467(3):1125–1137, 2007c. ISSN 0004-6361. doi: 10.1051/0004-6361:20077236.
- J. S. Urquhart, A. L. Busfield, M. G. Hoare, S. L. Lumsden, R. D. Oudmaijer, T. J. T. Moore, A. G. Gibb, C. R. Purcell, M. G. Burton, L. J. L. Marechal, Z. Jiang, and

- M. Wang. The RMS Survey: 13CO observations of candidate massive YSOs in the northern Galactic plane. *A&A*, 487:253–264, 2008. ISSN 00046361.
- J. S. Urquhart, M. G. Hoare, C. R. Purcell, S. L. Lumsden, R. D. Oudmaijer, T. J. T. Moore, A. L. Busfield, J. C. Mottram, and B. Davies. The RMS survey. 6 cm continuum VLA observations towards candidate massive YSOs in the northern hemisphere. *A&A*, 501:539, 2009. ISSN 0004-6361. doi: 10.1051/0004-6361/200912108.
- J. S. Urquhart, L. K. Morgan, C. C. Figura, T. J. T. Moore, S. L. Lumsden, M. G. Hoare, R. D. Oudmaijer, J. C. Mottram, B. Davies, and M. K. Dunham. The Red MSX Source survey: Ammonia and water maser analysis of massive star-forming regions. *MNRAS*, 418(3):1689–1706, 2011. ISSN 00358711. doi: 10.1111/j.1365-2966.2011.19594.x.
- J. S. Urquhart, M. G. Hoare, S. L. Lumsden, R. D. Oudmaijer, T. J. T. Moore, J. C. Mottram, H. D. B. Cooper, M. Mottram, and H. C. Rogers. The RMS survey: Resolving kinematic distance ambiguities towards a sample of compact H II regions using H I absorption. *MNRAS*, 420(2):1656–1672, 2012. ISSN 00358711. doi: 10.1111/j.1365-2966.2011.20157.x.
- J S Urquhart, T. J.T. Moore, F Schuller, F Wyrowski, K M Menten, M A Thompson, T Csengeri, C M Walmsley, L Bronfman, and C. König. ATLASGAL - environments of 6.7 GHz methanol masers. *MNRAS*, 431(2):1752–1776, 2013. ISSN 00358711. doi: 10.1093/mnras/stt287.
- J. S. Urquhart, T. Csengeri, F. Wyrowski, F. Schuller, S. Bontemps, L. Bronfman, K. M. Menten, C. M. Walmsley, Y. Contreras, H. Beuther, M. Wienen, and H. Linz. ATLASGAL Complete compact source catalogue: $280 < l < 60$. *A&A*, 568:A41, 2014a. ISSN 0004-6361. doi: 10.1051/0004-6361/201424126.
- J. S. Urquhart, C. C. Figura, T. J.T. Moore, M. G. Hoare, S. L. Lumsden, J. C. Mottram, M. A. Thompson, and R. D. Oudmaijer. The RMS survey: Galactic distribution of massive star formation. *MNRAS*, 437(2):1791–1807, 2014b. ISSN 00358711. doi: 10.1093/mnras/stt2006.
- J. S. Urquhart, C. C. Figura, T. J. T. Moore, T. Csengeri, S. L. Lumsden, T. Pillai, M. A. Thompson, D. J. Eden, and L. K. Morgan. The RMS survey: Ammonia mapping of the environment of massive young stellar objects. *Mon. Not. R. Astron. Soc.*, 452(4):4029–4053, 2015a. ISSN 13652966. doi: 10.1093/mnras/stv1514.
- J. S. Urquhart, T. J.T. Moore, K. M. Menten, C. König, F. Wyrowski, M. A. Thompson, T. Csengeri, S. Leurini, and D. J. Eden. The almost ubiquitous association

- of 6.7-GHz methanol masers with dust. *MNRAS*, 446(4):3461–3477, 2015b. ISSN 13652966. doi: 10.1093/mnras/stu2300.
- J. S. Urquhart, C. König, A. Giannetti, S. Leurini, T. J.T. Moore, D. J. Eden, T. Pillai, M. A. Thompson, C. Braiding, M. G. Burton, T. Csengeri, J. T. Dempsey, C. Figura, D. Froebrich, K. M. Menten, F. Schuller, M. D. Smith, and F. Wyrowski. ATLASGAL - Properties of a complete sample of Galactic clumps. *MNRAS*, 473(1): 1059–1102, 2018. ISSN 13652966. doi: 10.1093/mnras/stx2258.
- J. S. Urquhart, C. Figura, F. Wyrowski, A. Giannetti, W. J. Kim, M. Wienen, S. Leurini, T. Pillai, T. Csengeri, S. J. Gibson, K. M. Menten, T. J.T. Moore, and M. A. Thompson. ATLASGAL - Molecular fingerprints of a sample of massive star-forming clumps. *MNRAS*, 484(4):4444–4470, 2019. ISSN 13652966. doi: 10.1093/mnras/stz154.
- James Urquhart, Melvin Hoare, and Larry Morgan. The RMS Survey: Resolving Kinematic Distance Ambiguities in the Fourth Quadrant. ATNF Proposal, Oct 2010.
- D. J. Van Der Walt, E. Churchwell, M. J. Gaylard, and S. Goedhart. Radio continuum emission associated with Class II methanol maser sources. *MNRAS*, 276:270–276, 2003.
- D. J. Van Der Walt, S. Goedhart, and M. J. Gaylard. Periodic class II methanol masers in G9.62+0.20E. *MNRAS*, 398(2):961–970, 2009. ISSN 00358711. doi: 10.1111/j.1365-2966.2009.15147.x.
- J. Van Der Walt. On the number and lifetime of 6.7-GHz methanol masers. *MNRAS*, 360(1):153–158, 2005. ISSN 00358711. doi: 10.1111/j.1365-2966.2005.09026.x.
- E. Vázquez-Semadeni, A. Gazol, and J. Scalo. Is Thermal Instability Significant in Turbulent Galactic Gas? *Astrophys. J.*, 540(1):271–285, 2000. ISSN 15384357. doi: 10.1086/309318.
- E. Vázquez-Semadeni, M. Zamora-Avilés, R. Galván-Madrid, and J. Froebrich. Molecular cloud evolution - VI. Measuring cloud ages. *Mon. Not. R. Astron. Soc.*, 479(3): 3254–3263, 2018. ISSN 13652966. doi: 10.1093/mnras/sty1586.
- C. M. Walmsley and H. Ungerechts. Ammonia as a molecular cloud thermometer. *Astron. Astrophys. (ISSN 0004-6361)*, 122:164–170, 1983.
- A. J. Walsh, A. R. Hyland, G. Robinson, and M. G. Burton. Studies of ultracompact H II regions - I. Methanol maser survey of IRAS-selected sources. *MNRAS*, 291(2): 261–278, 1997. ISSN 00358711. doi: 10.1093/mnras/291.2.261.

- A. J. Walsh, M. G. Burton, A. R. Hyland, and G. Robinson. Studies of ultracompact H II regions - II. High-resolution radio continuum and methanol maser survey. *MNRAS*, 301(3):640–698, 1998. ISSN 00358711. doi: 10.1111/j.1365-8711.1998.02014.x.
- A. J. Walsh, F. Bertoldi, M. G. Burton, and T. Nikola. Mid-infrared observations of methanol maser sites and ultracompact H II regions: Signposts of high-mass star formation. *MNRAS*, 326:36–56, 2001. ISSN 00358711. doi: 10.1046/j.1365-8711.2001.04352.x.
- A. J. Walsh, S. L. Breen, T. Britton, K. J. Brooks, M. G. Burton, M. R. Cunningham, J. A. Green, L. Hindson, M. G. Hoare, B. Indermuehle, P. Jones, N. Lo, S. N. Longmore, V. Lowe, C. J. Phillips, C. R. Purcell, M. A. Thompson, J. S. Urquhart, M. A. Voronkov, G. L. White, and M. Whiting. The H₂O southern Galactic Plane Survey (HOPS): I. Techniques and H₂O maser data. *Sci. Technol.*, 000(March), 2011.
- A. J. Walsh, C. R. Purcell, S. N. Longmore, S. L. Breen, J. A. Green, L. Harvey-Smith, C. H. Jordan, and C. Macpherson. Accurate water maser positions from HOPS. *MNRAS*, 442(3):2240–2252, 2014. ISSN 13652966. doi: 10.1093/mnras/stu989.
- A. J. Walsh, H. Beuther, S. Bihr, K. G. Johnston, J. R. Dawson, J. Ott, S. N. Longmore, Q. Nguyễn Luong, R. S. Klessen, S. Ragan, N. McClure-Griffiths, A. Brunthaler, J. Urquhart, K. Menten, F. Bigiel, F. Wyrowski, and M. Rugel. A survey for hydroxyl in the THOR pilot region around W43. *MNRAS*, 455(4):3494–3510, 2016. ISSN 13652966. doi: 10.1093/mnras/stv2446.
- S. Weinreb, A. H. Barrett, M. L. Meeks, and J. C. Henry. Radio Observations of OH in the Interstellar Medium. *Nature*, 200(4909):829–831, Nov 1963. doi: 10.1038/200829a0.
- M. Wienen, F. Wyrowski, F. Schuller, K. M. Menten, C. M. Walmsley, L. Bronfman, and F. Motte. Ammonia from cold high-mass clumps discovered in the inner Galactic disk by the ATLASGAL survey. *A&A*, 544:A146, 2012. ISSN 0004-6361. doi: 10.1051/0004-6361/201118107.
- M. Wienen, F. Wyrowski, K. M. Menten, J. S. Urquhart, T. Csengeri, C. M. Walmsley, S. Bontemps, D. Russeil, L. Bronfman, B. S. Koribalski, and F. Schuller. ATLASGAL - Kinematic distances and the dense gas mass distribution of the inner Galaxy. *A&A*, 579, 2015. ISSN 0004-6361. doi: 10.1051/0004-6361/201424802.
- M. Wienen, F. Wyrowski, K. M. Menten, J. S. Urquhart, C. M. Walmsley, T. Csengeri, B. S. Koribalski, and F. Schuller. ATLASGAL Ammonia observations towards the

- southern Galactic plane. *A&A*, 609:A125, 2018. ISSN 0004-6361. doi: 10.1051/0004-6361/201526384.
- T. L. Wilson, K. Rohlfs, and S. Hüttemeister. *Tools of Radio Astronomy*. 2013. doi: 10.1007/978-3-642-39950-3.
- W. E. Wilson, R. H. Ferris, P. Axtens, A. Brown, E. Davis, G. Hampson, M. Leach, P. Roberts, S. Saunders, B. S. Koribalski, J. L. Caswell, E. Lenc, J. Stevens, M. A. Voronkov, M. H. Wieringa, K. Brooks, P. G. Edwards, R. D. Ekers, B. Emonts, L. Hindson, S. Johnston, S. T. Maddison, E. K. Mahony, S. S. Malu, M. Massardi, M. Y. Mao, D. McConnell, R. P. Norris, D. Schnitzeler, R. Subrahmanyam, J. S. Urquhart, M. A. Thompson, and R. M. Wark. The Australia Telescope Compact Array Broad-band Backend: Description and first results. *Mon. Not. R. Astron. Soc.*, 416(2):832–856, 2011. ISSN 00358711. doi: 10.1111/j.1365-2966.2011.19054.x.
- W. J. Wilson and A. H. Barrett. Discovery of OH Radio Emission from the Infrared Star NML Cygni. *The Astronomical Journal Supplement*, 73:209, Jan 1968.
- M. G. Wolfire, D. J. Hollenbach, and A. G. G. M. Tielens. CO1-0 line emission from giant molecular clouds. *Astrophys. J.*, 1993.
- E. L. Wright, P. R.M. Eisenhardt, A. K. Mainzer, M. E. Ressler, R. M. Cutri, T. Jarrett, J. D. Kirkpatrick, D. Padgett, R. S. McMillan, M. Skrutskie, S. A. Stanford, M. Cohen, R. G. Walker, J. C. Mather, D. Leisawitz, T. N. Gautier, I. McLean, D. Benford, C. J. Lonsdale, A. Blain, B. Mendez, W. R. Irace, V. Duval, Fe. Liu, D. Royer, I. Heinrichsen, J. Howard, M. Shannon, M. Kendall, A. L. Walsh, M. Larsen, J. G. Cardon, S. Schick, M. Schwalm, M. Abid, B. Fabinsky, L. Naes, and C. W. Tsai. The Wide-field Infrared Survey Explorer (wise): Mission description and initial on-orbit performance. *Astron. J.*, 140(6):1868–1881, 2010. ISSN 00046256. doi: 10.1088/0004-6256/140/6/1868.
- F. Wyrowski, R. Güsten, K. M. Menten, H. Wiesemeyer, T. Csengeri, S. Heyminck, B. Klein, C. König, and J. S. Urquhart. Infall through the evolution of high-mass star-forming clumps. *A&A*, 585:A149, 2016. ISSN 14320746. doi: 10.1051/0004-6361/201526361.
- Y. Xu, J. J. Li, K. Haschisuka, J. D. Pandian, K. M. Menten, and C. Henkel. A radio and near-infrared study of 6 . 7 GHz methanol maser sources A radio and near-infrared study of 6 . 7 GHz methanol maser sources. *A&A*, 485:729–734, 2008.

- K. Yang, X. Chen, Z.-Q. Shen, X.-Q. Li, J.-Z. Wang, D.-R. Jiang, J. Li, J. Dong, Y.-J. Wu, H.-H. Qiao, and Z. Ren. A 6.7 GHz Methanol Maser Survey at High Galactic Latitudes. *ApJ*, 846:160, 2017. ISSN 1538-4357. doi: 10.3847/1538-4357/aa8668.
- K. Yang, X. Chen, Z.-Q. Shen, X.-Q. Li, J.-Z. Wang, D.-R. Jiang, J. Li, J. Dong, Y.-J. Wu, and H.-H. Qiao. A 6.7 GHz Methanol Maser Survey. II. Low Galactic Latitudes. *Astrophys. J. Suppl. Ser.*, 241:18, 2019. ISSN 1538-4365. doi: 10.3847/1538-4357/aa8668.
- H. W. Yorke and P. Bodenheimer. Induced Angular Momentum Transport on Disk Structure and Appearance1. *ApJ*, 525:330–342, 1999.
- J. Zhu and M. Huang. Dust temperature maps of the Galactic plane: The Herschel spectral energy distribution fitting with Cloudy predictions. *Astron. Astrophys.*, 564: 1–5, 2014. ISSN 14320746. doi: 10.1051/0004-6361/201322723.
- H. Zinnecker and H. W. Yorke. Toward Understanding Massive Star Formation *. *Annu. Rev. Astron. Astrophys.*, 45:481–563, 2007. ISSN 0066-4146. doi: 10.1146/annurev.astro.44.051905.092549.
- B. Zuckerman and P. Palmer. Radio Radiation from Interstellar Molecules. *ARA&A*, 12:279, 1974.